UNIVERSITY OF CALIFORNIA

Los Angeles

Low-Power Magnetically Shielded Hall Thrusters

A dissertation submitted in partial satisfaction of the

requirements for the degree of Doctor of Philosophy

in Aerospace Engineering

by

Ryan William Conversano

2015

ABSTRACT OF THE DISSERTATION

Low-Power Magnetically Shielded Hall Thrusters

by

Ryan William Conversano
Doctor of Philosophy in Aerospace Engineering
University of California, Los Angles, 2015
Professor Richard E. Wirz, Chair

This dissertation presents an investigation of the applicability of magnetic shielding to low-power Hall thrusters as a means to significantly improve operational lifetime. The key life-limiting factors of conventional Hall thrusters, including ion-bombardment sputter erosion of the discharge channel and high-energy electron power deposition to the channel walls, have been investigated extensively for a wide range of thruster scales. As thruster power is reduced to the "miniature" (i.e. sub-500 W) power regime, the increased surface-to-volume ratio of the discharge channel and decreased thruster component sizes promotes increased plasma-wall interactions and susceptibility to overheating, thereby reducing thruster operational lifetime and performance. Although methods for compensating for these issues have been investigated, unshielded miniature Hall thrusters are generally limited to sub-45% anode efficiencies and maximum lifetimes on the order of 1,000 h. A magnetically shielded magnetic field topology aims to maintain a low electron temperature along the channel surfaces and a plasma potential near that of the discharge voltage along the entire surface of the discharge channel along its axial length. These features

result in a reduction of the kinetic energy of ions that impact the channel surfaces to near to or below the sputtering threshold, thus preventing significant ion-bombardment erosion of the discharge channel. Improved confinement of high-energy electrons is another byproduct of the field structure, aiding in the reduction of electron power deposition to the channel. Magnetic shielding has been shown to dramatically reduce plasma-wall interactions on 4 – 6 kW Hall thrusters, resulting in significant increases in projected operational lifetimes with minimal effects to thruster performance.

In an effort to explore the scalability of magnetic shielding to low-power devices, two magnetically shielded miniature Hall thrusters were designed, fabricated and tested. The performance of the first thruster, called the MaSMi-40, was characterized at an operating condition of 275 V and 325 W. A peak thrust of approximately 13 mN with a specific impulse of approximately 1,100 s at an anode efficiency of approximately 22% were measured at the nominal operating point. Observations of the near exit plasma discharge during operation, and the discharge channel after operation, suggested that the outer channel wall of the thruster was well shielded from ion bombardment while the inner channel wall appeared to be weakly shielded. Further analysis concluded that the MaSMi-40 generated a partially-magnetically shielded field topology. However, the shortcomings of the MaSMi-40's magnetic circuit design were investigated in detail and are now well understood.

The second design iteration in the development of a low-power magnetically shielded Hall thruster was the MaSMi-60. Magnetic field measurements confirmed that a symmetric and fully shielded magnetic field topology was generated by this device across a wide range of possible operating conditions. At operating powers of 160 W to nearly 750 W, the key performance metrics of the MaSMi-60 included a measured thrust ranging from approximately 8 mN to over

33 mN with anode specific impulses of up to approximately 1370 s at anode efficiencies of over 28%. Downstream plume measurements identified the primary factors contributing to the low anode efficiency. Visual observations of the discharge plasma and channel walls during and after thruster operation offered strong evidence of magnetic shielding. Erosion rates of the channel were approximated using carbon backsputter measurements; the results suggested a 10x - 100x decrease in wall erosion compared to unshielded Hall thrusters, corresponding to an equal increase in discharge channel lifetime compared to conventional miniature unshielded Hall thrusters.

The physics and behaviors of the MaSMi-60's plasma discharge upstream of and in the near-field of the thruster exit plane were investigated using Hall2De, the 2-D axisymmetric code developed at the Jet Propulsion Laboratory for the simulation of the partially ionized plasma in Hall thrusters. Simulations of the MaSMi-60 suggested that the thruster achieved the plasma properties required for effective magnetic shielding, including low electron temperatures and a near-constant plasma potential along the channel walls. This was the final piece of evidence suggesting that magnetic shielding was attained at the miniature scale. The experimentally measured performance of the MaSMi-60 was captured by the Hall2De model, offering physical explanations for the low measured anode efficiency and leading to suggestions for improving the performance in future design iterations.

The dissertation of Ryan William Conversano is approved.

Jeff D. Eldredge

Dan M Goebel

Nasr M. Ghoniem

Warren B. Mori

Richard E. Wirz, Committee Chair

University of California, Los Angeles

2015

"Shoot for the moon. Even if you miss you will land among the stars."

~ Les Brown

Table of Contents

List of Figures ..... **xiii**

List of Tables ..... **xxiii**

Nomenclature ..... **xxiv**

Acknowledgments ..... **xxx**

About the Author ..... **xxxiii**

Chapter 1: Introduction **1**

1.1 Motivation 1

1.2 Problem Statement 2

1.3 Dissertation Overview 3

Chapter 2: Electric Propulsion Overview **5**

2.1 Rocket Equation Basics 5

2.2 Electric Thruster Classes 7

2.2.1 Electrothermal 7

2.2.2 Electromagnetic 8

2.2.3 Electrostatic 9

2.3 Electric Propulsion Background 11

2.4 Concluding Remarks 13

Chapter 3: Hall Thrusters **14**

3.1 Electrostatic Propulsion Theory 14

3.2 Hall Thruster Geometry and Types 18

3.3 Operating Principles 20

3.4 Life-Limiting Factors....24
3.5 Low-Power Hall Thrusters....26
3.6 Magnetic Shielding Theory....31
3.7 Concluding Remarks....37
Chapter 4: Magnetically Shielded Miniature Hall Thruster: Preliminary Design and Projected Performance....38
4.1 Preliminary Design of the MaSMi-40....38
4.1.1 Scaling Methodology and Results....38
4.1.2 Geometry....41
4.1.3 Magnetic Field....41
4.2 Performance Modeling....42
4.2.1 Power Balance....42
4.2.2 Thermal Design....45
4.2.3 Separatrix Analysis....46
4.3 Concluding Remarks....49
Chapter 5: Experimental Facilitates, Diagnostics, and Test Setups....50
5.1 UCLA Electric Propulsion Test Facility....50
5.2 JPL High Bay Vacuum Facility....52
5.3 Assessment of the Magnetically Shielded Field Topology....55
5.4 Performance and Plume Characterization....57
5.4.1 Thrust Stand....57
5.4.2 Plasma and Thruster Diagnostics....58
5.4.2.1 Key Plasma and Thruster Performance Parameters....58

5.4.2.2 Emissive Probe.....59
5.4.2.2.1 Operation Principles.....59
5.4.2.2.2 Geometry and Data Collection Procedure 60
5.4.2.2.3 Uncertainty Analysis.....61
5.4.2.3 Planar and Faraday Probes.....61
5.4.2.3.1 Operation Principles.....61
5.4.2.3.2 Geometry and Data Collection Procedure 62
5.4.2.3.3 Uncertainty Analysis.....65
5.4.2.4 Retarding Potential Analyzer.....66
5.4.2.4.1 Operation Principles.....66
5.4.2.4.2 Geometry and Data Collection Procedure 68
5.4.2.4.3 Uncertainty Analysis.....70
5.4.2.5 **E**x**B** Probe.....70
5.4.2.5.1 Operation Principles.....70
5.4.2.5.2 Geometry and Data Collection Procedure 73
5.4.2.5.3 Uncertainty Analysis.....74
5.4.2.6 Langmuir Probe 74
5.4.2.6.1 Operation Principles.....74
5.4.2.6.2 Geometry and Data Collection Procedure 78
5.4.2.6.3 Uncertainty Analysis.....79
5.4.2.7 Quartz Crystal Microbalance 80
5.4.2.7.1 Operation Principles.....80
5.4.2.7.2 Geometry and Data Collection Procedure 81

5.4.2.7.3 Uncertainty Analysis 82
5.4.2.8 Installed Diagnostics 82
5.5 Concluding Remarks 84
Chapter 6: MaSMi-40 Performance Testing 85
Chapter 6, Part I: Electric Propulsion Test Facility, UCLA 86
6.1 Experimental Results and Discussion, UCLA EP Test Facility 86
6.1.1 Magnetic Shielding Assessment 87
6.1.2 Planar Probe Results 88
6.1.3 Retarding Potential Analyzer Results 89
6.1.4 Thrust, Efficiency, and Specific Impulse Calculations 91
6.2. Concluding Remarks, UCLA EP Test Facility 92
Chapter 6, Part II: High Bay Facility, JPL 93
6.3 Experimental Results and Discussion, JPL High Bay Facility 93
6.3.1 Operating Conditions 93
6.3.2 Magnetic Shielding Assessment 94
6.3.3 Performance Measurements: Thrust Stand 95
6.3.4 Performance Measurements: Plasma Diagnostics 97
6.3.4.1 Faraday Probe Results 97
6.3.4.2 Retarding Potential Analyzer Results 98
6.3.4.3 **E**x**B** Probe Results 100
6.3.4.4 Calculated Performance Summary 101
6.3.5 Discharge Current Oscillations 102
6.4 MaSMi-40 Performance Overview 103

6.4.1 MaSMi-40 Magnetic Field Topology: Investigation and Correction 105
6.5 Concluding Remarks.....106
Chapter 7: MaSMi-60 Development and Performance Testing 107
7.1 MaSMi-60 Thruster Design 107
7.1.1 Geometry.....107
7.1.2 Magnetic Field 108
7.1.3 Thermal Modeling 108
7.2 Experimental Results and Discussion.....110
7.2.1 Operating Conditions.....110
7.2.1.1 Defining Nominal Operation 113
7.2.2 Magnetic Shielding Assessment 115
7.2.3 Performance Measurements: Thrust Stand 119
7.2.3.1 Thrust.....119
7.2.3.2 Anode Specific Impulse.....119
7.2.3.3 Anode Efficiency 120
7.2.4 Performance Measurements: Plasma Diagnostics 121
7.2.4.1 Faraday Probe Results.....121
7.2.4.2 Retarding Potential Analyzer and Emissive Probe Results 124
7.2.4.3 **E**x**B** Probe Results 127
7.2.4.4 Calculated Performance Summary 131
7.3. Concluding Remarks.....133
Chapter 8: Computational Analysis of the MaSMi-60 Plasma Discharge 134

8.1. Motivation for Plasma Modeling in Low-Power Hall Thrusters 134
8.2. Brief History of Hall Thruster Numerical Models 135
8.3. Hall2De 136
8.3.1 Code Overview 136
8.3.2 Physics Model 139
8.3.2.1 Ion Governing Equations 139
8.3.2.2 Electron Governing Equations 140
8.3.2.2.1 Model of the Anomalous Collision Frequency 144
8.3.2.3 Neutral Particle Governing Equations 145
8.4. Hall2De Simulation Results for the MaSMi-60 146
8.4.1 Magnetic Shielding 146
8.4.2 Thruster Performance and Associated Physics 149
8.4.2.1 Physics Governing the MaSMi-60's Low Mass Utilization 150
8.4.2.2 Physics Governing the MaSMi-60's Low Current Utilization 162
8.4.2.3 Physics Governing the MaSMi-60's High Beam Divergence 163
8.5. Results Verification 167
8.5.1 Sensitivity Study Results 168
8.5.2 Near Exit Plane Plasma Measurement Results 178
8.6. Plasma Physics and Behaviors of Low-Power MS Hall Thrusters 180
8.7. Concluding Remarks 183

Chapter 9: Conclusion **184**

9.1. The Applicability of Magnetic Shielding to Low-Power Hall Thrusters 186

9.2. Physics and Limitations of Magnetic Shielding at Low Powers 187

9.3. Proposed Future Work 188

Appendix A: MaSMi-60 Retarding Potential Analyzer Profiles **191**

References **195**

List of Figures

Chapter 2

2.2-1 Illustration of the geometry and operation of a resistojet (top) and an arcjet (bottom).....8

2.2-2 Illustration of the geometry and operation of a magnetoplasmadynamic thruster / Lorentz-force accelerator.....9

2.2-3 Illustration of the geometry and operation of a gridded ion thruster 10

2.2-4 Illustration of the basic geometry of a Hall thruster. 11

Chapter 3

3.2-1 Hall thruster cross-section showing the applied electric and magnetic fields along with the xenon neutral, xenon ion, and electron paths.....19

3.2-2 TAL thruster cross-section showing the applied electric and magnetic fields along with the xenon neutral, xenon ion, and electron paths.....20

3.3-1 Typical Hall thruster voltage distribution along the length of the discharge channel 24

3.4-1 Illustration of the wall sheath potential structure (Φ_s) in an unshielded Hall thruster and its effect on the ion and electron populations in the bulk plasma.....25

3.4-2 Illustration of the magnetic field topology in an unshielded Hall thruster 26

3.5-1 Trends of discharge channel width-to-mean-diameter ratio vs. input power for a variety of Hall thrusters.....27

3.5-2 Photograph of the Busek BHT-200 Hall thruster 30

3.6-1 Illustration of the field topology in a magnetically shielded Hall thruster 32

3.6-2 Illustration of the upper half of a Hall thruster's discharge channel with representative magnetic field structures (top) and electron temperature and discharge plasma potential profiles (bottom). Left: general features of Hall thruster operation with typical profiles along the channel centerline (CL). Middle: field topology and profiles observed in unshielded Hall thrusters. Right: field topology and profiles observed in magnetically shielded Hall thrusters 34

3.6-3 Illustration of the wall sheath potential structure in a magnetically shielded Hall thruster and its effect on the ion and electron populations in the bulk plasma. The sheath potential structure for an unshielded thruster is also shown for comparison (dashed line) 36

Chapter 4

4.1-1 Predicted discharge power, thrust, and specific impulse for the MaSMi-40 based on scaling laws. The diamonds represent MaSMi-40's predicted performance based on each reference thruster (BHT-200, A3, and SPT-100) and the circles represent MaSMi-40's predicted performance averaged over the reference thrusters 41

4.2-1 Estimated electron temperature and total power deposition as a function of discharge voltage for a ~40 mm unshielded Hall thruster operating at 1.3 A discharge current 45

4.2-2 Photograph of the MaSMi-40 fitted with the "X-Wing" radiator and hollow cathode 46

4.2-3 Magnetic field structure of a Hall thruster with discrete outer coils showing the two species of magnetic field lines and the location of the separatrix.....48

Chapter 5

5.1-1 UCLA Electric Propulsion Test Facility chamber and supporting equipment 51

5.2-1 JPL High Bay Facility vacuum chamber and supporting equipment 53

5.2-2 High Bay Facility pressure as a function of total hot propellant flow rate at five discharge voltage operating points using the MaSMi-60 54

5.4-1 Photograph of the MaSMi-40 mounted to the thrust stand installed in the JPL High Bay vacuum chamber 58

5.4-2 Cross-sectional diagram of the filament-end of an emissive probe.....59

5.4-3 Cross-sectional diagram of a planar probe (left) and a Faraday probe (right) showing the effects of the negative collector bias on the incident plasma 61

5.4-4 Uncorrected and corrected current density profiles highlighting the charge-exchange effects on the measurement data.....65

5.4-5 Cross-sectional diagram of a 4-grid retarding potential analyzer.....67

5.4-6 Illustration of an **E**x**B** probe with the orientation of the electric and magnetic fields relative to the incident plasma specified.....71

5.4-7 Example Langmuir trace with a linear (top) and semi-log (bottom) vertical scale highlighting the ion saturation, electron saturation, and electron retardation regions 75

5.4-8 Example Langmuir trace showing the exponential fits to the electron retardation and electron saturation regions and highlighting the method for determining the electron temperature and plasma potential from exponential fits to the trace.....78

5.4-9 Illustration of the sensor element of a quartz crystal microbalance system 81

5.4-10 Experimental configuration inside the vacuum chamber at the UCLA EP Test Facility 83

5.4-11 Downstream experimental configuration at the JPL High Bay Facility showing complete coverage of all downstream diagnostics and structures in carbon materials (carbon felt, graphite, etc.) 83

5.4-12 Upstream experimental configuration at the JPL High Bay Facility (Langmuir probe, Langmuir probe drives, and QCM were used for the MaSMi-60 only).....84

Chapter 6

6.1-1 Operation of the MaSMi-40 at 275 V and 325 W (left) with a magnified view of the upper region of the discharge channel (right) showing a slight offset of the plasma from the wall typical of magnetic shielding.....87

6.1-2 Comparison of the MaSMi-40's discharge channel before and after approximately 4 hours of operation 88

6.1-3 Current density as a function of the planar probe's radial position from the thruster centerline, corrected for background charge-exchange effects and measured for nominal MaSMi-40 operating conditions at one and two discharge channel diameters downstream of the thruster face.....89

6.1-4 Normalized ion current and its derivative as functions of ion discriminator grid potential for MaSMi-40’s nominal operating condition.....91

6.3-1 Comparison of the MaSMi-40's discharge channel after operation in the jet mode (left) and the diffuse mode (right), showing a significant reduction in carbon deposition along the inner wall 95

6.3-2 The MaSMi-40’s near-exit plasma discharge while operating at 275 V and 1.2 A in the low-temperature jet mode (left) and the high-temperature diffuse mode (right) 96

6.3-3 Corrected ion current density as a function of lateral position from thruster centerline for the MaSMi-40 operating at nominal conditions in the jet and diffuse operating modes.....98

6.3-4 Normalized ion current (top) and its derivative (bottom) as functions of ion discriminator bias potential for nominal operation of the MaSMi-40 in the jet and diffuse modes 99

6.3-5 Normalized ion velocity spectra showing the MaSMi-40’s beam composition during operation at nominal conditions in the jet mode.....100

6.3-6 Normalized ion velocity spectra showing the MaSMi-40’s beam composition during operation at nominal conditions in the diffuse mode.....101

6.3-7 Comparison of the discharge current oscillations measured during operation of the MaSMi-40 in the low-temperature jet mode and the high-temperature diffuse mode.....103

Chapter 7

7.1-1 The MaSMi-60 mounted to the thermal radiator on the JPL High Bay Facility thrust stand 110

7.2-1 Discharge current as a function of inner coil current for operation of the MaSMi-60 at a discharge voltage of 200 V and anode flow rates of 12 and 14 sccm 113

7.2-2 Discharge current as a function of inner coil current for operation of the MaSMi-60 at discharge powers of 250 W (top), 400 W (middle), and 550 W (bottom) 114

7.2-3 Operation of the MaSMi-60 at 250 V and 335 W showing evidence of successful magnetic shielding through a clear offset of the plasma from the inner and outer discharge channel walls 115

7.2-4 Comparison of the MaSMi-60's discharge channel and pole faces before and after ~20 hours of operation. Note the level of front inner and outer pole face erosion 116

7.2-5 Thrust as a function of discharge power for the MaSMi-60 119

7.2-6 Anode specific impulse as a function of discharge power for the MaSMi-60 120

7.2-7 Anode efficiency as a function of discharge power for the MaSMi-60 121

7.2-8 Ion current density profiles for the MaSMi-60 at discharge powers of 250 W (top), 400 W (middle), and 550 W (bottom) 123

7.2-9 Normalized ion current as a function of RPA ion discriminator potential for 200 V, 250 V, and 300 V operation of the MaSMi-60 125

7.2-10 Normalized dI/dV as a function of RPA ion discriminator potential for 200 V, 250 V, and 300 V operation of the MaSMi-60 126

7.2-11 Emissive probe floating potential as a function of applied heater current across the full range of examined operating discharge voltages of the MaSMi-60 126

7.2-12 Normalized velocity spectra showing the MaSMi-60's beam composition during operation at 200 V and 250 W (top), 400 W (middle), and 550 W (bottom).....128

7.2-13 Normalized velocity spectra showing the MaSMi-60's beam composition during operation at 250 V and 250 W (top), 400 W (middle), and 550 W (bottom).....129

7.2-14 Normalized velocity spectra showing the MaSMi-60's beam composition during operation at 300 V and 250 W (top), 400 W (middle), and 550 W (bottom).....130

Chapter 8

8.4-1 Plasma potential (top) and electron temperature (bottom) contours from Hall2De simulations of the MaSMi-60 operating at 300 V and 1.4 A. 147

8.4-2 Plasma potential (blue) and electron temperature (red) plotted along the outer and inner discharge channel walls from Hall2De simulations of the MaSMi-60 operating at 300 V and 1.4 A 148

8.4-3 Published plasma potential (left) and electron temperature (right) contour plots for the H6MS (predicted using Hall2De).....149

8.4-4 Neutral density profiles for the MaSMi-60 (top) and H6MS (bottom) 151

8.4-5 Electron temperature (T_e) and electron density (n_e) predicted for the MaSMi-60 and H6MS as functions of axial position normalized to the MaSMi-60's discharge channel length 157

8.4-6 Ionization mean free path predicted for the MaSMi-60 and H6MS as a function of axial position, both normalized to the respective thruster's discharge channel length 159

8.4-7 Ionization fraction as functions of axial position normalized to the MaSMi-60's discharge channel length for the MaSMi-60 and H6MS 161

8.4-8 Plasma potential for the MaSMi-60 and H6MS from Hall2De simulations as a function of axial position normalized to the each thruster's respective discharge channel length 166

8.5-1 Comparison of the nominal and modified anomalous resistivity profiles with the relevant collision frequencies for the MaSMi-60 170

8.5-2 Comparison of the electron temperature and plasma potential profiles along the channel centerline based on the nominal and modified anomalous collision frequency profile for the MaSMi-60 171

8.5-3 Plasma potential (blue) and electron temperature (red) plotted along the outer and inner discharge channel walls from Hall2De simulations of the MaSMi-60 operating at 300 V and 1.4 A with the modified anomalous collision frequency profile 172

8.5-4 Comparison of the nominal, upstream-shifted, and downstream-shifted anomalous collision frequency profiles with the relevant collision frequencies for the MaSMi-60 174

8.5-5 Comparison of the electron temperature and plasma potential profiles along the channel centerline based on the nominal, upstream-shifted, and downstream-shifted anomalous collision frequency profile for the MaSMi-60 175

8.5-6 Plasma potential (blue) and electron temperature (red) plotted along the outer and inner discharge channel walls from Hall2De simulations of the MaSMi-60 operating at 300 V and 1.4 A with the upstream-shifted anomalous collision frequency profile 176

8.5-7 Plasma potential (blue) and electron temperature (red) plotted along the outer and inner discharge channel walls from Hall2De simulations of the MaSMi-60 operating at 300 V and 1.4 A with the downstream-shifted anomalous collision frequency profile 177

8.5-8 Comparison of experimental measurement, the nominal Hall2De simulation, and the scaled Hall2De simulation of electron temperature along the channel centerline for the MaSMi-60 operating at 300 V and 1.4 A 179

8.5-9 Comparison of experimental measurements and the nominal Hall2De simulation of the plasma potential along the channel centerline for the MaSMi-60 operating at 300 V and 1.4 A 180

Appendix A

A-1 Normalized ion current and dI/dV as a function of RPA ion discriminator potential for operation of the MaSMi-60 at 200 V and 250 W (top), 400 W (middle), and 550 W (bottom) 192

A-2 Normalized ion current and dI/dV as a function of RPA ion discriminator potential for operation of the MaSMi-60 at 250 V and 250 W (top), 400 W (middle), and 550 W (bottom)..... 193
A-3 Normalized ion current and dI/dV as a function of RPA ion discriminator potential for operation of the MaSMi-60 at 300 V and 250 W (top), 400 W (middle), and 550 W (bottom)..... 194

List of Tables

Chapter 3

3.5-1 Summary of the size, power, performance, and useful life of a selection of low-power Hall thrusters.....31

Chapter 6

6.1-1 Summary of the MaSMi-40's calculated anode performance, corrected for background neutrals, for operation at the UCLA Electric Propulsion Test Facility 92

6.3-1 Summary of the MaSMi-40's efficiencies measured and calculated at the JPL High Bay Facility.....102

Chapter 7

7.2-1 Operating conditions for the MaSMi-60 during thrust stand measurements, summarizing nominal power achieved as a function of discharge voltage and anode flow rate.....111

7.2-2 Summary of ion current density, divergence half-angle, and the associated uncertainties for operation of the MaSMi-60.....124

7.2-3 Summary of the most probable ion potential, downstream plasma potential, and the associated uncertainty for operation of the MaSMi-60.....127

7.2-4 Summary of ion species' contributions to the beam current for operation of the MaSMi-60 131

7.2-5 Summary of the MaSMi-60's measured and calculated efficiencies 132

Nomenclature

English Alphabet

A	Fitting coefficient
$\boldsymbol{A}$	Vector potential
A_{en}	Entrained neutral mass flow area [m^2]
A_p	Probe area [m^2]
A_{RPA}	RPA orifice area [m^2]
A_s	Surface area [m^2]
A_w	Channel surface area in contact with plasma [m^2]
A_x	Cross-sectional area perpendicular to heat flow [m^2]
B	Magnetic field (magnitude) [T,G]
$\boldsymbol{B}$	Magnetic field (vector) [T,G]
$B_{r,max}$	Peak radial magnetic field along channel centerline [T,G]
b	Discharge channel width [m]; exponential fit coefficient
b_{ref}	Reference discharge channel width [m]
d	**E**x**B** probe parallel plate separation distance [m]; temperature gradient distance [m]
d_m	Mean channel diameter [m]
d_{ref}	Reference mean channel diameter [m]
E	Electric field (magnitude) [V/m]; Energy [J]
$\boldsymbol{E}$	Electric field (vector) [V/m]
e	Electron charge [C]
$\boldsymbol{F}$	Lorentz force [N]; net force (vector) [N]
$\mathbf{F}_i$	Specific force on ions [N]
f	Electron distribution function
f_i	Current fraction of the i^{th} ion species; ion distribution function; ionized propellant fraction
f_n	Neutral particle distribution function; neutral propellant fraction
g	Earth's gravity constant [m/s^2]
$\mathbf{I}$	Delta tensor
$I^{+,++,...}$	Current of each ion charge species [A]
I_a	Anode current [A]
I_b	Beam current [A]
I_d	Discharge current [A]
$I_{d,corr}$	Corrected discharge current [A]
I_e	Electron current [A]

I_{en} Entrained ion current [A]

I_{ew} Electron current to channel walls [A]

$I_{e,sat}$ Electron saturation current [A]

I_i Current of the i^{th} ion species [A]

$I_{i,sat}$ Ion saturation current [A]

I_{iw} Ion current to channel walls [A]

I_p Probe collected current [A]

I_{sp} Specific impulse [s]

$I_{sp,corr}$ Corrected specific impulse [s]

J_i Ion current density [A/m^2]

j_{Te} Electron thermal flux [W]

$\boldsymbol{j}$, $\mathbf{j}$ Current density (vector) [A]

$\mathbf{j}_e$ Electron current density (vector) [A]

$\mathbf{j}_i$ Ion current density (vector) [A]

Kn Knudsen number

k Boltzmann constant [m^2 kg/s^2 K]

L Discharge channel length [m]

L_{ref} Reference discharge channel length [m]

M Xenon atomic mass [kg]

m Electron mass [kg]

m_{BN} Particle mass of BN [kg]

m_C Particle mass of carbon [kg]

m_d Delivered mass [kg]

m_p Propellant mass [kg]

$\dot{m}_a$ Anode mass flow rate [kg/s]

$\dot{m}_{a,corr}$ Corrected anode mass flow rate [kg/s]

$\dot{m}_b$ Beam mass flow rate [kg/s]

$\dot{m}_c$ Cathode mass flow rate [kg/s]

$\dot{m}_{en}$ Entrained neutral mass flow rate [kg/s]

$\dot{m}_i$ Ion mass flow rate [kg/s]

$\dot{m}_T$ Total propellant flow rate [kg/s]

n_a Anode propellant particle density [m^{-3}]

n_e Electron density [m^{-3}]

n_{e0} Channel centerline electron density [m^{-3}]

n_i Ion density [m^{-3}]

$n_{i,fast}$ Fast (beam) ion density [m^{-3}]

$n_{i,slow}$ Slow (charge-exchange) ion density [m^{-3}]

n_n Neutral density [m^{-3}]

n_{ref} Reference plasma density [m^{-3}]

P Vacuum chamber pressure [Pa]

P_a Power to anode from electron loss [W]

P_b Beam power [W]

P_d Discharge power [W]

P_i Power for ionization [W]

P_{jet} Jet power [W]

P_k Keeper power [W]

P_{mag} Magnet power [W]

P_R Plasma radiative power loss [W]

P_{ref} Reference discharge power [W]

P_T Total thruster input power [W];

pressure [Torr]

$P_{T,corr}$ Corrected total power [W]

P_w	Power deposited to channel walls [W]
$\mathbf{p}_e$	Electron pressure tensor
$\mathbf{p}_i$	Ion pressure tensor
p_e	Electron pressure
p_i	Ion pressure
$\mathbf{Q}_e$	Thermal conduction heat flux tensor
$\dot{Q}_{cond}$	Conductive heat transfer [W]
$\dot{Q}_{rad}$	Radiative heat transfer [W]
q	Particle charge [C]
q_e	Electron charge [C]
$\mathbf{q}_e$	Conductive heat flux [W]
q_i	Ion charge [C]
R_C	Carbon backsputter rate [μm/h]
R_e	Electron drag force [N]
R_i	Ion drag force [N]
R_L	Ion Larmor (gyro-) radius [m]
R_n	n^{th} radial distance of the probe from centerline [m]
$\mathbf{r}$	Position (vector) [m]
r_L	Electron Larmor (gyro-) radius [m]
T	Thrust [N]
T_1	Temperature of zone rejecting heat (heat out-flux) [K]
T_2	Temperature of zone receiving heat (heat in-flux) [K]
T_{corr}	Corrected thrust [N]
T_e, T_{eV}	Electron temperature [K,eV]
T_{e0}	Channel centerline electron temperature [K]
T_i	Ion temperature [K]
T_n	Neutral gas temperature [K]
t	Discharge plasma thickness [m]; time [s]
t_{BN}	Discharge channel thickness [m]
t_{grid}	Total RPA grid transparency
U^+	Ionization potential [V]
$\mathbf{u}_e$	Mean electron velocity [m/s]
$\mathbf{u}_i$	Mean ion velocity [m/s]
u_i	Normal component of ion velocity [m/s]
V	Plasma volume [m^3]
V_A	Anode potential [V]
V_b	Beam voltage [V]
V_{bias}	Bias potential [V]
V_{cg}	Cathode-to-ground voltage [V]
V_d	Discharge Voltage [V]
V_{float}	Floating potential [V]
V_g	RPA grid potential difference [V]
V_p	Plasma potential [V]
V_{ref}	Reference discharge voltage [V]
$V_\perp$	Ion velocity perpendicular to the magnetic field [m/s]
v	Particle velocity [m/s]
$\boldsymbol{v}$,$\mathbf{v}$	Particle velocity (vector) [m/s]

v_E	ExB drift velocity [m/s]
v_e	Electron velocity [m/s]
v_{ex}	Effective exhaust velocity [m/s]
v_i	Ion velocity [m/s]
v_n	Neutral velocity [m/s]
v_{th}	Neutral thermal velocity [m/s]
$v_\perp$	Electron velocity perpendicular to the magnetic field [m/s]
w	Radial width of plasma beam sampled by probe [m]
x	RPA grid spacing [m]
$Y_{Xe\text{-}BN}$	Sputter yield of BN under xenon ion incidence
$Y_{Xe\text{-}C/BN}$	Sputter yield of carbon-coated BN under xenon ion incidence
Z	Ion charge state
Z_i	Charge state of the i^{th} ion species
z	Axial location [m]

Greek Alphabet

α	Doubly charged correction factor; sticking coefficient
β	Bohm coefficient
Γ_{exit}	Ionized particle flux exiting the discharge plasma [$m^{-2}s^{-1}$]
$\Gamma_{incident}$	Neutral particle flux entering the discharge plasma [$m^{-2}s^{-1}$]
Γ_n	Neutral particle flux [s^{-1}]
γ	Secondary electron yield
γ_i	Ion adiabatic coefficient
ΔV	Change of velocity [m/s]
ε	Emissivity
$\boldsymbol{\varepsilon}$	Pre-sheath energy [J]
ε_0	Vacuum permittivity [$A^2 s^4/kg\ m^3$]
$\varepsilon_{Xe\text{-}BN}$	Erosion rate of BN under xenon ion incidence [m/h]
ζ_{en}	Entrained mass utilization factor
η_a	Anode efficiency
η_b	Beam current utilization efficiency
η_c	Cathode efficiency
$\eta_{c,corr}$	Corrected cathode efficiency
η_d	Plume divergence efficiency
η_{loss}	Wall, anode, and ionization power loss factor
η_m	Mass utilization efficiency
η_o	Electrical utilization efficiency
$\eta_{o,corr}$	Corrected electrical efficiency
η_q	Charge utilization efficiency
η_T	Total efficiency
$\eta_{T,corr}$	Corrected total efficiency
η_{tc}	Effective thruster efficiency
η_v	Beam voltage utilization efficiency
θ	Beam divergence half-angle [Rad]
κ	Thermal conductivity [$W/m^2 K$]
κ_e	Electron thermal conductivity [$W/m^2 K$]
λ	Mean free path [m]
λ_D	Debye length [m]
λ_i	Ionization mean free path [m]
ν_a	Anomalous collision frequency [1/s]
ν_e	(Total) electron collision frequency [1/s]
ν_{en}	Electron-neutral collision frequency [1/s]
ν_{en}^I	Electron-neutral ionization collision frequency [1/s]
ρ_{BN}	BN mass density [kg/m^3]
ρ_C	Carbon mass density [kg/m^3]
σ	Stefan-Boltzmann constant [W/m^2K^4]
σ_i	Ionization cross section [m^2]

σ_*	Excitation cross section [m^2]	Ω_e	Electron Hall parameter
Φ	Plasma potential [V]	Ω_i	Ion gyrofrequency (i.e. cyclotron frequency) [rad/s]
Φ_0	Channel centerline plasma potential [V]		
Φ_s	Sheath potential [V]	ω_c	Electron gyrofrequency (i.e. cyclotron frequency) [rad/s]
ϕ	Potential [V]		

ACKNOWLEDGMENTS

I firmly believe that behind every successful endeavor is a team of family, friends, and colleagues that make the effort possible, and my experience leading to the preparation of this dissertation is no exception. While it is impossible to acknowledge every individual who has supported this academic undertaking, I wish to take a few moments to thank some of the individuals who helped me on the path to my Ph.D.

Firstly, to my wife, Julia. You offered boundless compassion and unwavering support throughout my graduate school career. Through thick and thin, you was always a guiding hand, an inspirational muse, and my best friend. Thank you for accompanying me on this journey.

To my parents, Mary and Henry. You provided me with both emotional and financial support during my decade-long tenure as a UCLA student. You allowed me to set the foundations for my life and future career, and I quite literally would not be here without you!

To my brothers, Brad and Todd. Spending time with you two was always special for me. You were my closest friends (apart from my wife), and some of the best anyone could ask for. Thank you for being there when I need support, a good laugh, and for smiling and nodding politely on those days when I described my technical work and publications to you in insufferable detail. Good times…

To my "SoCal family," Annette, Mark, and Janelle. You became some of the most important, loving, and caring (and a little goofy) people in my life. A home-away-from-home was never so fun, spontaneous, and loving as the Kulik household.

To my UCLA advisor, Richie Wirz. You provided me my first insight into the fascinating fields of astrodynamics, spacecraft design, and ultimately electric propulsion. You took a chance by offering me an undergraduate appointment in your lab and pushed me to be an independent

and creative thinker throughout our six years together. You helped me develop into a successful engineer, and I am very appreciative of your efforts.

To my JPL advisor, Dan Goebel. You knew something (and often, damn near everything) about everything. You offered yourself as a role model, a counselor, and a friend during my journey towards my doctorate. You were the Virgil to my Dante, and I am truly fortunate to have been able to work so closely with someone so highly esteemed by the aerospace engineering community.

To the many individuals who enabled my experimental investigation and educational enrichment at the Jet Propulsion Laboratory by offering me a state-of-the-art facility in which to conduct my research. Rich Hofer, you taught me the art of Hall thruster design, the importance of good research documentation and organization, and the necessity of sufficient scrutiny in the assessment of my own work (as well as that of others) to ensure success. Yiangos Mikellides, you showed me the applications and value of computational modeling and offered yourself as a plasma physics instructor when various Hall thruster phenomena were unclear to me. Ira Katz, your support of my work at the lab and beyond helped make my thesis research project into a potential flight-project thruster and I am excited to see if this technology can help guide the future of spaceflight. Steve Snyder and Jay Polk, you offered invaluable guidance in the preparation of my experimental facility and were always available to answer questions about my research. Ray Swindlehurst and Nowell Niblett, you kept me safe in the machine shop and helped me troubleshoot the various problems (big and small) that I encountered with my experimental facility.

To my funding sources and sponsors that enabled the completion of my dissertation: the NASA Space Technology Research Fellowship, the NSF SEE-LA GK12 Fellowship Program, the

AeroClub of Southern California, the UCLA Chancellor's Prize Fund, the UCLA Graduate Student Research Mentorship Fund, and the UCLA Graduate Division Student Support Fund. I would also like to extend my appreciation to Mr. Stephen Lyle of the Saint-Gobain Company for his continued generosity and support of my thesis research.

And lastly, to the members of my dissertation committee: Jeff Eldredge, Nasr Ghoniem, and Warren Mori. You critiqued my thesis research and reviewed my dissertation, ensuring that I was fully prepared to receive my Ph.D.

To all of you, I offer a resounding “THANK YOU!”

RWC
Los Angeles, CA
August 2015

P.S. These acknowledgements would not be complete without mention of Sven, my loving, loyal, and trustworthy German Shepherd. He graced the lives of Julia and I in April 2014 and has inspired more happiness in our lives than we ever thought possible. Here's to you, pup!

ABOUT THE AUTHOR

Ryan William Conversano received a B.S. in aerospace engineering from the University of California, Los Angeles in 2010, graduating with honors, and an M.S. in aerospace engineering from the University of California, Los Angeles in 2011. He has remained a member of the Dean's Honor List during his entire graduate career. Mr. Conversano also earned a Certificate of Completion of *Advanced Flight Tests*, a short course by the University of Kansas and hosted by Edwards AFB, in 2007.

Since mid-2012, Mr. Conversano's research has focused on the development and testing of a low-power magnetically shielded Hall thruster with the hope of eventually evolving the device into a flight-ready prototype. While supported by a combination of UCLA and NASA funding, the majority of this research was conducted at NASA's Jet Propulsion Laboratory where Mr. Conversano held a JPL Affiliate status. From 2008 to mid-2012, he was active in a variety of research disciplines, including low-power plasma-material interactions, lunar mission CubeSat mission studies, CubeSat mission design and analysis, biologically inspired flexible wing design, cylindrical ring-wing projectile performance analysis, and piezoelectric actuator testing for use in military rotorcraft. In 2007, Mr. Conversano held a position with the 771st Test Squadron of the Electronic Warfare Group at Edwards AFB where he developed software involving the interactions of RADAR and RADAR-jamming signals. He has authored 12 technical publications, including four peer-reviewed journal articles, presented a technical poster, and is the lead inventor on a pending patent. Mr. Conversano's publication related honors include "Best Paper in Session" at the 2013 International Electric Propulsion Conference and "Best Poster" at the 2014 UCLA Tech Forum.

Mr. Conversano was awarded the NASA Space Technology Research Fellowship in 2013 in support of this thesis research to develop a low-power magnetically shielded Hall thruster. He was a recipient of NSF SEE-LA GK12 Fellowship in 2012, where he was a "resident scientist" part-time teacher for an 8th grade physics, chemistry, and astronomy class at a local elementary school. Mr. Conversano's other honors include the AeroClub of Southern California Scholarship Award (2011), the UCLA Chancellor's Prize for Academic Excellence (2011), UCLA Graduate Student Research Mentorship (2010), and UCLA Graduate Division Student Support Award (2010).

Chapter 1

INTRODUCTION

1.1. Motivation

Propulsion is, by definition, a means of generating a force that leads to motion of a body. Spacecraft propulsion is generally achieved by ejecting mass in the opposite direction of desired motion, thereby realizing a net change in momentum and a resulting acceleration of the spacecraft. Two primary means of propulsion are available today for spacecraft mobility: chemical and electric. Chemical propulsion relies on the heating and accelerating of a propellant using the energy stored within the propellant itself to achieve thrust. Electric propulsion (EP), by contrast, is a technology that uses electricity to generate thrust by accelerating charged particles at high exhaust velocities. The energy used to accelerate the propellant in an EP thruster is generated by an external power source, such as solar energy, and transferred to the EP system from an on-board power-processing unit. While chemical propulsion has been used on spacecraft since the dawn of space flight, the unique advantages of electric propulsion has led to an increasing number of successful missions employing EP devices.

The figures of merit for EP thrusters are similar to those for conventional chemical propulsion devices, allowing for fair comparisons between the two technologies. These include thrust (T), efficiency (η), and specific impulse (I_{sp}) as they relate to the delivered payload mass and total change in spacecraft velocity during a mission. Chemical thrusters generally deliver significant impulse at relatively low I_{sp} over short firing periods, often limiting the importance of long-duration thruster operation. Unlike many chemical systems, improving the useful life of EP

thrusters is an important area of research for the aerospace community. EP devices generate significantly lower thrust at much higher I_{sp} than chemical systems, offering improved "fuel efficiency" of the system while requiring significantly longer firing periods to achieve the mission-required impulse. Therefore, operational lifetime for EP devices, which directly translates to total delivered impulse, is a major concern for EP-based space missions.

1.2. Problem Statement

The goal of this research is to investigate the miniature-scale application of a magnetic shielding to extend the operational lifetime of low-power Hall thrusters. As this is a vast undertaking, this thesis focuses on the scalability of magnetic shielding by developing and testing a magnetically shielded miniature Hall thruster in an effort to demonstrate and understand the performance, plasma physics, and challenges of scaling magnetic shielding to low-power devices. It has been reported in the literature that the primary life-limiting mechanisms for Hall thrusters can be effectively eliminated by use of magnetic shielding (MS); to date, this has been demonstrated only on >1 kW devices [1,2]. In this thesis, we aim to develop a detailed understanding of the physical mechanisms of magnetic shielding as it is applied to low-power Hall thrusters.

This investigation is divided into three distinct tasks:

1) Design, fabricate, and experimentally test a low-power Hall thruster with a magnetically shielded field topology to determine the device's performance (thrust, efficiency, approximate lifetime, etc.) in comparison to unshielded low-power Hall thrusters.
2) Use a state-of-the-art computational Hall thruster plasma code to model the discharge plasma of the magnetically shielded miniature Hall thruster. These

results are then used to validate the claims of MS made during the experimental portion of this investigation.

3) Use the experimental performance analysis and computational results to draw conclusions about the overall performance, plasma-physical behavior, and unique challenges of MS as it is applied to low-power Hall thrusters.

The thruster that was designed, fabricated, and tested for this investigation will herein be called the MaSMi (**Mag**netically **S**hielded **Mi**niature) Hall thruster. Two versions of the thruster were ultimately fabricated:

- MaSMi-40 - discharge channel outer diameter of ~40 mm
- MaSMi-60 - discharge channel outer diameter of ~60 mm

The discussion of the development and testing of these devices is presented in Chapters 6 and 7, respectively, to maintain chronology of the investigation throughout this thesis.

1.3. Dissertation Overview

This thesis is organized based on the chronology of events that led to the successful completion of the investigation.

Chapter 2 introduces electric propulsion and describes its unique advantages when compared to chemical propulsion. A brief overview and the major classes of EP thrusters are also presented.

Chapter 3 presents an overview of Hall thruster types, operational principles, performance theory, and life-limiting factors. The heritage and limitations of low-power Hall thruster is reviewed, and the unique Hall thruster magnetic field structure known as magnetic shielding is thoroughly explained.

Chapter 4 presents the development process and design features of the MaSMi-40. The pre-experimental testing analysis used to predict the thruster's performance is also discussed.

Chapter 5 reviews the necessary facilities and tools required for Hall thruster performance analysis. This includes a description of the experimental setups at the two experimental facilities used in this investigation as well as the various diagnostics utilized to measure the performance of a Hall thruster.

Chapter 6 presets the performance analysis of the MaSMi-40. This chapter is broken into two sections: the first reviews the performance of the MaSMi-40 measured at the University of California, Los Angeles (UCLA) Electric Propulsion Test Facility while the second discusses the performance results measured at NASA's Jet Propulsion Lab (JPL) High Bay Facility.

Chapter 7 reviews the experimental characterization of the MaSMi-60, which was completed exclusively at the JPL High Bay Facility.

Chapter 8 introduces Hall2De, a computational tool used to model the discharge plasma inside and just downstream of a Hall thruster. The plasma simulation results for the MaSMi-40 and MaSMi-60 are presented and compared with one another and with low-power magnetically shielded Hall thrusters.

Chapter 9 offers concluding remarks about this investigation and suggests future efforts as a continuation of this research.

Chapter 2

ELECTRIC PROPULSION OVERVIEW

In this chapter, a general overview of electric propulsion is presented. The fundamental differences between chemical and electric propulsion are explored in Section 2.1, including the advantages and limitations of EP systems. Section 2.2 outlines the three general classes of EP devices: electrothermal, electromagnetic, and electrostatic. A brief history of the development and flight heritage of EP thrusters is reviewed in Section 2.3. Concluding remarks are made in Section 2.4.

2.1. Rocket Propulsion Basics

The thrust generation mechanism for EP and chemical thrusters is the same: accelerate a stored propellant (mass) and eject it at high velocity to generate a force on the spacecraft. To highlight the benefits of electric propulsion, we must examine the relationship between a spacecraft's change in velocity and mass during thruster firing, as shown by the Rocket Equation:

$$m_p = m_d\left[e^{\Delta V/v_{ex}} - 1\right] = m_d\left[e^{\Delta V/(I_{sp}*g)} - 1\right] \qquad 1.1\text{-}1$$

where m_p is the propellant mass, m_d is the delivered mass, ΔV is the change in spacecraft velocity, v_{ex} is the effective exhaust velocity of the propellant, I_{sp} is the specific impulse, and g is the acceleration of gravity at the Earth's surface. This equation shows a key relation involved in spacecraft propulsion: the amount of propellant required to change the velocity of a given delivered payload decreases as the effective exhaust velocity (specific impulse) increases.

Chemical rockets store the energy used to generate thrust in a propellant and are thereby limited by the energy density of available propellants. Chemical thrusters using modern

propellants provide typical specific impulse values ranging from 300 - 450 s with exhaust velocities of 3 - 4 km/s [3]. Electric thrusters use energy from an external source such as the Sun to accelerate a propellant. This energy is processed with an onboard power system and used to accelerate the propellant mass in the form of energetic charged particles. The limitation on the performance of electric thrusters is therefore related to the power available rather than the propellant energy density, yielding much higher specific impulses and exhaust velocities than chemical systems (I_{sp} of 2,000 - 10,000 s and v_{ex} 100+ km/s) [3].

A direct result of the high exhaust velocities attainable by EP thrusters is a significantly lower required propellant mass (on the order of 10x) for EP-based missions. As the exhaust velocity increases, however, the mass flow rate of the ejected particles must decrease for a given system's thrust and power; increasing the thrust from an EP system a constant thruster efficiency without a proportional increase in propellant flow rate is impossible without an increase in power at (the physics of this relationship are discussed in Chapter 3). The high specific impulse combined with the low mass flow rates characteristic of EP systems yield significantly lower thrust values than chemical propulsion systems; therefore, longer mission trip times (on the order of 2x) are generally observed. This is seen by examining the total impulse equation, where constant thrust is assumed:

$$Impulse = \int T dt \qquad 1.1\text{-}2$$

where t is time. Equation 1.1-2 shows that to achieve a given impulse, thruster operation time must increase as thrust is decreased. The long thruster operation times required by EP-based spacecraft to deliver a mission-specified impulse emphasizes the need for long lifetimes of EP thrusters.

It should be noted that electric thrusters require an additional onboard power-processing system that is not necessary for chemical thrusters. The mass of this power system, however, is usually significantly less than the propellant mass required for chemical thrusters to achieve a given mission trajectory. Therefore, the lower total propulsion system mass (thruster, supporting equipment, and propellant) of EP systems equates to lower launch masses than chemical propulsion systems, yielding lower total mission costs.

2.2. Electric Thruster Classes

2.2.1. Electrothermal

Electrothermal thrusters (resistojets and arcjets) use electricity to thermally heat a propellant before it is ejected to produce thrust. In a resistojet, increased exhaust velocities are attained by passing a propellant over a resistively heated element or chamber before entering a downstream nozzle, yielding specific impulses of approximately 500 s [3]. Arcjets, on the other hand, pass a propellant through a high-current arc before it is sent to a downstream nozzle. Plasma effects in these thrusters are negligible because the propellant is only weakly ionized, and specific impulses of less than 700 s are common [3]. To show the basic differences in geometry, Figure 2.2-1 shows an illustration of a resistojet and an arcjet.

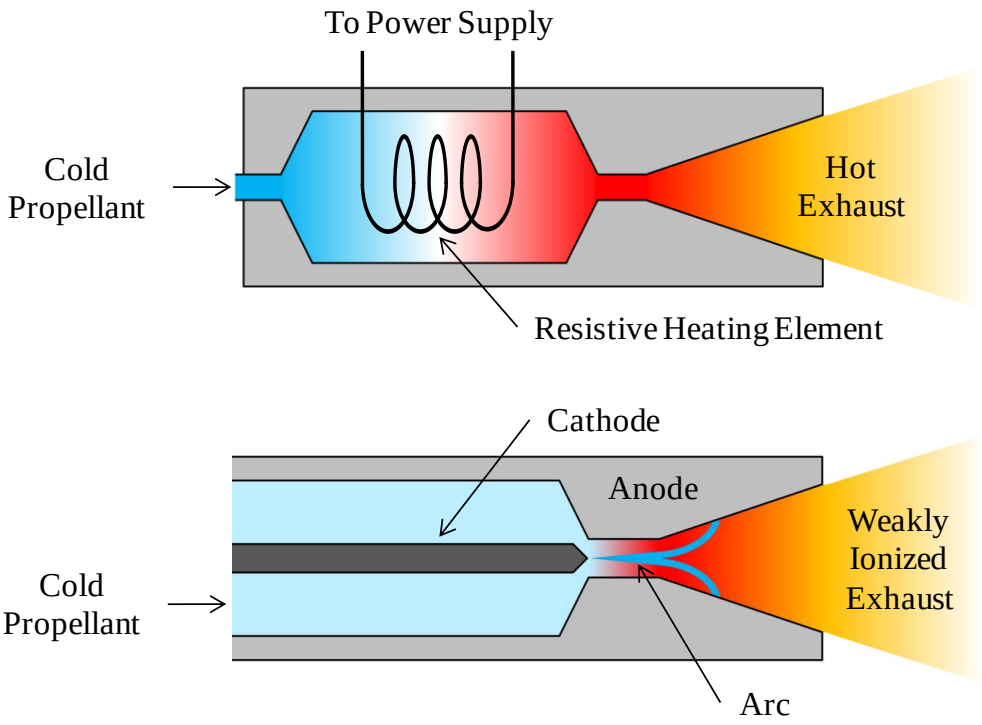

Figure 2.2-1: *Illustration of the geometry and operation of a resistojet (top) and an arcjet (bottom).*

2.2.2. Electromagnetic

Electromagnetic thrusters (pulsed plasma and magnetoplasmadynamic thrusters) accelerate an ionized (charged) propellant by use of an electromagnetic force. Because of their thrust generating mechanism, these devices are also known as Lorentz-force accelerators (LFA). A pulsed plasma thruster (PPT) uses a pulsed discharge to ablate and ionize a fraction of a solid propellant into a plasma and accelerate it using electromagnetic effects. Specific impulses of up to 1,200 s are achievable with PPT's [3]. Magnetoplasmadynamic (MPD) thrusters utilize a high-current arc to ionize a propellant and then accelerate the charged particles using electromagnetic forces. These devices usually require very high powers to operate at high specific impulse, which can exceed 10,000 s [3]. An illustration of an MPD thruster is shown in Figure 2.2-2, where $\boldsymbol{j}$ is the current density, $\boldsymbol{B}$ is the magnetic field, and $\boldsymbol{F}$ is the Lorentz force.

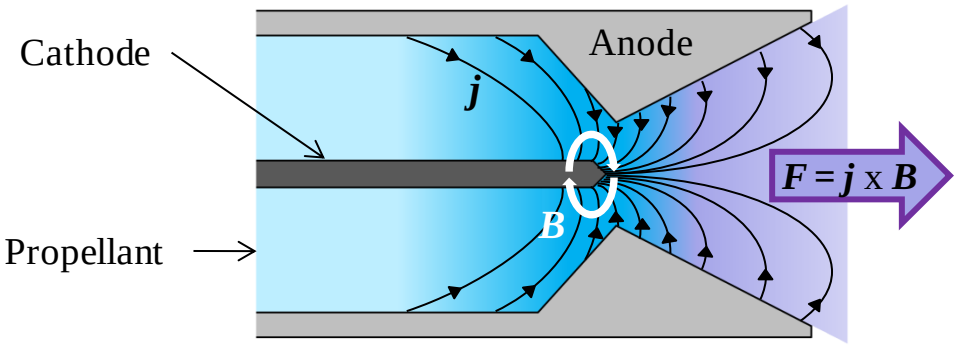

Figure 2.2-2: *Illustration of the geometry and operation of a magnetoplasmadynamic thruster / Lorentz-force accelerator.*

2.2.3. Electrostatic

Electrostatic thrusters, which include gridded ion thrusters and Hall thrusters, ionize a propellant through electron bombardment and then use a stationary applied electric field to electrostatically accelerate the charged propellant. While the electrostatic classification is clear for ion thrusters, some maintain that Hall thrusters should be classified as electromagnetic devices because the thrust force is transferred between the ions and the thruster through the magnetic field. However, the acceleration of the propellant which generates the thrust force is achieved through the application of a stationary electric field, therefore justifying the classification of Hall thrusters as electrostatic devices.

Ion thrusters use electrically biased grids to selectively extract and accelerate ions from a magnetically confined plasma. These devices demonstrate the highest efficiency of all EP devices (up to >80%) and can produce specific impulses of between 2,000 s and 10,000 s [3]. An illustration of a cylindrical gridded ion thruster's geometry and operation is shown in Figure 2.2-3. Note that various anode geometries, with most of the distinguishing features occurring near the back region, have been used in ion thruster design.

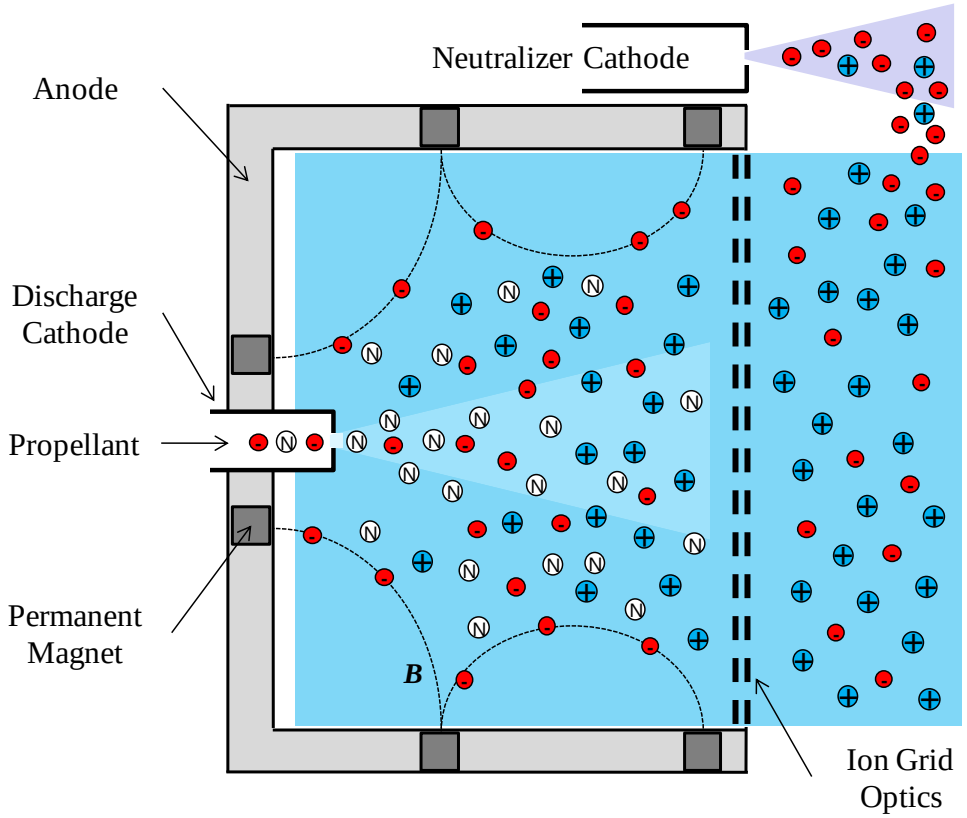

Figure 2.2-3: *Illustration of the geometry and operation of a gridded ion thruster.*

Hall thrusters use the Hall Effect (transverse particle motion from the application of perpendicular magnetic and electric fields) to generate and confine a plasma discharge. The transverse magnetic field creates resistivity in the plasma, effectively restricting electron mobility towards the anode and producing an axial electric field that accelerates ions from the plasma discharge. Specific impulse and efficiency are usually lower in Hall thrusters when compared to ion thrusters (1,000 - 3,000 s), but higher thrust and thrust-to-power ratios are achievable [3]. Figure 2.2-4 illustrates the basic geometry of a Hall thruster, where ***E*** is the electric field (a detailed explanation of the operation is given in Section 3.2). This class of electrostatic thrusters is the focus of this research investigation.

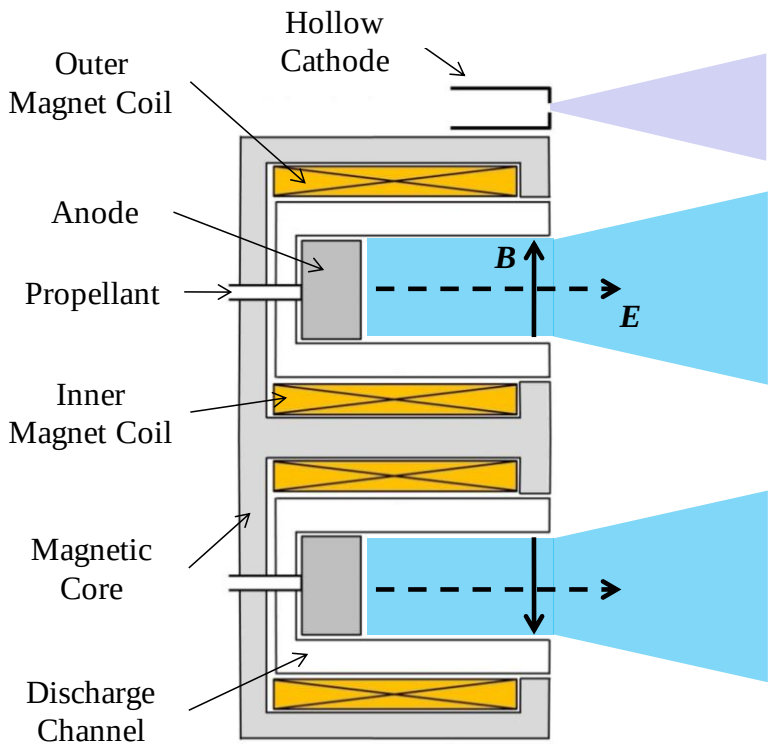

Figure 2.2-3: *Illustration of the basic geometry of a Hall thruster.*

2.3. Electric Propulsion Background

The first record of the concept of electric propulsion was published by Goddard in 1906, followed by an independent study by Tsiolkovskiy in Russia in 1911 [4,5]. Although other scientists suggested uses and concepts for EP, the first complete analysis of the technology was made by Stuhlihger in 1964; a thorough analysis of the physics of EP thrusters by Jahn followed in 1968 [6,7]. Early electric propulsion devices used mercury and cesium propellants and were intended for basic low thrust mission trajectories [8]. Numerous text book chapters discussing the operation principles and characteristics of electric propulsion devices have been published [9–12].

In the 1960's, the National Aeronautics and Space Administration (NASA) established extensive electric propulsion research programs in the United States and Russia to develop thrusters for deep-space propulsion and station-keeping. The first experimental ion thrusters were

launched in the early 1960's and continued into the 1980's [3]. The Russian's use of the SPT-60 on the 1971 Meteor satellite marked the first extensive use of Hall thrusters for on-orbit station-keeping [13]. The commercial use of Hall thrusters began for the U.S. in 2004 on Space System Loral's MBSAT, which used a Fakel SPT-100 thruster [14]. The first ion thruster system intended for station-keeping was launched by Japan in 1995 on the Engineering Test Satellite (ETS); the ion thrusters were successfully operated in space despite a failure that prevented the system from providing accurate station-keeping to the satellite [15]. The commercial use of ion thrusters in the U.S. began with the 1997 launch of a Hughes Xenon Ion Propulsion System (XIPS) [16]. This was shortly followed by NASA's first deep space application of electric propulsion, marked by the 1998 launch of NASA's Solar Electric Propulsion Technology Applications Readiness (NSTAR) ion thruster on the Deep Space 1 spacecraft [17]. The Japanese asteroid sample return Hayabusa mission used microwave discharge ion thrusters as the prime mean of propulsion in 2003; the same year, the European Space Agency (ESA) launched the SMART-1 spacecraft which performed operations around the Moon using the SNECMA PPS-1350-G Hall thruster [18,19]. The launch of the DAWN spacecraft in 2007 marked the beginning of perhaps the most challenging EP-based missions in history. Six years later, DAWN's successful (and ongoing) tour of two separate celestial bodies in a single deep space mission using an ion propulsion system represents the culmination of modern electric propulsion technologies, showcasing the capabilities of EP for future missions [20–25]. To date, over 250 electric thrusters have flown on more than 50 communications satellites and deep space mission spacecraft [3,26,27].

2.4. Concluding Remarks

In this chapter, an overview of electric propulsion technologies was presented. The distinctions between chemical and EP thrusters was discussed, highlighting the unique advantages of EP devices. Most notable is the significantly higher propellant exhaust velocities attainable with EP thrusters, which translates to higher specific impulse and lower propellant mass required for a mission at the expense of increased mission times. The basic operation of the three classes of EP devices was presented, followed by a brief review of the flight heritage of electric propulsion. Chapter 3 continues with a review of Hall thruster propulsion theory followed by a detailed overview of Hall thrusters, including geometry, operating principles, and limitations to operational life. The performance and heritage of low-power Hall thrusters, as well as a review of magnetic shielding, are also presented.

Chapter 3

HALL THRUSTERS

This chapter offers a detailed overview of the geometry, operation, and limitations of Hall thrusters. The theory used to characterize the performance of Hall thrusters is presented in Section 3.1. Section 3.2 introduces the two primary types of Hall thruster: the Hall effect thruster and the TAL thruster. Section 3.3 presents the general operational principles of Hall thrusters, including a discussion of the physics involved in maintaining the thrust-producing discharge plasma. Section 3.4 discusses the primary life-limiting factors for conventional Hall thrusters. The heritage and limitations of low-power Hall thrusters is presented in Section 3.5. The chapter concludes with a thorough discussion of the theory and applications of magnetic shielding in Section 3.6, followed by concluding remarks in Section 3.7.

3.1. Electrostatic Propulsion Theory

A key component of this thesis investigation is the characterization and testing of a Hall thruster using plasma probe diagnostics and EP theory. The governing equations for the methods used in this research are herein described.

The thrust (T) generated by an electrostatic thruster is given by

$$T = \sum_i \dot{m}_i \langle v_i \rangle = \eta_b I_d \sqrt{\frac{2MV_d \eta_v \eta_d}{e}} \sum_i \frac{f_i}{Z_i} \qquad 3.1\text{-}1$$

where $\dot{m}_i$ is the ion mass flow rate, $\langle v_i \rangle$ is the average ion velocity, η_b is the beam current utilization efficiency, I_d is the discharge current, M is the mass of a xenon atom, η_v is the beam

voltage utilization efficiency, η_d is the plume divergence efficiency, e is the charge of an electron, Z_i is the charge state of the i^{th} ion species, and f_i is the current fraction of the i^{th} species given by

$$f_i = \frac{I_i}{I_b} \tag{3.1-2}$$

where I_i is the current of the i^{th} ion species and I_b is the beam current (the efficiencies in Equation 3.1-1 are defined below). It is important to note that I_d is the current input to the thruster's plasma discharge while I_b is the current produced by the thruster to generate useful thrust. The correction term in Equation 3.1-1, which accounts for the presence of multiply charged species in the ion beam, can be calculated for any number of ion charge states as

$$\sum_i \frac{f_i}{Z_i} = \frac{I^+ + \frac{1}{2}I^{++} + \frac{1}{3}I^{+++} + \cdots}{I_b} \tag{3.1-3}$$

where I^+, I^{++}, and I^{+++} are the currents of singly, doubly, and triply ionized particles in the plasma beam.

The anode specific impulse is given by

$$I_{sp} = \frac{T}{\dot{m}_a g} = \frac{\eta_m}{g}\sqrt{\frac{2eV_d\eta_v\eta_d}{M}}\left(\frac{\sum_i \frac{f_i}{\sqrt{Z_i}}}{\sum_i \frac{f_i}{Z_i}}\right) \tag{3.1-4}$$

where $\dot{m}_a$ is the thruster anode mass flow rate, η_m is the mass utilization efficiency (defined below), V_d is the discharge voltage, and

$$\sum_i \frac{f_i}{\sqrt{Z_i}} = \frac{I^+ + \sqrt{\frac{1}{2}}I^{++} + \sqrt{\frac{1}{3}}I^{+++} + \cdots}{I_b} \; . \tag{3.1-5}$$

Note that this can easily be converted to thruster I_{sp} by using the total mass flow rate instead of the anode mass flow rate.

The total efficiency (η_T) is the ratio of the jet power (P_{jet}) in the thruster exhaust to the total thruster input power (P_T):

$$\eta_T = \frac{P_{jet}}{P_T} = \left(\frac{T^2}{2\dot{m}_a P_d}\right)\left(\frac{\dot{m}_a}{\dot{m}_T}\right)\left(\frac{P_d}{P_T}\right) = \eta_a \eta_c \eta_o = \eta_{tc}\eta_o \qquad 3.1\text{-}6$$

where P_d is the discharge power (discharge current multiplied by the discharge voltage), $\dot{m}_T$ is the total propellant flow rate (sum of the anode and cathode flow rates), η_a is the anode efficiency, η_c is the cathode efficiency, η_o is the electrical utilization efficiency, and η_{tc} is an effective thruster efficiency consisting of the efficiency contributions of the thruster and cathode. The anode efficiency can be broken into the product of five utilization efficiencies given by

$$\eta_a = \frac{T^2}{2\dot{m}_a P_d} = \eta_v \eta_b \eta_m \eta_d \eta_q \qquad 3.1\text{-}7$$

where the utilization efficiencies for the beam voltage, beam current, mass, beam divergence, and charge (η_q) are

$$\eta_v = \frac{V_b}{V_d}, \quad \eta_b = \frac{I_b}{I_d}, \quad \eta_m = \frac{\dot{m}_b}{\dot{m}_a} = \frac{MI_d}{\dot{m}_a e}\eta_b \sum_i \frac{f_i}{Z_i},$$

$$\eta_d = (cos\theta)^2, \quad \eta_q = \frac{\left(\sum_i \frac{f_i}{\sqrt{Z_i}}\right)^2}{\sum_i \frac{f_i}{Z_i}}. \qquad 3.1\text{-}8$$

In these equations, V_b is the beam voltage, $\dot{m}_b$ is the beam propellant mass flow rate, and θ is the beam divergence half-angle. The cathode, electrical utilization, and effective thruster efficiencies are given as

$$\eta_c = \frac{\dot{m}_a}{\dot{m}_a + \dot{m}_c} = \frac{\dot{m}_a}{\dot{m}_T}, \quad \eta_o = \frac{P_d}{P_T} = \frac{V_d I_d}{V_d I_d + P_{mag} + P_k}, \quad \eta_{tc} = \eta_a \eta_c \qquad 3.1\text{-}9$$

where $\dot{m}_c$ is the cathode mass flow rate, P_{mag} is the magnet power, and P_k is the keeper power.

Because thruster experiments are conducted in an imperfect vacuum environment, a correction can be made to yield estimates of the true vacuum performance values. The effects of background pressures observed during thruster operation are accounted for through a method of compensating for neutral gas entrained into the thruster channel and subsequently used to generate excess thrust [28]. The entrained neutral mass flow rate ($\dot{m}_{en}$) is given by

$$\dot{m}_{en} = A_{en}\,\frac{n_n M}{4}\left(\frac{8kT_n}{\pi M}\right)^{1/2} = A_{en}P\left(\frac{M}{2\pi kT_n}\right)^{1/2} \qquad 3.1\text{-}10$$

where A_{en} is the entrainment area approximated as a hemisphere with a radius equal to the discharge channel outer diameter, n_n is the background neutral density, k is the Boltzmann constant, T_n is the temperature of the background neutral particles, and P is the Facility pressure. This entrained mass flow can be used to approximate the excess discharge current (I_{en}) produced by the thruster due to ingestion of entrained neutrals, given by

$$I_{en} = \dot{m}_{en}\frac{e}{M} \qquad 3.1\text{-}11$$

where it is assumed that the neutral particles are singly ionized. Similar corrections can be applied to the measured discharge current and anode flow rate:

$$I_{d,corr} = I_d - I_{en}\,, \quad \dot{m}_{a,corr} = \dot{m}_a + \dot{m}_{en}\,. \qquad 3.1\text{-}12$$

where the subscript *corr* represents the values corrected for a complete vacuum environment (background pressure of 0 Torr). The entrained mass correction for thrust (T_{corr}) is given by

$$T_{corr} = T\left(1 - \zeta_{en}\frac{\dot{m}_{en}}{\dot{m}_{a,corr}}\right) \qquad 3.1\text{-}13$$

where ζ_{en} is the entrained mass utilization factor used to account for ingested neutrals that were ionized but that did not contribute to useful thrust. The value of the entrained mass utilization factor is 0.5 according to the literature [28]. The vacuum specific impulse ($I_{sp,corr}$) can then be calculated from Equation 3.1-4 using the corrected thrust (Equation 3.1-13) and the measured

anode propellant flow rate; this is because only the thrust term is dependent on the facility pressure. Using the corrected thrust and specific impulse, a vacuum total efficiency ($\eta_{T,corr}$) can be calculated using a modified form of Equation 3.1-6 given as

$$\eta_{T,corr} = \left[\frac{g}{2}\left(\frac{I_{sp,corr}T_{corr}}{P_{T,corr}}\right)\right]\eta_{o,corr}\eta_{c,corr} \qquad 3.1\text{-}14$$

where $P_{T,corr}$, $\eta_{o,corr}$, and $\eta_{c,corr}$ are given by

$$P_{T,corr} = V_d I_{d,corr} + P_{mag} + P_k \,,$$
$$\eta_{o,corr} = \frac{V_d I_{d,corr}}{P_{T,corr}} \,, \quad \eta_{c,corr} = \frac{\dot{m}_{a,corr}}{\dot{m}_{a,corr} + \dot{m}_c} \,. \qquad 3.1\text{-}15$$

3.2. Hall Thruster Geometry and Types

A Hall thruster consists of a cylindrical channel containing an interior anode, an internal magnetic circuit that generates a radial magnetic field across the channel gap, and a hollow cathode outside of the channel. Two general types of Hall thrusters exist: Hall thrusters (also called Hall effect thrusters [HET's], stationary plasma thrusters [SPT's], and magnetic layer thrusters) and TAL thrusters (thruster with anode layer). Hall thrusters use a metallic, electrically biased anode at the base of an annular discharge channel to inject the majority of the thruster's propellant into the discharge. The remainder of the propellant is used to operate a hollow cathode located either outside of the thruster's body or along the thruster centerline. Hall Thrusters use a plasma discharge channel constructed from a dielectric insulator with a low sputtering yield under bombardment from the ionized propellant (usually xenon) to reduce erosion. Common channel materials include boron nitride (BN) and borosilicate glass (a.k.a. borosil, BN-SiO_2) [3]. Figure 3.2-1 shows a cross section of a Hall thruster with an externally mounted hollow cathode. The figure displays the radial magnetic field and the axial electric field generated by the thruster and labels the paths of electrons and xenon atoms to demonstrate how they interact with these fields.

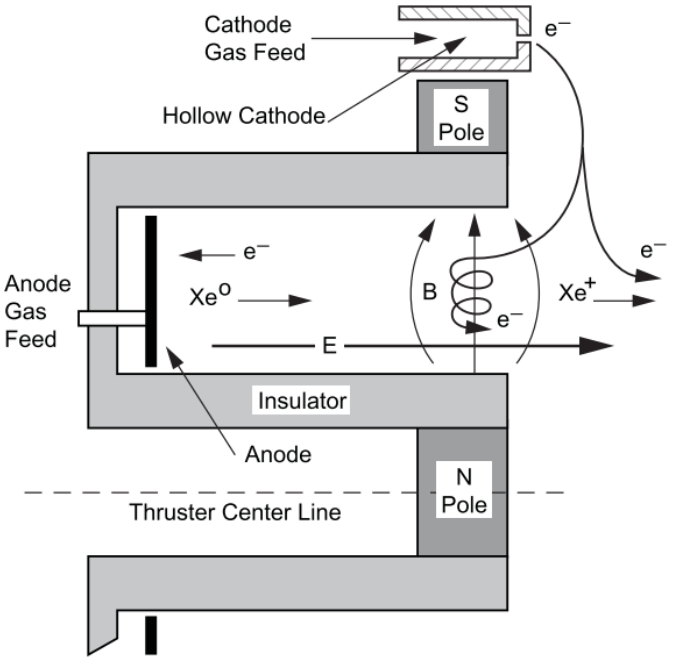

Figure 3.2-1: *Hall thruster cross-section showing the applied electric and magnetic fields along with the xenon neutral, xenon ion, and electron paths [3].*

TAL thrusters use metallic conducing discharge channel walls instead of insulating walls. The electric field region where ionization occurs is therefore shortened and significantly narrowed [29]. The metallic channel walls, often used as a component of the magnetic circuit, are biased negatively to prevent electron power deposition by repelling electrons in the ionization region. Further differences between these devices can be found in the literature [30]. Figure 3.2-2 shows a cross section of a TAL thruster with an externally mounted hollow cathode. As with Figure 3.2-1, the paths of electrons and xenon atoms are shown to highlight their interaction with the thruster's magnetic and electric fields.

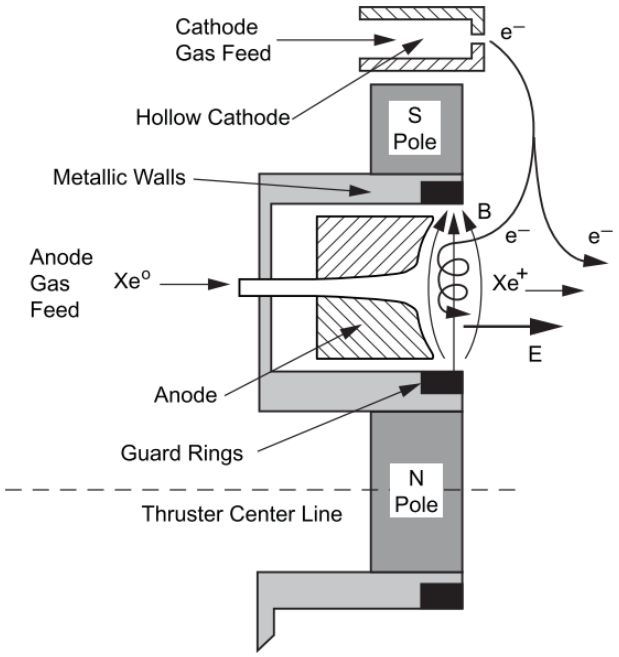

Figure 3.2-2: *TAL thruster cross-section showing the applied electric and magnetic fields along with the xenon neutral, xenon ion, and electron paths [3].*

3.3. Operation Principles

In Hall thrusters, a voltage is applied between the anode at the base of the discharge channel and the hollow cathode mounted outside of the discharge channel, drawing electrons from the cathode towards the anode. The thruster's internal magnetic circuit generates a radial (transverse) field used to prevent cathode electrons from streaming directly to the anode. The electrons instead gyrate along the magnetic field lines inside the discharge channel with a gyroradius (or Larmor radius, r_L) defined by the applied magnetic field and the particle's velocity perpendicular to the magnetic field ($v_\perp$):

$$r_L = \frac{mv_\perp}{qB} = \frac{v_\perp}{\omega_c} \qquad 3.3\text{-}1$$

where m is the mass of an electron, q is the particle's charge, B is the magnetic field magnitude, and ω_c is the electron cyclotron frequency. Similarly, ions gyrate due to the presence of the applied magnetic field according to

$$R_L = \frac{MV_\perp}{qB} = \frac{V_\perp}{\Omega_i} \qquad 3.3\text{-}2$$

where R_L is the ion Larmor radius, $V_\perp$ is the ion velocity perpendicular to the magnetic field, and Ω_i is the ion cyclotron frequency. However, the gyroradius of an ion (on the order of km's) is many orders of magnitude greater than that of an electron (on the order of mm's) for a typical Hall thruster magnetic fields due to the mass ratio of the two particles (M ~ 2.18x10^{-25} kg vs. m ~ 9.1x10^{-31} kg). With Hall thruster peak radial magnetic field strengths rarely exceeding 300 G, Equations 3.3-1 and 3.3-2 show that electrons are well confined to the discharge channel via the magnetic field (these electrons are considered "magnetized") whereas ions are largely unaffected by the magnetic field.

The electrical circuit created between the anode and cathode is closed by diffusion of the electrons to the anode enabled by collisional processes and electrostatic fluctuations in the plasma discharge; similar phenomena cause diffusion of a portion of the electron population to the discharge channel walls. Because the strong radial magnetic field significantly reduces axial electron mobility, the discharge voltage created between the anode and cathode is distributed axially within the quasi-neutral plasma over long distances compared to the Debye length [3]. This results in a predominantly axial electric field across the discharge channel's width and along its length.

In addition to the gyration induced by the radial magnetic field, the perpendicular intersection of the magnetic and electric fields generate an azimuthal (**E**x**B**) drift on the electrons based on the Lorentz force:

$$\boldsymbol{F} = q(\boldsymbol{E} + \boldsymbol{v} \times \boldsymbol{B}) \qquad 3.3\text{-}3$$

where $\boldsymbol{F}$ is the net force vector on the particle and $\boldsymbol{v}$ is the particle's velocity vector. Solving this equation for the transverse velocity of the particle gives

$$v_E = \frac{\boldsymbol{E} \times \boldsymbol{B}}{B^2} \tag{3.3-4}$$

where v_E is the **E**x**B** ("E cross B") drift velocity of the electrons. Although this drift is generally considered the sole mechanism of confining electrons to their azimuthal paths around the annular discharge channel, recent studies have suggested that electrons may travel in predominantly linear paths between the inner and outer channel walls (essentially bouncing between them) while migrating azimuthally around the channel. These paths trace helical trajectories in the azimuthal direction and are caused by the non-axial electric field near the discharge channel walls (a plasma sheath effect that repels electrons towards the channel centerline) and the magnetic mirroring effect of the thruster's magnetic circuit near channel surfaces [31]. The combination of the cyclotron motion of electrons along the magnetic lines of force and the **E**x**B** drift effectively confines the electrons within the discharge channel.

The electrons confined to the magnetic field near the discharge channel's exit efficiently ionize neutral gas particles injected into the channel from the anode; this occurs in what is known as the ionization region. Care must be taken in the design of a Hall thruster such that the vast majority of injected neutral propellant becomes ionized and accelerated to generate useful thrust. The ratio of the ionized particle flux exiting the discharge plasma (Γ_{exit}) to the neutral particle flux incident on the discharge plasma ($\Gamma_{incident}$) over the discharge plasma thickness (t) is represented by

$$\frac{\Gamma_{exit}}{\Gamma_{incident}} = 1 - e^{-t/\lambda_i} \tag{3.3-5}$$

where λ_i is the ionization mean free path. According to Equation 3.3-5, achieving a minimum ionization fraction of 95% requires the plasma thickness to be at least three times the ionization mean free path. This leads to a key Hall thruster scaling law:

$$\frac{\lambda_i}{t} = constant \gg 1 \ . \qquad 3.3\text{-}6$$

Neutrals that are successfully ionized by the energetic electrons confined in the discharge plasma are too massive to be significantly affected by the transverse magnetic field as shown by Equation 3.3-1; these ions are electrostatically accelerated by the axial electric field to produce thrust.

Low-frequency oscillatory behavior is a common characteristic of Hall thruster operation. The discharge's ion density fluctuates due to a periodic depletion of neutral gas in the ionization region, giving way to related fluctuations in electron conductivity through the radial magnetic field (towards the anode). These effects, which are essentially predator-prey interactions between the electrons and neutral particles in the ionization zone, yield discharge current oscillations on the time scale of neutral replenishment. These oscillations are called "breathing modes" or "predator-prey modes" and typically occur with an amplitude of between 30% - 100 % of the discharge current at a frequency on the order of 10 - 30 kHz [3].

Unlike gridded ion thrusters, space charge limitations are not a concern for Hall thrusters as the acceleration of ions occurs in the plasma region near the discharge channel exit, allowing for higher ion current and thrust densities [3]. Additionally, Hall thrusters require a single hollow cathode to provide electrons to both ionize the neutral propellant (thereby maintaining the plasma discharge) and to neutralize the beam. By contrast, gridded ion thrusters require two hollow cathodes: one to ionize the propellant inside the thruster and a second to neutralize the external plasma beam.

A diagram of the voltage distribution common in Hall thrusters is shown in Figure 3.3-1. The potential between the anode and cathode is the discharge voltage. The cathode-ground voltage (V_{cg}) is the negative potential between the cathode and ground. The plasma potential (V_p) is the voltage measured from ground to the beam's floating potential. The beam voltage, which

represents the net accelerating potential for ions born inside a Hall thruster's discharge channel, is the potential between the anode and the plasma potential.

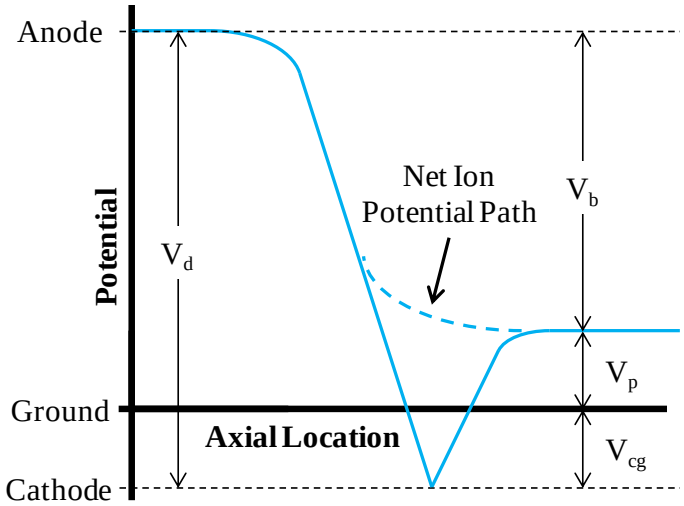

Figure 3.3-1: *Typical Hall thruster voltage distribution along the length of the discharge channel.*

The plasma physics involved in Hall thrusters are far more complicated than in ion thrusters; the results of these physics have a direct relation to the thruster's efficiency, performance, and life as has been discussed in the literature [29–34]. In general, flight-qualified Hall thrusters have lower efficiency and specific impulse than ion thrusters at the same power level, but tend to yield higher thrust-to-power ratios [35,36]. Additionally, the propellant throughput of conventional Hall thrusters is generally greater than ion thrusters despite their shorter useful life, generating nearly comparable total delivered impulse [3].

3.4. Life-Limiting Factors

The primary life-limiting factor for Hall thrusters is ion bombardment erosion of the discharge channel walls. Due to the zero net current condition at the insulating walls, a large sheath potential forms to reject the bulk of the electron population. This electron repelling sheath generates a significant drop in the potential structure and creates a radial electric field component

local to the channel surfaces that, along with variations in the discharge potential (discussed in Section 3.6), accelerates nearby ions into the walls; this is shown in Figure 3.4-1 [1,37–39]. The resulting sputter erosion is concentrated near the exit plane and can wear through the discharge channel walls, exposing the thruster's pole pieces to ion bombardment. The complete erosion of the discharge channel walls is considered a "soft failure" as it does not necessarily end the useful life of the Hall thruster; the device may operate after the discharge channel walls erode with only a minor impact on performance [40]. This suggests that, while soft failures may be used to characterize the longevity of certain Hall thruster components, the complete erosion of the discharge channel walls and exposure of the pole pieces to the plasma is only a part of the total operational lifetime of a Hall thruster [40].

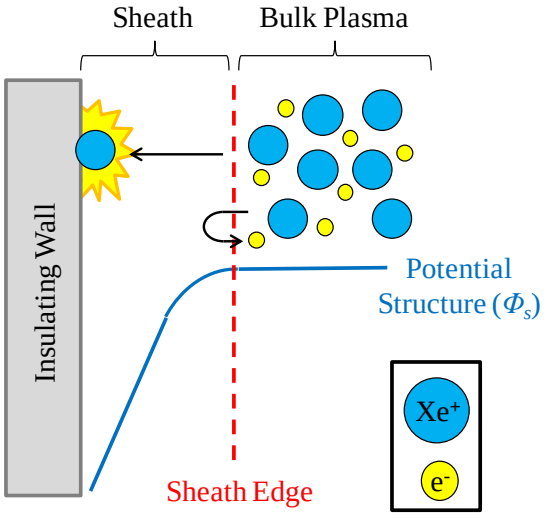

***Figure 3.4-1**: Illustration of the wall sheath potential structure (Φ_s) in an unshielded Hall thruster and its effect on the ion and electron populations in the bulk plasma.*

Another key performance-limiting factor in Hall thrusters is high-energy electron power loss to the discharge channel walls causing overheating and adverse thermal effects. In conventional Hall thrusters, the radial magnetic field lines near the exit plane intersect the channel walls, as shown in Figure 2.4-1. High-energy electrons gyrate along these field lines, and the

most energetic ones bombard the discharge channel walls while the bulk of the distribution is reflected back into the plasma by either the plasma sheath or the magnetic mirror created at the pole pieces. This high-energy electron power deposition results in performance-robbing heating of the Hall thruster structure that can also affect operational lifetime due to temperature limitations of the thruster's materials and construction [3,41].

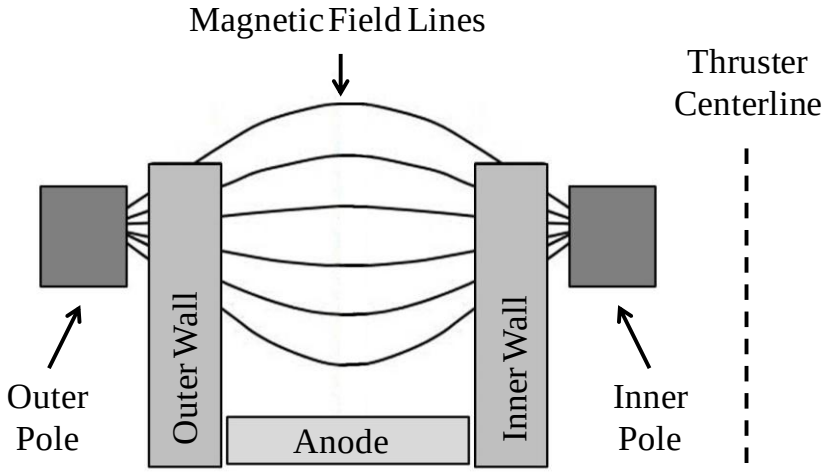

Figure 3.4-2*: Illustration of the magnetic field topology in an unshielded Hall thruster.*

The effects of ion bombardment and electron power loss increase rapidly in low-power Hall thrusters, primarily due to their characteristically larger surface-to-volume ratios. The erosion rates of conventionally sized and miniature Hall thrusters may be comparable; however, shorter operational lifetimes are always observed in miniature devices due to their reduced channel wall thickness. Operational lifetimes of miniature Hall thrusters are generally low, ranging from tens of minutes to hundreds of hours with few devices surviving beyond 1,000 hours [42–49].

3.5. Low-Power Hall Thrusters

A significant portion of the recent research on micro-propulsion technologies has focused on gridded ion thrusters due to their favorable performance at the 1 – 5 cm scale [50–57]. Of note

is the 3 cm Miniature Xenon Ion (MiXI) thruster developed by R. Wirz, *et al*, which demonstrated thrust values of up to 1.55 mN with a specific impulse of over 3,000 s and a total efficiency of up to 56% [54,57]. On the other hand, Hall thrusters tend to show poor efficiency (generally below 50%) and life (generally 100's of hours, sometimes exceeding 1,000 hours) when scaled down to the sub-7 cm regime [46–49,58–60]. To combat low performance and efficiency caused by high surface-to-volume ratios, miniature Hall thrusters are often designed with large discharge channels relative to the size of the thruster. This corresponds to an increased channel volume compared to the channel surface area, thereby reducing the surface-to-volume ratio at reduced scales. The discharge channel width-to-mean-diameter ratios (b/d_m) for a variety Hall thrusters are plotted in Figure 3.5-1 against their power level, showing the increasing trend of b/d_m as a Hall thruster's scale is reduced.

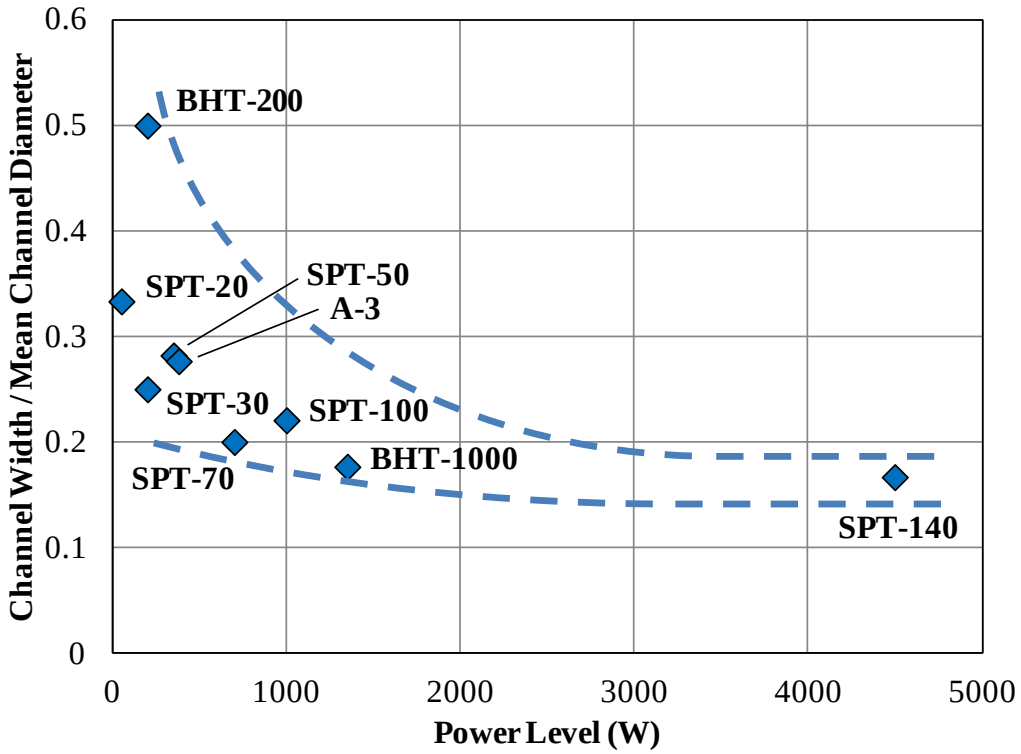

Figure 3.5-1: *Trends of discharge channel width-to-mean-diameter ratio vs. input power for a variety of Hall thrusters [46–48,58–61].*

Low-power Hall thrusters have traditionally been used for spacecraft station keeping, and numerous devices of varying sizes and performance levels have been developed over the past several decades to this end. The French designed SPT-20 thruster has an operational power of approximately 50 W with 20 mm discharge channel outer diameter. It has demonstrated up to 5 mN of thrust with a specific impulse of 1,000 s at an efficiency of approximately 15% [61]. The SPT-30 is a Russian-developed miniature Hall thruster with a 30 mm discharge channel outer diameter which nominally operates at 200 W. At this power condition, the SPT-30 produces approximately 11 mN of thrust at an specific impulse of 1,170 s with an efficiency of up to 32% and has an estimated operational lifetime of more than 600 h [58]. The Russian SPT-50 employs a 50 mm discharge channel outer diameter and, during operation between 350 - 500 W, demonstrates a maximum anode efficiency of nearly 40% with a thrust of between 20 - 30 mN and a specific impulse of between 1,300 - 2,000 s; a flight-demonstrated lifetime of approximately 2,500 h is reported in the literature [49,61]. The A3 thruster, a 60 mm Russian design, shows very similar thrust, specific impulse, and efficiency performance to the SPT-50 [61]. The Russian SPT-70 (70 mm discharge channel outer diameter) has a nominal power of approximately 700 W and develops approximately 40 mN of thrust, a specific impulse of approximately 1,500 s, and has a claimed flight-demonstrated lifetime of approximately 3,100 h [49]. In an effort to examine the operation of micro-Hall thrusters, a 4 mm channel diameter Hall thruster was developed at Stanford University. The thruster was operated at 10 - 40 W, yielding 0.6 - 1.6 mN of thrust at a specific impulse of 300 - 850 s [42,43]. The anode efficiency remained in the range of 10 - 15% and the device demonstrated a limited useful operational lifetime of ~20 minutes before the discharge stability was compromised by thermal drift [42,43].

In recent years, several new high performance low-power Hall thrusters have been developed. The CAM200, a derivative of the CAMILA thruster developed in Israel, has been demonstrated from approximately 100 W up to nearly 400 W with a nominal power in the 250 W range [62]. This device demonstrated a maximum thrust of over 20 mN with a specific impulse of approximately 1700s at an anode efficiency of approximately 47%; the nominal performance is approximately 11 mN, 1500 s, and 37%, respectively [62]. The Fakel-designed Plas-40 Hall thruster has been demonstrated over a power range of 100 W to 650 W with maximum thrust, specific impulse, and anode efficiency of over 40 mN, over 1,800 s, and nearly 50%, respectively [63]. While a nominal operating point was not specified in the cited literature, the thruster is reported to have a lifetime of over 4,000 h at an operating power of 200 W (V_d of 160 V), corresponding to a thrust of 15 mN, a specific impulse of over 800 s, and an anode efficiency of approximately 30% [63]. Sitael (Italy) has developed two low-power Hall thruster, the HT100 and HT400, which have also shown promising performance. The HT100 has a nominal thrust of 8.5 mN at an anode efficiency of nearly 35% at a discharge power of 175W; thrust and specific impulse values of up to 16 mN and 1,450 s have been reported over the thruster's power range of 120 W to 300 W [64]. Additionally, the HT100 has completed over 940 h published (approximately 1,700 h reported at the time of the paper's presentation) of continuous firing during an endurance life test [64]. While the HT400 is still under development, it has a demonstrated power range of 350W to 800 W, thrust values between 20 mN and 50 mN, a specific impulse range of 1,100 s to 1,800 s, anode efficiencies ranging from 30% to 50%, and has a predicted lifetime of 4,000 h [64].

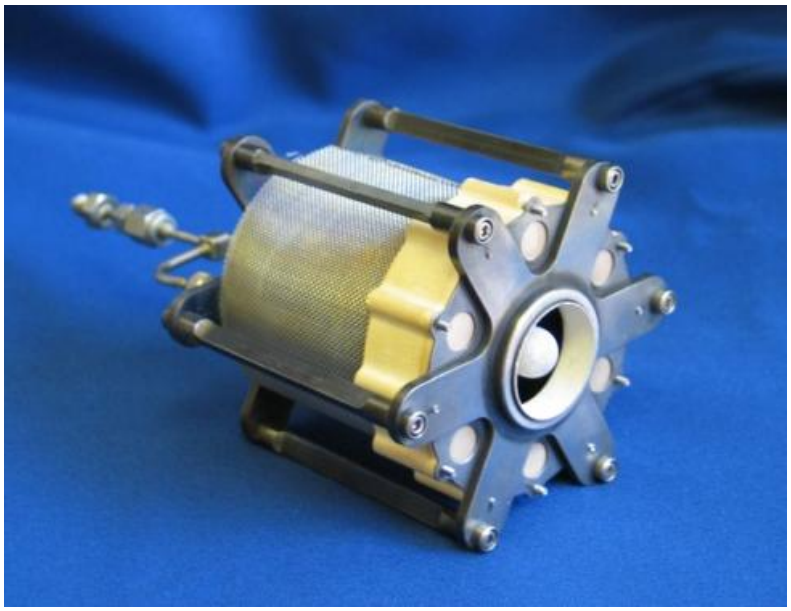

Figure 3.5-2: *Photograph of the Busek BHT-200 Hall thruster* [68].

One of the most well-documented low-power Hall thrusters is the Busek BHT-200, shown in Figure 3.5-2. This 200 W Hall thruster employs a 3 cm discharge channel outer diameter and is capable of 12.8 mN of thrust and a specific impulse of 1,390 s at an anode efficiency of 44%; a second nominal point specified in the literature is 11.4 mN, 1,570 s, and 42% [44–48,65]. It has been utilized to validate numerous computational plume models for laboratory thrusters and has been used for a variety of Hall thruster cluster investigations [46,47,66,67]. Experimentally determined useful lifetimes of over 1,700 h have been observed; however, operational times between 1,300 - 1,500 h have led to failure of the thruster's nose-cone, exposing the centerline pole pieces to ion bombardment [48]. As the current state of the art in low-power Hall thruster design, the BHT-200 is considered a benchmark of miniature Hall thruster performance.

A summary of the size, power level, and performance of the aforementioned low-power Hall thrusters is presented in Table 3.5-1.

Table 3.5-1. *Summary of the size, power, performance, and useful life of a selection of low-power Hall thrusters.*

Name	$d_{channel}$ (mm)	P_d (W)	T (mN)	I_{sp} (s)	η_a	Useful Life (h)
Micro-Hall	4	10 - 40	0.6 - 1.6	300 - 850	10 - 15%	0.33
SPT-20	20	50	5	1,000	15%	-
HT100	-	175	8.5	-	35%	1700+
	-	120 - 300	16	1,450	-	-
BHT-200	30	200	12.8	1,390	44%	-
	30	200	11.4	1,570	42%	1700+
SPT-30	30	200	11	1,170	32%	600
Plas-40	40	200	17	950	30%	4000
	40	100 - 650	40	<1880	50%	-
CAM200	-	250	11	1,500	37%	-
	-	100 - 400	20	1,700	47%	-
HT400	-	350 - 800	20 - 50	1,100 - 1,800	30 - 50%	-
SPT-50	50	350 - 500	20 - 30	1,300 - 2,000	40%	2500
A3	60	350 - 500	20 - 30	1,300 - 2,000	40%	-
SPT-70	70	700	40	1,500		3100

3.6. Magnetic Shielding Theory

Magnetic shielding is a method of significantly reducing the life-limiting factors of Hall thruster through the careful design of the magnetic field topology, yielding improvements to operational lifetimes on the order of 100 - 1000x [1]. Magnetic shielding was first described by JPL and Aerojet-Rocketdyne after the BPT-4000 reached a near-zero-erosion state after approximately 5,600 hours into a 10,400 hour wear test [2,38]. In a series of simulations and experiments using a modified version of JPL's 6 kW H6 Hall thruster (called the H6MS), a more complete understanding of the physics of magnetic shielding was realized; the unique field

topology was shown to reduce erosion rates by up to three orders of magnitude compared to unshielded Hall thrusters [1,38,39]. The extensibility of magnetic shielding to higher specific impulse, high power density, higher power, lower power, and alternate wall materials are key questions now being addressed by NASA as the limits of magnetic shielding are explored [69–75].

Magnetically shielded Hall thrusters benefit from a unique magnetic field topology that prevents the field lines from intersecting the discharge channel walls in the ionization and acceleration regions. Instead, the lines of force originating from both the inner and outer poles curve around the downstream edges of the discharge channel and follow the channel surfaces towards the anode (see Figure 3.6-1). It should be noted that the magnetic field line passing closest to, but not touching or intersecting, the discharge channel walls is known as the "grazing line." The shape and depth of penetration of the grazing line are key factors in the ultimate performance of a magnetically shielded Hall thruster.

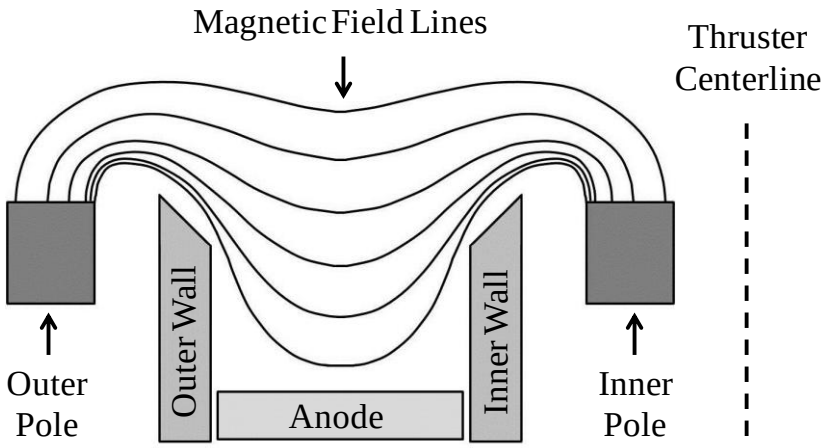

Figure 3.6-1*: Illustration of the field topology in a magnetically shielded Hall thruster.*

Two important properties of Hall thrusters originally identified by Morozov in the 1960's and 1970's are exploited in a magnetically shielded field topology: the near isothermality and

approximate equipotentialization of the magnetic field lines [34,76,77]. The isothermality of the lines of force means that the electron temperature (T_e) along a field line is essentially constant:

$$T_e \approx T_{e0} \tag{3.6-1}$$

where T_{e0} is the reference, or channel centerline, electron temperature. This is a valid assumption due to the high electron mobility along a field line, which enables any fluctuations in electron energy to be nearly immediately distributed throughout that field line's electron population. This property allows the deep-penetrating magnetic field lines in an MS configuration to capture cold (~5 eV) electrons near the anode and transport them adjacent to the discharge channel surfaces, maintaining a low average T_e near the wall [1,39,78]. Because the sheath potential is a function of T_e for a given material, low electron temperatures at the discharge channel surfaces produce reduced wall sheath potential drops. This then reduces the energy of ions passing through the sheath potential and bombarding the wall.

Another byproduct of the cold electron temperature near the channel walls is observed through the thermalized potential equation:

$$\Phi = \Phi_0 + T_{e0}\, ln\left(\frac{n_e}{n_{e0}}\right) \tag{3.6-2}$$

where Φ is the plasma potential, n_e is the electron density, and the subscript *0* denotes the channel centerline (reference) values. The electron density decreases away from the discharge channel centerline as a result of two primary factors: first, the majority of the electron population is reflected away from the walls due to the plasma sheath with a minor, if not negligible, contribution from magnetic mirroring effects; second, the highest energy electrons that are not reflected by the sheath subsequently are lost to the channel walls [31]. This radial electron density variation causes the natural log term in Equation 3.6-2 to be negative, thereby reducing the plasma potential across the discharge channel. However, cold electron temperatures near the

channel surfaces (a result of field line isothermality and a magnetically shielded field topology) reduces the value of the temperature term attached to the natural log, making the total change in plasma potential small compared to the reference (centerline) value. This enables the assumption of magnetic-force-line equipotentialization to hold to a greater extent near the channel walls than in unshielded Hall thrusters, maintaining a plasma potential close to that of the discharge voltage along the length of the discharge channel [1,39,78]. The effects of the approximate field line isothermality and equipotentialization on electron temperature and discharge potential are shown in Figure 3.6-2, where the upper half of a Hall thruster's discharge channel is depicted with representative magnetic field structures and resulting electric field orientations [37].

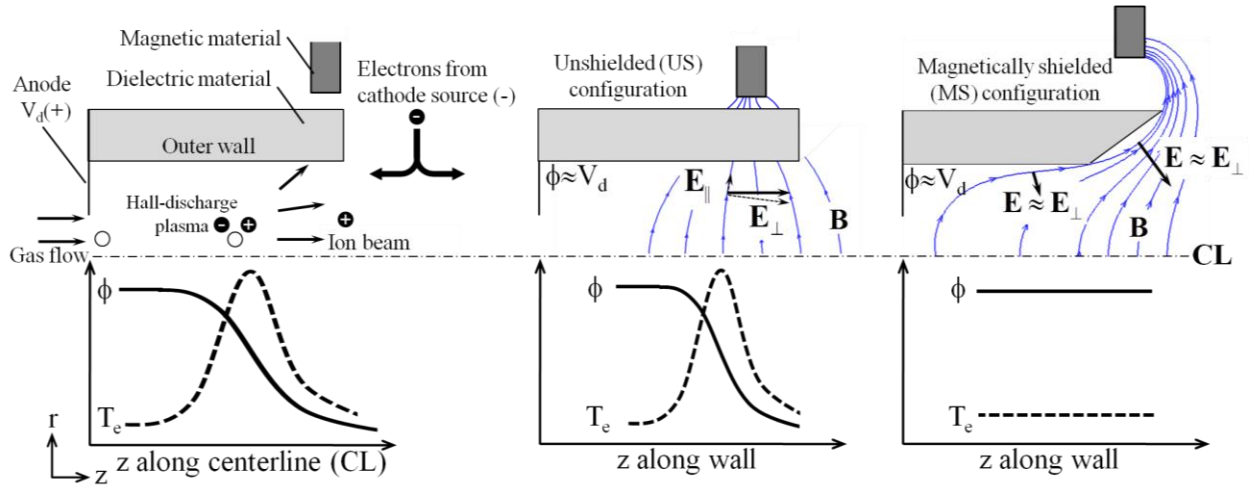

Figure 3.6-2*: Illustration of the upper half of a Hall thruster's discharge channel with representative magnetic field structures (top) and electron temperature and discharge plasma potential profiles (bottom) [37]. Left: general features of Hall thruster operation with typical profiles along the channel centerline (CL). Middle: field topology and profiles observed in unshielded Hall thrusters. Right: field topology and profiles observed in magnetically shielded Hall thrusters.*

The combination of the approximate isothermality and equipotentialization of the field lines in a magnetically shielded Hall thruster ultimately enables the observed increase in thruster

operational life. The essentially constant discharge potential across and along the channel nearly eliminates the radial component of the electric field near the channel surfaces, preventing ions from being accelerated with significant energy towards the channel walls. A carefully selected channel geometry and magnetic field design aids in directing the electric field nearly perpendicular to the discharge channel surfaces (see Figure 3.6-2) [1,37,39,78]. The kinetic energy gained by ions that are accelerated towards the channel walls is further reduced by the low sheath potential drops along the channel surfaces. Ion bombardment sputter erosion of the channel is therefore effectively eliminated, resulting in an increase of thruster lifetimes by as much as a factor of 1,000 compared to unshielded Hall thrusters [1,39,78]. Additionally, because the field lines do not intersect with the channel walls, high-energy electron confinement is improved while power deposition to the walls is reduced [1,39,78]. A representative illustration of the wall sheath potential structure and the paths of ions and electrons near the channel walls in a magnetically shielded Hall thruster is presented in Figure 3.6-3, showing that ions accelerated towards the insulating channel walls have insufficient energy to cause significant ion bombardment erosion.

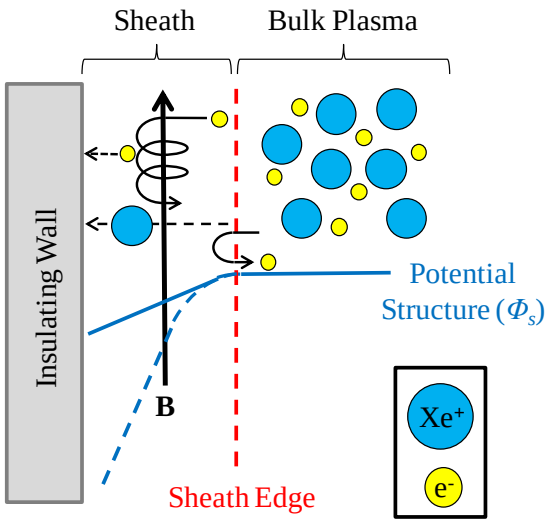

***Figure 3.6-3**: Illustration of the wall sheath potential structure in a magnetically shielded Hall thruster and its effect on the ion and electron populations in the bulk plasma. The sheath potential structure for an unshielded thruster is also shown for comparison (dashed line).*

During the testing of EP devices, energetic carbon atoms are liberated from the graphite material lining the vacuum chamber walls due to the incident plasma beam. These atoms travel randomly and are generally deposited on the first surface they contact. The buildup of carbon on a surface suggests a lack of plasma-induced erosion; "cleaning" of a surfaces is caused by ion-bombardment or other plasma-surface interaction mechanisms. In the case of a magnetically shielded Hall thruster, the lack of significant ion bombardment sputter erosion of the discharge channel walls enables a net deposition of these carbon atoms on the channel surfaces, resulting in a significant blackening the discharge channel after a sufficiently long test (on the order of ~10 h or less) [1,74]. While this is not conclusive evidence, this feature enables a visual indication that magnetic shielding may have been achieved.

In terms of performance, the implementation of magnetic shielding on the H6 Hall thruster resulted in a slight drop in efficiency (<2%), a significant drop in insulator ring (discharge channel downstream edge) temperature (12-16%), and an increase in specific impulse (~3%)

primarily due to an increase in multiply charged ions from the decreased electron wall losses and resulting higher electron temperature [1,37,39,78].

3.7. Concluding Remarks

In this chapter, the geometry, types, operation, performance theory, and magnetic shielding of Hall thrusters was discussed. The life limiting factors of Hall thrusters, including sputter erosion and electron power loss to the channel walls, were introduced. These life limiting factors were shown to have a greater effect on a thruster's operational life as the scale (power) of the device is reduced due to an increasing surface-to-volume ration of the discharge channel, which encourages increased plasma-wall interactions. A review of numerous low-power Hall thrusters was presented, showing that anode efficiencies of approximately 40% or less and total operational lifetimes on the order of 1,000 hours are common. The chapter concluded with a summary of the concept and theory behind magnetically shielded Hall thrusters. By achieving a specific magnetic field topology, two key properties of Hall thruster operation are exploited: near field line isothermality and approximate force-line equipotentialization. These factors significantly decrease ion bombardment erosion and electron heating of the discharge channel walls, resulting in a significant increase of a thruster's useful life. The 6 kW H6MS magnetically shielded Hall thruster was calculated to a ~1,000x improvement in useful life with minimal effects to its performance. To explore the scalability of magnetic shielding, a magnetically shielded miniature Hall thruster was developed and tested. Chapter 4 introduces this thruster, providing an overview of its key design features and projected performance.

Chapter 4

MAGNETICALLY SHIELDED MINIATURE HALL THRUSTER: PRELIMINARY DESIGN AND PROJECTED PERFORMANCE

This chapter introduces the device designed and built to undertake this thesis research: the magnetically shielded miniature (MaSMi) Hall thruster. Section 4.1 discusses the early development of the thruster and initial performance estimates based on scaling arguments. The key features of the device are also outlined. More detailed performance modeling for the magnetically shielded miniature Hall thruster are presented in Section 4.2. Included is a discussion of the unique features of the magnetically shielded miniature Hall thruster's far-field magnetic field topology. Concluding remarks are presented in Section 4.3.

4.1. Preliminary Design of the MaSMi-40

4.1.1. Scaling Methodology and Results

Hall thrusters present unique design challenges as they are scaled to the sub-7 cm outer channel diameter regime. These challenges include, but are not limited to, reducing the ion bombardment erosion of the discharge channel, decreasing high-energy electron loss to the channel walls, and developing a symmetric magnetic circuit to avoid localized magnetic field concentrations [41]. Although these challenges are not dissimilar to those faced in the design of conventionally sized Hall thrusters, their effects are more significant in miniature devices due to higher surface-to-volume ratios and reduced discharge channel dimensions. The increasing surface-to-volume ratio as nominal power level is reduced significantly contributes to the non-linear scaling of miniature Hall thrusters [59,60]. No scaling methods have been developed for

magnetically shielded thrusters to date; therefore, a proven scaling methodology for unshielded Hall thrusters was applied to the MaSMi-40 as a means to roughly approximate the performance of the device [59,60]. The scaling method requires full knowledge of the geometry and performance of several reference thrusters which will be effectively scaled to the desired power level [59,60]. The performance of the scaled thruster can then be predicted using a set of physical relationships based on the ratios of the scaled and reference thrusters' fundamental performance parameters.

The five fundamental parameters required for this scaling procedure are discharge channel mean diameter, discharge channel width, discharge channel length (L), discharge voltage, and propellant gas particle density exiting the anode (n_a). Values for both the reference thruster(s) (*ref*) and the target thruster design are needed for each of these five parameters; ratios between the target thruster and the reference thruster are used for the scaling process:

$$\frac{d_m}{d_{ref}}, \frac{b}{b_{ref}}, \frac{L}{L_{ref}}, \frac{V_d}{V_{ref}}, \frac{n_a}{n_{ref}}. \tag{4.1-1}$$

The discharge current is proportional to the anode propellant mass flow rate, which in turn is proportional to the product of the anode propellant particle density, the mass of a xenon atom, the effective exhaust velocity, the discharge channel mean diameter, and the discharge channel width. This is expressed as

$$I_d \propto \dot{m}_a \propto n_a M v_{ex} d_m b. \tag{4.1-2}$$

Therefore, assuming the same exhaust velocity and propellant type for the reference and target thrusters, the ratio of discharge currents between the two can be calculated as

$$\frac{I_d}{I_{ref}} = \left(\frac{n_a}{n_{ref}}\right)\left(\frac{d_m}{d_{ref}}\right)\left(\frac{b}{b_{ref}}\right). \tag{4.1-3}$$

Multiplying Equation 4.1-3 by the voltage term from Equation 4.1-1 yields the discharge power ratio for the reference (P_{ref}) and target thruster, defined as

$$\frac{P_d}{P_{ref}} = \left(\frac{V_d}{V_{ref}}\right)\left(\frac{n_a}{n_{ref}}\right)\left(\frac{d_m}{d_{ref}}\right)\left(\frac{b}{b_{ref}}\right) . \quad 4.1\text{-}4$$

The thrust can be calculated from a slightly modified version of Equation 3.1-1:

$$T = \dot{m}_i v_i \quad 4.1\text{-}5$$

where the ion exhaust velocity and ion mass flow rate only consider singly and doubly charged ions and are given by

$$v_i = (1-\alpha)\sqrt{\frac{2eV_d\eta_{loss}\eta_q\eta_d}{M}} + \alpha\sqrt{\frac{2(2e)V_d\eta_{loss}\eta_q\eta_d}{M}} \quad 4.1\text{-}6$$

$$\dot{m}_i = \left(\frac{\eta_b I_d}{e}\right)(1+\alpha)M \quad 4.1\text{-}7$$

where α is the doubly charged correction factor and η_{loss} accounts for power losses to the wall, anode, and propellant ionization. Lastly, the specific impulse used for this scaling method is calculated by combining Equations 4.1-5 and 3.1-4.

Using the BHT-200, A-3, and SPT-100 as the reference thrusters, a thruster model with a ~40 mm discharge channel outer diameter was generated (the MaSMi-40) [47,48,58–60]. The discharge power, thrust, and specific impulse were calculated and plotted against the reference thrusters' channel diameters, as shown in Figure 4.1-1. The non-linear scaling trends result from the many variables changing in the optimization of each design. The applied scaling laws predict a discharge power of approximately 320 W, a thrust of approximately 19 mN, and a specific impulse of approximately 1380 s.

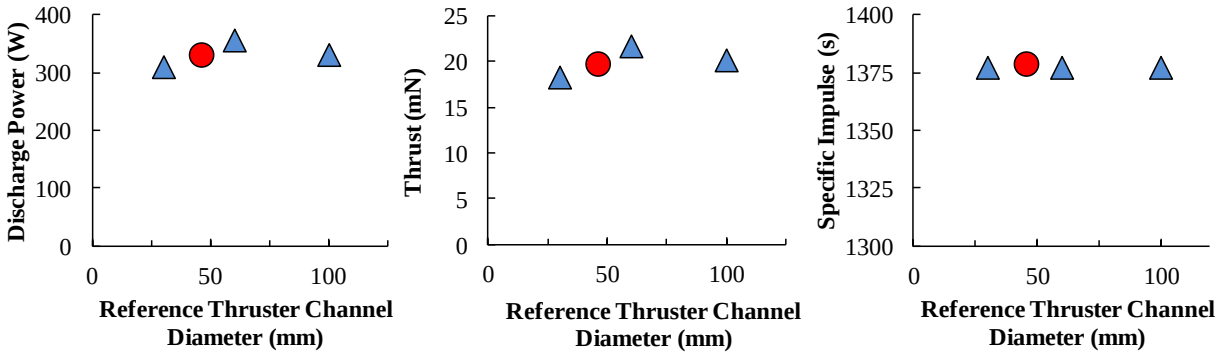

Figure 4.1-1: *Predicted discharge power, thrust, and specific impulse for the MaSMi-40 based on scaling laws. The diamonds represent MaSMi-40's predicted performance based on each reference thruster (BHT-200, A3, and SPT-100) and the circles represent MaSMi-40's predicted performance averaged over the reference thrusters.*

4.1.2. Geometry

The design of the MaSMi-40's magnetic circuit was completed using the design process outlined in [79]. The thruster has a channel width-to-mean-diameter ratio of 0.222, placing it in line with the trends of unshielded miniature Hall thrusters shown in Figure 3.5-1. The MaSMi-40 employs a variable-placement anode, permitting a discharge channel length of up to twice the width.

4.1.3. Magnetic Field

The computational model of the thruster's magnetic circuit predicted a magnetically shielded field topology with no intersection of the magnetic field lines and the discharge channel walls. Additionally, a maximum radial magnetic field strength along the channel centerline ($B_{r,max}$) of over 200 G was predicted. This exceeded the $B_{r,max}$ required to constrain electron Larmor radii to 10% of the discharge channel width (assuming an electron temperature of 20 eV) as is generally deemed optimal [3].

4.2. Performance Modeling

4.2.1. Power Balance

The total power deposition to the discharge channel walls and anode was estimated based on the thruster's expected operational parameters. It should be noted that the equations used for this power deposition model were developed for unshielded Hall thrusters. A linear curve fit of the secondary electron yield of boron nitride was used to predict finite secondary electron yields at low incident energies [80]. The electron temperature at the thruster exit plane was then calculated using an iterative process outlined in the literature based on the linear secondary electron yields and the thruster operating parameters [3]. The discharge power, which by definition is equal to the total power out of the thruster, is modeled to the first order as

$$P_d = P_b + P_w + P_a + P_R + P_i \tag{4.2-1}$$

where P_b is the beam power, P_w is the power deposited to the discharge channel walls by electrons and ions, P_a is the power deposited to the anode by electrons, P_R is the plasma's radiative power loss, and P_i is the power to produce ions that either become the beam or bombard the channel walls. These power terms are presented in the literature as

$$P_b = V_b I_b \tag{4.2-2}$$

$$P_w = n_e e A_w \left[\left(\frac{kT_e}{e} \right)^{3/2} \left(\frac{2e}{\pi m} \right)^{1/2} e^{\frac{e\Phi_s}{kT_e}} + \frac{1}{2} \sqrt{\frac{kT_e}{M}} (\boldsymbol{\varepsilon} - \Phi_s) \right] \tag{4.2-3}$$

$$P_a = 2T_{eV} I_a \approx 2T_{eV} I_d \tag{4.2-4}$$

$$P_R = n_o n_e \langle \sigma_* v_e \rangle V_p \tag{4.2-5}$$

$$P_i = (I_b + I_{iw}) U^+ = [\eta_b + I_{ew}(1 - \gamma)] I_d U^+ \tag{4.2-6}$$

where A_w is the surface area of the inner and outer discharge channel walls in contact with the plasma, $\boldsymbol{\varepsilon}$ is the pre-sheath ion energy, T_{eV} is the electron temperature in electron volts, I_a is the

current to the anode, $\langle \sigma_* v_e \rangle$ is the excitation reaction rate coefficient including the excitation cross section and the electron velocity, V is the volume of the high-temperature plasma region, I_{iw} is the ion current to the walls, U^+ is the ionization potential, I_{ew} is the electron current to the walls, and γ is the secondary electron yield [3].

To complete this analysis, several assumptions were made. The anode-region electron temperature was assumed to be 4 eV and the axial depth of the high-density plasma near the exit-region of the thruster was assumed to be 3 mm. The current and voltage efficiencies were assumed to be 70% and 90%, respectively, and the magnetic field strength at the peak field point was assumed to be 160 G. A discharge current of 1.3 A and a total propellant flow rate of 20 sccm were also assumed. Using these assumptions and the known MaSMi-40 thruster dimensions, the various power loss terms presented in Equations 4.2-2 through 4.2-6, in addition to the beam power and the electron temperature, were calculated as functions of the discharge voltage.

The beam power, the net power carried by the plasma beam, was approximately 245 W according to the unshielded power model. The power deposited to the channel walls is broken into two terms: the first is the power deposition of electrons that overcome the repelling sheath potential and the second is the power deposition of ions that fall through the pre-sheath and sheath potentials (the cooling effect of emitted secondary electrons is neglected). Electron and ion heating of the walls accounted for approximately 115 W and 5 W, respectively, of the predicted total 145 W of power dissipated to the discharge channel walls. The remaining 25 W consisted of contributions from xenon ionization, electron power deposition to the anode, and radiation. The xenon ionization power predicted to be approximately 13 W and was not sensitive to changes in the thruster model's operation conditions. The power deposited to the anode was calculated based

on the assumption that the discharge current was effectively equal to the electron current collected at the anode and assumed that the plasma potential was equal or slightly higher than the anode potential. Electrons were assumed to deposit $2T_{eV}$ of energy from the plasma to the anode, totaling to approximately 11 W of power loss for the unshielded model. The radiative power loss is the thermal power radiated by the plasma volume (the product of the discharge channel cross-sectional area and the axial thickness of the high-temperature plasma region) based on the excitation of neutrals in the plasma. Radiative power losses for the unshielded thruster totaled to approximately 3 W. The power to produce ions is the sum of the power used to generate the beam ions (product of the beam current and the ionization potential) and the power used to create ions that will bombard the discharge channel walls (product of the ion current to the walls and the ionization potential). Alternatively, this power can be calculated based on the beam efficiency and the electron current to the discharge channel walls, accounting for emitted secondary electrons; the sum of these factors is multiplied by the discharge current and ionization potential. Ionization power to the beam and wall ions totaled to approximately 17 W for the unshielded thruster model. Other terms, including the power electrons may carry into the beam, are generally small and were neglected [3].

For MaSMi-40's original expected operating conditions (300 V, 1.3 A), the electron temperature was calculated to be approximately 18 eV with a total power deposition of approximately 145 W according to the power model. Figure 4.2-1 shows the electron temperature and total power deposition to the discharge channel walls and anode for a variety of discharge voltages at the expected operation discharge current of 1.3 A. An additional 35 W of power was expected to be generated by the two magnetic coils during nominal operation based on a temperature-sensitive model relating applied current and resulting magnetic field strength. The

180 W of thermal power generated by the operation of the MaSMi-40 represented a significant challenge for long-duration operation.

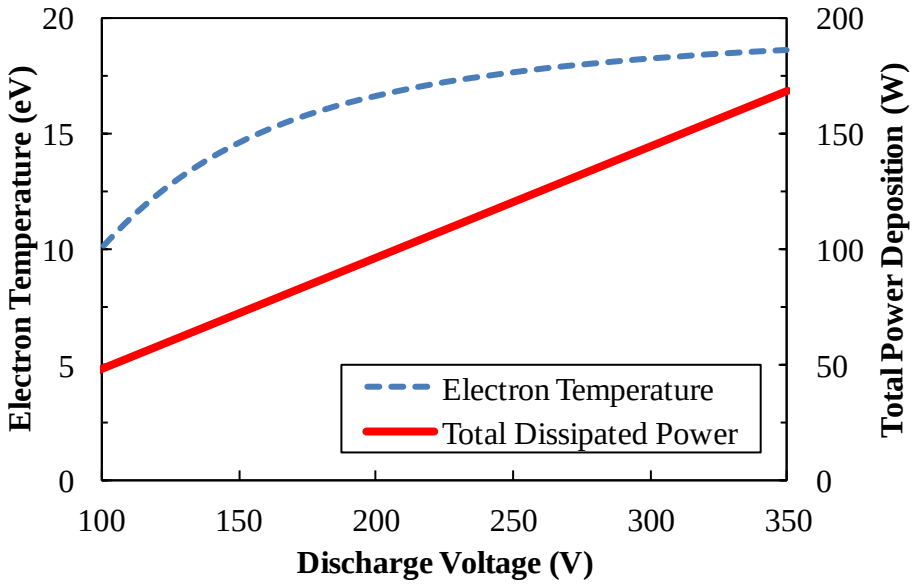

Figure 4.2-1: *Estimated electron temperature and total power deposition as a function of discharge voltage for a ~40 mm unshielded Hall thruster operating at 1.3 A discharge current.*

4.2.2. Thermal Design

A basic radiative-heat transfer thermal balance was performed to determine MaSMi-40's approximate operating temperature based on the power deposition model presented in Section 4.2.1. Assuming no conduction, a total power loss of 180 W, an emissivity of 0.3 (bare Hiperco), and a radiation area equal to the surface area of the thruster body, the predicted equilibrium operation temperature was approximately 660°C, which far exceeded the thermal rating of the insulated magnet coil wire (~ 400°C). In order to efficiently dissipate the predicted 180 W of power loss, a thermal radiator was constructed to fit over the thruster's outer core. The radiator (affectionately called the "X-Wing" radiator) was constructed from four 1.6 mm copper sheets with a quarter-circular bend in the center and bolted together tightly in the shape of an "X" to ensure thermal contact with the thruster body. The two upper fins were spread apart for greater

surface area. The radiator, with a total space-viewing surface area of approximately 1000 cm^2, was oxidized (emissivity approximated at 0.75) to yield a predicted thruster operation temperature of approximately 370°C, assuming a 50% radiator efficiency. A photograph of the MaSMi-40 mounted in its thermal radiator is presented in Figure 4.2-2.

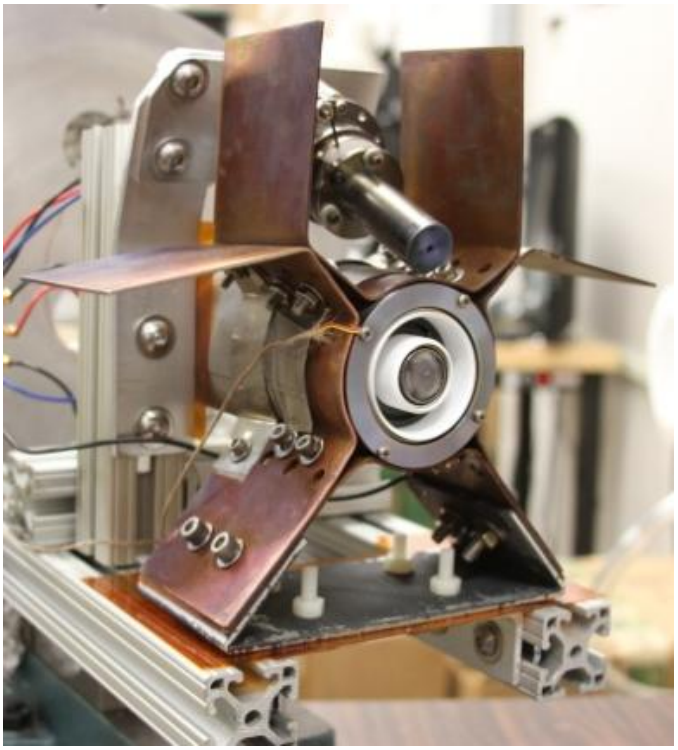

Figure 4.2-2: *Photograph of the MaSMi-40 fitted with the "X-Wing" radiator and hollow cathode.*

4.2.3. Separatrix Analysis

Conventional Hall thrusters generally have one of two magnetic coil configurations to achieve the desired field topology. The first configuration uses discrete outer coils located at multiple, equally spaced azimuthal locations oriented parallel to the thruster's axis. These coils are magnetically coupled to the thruster's magnetic core to complete the thruster's magnetic circuit. The second thruster configuration uses a single outer coil, concentric with the thruster discharge channel and oriented along the thruster axis. This single coil is generally sheathed by

the thruster's outer magnetic core to connect the coil to the thruster's magnetic circuit. In either thruster design, a single inner magnet coil located radially inward from the inner wall of the discharge channel may be implemented. Thrusters using discrete outer coils generate two species of field lines that extend outside the thruster body. The first circulates through the magnetic circuit and then travels from the inner pole to the outer pole. The second extends from the front of the outer coils and reconnects at the back of the outer coils, traveling around the thruster body (not conducted by the magnetic circuit). The boundary between the two regions of similarly connected flux lines is called the separatrix. Figure 4.2-3 shows the magnetic field structure of a Hall thruster using discrete outer coils, highlighting the location of the separatrix. Thrusters using a single outer coil generate only one magnetic field line species that extend outside the thruster body. These field lines travel from the thruster inner pole and reconnect at the outer pole, sides, and rear of the thruster body to be circulated through the thruster's magnetic circuit. In this type of thruster configuration, no separatrix exists in the magnetic field topology.

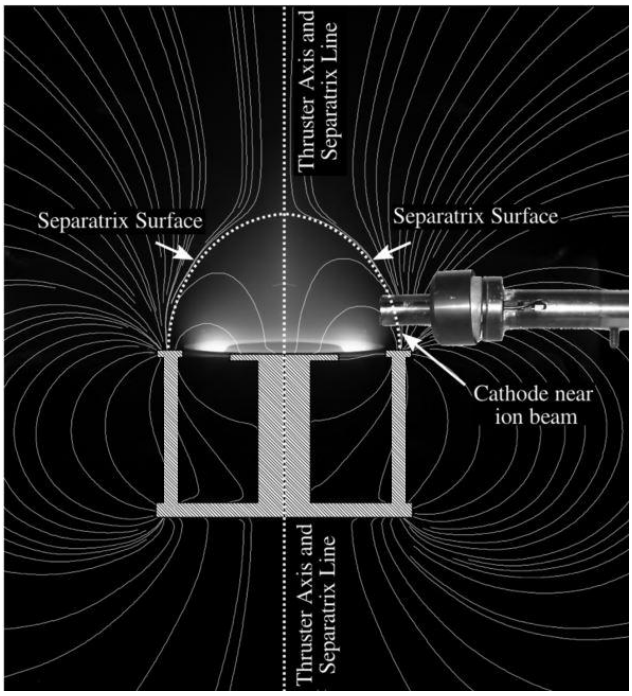

Figure 4.2-3: *Magnetic field structure of a Hall thruster with discrete outer coils showing the two species of magnetic field lines and the location of the separatrix [81].*

The placement of the thruster's hollow cathode is a critical design feature depending on a thruster's magnetic coil configuration. Work is necessary for electrons born from the cathode to travel to the anode and ion beam, overcoming both strong magnetic fields and insufficient collision frequency, to maintain charge quasi-neutrality. The minimization of this work, which can be considered an energy loss mechanism, results in more effective cathode coupling with the thruster and improved thruster efficiency [82,83]. In a series of cathode coupling investigations using a BPT-2000 Hall thruster (which uses four discrete outer coils), it was determined that placing a Hall thruster's hollow cathode orifice within the separatrix (towards the thruster's centerline) yielded significantly better thruster efficiency and improved cathode coupling [82,83].

To demonstrate that cathode coupling issues should be minor with the MaSMi-40, the thruster's far-field magnetic field structure was simulated to confirm that no separatrix existed in the field topology (recall that the MaSMi-40 utilizes a single outer magnetic coil design). As

expected, the fields model predicted that that no separatrix exists in MaSMi-40's external magnetic field structure. Therefore, cathode placement was expected to have a minimal impact on thruster performance.

4.3. Concluding Remarks

The basic design and features of the MaSMi-40 were discussed throughout this chapter. The scaling methodology used to predict ballpark performance figures of the MaSMi-40 was reviewed. More involved performance estimates were made, accompanied by a discharge channel power balance and thermal balance model to predict the thruster's plasma-wall interaction effects and operating temperature. MaSMi-40's local and far-field magnetic field topology was also predicted by commercial magnetic fields modeling software. Results from the simulations suggested that strong cathode coupling would be relatively insensitive to cathode placement relative to the thruster. With design and fabrication complete, the MaSMi-40 was prepared for experimental testing. An overview of the experimental facilities and diagnostics used for the performance testing are presented in Chapter 5.

Chapter 5

EXPERIMENTAL FACILITIES, DIAGNOSTICS, AND TEST SETUPS

Chapter 5 reviews the tools utilized to characterize the performance of the MaSMi Hall thruster. Section 5.1 describes the vacuum chamber and experimental equipment central to the UCLA Electric Propulsion Test Facility. Section 5.2 presents the experimental vacuum system and diagnostic equipment at the NASA Jet Propulsion Laboratory's High Bay Facility. A discussion of the various diagnostics used to measure the performance of a Hall thruster and to analyze the plasma beam is presented in Section 5.3. The chapter ends with concluding remarks in Section 5.4.

5.1. UCLA Electric Propulsion Test Facility

The first set of experiments characterizing the MaSMi-40 were carried out at the Electric Propulsion Test Facility in the Plasma and Space Propulsion Laboratory at UCLA. The UCLA Electric Propulsion Test Facility, shown in Figure 5.1-1, uses a custom built cylindrical vacuum chamber measuring 2.8 m long with a diameter of 1.8 m. Two CTI CryoTorr 10 cryogenic pumps operate in parallel for a combined xenon pumping speed of approximately 1,300 l/s. Pressures were monitored by a wall-mounted ionization gauge located approximately 0.5 m downstream of the thruster. This system is capable of achieving a nitrogen base pressure of approximately 5×10^{-7} Torr, and during operation with a 10 - 15 sccm xenon flow the chamber pressure remains in the mid-high 10^{-5} Torr range, corrected for xenon. To prevent energetic ion sputtering, electric charging, and heating of the vacuum chamber, a high-energy beam dump was installed downstream of the thruster. The beam dump safely absorbs high energy electrons and

ions, preventing them from reaching the vacuum chamber walls. Beam dumps can be made from a variety of materials, including copper, aluminum, and carbon; however, carbon materials are highly favorable due to their low sputter yield under xenon ion bombardment [84]. The Electric Propulsion Test Facility high energy beam dump, consisting of a 1.25 m x 1.25 m square of 1.6 mm carbon felt mounted to a grounded aluminum frame, was mounted approximately 80 cm downstream of the MaSMi-40. The close proximity of the beam dump to the thruster was selected to provide a short path for energetic carbon atoms ejected from the felt to easily backsputter onto the thruster discharge channel, enabling a visual verification of successful magnetic shielding.

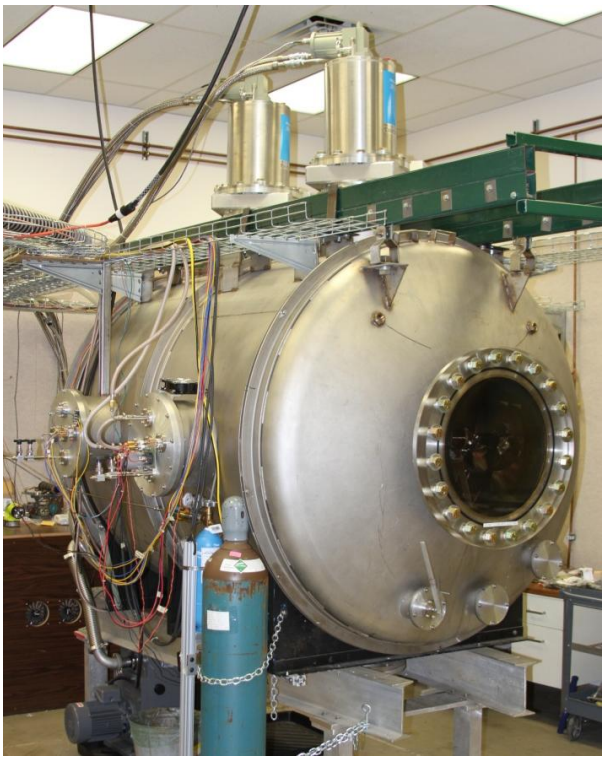

Figure 5.1-1: *UCLA Electric Propulsion Test Facility chamber and supporting equipment.*

Commercially available power supplies and mass flow controllers were used to operate the MaSMi-40. All power required by the thruster, including the anode, coil magnets, cathode heater, and cathode keeper was supplied by Sorensen DLM-series power supplies. Research

grade xenon was supplied to the thruster and cathode by Apex mass flow controllers (calibrated at 0°C) via stainless steel propellant lines. The MaSMi-40 was coupled to a BaO-W cathode similar to the ISS plasma contactor and the NSTAR ion thruster cathodes. The MaSMi-40's cathode has a 0.75 mm diameter cathode orifice and a tantalum keeper with a 4.76 mm diameter orifice. All other dimensions are similar to the NSTAR hollow cathode. The cathode was mounted at an angle of approximately 23° angle relative to the thruster's centerline axis with the orifice approximately one discharge channel outer diameter above the thruster centerline in the plane of the thruster exit and directed towards the beam.

5.2. JPL High Bay Vacuum Facility

The second phase of experimental testing was conducted at the High Bay vacuum Facility at the Jet Propulsion Laboratory. The High Bay Facility, shown in Figure 5.2-1, utilizes a cylindrical vacuum chamber measuring 2.6 m in diameter and 5.2 m long. All internal surfaces of the chamber with line-of-sight to the thruster's discharge channel are covered with either graphite panels or other carbon material to protect the vacuum chamber walls from ion bombardment erosion. Three cryogenic pumps are operated in parallel for a combined xenon pumping speed of over 40,000 l/s. The chamber pressure is monitored by two ionization gauges calibrated for xenon. The first gauge is located on the thruster exit plane approximately 1 m from the thruster and is used as the primary indication of chamber pressure. The second gauge, used to confirm pressure readings from the first gauge, is mounted along the chamber wall just downstream of the thruster exit plane. For these experiments, the nitrogen base pressure of the system was less than $5x10^{-8}$ Torr. During operation with xenon flow of approximately 30 sccm, the chamber pressure remains below $1.5x10^{-5}$ Torr, corrected for xenon. A xenon flow bypass, regulated by a hand-operated needle valve, is incorporated into the flow system (flow outlet

located approximately 2 m downstream of and oriented away from thruster face) to increase the facility background pressure if desired.

Figure 5.2-1. *JPL High Bay Facility vacuum chamber and supporting equipment.*

To characterize the performance of the High Bay Facility, the chamber pressure as a function of the total hot propellant flow rate (during thruster operation) was recorded. Figure 5.2-2 presents these results, showing a highly linear trend of pressure with increasing propellant flow. Slightly higher pressures were observed as the discharge voltage increased (seen as a vertical displacement of the curves), likely due to the more energetic ion populations inside the chamber. Overall, the facility showed linear and predictable pressure behavior with increasing propellant flow rate.

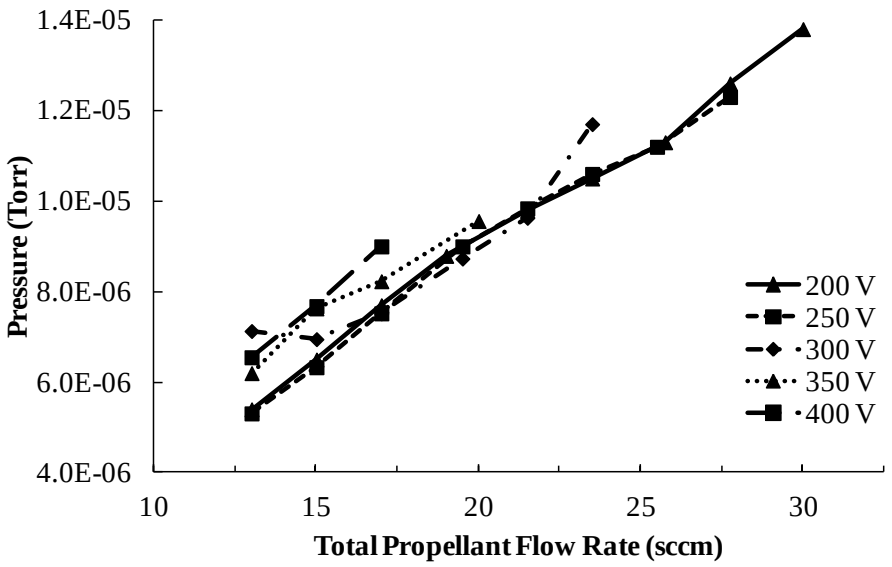

Figure 5.2-2. *High Bay Facility pressure as a function of total propellant flow rate at five discharge voltage operating points using the MaSMi-60.*

Commercially available power supplies and propellant flow controllers were used for all experiments. Thruster discharge, cathode heater, and cathode keeper power was supplied by Sorensen DLM-series power supplies while the coil magnets were powered by Power Ten supplies. Research grade xenon was supplied to the thruster and cathode by Apex mass flow controllers (calibrated at 0°C) via stainless steel lines. Both controllers were calibrated prior to testing and were digitally controlled to an accuracy of ± 1% of the set point. The same BaO-W cathode used during the UCLA testing was utilized for all JPL experiments. The cathode positioning and orientation was maintained from the UCLA testing for the MaSMi-40 (23° relative to the thruster axis with the orifice at the thruster exit plane and one discharge channel outer diameter above centerline). During testing of the MaSMi-60, the cathode was placed at a 45° angle with respect to the thruster axis with the orifice placed one discharge channel outer diameter above centerline and in the plane of the thruster exit. The modification in cathode

position from the MaSMi-40 setup was made based on the cathode positions used on two flight thrusters: the BHT-200 and the SPT-100 [65,66,85–87].

5.3. Assessment of the Magnetically Shielded Field Topology

The driving motivation of this thesis work is to demonstrate that magnetic shielding can be applied to low-power Hall thrusters as a means to extend their useful lifetimes. Therefore, the results from both the experimental and computational portions of this work must offer conclusive evidence that the MaSMi thruster produced a magnetically shielded field topology. Traditionally, probes have been embedded into the discharge channel walls of magnetically shielded Hall thrusters to measure the electron temperature, plasma potential, and approximate erosion rates along these surfaces [1]. The measurement of low electron temperature and plasma potentials close to that of the discharge voltage by wall probes suggest that the two key features of a MS are satisfied (see Section 3.6). The calculated erosion rates, along with the approximate bounding of the wall erosion (see Section 5.3.2.8.1), offers further evidence of MS. The small discharge channel dimensions of the MaSMi Hall thruster, however, prevent the use of wall probes; alternative methods must therefore be employed to confirm the presence of a magnetically shielded field topology.

1) *Magnetic Field Measurements:* The magnetic field of the MaSMi Hall thruster was measured in ambient conditions to determine its strength and topology. Due to the sensitive in nature of these results, they are not be presented in this document but are available in an export-controlled publication [79].
2) *Visual Observations:* Two unique visual features of a magnetically shielded Hall thruster are a clear offset of the near-exit plasma from the discharge channel walls (i.e. the plasma forms a toroidal shape and is confined between the walls rather than being in contact with

them) and a carbon coated discharge channel observed after operation [1]. During and after operation of the MaSMi Hall thruster, observations were made to confirm the presence of these two features suggesting successful MS; these results are presented alongside the experimentally measured performance for the MaSMi-40 and MaSMi-60 in Chapters 6 and 7, respectively.

3) *Beam Composition:* The ion species content of an MS Hall thruster's discharge is significantly different than an unshielded Hall thruster. Unshielded Hall thrusters of all power levels generate favorable ion species mixes. The BHT-200-X3, for example, produces approximately 95.5% singly charged, 3.7% doubly charged, and 0.8% triply charged ions [88]. By contrast, the H6MS Hall thruster generates a species mix of 57.5% singly, 25.9% doubly, and 16.6% triply and quadruply charged ions; the larger populations of multiply charged ions is a result of an MS field's improved confinement and retention of higher-energy electrons compared to unshielded Hall thrusters [1,37]. Therefore, the ion species contents of the MaSMi-40 and the MaSMi-60 were measured and compared to results published for the H6MS to confirm a similarly high content of multiply charged ions in the beam.

4) *Numerical Simulations:* Simulations of the MaSMi Hall thruster's discharge plasma using Hall2De provided predictions of the electron temperature, discharge potential, and erosion rates along the channel surfaces. For the MaSMi-60, the predicted electron temperature and plasma potential were compared to experimentally measured values downstream of the thruster's exit plane. Results from the computational investigation, including the sensitivity study to determine the variability of Hall2De's outputs as a function of the user inputs, are presented in Chapter 8.

5.4. Performance and Plume Characterization

To determine the performance of a Hall thruster and to understand the plasma environment in the thruster plume, a variety of diagnostics must be employed. These diagnostics are used to measure the thrust and efficiency of the device along with a variety of plasma parameters, including plasma potential, plasma density, ion energy, and electron temperature. Each of these parameters and the methods used to measure them are described below.

5.4.1. Thrust Stand

A thrust stand is a device that allows for the direct measurement of the thrust produced by an EP device. A custom-built water-cooled inverted-pendulum thrust stand was used to take thrust measurements at the JPL High Bay Facility. Displacement of the thrust stand pendulum due to an applied thrust is converted to a digital signal via a linear variable differential transformer (LVDT). This signal is passed through a feedback-based damping control system which eliminates any AC component of the pendulum displacement caused by plasma oscillations, cryogenic pump operation vibrations, external facility vibrations, etc., maintaining that only the DC component of thrust is reported by the LVDT. A force-to-displacement calibration of the thrust stand is performed prior to each test to ensure accuracy in the LVDT output. Throughout testing, the thrust stand demonstrated a minimum thrust resolution of approximately 0.1 mN with a measurement uncertainty of less than 5% of the reported thrust value. A photograph of the thrust stand installed in the experimental facility is shown in Figure 5.4-1.

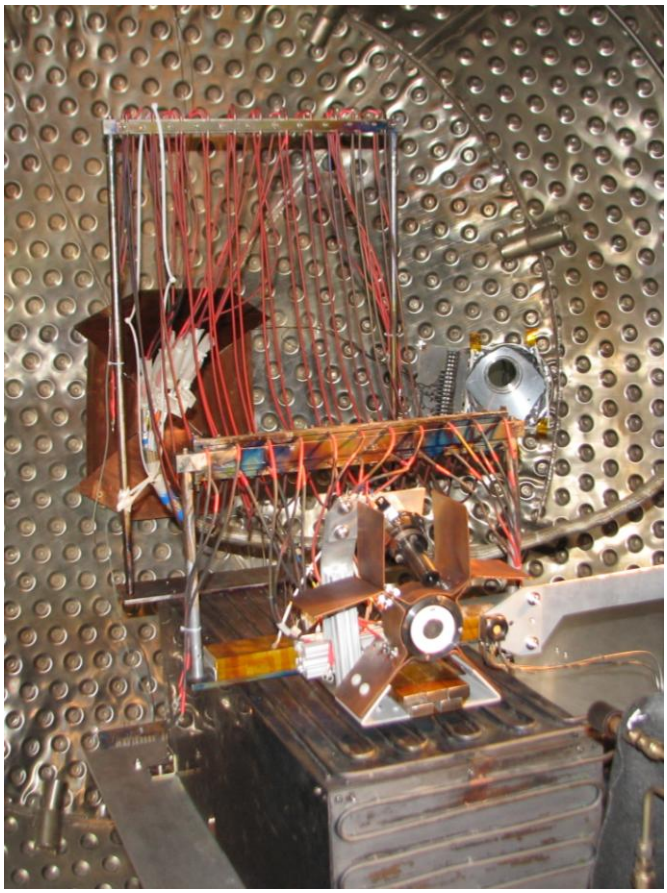

Figure 5.4-1. *Photograph of the MaSMi-40 mounted to the thrust stand installed in the JPL High Bay vacuum chamber.*

5.4.2. Plasma and Thruster Diagnostics

The key plasma parameters involved in determining a Hall thruster's performance are described below. A review of the plasma diagnostics used to measure these parameters follows. Included are operation principles, geometry and data collection procedures, and descriptions of the applied uncertainty analysis techniques (where applicable) of the probes used during this investigation.

5.4.2.1. Key Plasma and Thruster Performance Parameters

While details on the diagnostics used to determine the plasma parameters pertaining to Hall thruster performance are detailed in the next section, a brief description of these parameters

are given here. The plasma potential, or coupling voltage, is the local voltage to which the plasma floats above ground. Emissive probes are ideal for measuring the plasma potential directly. The ion current density is the number of particles per unit area accelerated by the thruster at a given downstream location. This plasma parameter, along with the beam current and beam profile, can be easily determined by utilizing a scanning planar or Faraday probe.

The ion energy (also known as the most probable ion potential) is the net potential drop through which beam ions are accelerated. This is, by definition, equivalent to the beam voltage. This parameter can be measured using a retarding potential analyzer. The beam composition, or ion species mix, is the current contribution of each ion charge species in the plasma beam relative to the total beam current. This can be determined by use of an **E**x**B** probe. The electron temperature is a measure of the energy of electrons. This can be measured by using a Langmuir probe. The discharge channel erosion rate due to ion bombardment can be estimated based on the rate of carbon deposition onto the channel walls. The rate of carbon deposition is measured by a quartz-crystal microbalance.

5.4.2.2. Emissive Probe

5.4.2.2.1. Operation Principles

An emissive probe is used to directly measure the plasma potential; a cross-sectional diagram of an emissive probe is shown in Figure 5.4-2.

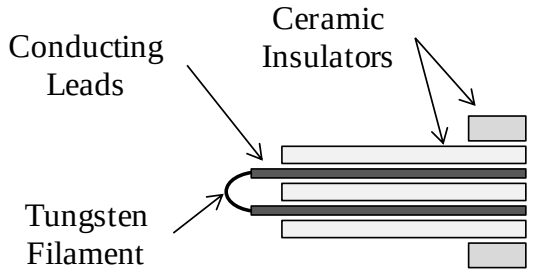

Figure 5.4-2: *Cross-sectional diagram of the filament-end of an emissive probe.*

These probes operate by passing a current through an electrode (generally tungsten) that causes electron emission. If sufficient current is passed through the electrode while it is immersed in a thruster's plasma beam, the probe's electron emission and collection will reach equilibrium and the probe will float to near the plasma potential. By convention, this is identified by the approximate location of the knee in the floating potential vs. heater current trace. Because the emissive probe can never float to the actual plasma potential (the filament melts before this point), a small correction must be applied to the measured probe floating potential based on the electron temperature local to the emissive probe. While for form of this correction depends on the emissive probe measurement location (upstream of the exit plane, near-plume region, or far-field region), the correction used for this investigation was

$$V_{float} = V_p - \frac{T_e}{2} \qquad 5.4\text{-}1$$

where V_{float} is the measured floating potential. Although an emissive probe provides a direct method of measuring plasma potential, it is very challenging to determine and apply the correct amount of current to float the probe electrode to the plasma potential and not melt the filament. Therefore this measurement has some uncertainty in determining the actual plasma potential.

5.4.2.2.2. Geometry and Data Collection Procedure

The emissive probe used at the JPL High Bay Facility consisted of a 0.13 mm tungsten filament spot-welded to a pair of 0.51mm tantalum rods sheathed in alumina insulators. The probe was mounted on a grounded, stationary structure approximately 40 cm downstream of the thruster exit plane. A heater current from a Kepco 4 A power supply was applied to the filament while the probe's floating potential was recorded; both the heater current and floating potential were measured by a simple data acquisition system. The floating potential was plotted against the applied heater current to find the knee in the curve, indicating the correct heater current to

identify the local plasma potential. No emissive probe measurements were taken during the testing of the MaSMi-40 at either the UCLA EP Test Facility or the JPL High Bay Facility.

5.4.2.2.3. Uncertainty Analysis

The uncertainty analysis in the plasma potential measurements was based on the assumed electron temperature local to the emissive probe. The electron temperature was assumed to fall between 2 eV to 4 eV; based on Equation 5.4-1, this corresponds to an uncertainty of approximately +/-1 V in the plasma potential measurement.

5.4.2.3. Planar and Faraday Probes

5.4.2.3.1. Operation Principles

Planar probes and Faraday probes are used to determine the ion current density, integrated beam current, and beam profile of a thruster plume. Cross-sectional diagrams of a planar probe and a Faraday probe are shown in Figure 5.4-3.

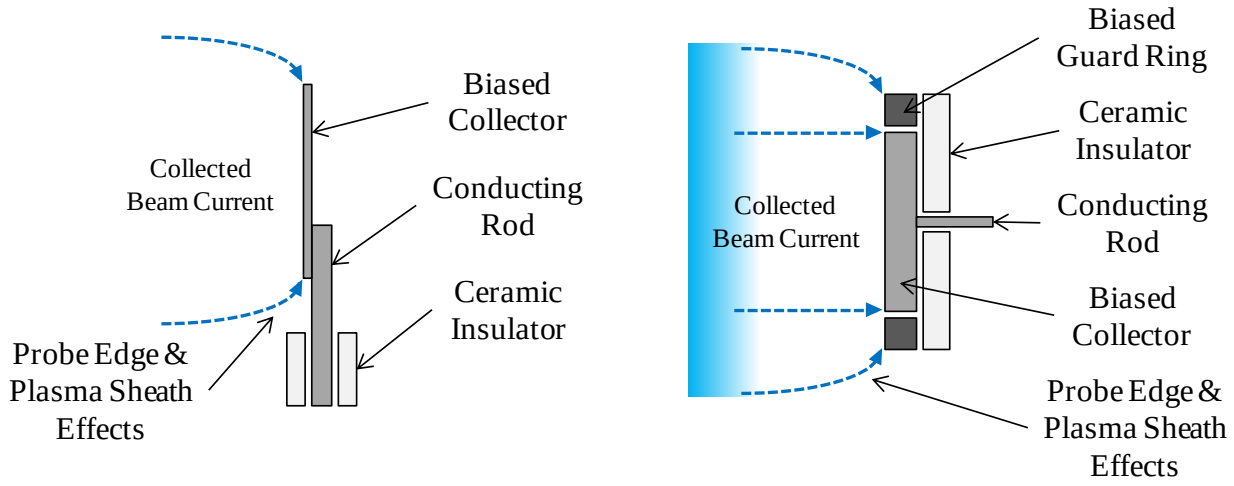

Figure 5.4-3: *Cross-sectional diagram of a planar probe (left) and a Faraday probe (right) showing the effects of the negative collector bias on the incident plasma.*

A scanning planar probe is comprised of a flat single-sided disk electrode with a negative voltage bias. A Faraday probe has a similar geometry, but incorporates a shield around the disk electrode set at the same bias as the electrode to inhibit plasma sheath expansion effects at the

disk edge from changing the disk's collected current (as represented in Figure 5.4-3 by the dashed arrows). In both cases, the negative bias voltage provides for ion collection by the probe while eliminating the collection of electrons.

The ion current density in the plasma plume (J_i) is calculated as

$$J_i = I_p / A_p \tag{5.4-2}$$

where I_p is the ion current collected by the negatively biased probe and A_p is the probe area. A single probe scan measures the ion current density profile across the entire thruster plume. The total beam (ion) current is determined by integrating the ion current density at each measurement location around half of the azimuthal distance of the beam. The current from the two azimuthal halves of the ion beam are then summed to account for slight asymmetries in the beam profile from one side of the thruster to the other. This simplifies to

$$I_b = \pi w \sum J_{i,n} R_n \tag{5.4-3}$$

where w is the width of the beam sampled by the probe (usually equal to the resolution of the scan) and R_n is the n^{th} radial distance of the probe from the thruster's centerline (in the plane of the probe trace).

The angular spread in the plasma beam, which relates to the amount of useful thrust generated parallel to the thruster's axis, is characterized by the beam's divergence half-angle. The divergence half-angle is approximated as the beam angle which encompasses 95% of the momentum-weighted ion current, which is described in detail in [89].

5.4.2.3.2. Geometry and Data Collection Procedure

To measure the ion current density profile of the MaSMi Hall thruster, a planar probe was used at the UCLA EP Test Facility while a shielded Faraday probe was used at the JPL High Bay Facility. During the early stages of this investigation at UCLA, planar probes were used due to

their simplicity in construction. However, as the project matured and moved to the JPL facility, existing Faraday probes were made available for use with the MaSMi thrusters. The planar probe used at UCLA was a 4 mm diameter, 0.125 mm thick molybdenum disk electrode connected to an alumina-insulated 1.25 mm diameter tantalum wire. The probe's electron-repelling bias was measured at -28 V relative to chamber ground. The planar probe was scanned +/-12 cm from the thruster's centerline in the radial direction at two locations, 1 *L* and 2 *L*, downstream of the thruster's exit plane. A scan at approximately one discharge channel outer diameter downstream of the exit plane was used for ion current density measurements because charge-exchange effects are minimized near the thruster exit plane. A scan at approximately two discharge channel outer diameters downstream of the exit plane offered insight into the evolution of the beam's properties downstream of the thruster while helping reduce the effects of the negatively biased body on the discharge plasma local to the thruster. A Velmex single-axis mechanical translation stage with supporting Velmex VXM stepping motor controller provided horizontal motion across the thruster face. Only one probe stage was available in the UCLA Electric Propulsion Test Facility at the time of testing; therefore, the axial location of the probe was locked prior to pump-down of the chamber.

Ion current density measurements at JPL were taken using a 24 mm outer diameter cylindrical graphite Faraday probe with a collector diameter of 19 mm. The probe was biased to -28 V for all testing. Perpendicularly mounted LinTech stages driven by Vexta stepper motors operated by Velmex VXM stepping motor controllers were used to first establish the desired axial position of the probe downstream of the thruster and then to translate the probe +/-35 cm from the thruster centerline in the radial direction. At each radial position, the probe's reported measurement was the average of 2000 data points captured at 200 kHz in an effort to account for

discharge oscillations that may skew a single-point measurement. Early measurements were taken at approximately two discharge channel outer diameters downstream of the thruster exit plane to match the UCLA experiments. However, observations of the discharge plasma coupling to the negatively biased probe motivated later measurements to be taken at approximately five discharge channel outer diameters downstream of the exit plane.

A correction is necessary for both planar and Faraday probe measurements to account for charge-exchange (CEX) effects, which result from an imperfect vacuum environment. These effects are observed across the full ion current density profile and are most easily identified by the "wings" of the probe trace near the radially outward edges of the plasma beam. The correction is made by subtracting the value of the wings from the ion current density measurement across the full profile to account for effects of background charge-exchange effects [90]. An example of this is shown in Figure 5.4-4. The calculated ion current using this charge-exchange correction is slightly more conservative than alternative methods suggested in the literature, which involves fitting an exponential curve to the data collected near the thruster centerline and extending it to the limits of the data collection range [67].

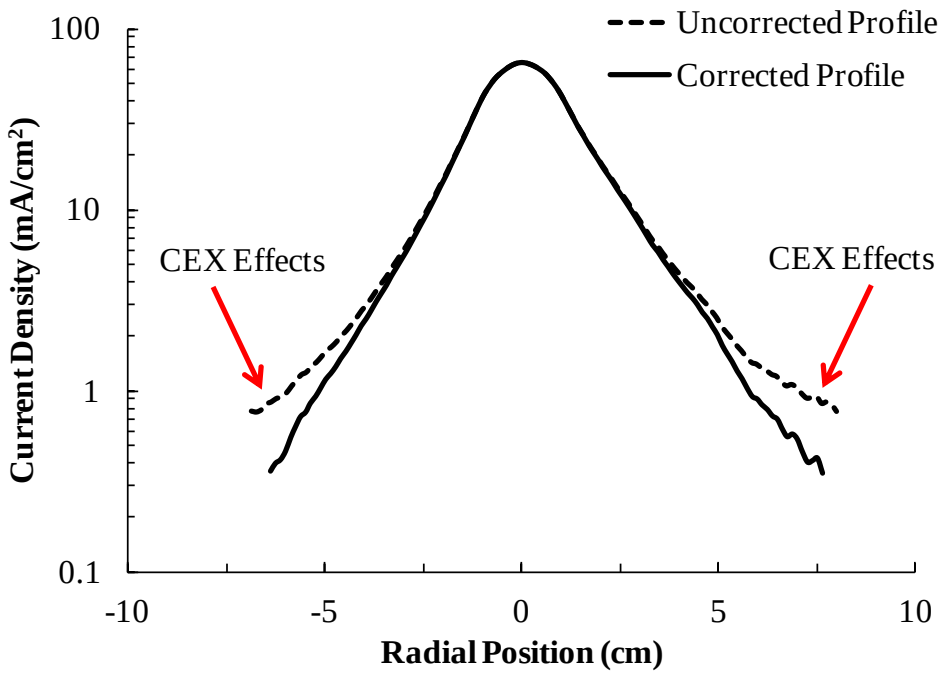

Figure 5.4-4: *Uncorrected and corrected current density profiles highlighting the charge-exchange effects on the measurement data.*

5.4.2.3.3. Uncertainty Analysis

Several methods were employed to determine the approximate uncertainty of the planar probe measurements. Sheath expansion effects were considered based on the studies of probe-plasma interactions by Sheridan; however, the results presented are applicable to a double-sided flat probe in a stationary plasma [91]. The ions in a Hall thruster discharge comprise a flowing plasma (on the order of 10's of km/s) and the planar probe utilized was single-sided and of a very small size; however, the high background pressures observed during thruster operation would lead to increased presence of charge-exchange ions in the near-exit region of the thruster that would not be accounted for using established correction techniques. This was accounted for by the assumption of a probe sheath expansion of 33%, directly applied to the planar probe's collection area. This led to an uncertainty in the ion current density measurements of approximately +/-0.25 mA/cm^2. A beam divergence half-angle uncertainty of +/-5° was

estimated based on a combination of the position accuracy of the probe stages and the uncertainty in the integration of the probe current profile due to the error in the ion current density estimate from the probe.

The uncertainty of the ion current density measurements using the Faraday probe was approximately +/-0.05 mA/cm^2, based on the probe measurement resolution and the post-processing electronics' sensitivities to the ion current signal. The uncertainty in the divergence half-angle was approximately +/-2.5°, based on uncertainty in the probe's ion current density measurements and position data recorded by calibrated string pots attached to the probe stages. The improvement in uncertainty observed with the Faraday probe is largely attributed to the lack of sheath expansion effects enabled by the Faraday shield and the larger probe area (ratio of current collected by sheath effects compared to the total collected current decreases as the area of the probe increases).

5.4.2.4. Retarding Potential Analyzer

5.4.2.4.1. Operation Principles

A retarding potential analyzer (RPA) utilizes a series of biased grids to measure ion energy. A cross-sectional diagram of a typical 4-grid RPA is shown in Figure 5.4-5.

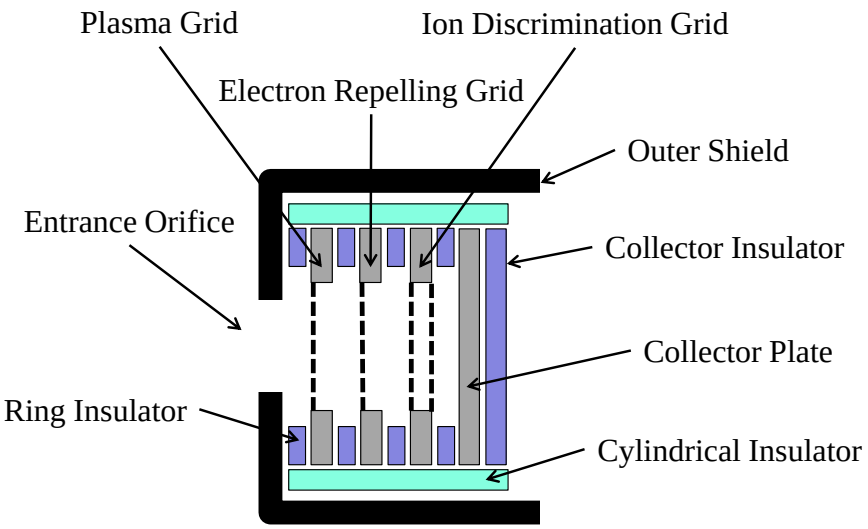

Figure 5.4-5: *Cross-sectional diagram of a 4-grid retarding potential analyzer.*

The first grid, used to reduce the influx of plasma into the probe based on its transparency, is in contact with the plasma and floats to the plasma potential. The second grid is negatively biased to repel electrons and prevent them from being registered by the collector electrode. The third (and sometimes fourth) grid is used as a positively biased ion discriminator, allowing only ions with energies greater than the applied voltage to reach the collector. Sometimes a final negatively biased grid is used to repel any secondary electrons generated at the collector to prevent current losses. An electrode is placed behind the series of grids to collect ions that pass through the grid optics, yielding an ion current measurement. The ion energy (velocity) distribution is obtained by taking the first derivative of the collected ion current with respect to the ion discriminator bias potential (V_{bias}), shown in Equation 5.4-4, which should yield a clear peak slightly below the applied discharge voltage [92,93]:

$$-\frac{dI_p}{dV_{bias}} = \frac{(Ze)^2 n_i A_p}{TM} f_i(V) \qquad 5.4\text{-}4$$

where Z is the ion charge state, t_{grid} is the total RPA grid transparency, and $f_i(V)$ is the ion energy distribution function with respect to potential. Taking the maximum value of this peak and

subtracting the local plasma potential, measured by an emissive probe adjacent to the RPA, yields the most probable ion potential; the plasma potential must be subtracted to achieve the net accelerating potential experienced by the ion, as shown in Figure 3.3-1. The spread of ion velocities is described by the width of the distribution at half of the peak value, called the full width at half maximum, or FWHM.

5.4.2.4.2. Geometry and Data Collection Procedure

While the scale and number of grids may differ depending on the specific application of an RPA, the general architecture of the device remains similar. The spacing of the electron repeller grid and ion discriminator grid inside of an RPA is critical due to space-charge limitations, which occurs when a charged species (positive or negative) is selectively removed from the flow. This results in a build-up of charge between the grids, yielding a potential hill that may become greater than the applied voltage and thereby may disrupt the proper operation of the RPA. Assuming the plasma density is the maximum possible before space charge limitations affect the RPA, the relationship between the grid spacing (x) and the potential difference between the electron repeller and ion discriminator grids (V_g) is given by

$$\frac{x}{\lambda_D} = 1.02\left(\frac{eV_g}{kT_e}\right)^{3/4} \qquad 5.4\text{-}5$$

where λ_D is the Debye length [94,95]. In general, V_g is several times larger than T_e to ensure that electrons are repelled; this leads to a spacing requirement for the electron-ion grids:

$$x < 4\lambda_d\,. \qquad 5.4\text{-}6$$

An RPA was custom built for all of the UCLA testing and a portion of the JPL testing. It has a 9.5 mm diameter entrance orifice to the grid assembly. Stainless steel grids mounted to 0.5 mm stainless steel rings reduce the plasma flux to the collector plate; the plasma, electron

repeller, and ion discriminator grid transparencies are 36%, 44%, and 40%, respectively. Each grid is separated by a 0.4 mm insulator ring, and the entire assembly is insulated from the aluminum outer shield by a cylindrical insulator. RPAs using a single grid ion discriminator may permit lower-than-desired energy ions through the gird due to reductions in the discriminator potential at the centers of the ion grid orifices, leading to an over-estimate of collected ion current for a given discriminator potential [96]. To combat this effect and improve ion energy resolution, the UCLA RPA employs a four-grid design where the third and fourth grids act as a double ion discriminator (therefore, the effective grid transparency of the ion discriminator is 0.16). At the end of the assembly is a 0.75 mm stainless steel disk acting as a simple collector plate.

It should be noted that, while the operation principles remain the same, a custom JPL-designed 5-grid RPA (including a secondary electron repelling grid in between the ion discriminator grids and the collector plate) with a 19 mm orifice was used for several of the MaSMi-40 experiments conducted at the JPL High Bay Facility. Poor current resolution across the saturated portion of the ion current trace, however, led to the use of the UCLA RPA at the JPL facility for experiments with the MaSMi-60.

The RPA's electron repelling grid(s) was biased to between -20 V and -30 V relative to ground (whichever produced the cleanest ion current trace) while the potential applied to the ion discriminator grid was swept from 0 V to 400 V. The RPA was mounted on a stationary grounded structure approximately 80 cm downstream of the thruster exit plane at the UCLA EP Test Facility; this distance was reduced to 40 cm at the JPL High Bay Facility for improved ion current resolution.

5.4.2.4.3. Uncertainty Analysis

The uncertainty in the UCLA RPA's reported most probable ion potential was estimated at +/-10 V based on the uncertainly in the plasma potential from the emissive probe, the measurement of V_{cg} used to determine the coupling voltage, and broadening in the RPA measurements related to the ion optics possibly due to a build-up of pressure inside the probe [27]. The uncertainty of the 5-grid JPL RPA was assumed to be the same as the UCLA RPA. For the RPA measurements at the UCLA EP Test Facility, an additional uncertainly of $2T_e$ (6 V) was assumed to account for the absence of an emissive probe measurement.

5.4.2.5. ExB Probe

5.4.2.5.1. Operation Principles

An **E**x**B** probe is a band-pass filter used to determine the charge-state of ions in a plasma (singly charged, doubly charged, etc). An illustration of this **E**x**B** probe is shown in Figure 5.4-6.

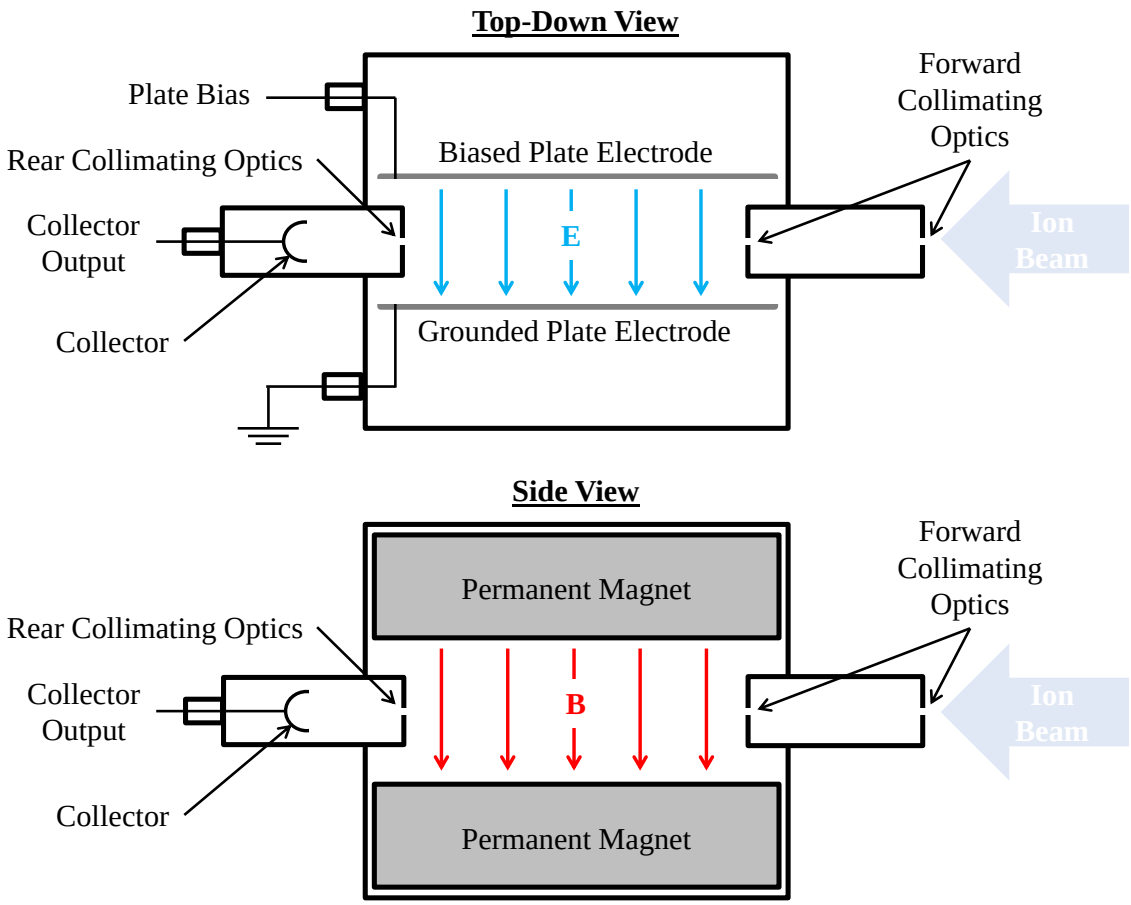

Figure 5.4-6: *Illustration of an* ***ExB*** *probe with the orientation of the electric and magnetic fields relative to the incident plasma specified.*

Ions entering the probe are exposed to perpendicularly-oriented uniform electric and magnetic fields, both oriented perpendicular to the ion velocity vector. The net force on these particles is described by the Lorentz equation, modified here to show the charge state of ions:

$$\boldsymbol{F} = eZ(\boldsymbol{E} + \boldsymbol{v} \times \boldsymbol{B}) \,. \qquad 5.4\text{-}7$$

Based on Equation 5.4-7, the probe's internal fields generate opposing forces on the ions: a linear force along the electric field, an azimuthal (i.e. turning) force around the magnetic field lines, and a drift force perpendicular to both the electric and magnetic fields. For an ion to pass through the filter and be collected, the particle must travel in an axial trajectory through the probe (i.e. have no net turning forces). Applying this feature to Equation 5.4-7 yields

$$0 = eZ(\boldsymbol{E} + \boldsymbol{v} \times \boldsymbol{B}) \,. \tag{5.4-8}$$

Assuming the electric and mangetic fields are perpendicular, the velocity of ions passing through the probe is deterimned by solving Equation 5.4-8, giving

$$v = -\frac{E}{B} \tag{5.4-8}$$

which, interestingly, is independent of the ion charge state and mass. From Equation 5.4-8, it is clear that the ion velocity can be adjusted by changing the applied (crossed) electric and mangetic fields. Generally, **E**x**B** probes use permanent magnets to generate a constant and approximately uniform magnetic field. The spectrum of the beam composition collected by the probe's detector is therefore generated by sweeping the magnitude of the electric field, which is accomplished by changing the applied bias potential between the two internal parallel plates separated by a fixed distance (*d*):

$$E = -\frac{V_{bias}}{d} \,. \tag{5.4-9}$$

Combining Equations 5.4-8 and 5.4-9 yiels the velocity of the ions inside the probe, yielding

$$v = \frac{V_{bias}}{Bd} \,. \tag{5.4-10}$$

Therefore, an **E**x**B** probe is simply a velocity discriminator.

The acceleration of an ion as it passes through a potential drop is proportional to the square root of the ion's charge-state, thereby generating different velocities for each ion charge-state species in a thruster's plume. This can be shown based on the energy equation for charged particles (in this case, xenon ions):

$$E = \frac{1}{2} M {v_i}^2 \;\rightarrow\; |v_i| = \sqrt{\frac{2E}{M}} = \sqrt{\frac{2eZV_b}{M}} \tag{5.4-11}$$

where E is the ion energy, and the acceleration potential through which an ion in a Hall thruster travels is the beam voltage. Substituting Equation 5.4-11 into Equation 5.4-10 and solving for the applied potential in the **E**x**B** probe gives

$$V_{bias} = Bd\sqrt{\frac{2eZV_b}{M}} \; . \qquad 5.4\text{-}12$$

This shows that the velocity distribution function in the ion beam is a function of the effective accelerating potential for each ion charge state. Because the acceleration potential experienced by ions depend on their charge state, each ion species entering the **E**x**B** probe will experience different intensities of the applied electromagnetic forces based on its velocity. By sweeping V_{probe} across a sufficiently wide potential band, the fractional populations of each ion charge species in the thruster beam can be identified.

5.4.2.5.2. Geometry and Data Collection Procedure

A custom-built **E**x**B** probe placed approximately 40 cm downstream of the thruster was used to measure the ion species mix in the thruster's plasma beam at the JPL High Bay Facility. The forward collimating optics included 0.075 mm diameter orifices while the rear optics consisted of a 2.2 mm x 5.7 mm slot. A parabolic collector was used to aid in the recovery of secondary electrons generated by ions impacting the collector electrode, thereby improving the accuracy of the ion current measurements. A stationary, vertically-oriented magnetic field with a centerline magnitude of approximately 0.12 T was generated by a pair of permanent magnets. The perpendicular electric field was generated between two plate electrodes spaced 31 mm apart; a swept potential from 0 V to 200 V (yielding a maximum electric field magnitude of over 6,400 V/m) was applied to one plate while the second plate was grounded to the chamber.

Gaussian curves are fit to the **E**x**B** probe traces to estimate the charged species content of the plasma beam. The relative areas under the Gaussian curves of each ion species are directly proportional to each species' fractional contribution to the total beam current. To account for any lack of resolution in the ion velocity spectra, the sum of the Gaussian curves for the three ion species were matched with the measurement. Additionally, each Gaussian was approximately centered at the expected bias potential required to balance the **E**x**B** probe's stationary magnetic field based on the probe's geometry.

5.4.2.5.3. Uncertainty Analysis

The uncertainty in the ion current fraction for each charge species was estimated based on the **E**x**B** probe's measurement sensitivity for each ion species, the probe's resolution, and the probe's misalignment to the plasma beam. This resulted in an uncertainty of approximately +/-0.05 for each of the ion species fractions. Combined with the uncertainty in the ion current measurements and the mass flow meters' reported uncertainty, this leads to an uncertainty in the mass utilization efficiency of approximately +/-8%.

5.4.2.6. Langmuir Probe

5.4.2.6.1. Operation Principles

A Langmuir probe is a common plasma diagnostic used to determine the plasma potential, plasma density, and electron temperature from a single trace measurement. A current-voltage (*I*-*V*) characteristic (i.e. trace) results from current and voltage measurements of a plasma, yielding the abovementioned plasma parameters. The probe consists of an electrode placed in a plasma with an applied voltage sweep. The negative portion of the voltage sweep collects ion current while the positive portion results in electron current collection. An example Langmuir *I*-*V* characteristic is presented in the two plots shown in Figure 5.4-7 with the three

key regions of the trace highlighted; the first plot uses a linear vertical scale while the second plot uses a semi-log plot vertical scale (note that the values in the second plot have been scaled to avoid values below zero). The example data have been multiplied by -1, by convention, because more electron current is collected than ion current due to the electrons' higher velocity.

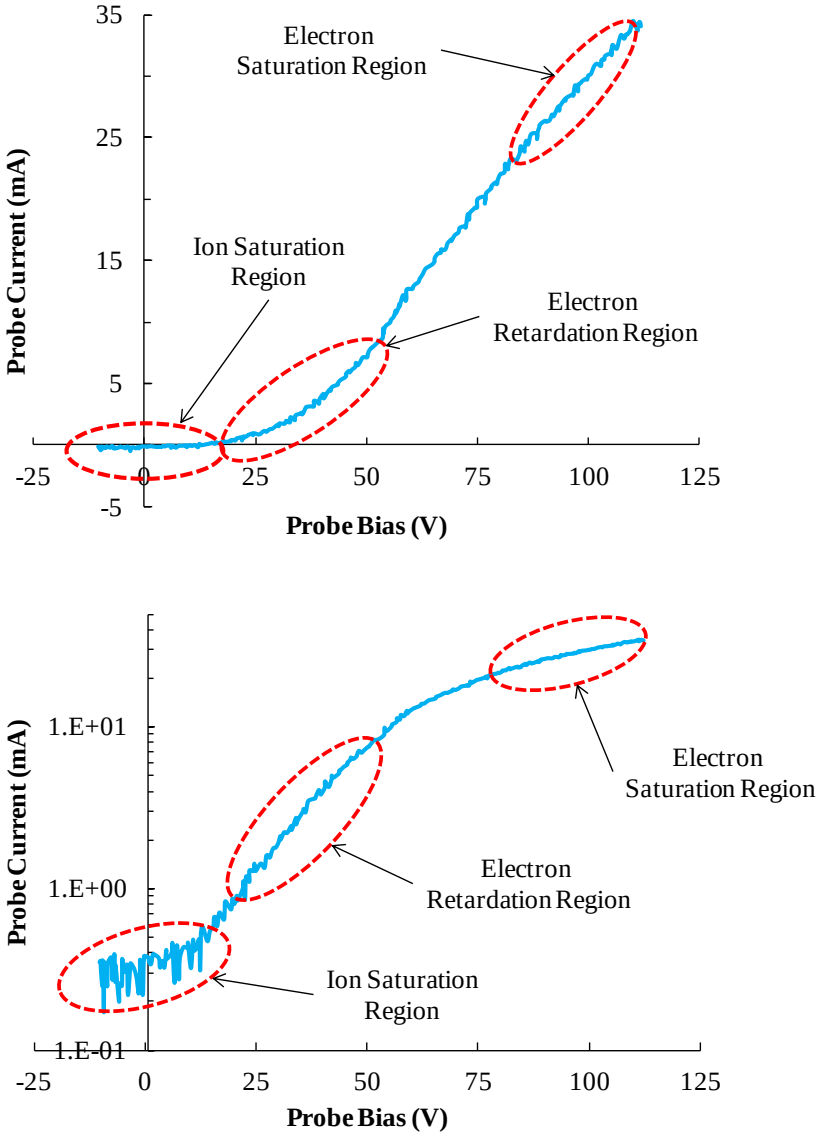

Figure 5.4-7: *Example Langmuir trace with a linear (top) and semi-log (bottom) vertical scale highlighting the ion saturation, electron saturation, and electron retardation regions.*

In the ion saturation region, the large negative probe bias repels nearly all electrons and causes ions to be accelerated through the established probe sheath to be collected. The ion velocity to the probe will satisfy the Bohm sheath criterion required for plasma and potential stability at the sheath edge, given by

$$v_i = \sqrt{\frac{k(T_e + Z\gamma_i T_i)}{M}} \approx \sqrt{\frac{kT_e}{M}}. \qquad 5.4\text{-}13$$

where γ_i is the adiabatic coefficient for the ions and T_i is the ion temperature [3]. Assuming a quasineutral plasma, the ion current density is described by

$$j_i = en_e v_i . \qquad 5.4\text{-}14$$

The current density is therefore not a function of bias potential (neglecting sheath effects); however a sufficient bias must be used to repel the higher energy tail of the electron distribution. Combining Equations 5.4-13 and 5.4-14 gives the ion saturation current ($I_{i,sat}$):

$$I_{i,sat} = \beta n_e e A_p \sqrt{\frac{kT_e}{M}}. \qquad 5.4\text{-}15$$

where β is the Bohm coefficient. Assuming a collisionless plasma such as in a Hall thruster, the value of β is conventionally 0.5 [97,98].

As the probe bias becomes less negative (but still below the plasma potential), some high energy electrons will be collected by the probe while the low energy population will continue to be repelled; this is the transition into the electron retardation region of the Langmuir trace. A Boltzmann distribution can be used to model electrons at the probe sheath edge:

$$f(v) = \left(\frac{m}{2\pi kT_e}\right)^{1/2} \exp\left(\frac{\frac{1}{2}mv^2}{kT_e}\right) . \qquad 5.4\text{-}16$$

The electron current to the probe (I_e) therefore becomes

$$I_e = \frac{1}{4} e n_e A_p \left(\frac{8kT_e}{\pi m}\right)^{1/2} exp\left(-\frac{e\Phi_s}{kT_e}\right) . \quad 5.4\text{-}17$$

The local electron temperature can be extracted from Equation 5.4-17, assuming the electron population is Maxwellian. This is also accomplished by generating an exponential fit to the electron retardation region of the Langmuir trace in the form of $I_p = Ae^{bV_{bias}}$: A is a fitting coefficient and b is the exponent fit coefficient. The electron temperature is inversely proportional to b, as shown in Figure 5.4-8.

As the probe bias becomes positive relative to the plasma potential, ions will be repelled from and electrons will be accelerated to the probe. Because no electron-repelling sheath exists in this condition, the effective probe area remains constant with further increases to probe bias and the collected current will saturate. This yields the electron saturation current,

$$I_{e,sat} = \frac{1}{4} e n_e A_p \left(\frac{8kT_e}{\pi m}\right)^{1/2} \quad 5.4\text{-}18$$

which is derived from Equation 5.4-18 with a sheath potential equal to zero. As with the electron retardation region, an exponential fit can be made to this portion of the Langmuir trace, using the same formulation as before, which allows for the approximation of the plasma potential. Note that a complete derivation of Equation 5.4-17 is presented in the literature [3,99].

The plasma potential can then be roughly determined by finding the intersection of the exponential curve fits to the electron retardation and electron saturation regions, which is most easily accomplished by plotting the fits on a semi-log plot. While this method gives a rough approximation of the plasma potential, large uncertainties are associated with approximate fits to the exponential curves which cause significant changes in the estimated plasma potential; therefore, other methods, such as an emissive probe, should be considered to gather more accurate plasma potential data. Figure 5.4-8 presents an example of the exponential fists

mentioned above and identifies the values of the electron temperature and plasma potential based on the selected fits; note that only the electron retardation and electron saturation regions are shown in the figure.

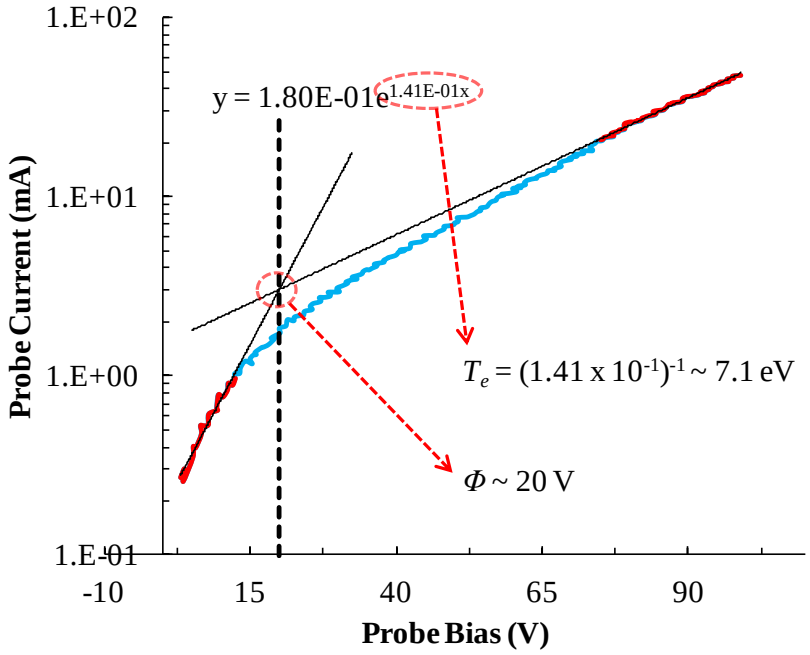

Figure 5.4-8: *Example Langmuir trace showing the exponential fits to the electron retardation and electron saturation regions and highlighting the method for determining the electron temperature and plasma potential from exponential fits to the trace.*

5.4.2.6.2. Geometry and Data Collection Procedure

The Langmuir probe used for this investigation consisted of a 1.5 mm long blunt-ended cylindrical electrode made from 0.127 mm diameter Ta wire. The wire was fed through an alumina sheath for electrical isolation and structural support. A BN sleeve approximately 25 mm long was placed over the alumina tube nearest to, but not shadowing, the electrode. This sleeve allows for more accurate measurements in the high density plasma region just downstream of the thruster exit plane due to BN's low secondary electron yield under xenon ion bombardment.

The Langmuir probe was mounted to a vertically-oriented Velmex fast-scanning probe stage with a sweep range of three thruster diameters, centered at the thruster centerline. The fast-scanning stage was mounted to an axially-oriented Velmex probe stage, enabling axial placement of the Langmuir probe from approximately 2.5 mm to over 30 mm downstream of the thruster exit plane. Both stages were driven by a VXM stepper motor controller and string pots mounted to each probe stage recorded position data. A Wavetek 178 function generator driving a Kepco high voltage power supply was used to bias the Langmuir probe with potential ramps fro +/-50 V at a frequency of 50 Hz. Measurements were taken across the entire thruster face at z/L values of approximately 1.15 to 1.9 by increments of 0.15. From these data, the Langmuir trace associated with the channel centerline was selected and processed.

5.4.2.6.3. Uncertainty Analysis

Two sources of uncertainty in the Langmuir probe analysis were considered: the selected fits to the probe data and the physical location of the probe relative to the thruster. The primary source of uncertainty in the Langmuir probe data was the selection of the most representative portion of the data (specifically, the slope of the electron retardation region) to determine the electron temperature and plasma potential. As can be deduced from Figure 5.4-8, the value of the electron temperature can change, sometimes significantly, with minor changes to the selected exponential fit to the electron retardation portion of the Langmuir trace. To estimate the uncertainty associated with the selected curve fit, several exponential fits were applied to each Langmuir trace to effectively span the range of (subjectively) good fits to the data. The uncertainty in the electron temperature was then approximated based on the spread of electron temperatures from the different fits. The same method was used to approximate the uncertainty in the plasma potential measurements. This led to uncertainties in the electron temperature

spanning from less than +/-2 eV to over +/- 8 eV and in the plasma potential ranging from +/-4 V to +/-27 V.

A secondary source of uncertainty was the axial position of the Langmuir probe relative (physically) to the thruster exit plane, but more importantly, relative to the discharge plasma. When probe scans were taken near to and through the acceleration zone, a clear perturbation of the plasma was observed. In these regions, an uncertainty of +/-10% of the MaSMi-60's discharge channel length was assumed to encompass both the uncertainty of the physical probe location and the magnitude of the shift in the plasma (discussed in Chapter 8). Probe scans taken at locations which left the plasma unperturbed had an axial uncertainty of approximately +/-2.5% of the MaSMi-60's discharge channel length based on the alignment of the probe relative to the thruster and the position data recorded by calibrated string pots attached to the probe stages.

Because the above uncertainties were dependent on each individual Langmuir trace, error bars were added to the plotted data to represent the uncertainty in the specific measurement.

5.4.2.7. Quartz Crystal Microbalance

5.4.2.7.1. Operation Principles

A quartz crystal microbalance (QCM) is a diagnostic that measures the rate of material sputtered from a surface and collected by the probe. An illustration of the QCM sensor is presented in Figure 5.4-9.

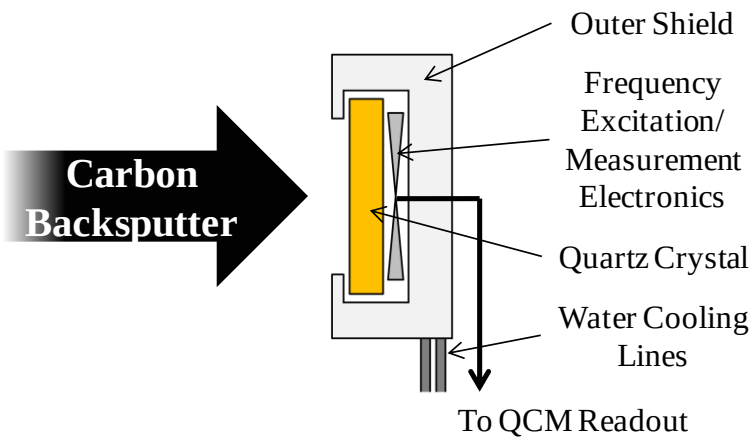

Figure 5.4-9: *Illustration of the sensor element of a quartz crystal microbalance system.*

QCMs operate by stimulating a piezoelectrically active crystal to vibrate at its resonant frequency. As atoms sputtered from a surface are deposited onto the QCM's crystal, the mass of the crystal (and therefore its resonant frequency) changes as a function of time. This frequency change can then be converted to a mass flux to the crystal surface, which corresponds to a sputter and redeposition rate for the plasma environment surrounding the QCM. It should be noted that temperature control of the QCM sensor is important to ensure accuracy of the reported measurements; as such, most QCM sensors (i.e. crystal holders) feature water-cooling to maintain constant operating temperatures and prevent thermal drift.

5.4.2.7.2. Geometry and Data Collection Procedure

An Inficon QCM system was used to measure carbon backsputter rates during operation of the MaSMi-60 at the JPL High Bay Facility. Standard Inficon gold-plated crystals optimized for thin-film deposition measurements were used in an Inficon water-cooled crystal sensor. The sensor was mounted approximately 20 cm laterally away from the thruster centerline with the sensor face in the plane of the thruster exit.

The carbon backsputter rate, measured by a QCM, can be used to estimate the lifetime of the channel before it fails due to ion bombardment erosion (discussed in greater detail in

Section 7.2). This offers an estimate on the total useful life of the Hall thruster based on the most common failure mechanisms. The QCM measurement system was calibrated for the measurement of carbon deposition prior to operation. The total carbon deposition as a function of time was monitored throughout a minimum of 20 minutes of continuous thruster operation to ensure a constant deposition rate was measured. This rate was then used approximate an upper bound on the discharge channel erosion rate (see Section 7.2).

5.4.2.7.3. Uncertainty Analysis

According to the Inficon QCM user manual, the measurement uncertainty in the total deposited film thickness is approximately +/-5 % of the reported value. Despite the highly conservative approach to estimating the discharge channel erosion rate (making the QCM measurement uncertainty effectively negligible compared to the applied assumptions), this uncertainty was nevertheless carried through the discharge channel erosion rate calculation.

5.4.2.8. Installed Diagnostics

Images of the experimental configurations used during testing of the MaSMi-40 and MaSMi-60 at the UCLA EP Test Facility and the JPL High Bay Facility are shown below. Figure 5.4-10 shows the test setup for the MaSMi-40 at the UCLA facility. Figures 5.4-11 and 5.4-12 show the test setup used for both the MaSMi-40 and MaSMi-60 at the JPL facility.

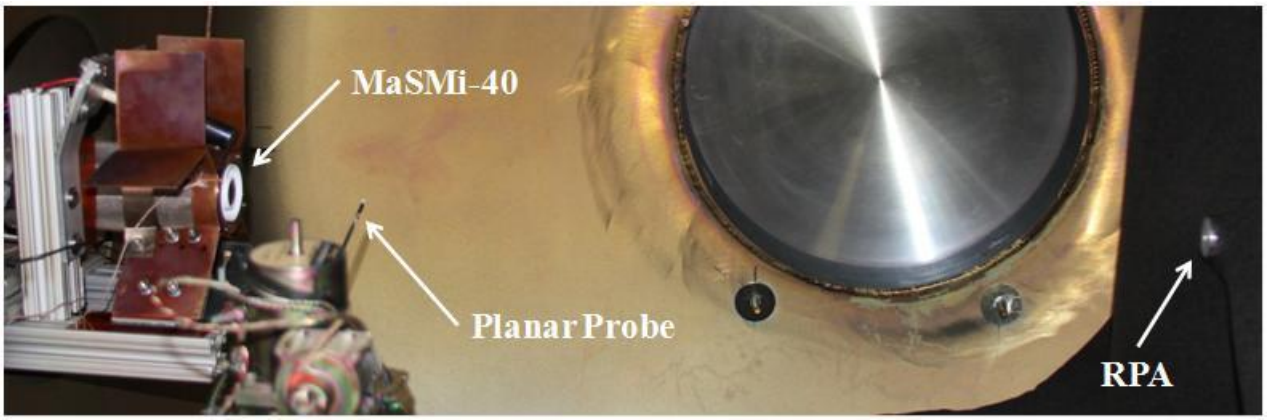

Figure 5.4-10: *Experimental configuration inside the vacuum chamber at the UCLA EP Test Facility.*

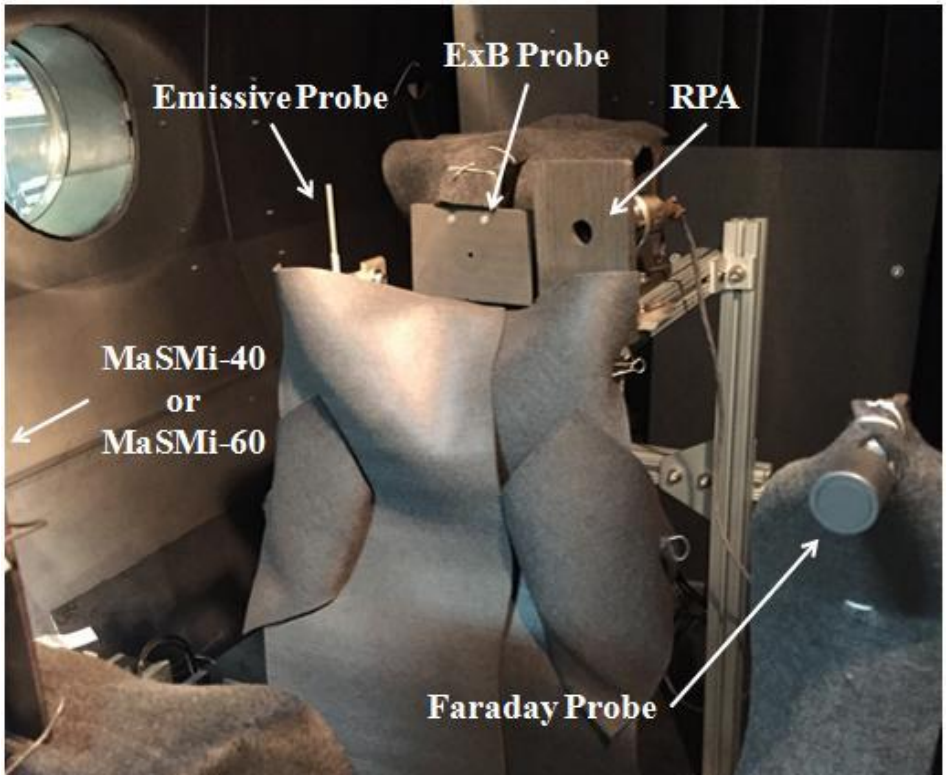

Figure 5.4-11: *Downstream experimental configuration at the JPL High Bay Facility showing complete coverage of all downstream diagnostics structures in carbon materials.*

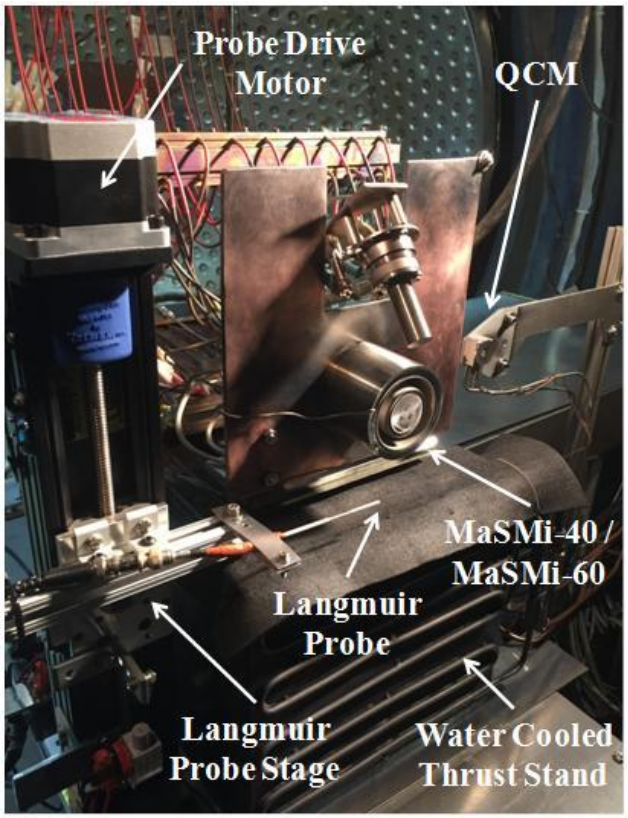

Figure 5.4-12: *Upstream experimental configuration at the JPL High Bay Facility (Langmuir probe, Langmuir probe drives, and QCM were used for the MaSMi-60 only).*

5.5. Concluding Remarks

The facilities and thruster diagnostics used to characterize the performance of the MaSMi Hall thruster were reviewed throughout this Chapter. Details about the dimensions and capabilities of the UCLA Electric Propulsion Test Facility and the JPL High Bay Facility were reviewed. A thorough explanation of the operating principles, geometry, data collection procedure, and uncertainty estimation for each of the nine thruster diagnostics was presented. The methods for assessing the quality of the magnetically shielded field topology generated by the MaSMi Hall thrusters was also discussed. These facilities and diagnostics were used to experimentally measure the performance of the MaSMI-40 and MaSMi-60, the details of which are presented in Chapter 6 and Chapter 7, respectively.

Chapter 6

MaSMi-40 PERFRMANCE TESTING

Chapter 6 reviews the performance testing and analysis of the MaSMi-40. Chapter 6, Part I details the initial performance testing of the MaSMi-40 conducted at the UCLA Plasma and Space Propulsion Laboratory's Electric Propulsion Test Facility. Section 6.1 describes the results from the performance testing of the MaSMi-40, including a discussion of the measurements from each plume diagnostic used and a summary of the thruster's overall performance. Concluding remarks about the UCLA phase of testing are made in Section 6.2. Chapter 6, Part II presents the continued experimental performance testing of the MaSMi-40 conducted at the Jet Propulsion Laboratory's High Bay Facility. Section 6.3 presents the performance results for the MaSMi-40. Section 6.4 reviews the behavior of the MaSMi-40, identifying features that may have led to its poor performance. Concluding remarks regarding the testing the MaSMi-40 at JPL are made in Section 6.5.

CHAPTER 6, PART I: ELECTRIC PROPULSION TEST FACILITY, UCLA

6.1. Experimental Results and Discussion, UCLA EP Test Facility

Initial performance characterization experiments for the MaSMi-40 were conducted at a discharge voltage of 275 V and a discharge power of 325 W. Early operation point optimization began at 300 V and 1.3 A in an effort to achieve the original design point of 390 W; however, testing revealed that the final operation conditions (275 V and 325 W) yielded a more stable discharge and constant temperatures throughout the duration of a given test. It should be noted that the nominal operation point is nearly identical to the predicted discharge power suggested by scaling laws utilized prior to thruster fabrication (Section 4.1.1). The inner and outer magnet coils were operated at 5.2 A and 1.5 A, respectively, to achieve a sufficiently high channel centerline field strength. The total propellant flow rate was approximately 12 sccm of xenon with a cathode flow split of approximately 10%. The cathode keeper was supplied with a current of 2 A during all testing to avoid having to restart the cathode heater if the anode discharge extinguished. The discharge channel length was set to twice the channel width, based on anode placement. The thruster body was grounded during all tests at UCLA. Average operational temperatures of approximately 450°C and 475°C were measured with K-type thermocouples at the base of the discharge channel and at the front pole piece, respectively.

Two minor cracks in the thruster parts occurred during the final stages of testing (after the operation point was optimized to 325 W). The first was an axial crack along the outer wall of the discharge channel; the second was a radial crack on the inner graphite ring of the anode (see Figure 6.1-2). These cracks were found to be due to thermal expansion of the anode; additional margin was built into later versions of the discharge channel. The operation of the MaSMi-40

thruster at nominal conditions was unaffected by these cracks and testing was concluded before the parts were replaced.

6.1.1. Magnetic Shielding Assessment

A photograph of the MaSMi-40 during nominal operation, with a magnified view of the upper discharge channel, is presented in Figure 6.1-1. To the naked eye, the plasma discharge appeared to be slightly offset from the outer channel wall and more concentrated towards the center of the discharge channel. Similar to the visual observations with the H6MS, this was the first evidence suggesting that MaSMi-40 achieved at least partial magnetic shielding [1]. The brightness of the discharge and the small scale of the thruster make it difficult to visually determine if the discharge was similarly offset from the inner channel wall.

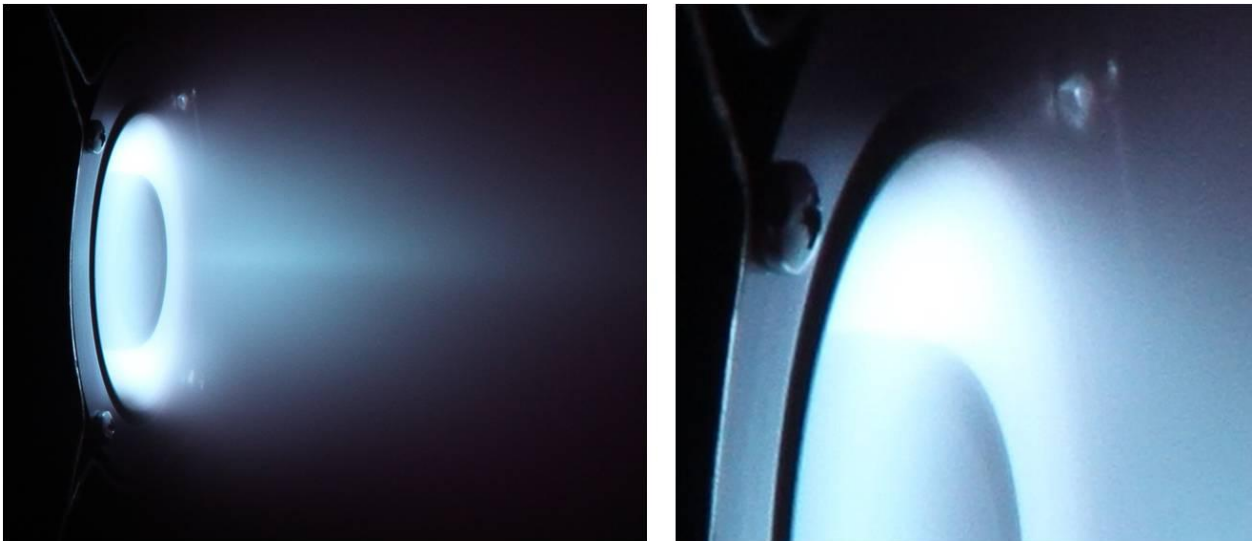

Figure 6.1-1. *Operation of the MaSMi-40 at 275 V and 325 W (left) with a magnified view of the upper region of the discharge channel (right) showing a slight offset of the plasma from the wall typical of magnetic shielding.*

A visual inspection of the MaSMi-40's inner and outer discharge channel walls was conducted after each performance test. Figure 6.1-2 shows a comparison of MaSMi-40's discharge channel before and after approximately 4 hours of experimental testing. An even

coating of carbon was deposited on the outer wall of the discharge channel along its full axial length and the chamfered exit region; no exposed BN was visible anywhere on the outer channel wall. The inner wall of the discharge channel was found to be slightly darker (more gray) in color than it was before testing, but significantly lighter in color than the outer discharge channel wall. Additionally, thin exposed rings of clean BN were found along the edges of the chamfers on the inner wall near the downstream edge. The carbon coating of the outer wall suggested that the backsputter rate of carbon from the high-energy beam dump may have exceeded the ion sputter (erosion) rate of the outer wall material. The inner wall, however, showed little evidence that plasma-wall interactions had been significantly reduced, suggesting the need for further investigation into the magnetic field topology in this region.

Figure 6.1-2. *Comparison of the MaSMi-40's discharge channel before and after approximately 4 hours of operation.*

6.1.2. Planar Probe Results

The measured ion current, corrected for background charge-exchange effects, was 0.78 A. A momentum-weighted beam divergence half-angle of approximately 42° was also observed. The corrected ion current density as a function of the probe's radial position from the thruster centerline at the two measurement locations is shown in Figure 6.1-3. As expected, a strong

peak near centerline is measured by the probe scan nearest to the discharge channel exit while a wider beam profile is measured further downstream of the thruster.

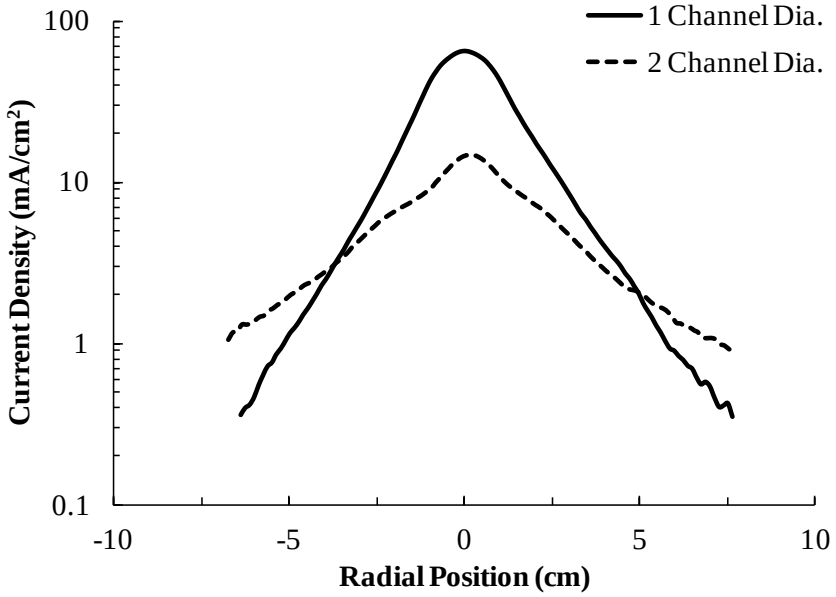

Figure 6.1-3. *Current density as a function of the planar probe's radial position from the thruster centerline, corrected for background charge-exchange effects and measured for nominal MaSMi-40 operating conditions at one and two discharge channel diameters downstream of the thruster face.*

6.1.3. Retarding Potential Analyzer Results

The most probable ion potential measured directly from the RPA was approximately 261 V. The floating potential was measured from the RPA's plasma grid during each thruster test; values were approximately 1 V. Because an emissive probe was unavailable to directly measure the plasma potential at the RPA location, a series of assumptions were made to estimate this value. First, a local electron temperature of 3 eV was assumed at the RPA location; this relatively high value was selected to maintain a conservative estimate of the plasma potential. Second, the plasma potential was approximated by equating the electron current with the fast (beam) and slow (charge-exchange) ion currents local to the RPA, taking the form of

$$\frac{1}{4} n_e e A_{RPA} \sqrt{\frac{8kT_e}{\pi m}} e^{-\frac{e\Phi}{kT_e}} = e A_{RPA} \left(\frac{1}{2} n_{i,slow} \sqrt{\frac{kT_e}{M}} + n_{i,fast} \sqrt{\frac{2e\eta_v V_d}{M}} \right) \qquad 6.1\text{-}1$$

where A_{RPA} is the area of the RPA orifice, $n_{i,slow}$ is the slow ion density, and $n_{i,fast}$ is the fast ion density. The fast ion density near the RPA was approximated based on the plasma density calculated from the planar probe measurements taken at one and two discharge channel diameters downstream of the thruster and then extrapolated for a 42° plume expansion based on the ratio planar probe measurements. The centerline values of the plasma density were used for this calculation as the RPA was located axially downstream of the thruster. This resulted in a plasma density reduction factor of approximately $2\text{x}10^{15}$ m^{-1} divided by the beam area at a given downstream location, yielding a fast ion density of approximately $2\text{x}10^{15}$ m^{-3} near the RPA. The slow ion density was calculated based on equating the rate of charge-exchange ion production in the beam and the rate of ions lost from the beam traveling at the Bohm velocity. The resulting slow ion density was several orders of magnitude smaller than the fast ion density and was neglected, which allowed for the assumption of quasineutrality ($n_e \approx n_{i,fast}$). The voltage utilization efficiency was initially guessed and then iterated on simultaneously with the plasma potential (note that Equation 6.1-1 is a function of both the plasma potential and the voltage utilization efficiency). The result was a calculated plasma potential of 8 V, or roughly $3T_e$, above the local floating potential. Subtracting the calculated plasma potential and measured floating potential from the RPA-measured ion energy results in a most probable ion potential of 252 V. Figure 6.1-5 shows the normalized ion current and its normalized derivative plotted as functions of the ion discriminator grid bias for the nominal operation point of the MaSMi-40.

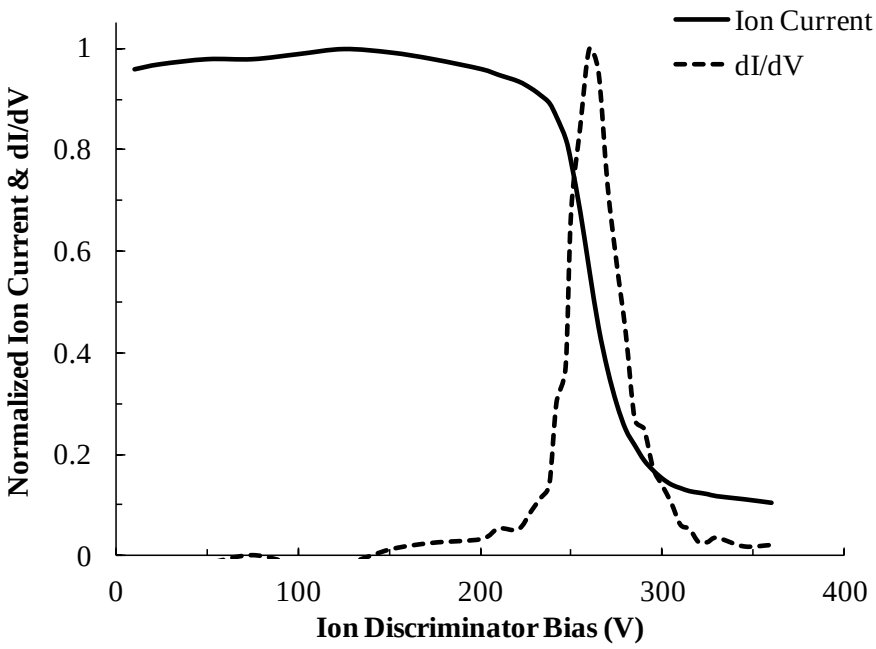

Figure 6.1-4. *Normalized ion current and its derivative as functions of ion discriminator grid potential for MaSMi-40's nominal operating condition.*

6.1.4. Thrust, Efficiency, and Specific Impulse Calculations

To calculate the MaSMi-40's anode efficiency, the beam composition was assumed because **E**x**B** probe measurements were unavailable during early experimental testing. In an effort to maintain conservative results similar to those demonstrated by magnetically shielded Hall thrusters, the MaSMi-40's beam was assumed to be composed of three ion charge states with a species mix equal to that produced by the H6MS (57.5% singles, 25.9% doubles, and 16.6% triples and quadruples) [37]. Using these assumed values along with the plasma diagnostic measurements, the MaSMi-40's voltage utilization, current utilization, mass utilization, divergence, charge utilization, and anode efficiencies were calculated. However, the measurements discussed above were taken during operation of the MaSMi-40 at relatively high background pressures (~7×10^{-5} Torr) and must therefore be corrected for the presence of entrained background neutrals (see Equations 3.1-10 to 3.1-15). An entrained mass flow of

approximately 8.2×10^{-8} kg/s was calculated, yielding an entrained current of approximately 60 mA or 5% of the discharge current. A summary of the calculated performance demonstrated by the MaSMi-40, corrected for the presence of background neutrals, is presented in Table 6.1-1.

Table 6.1-1. *Summary of the MaSMi-40's calculated anode performance, corrected for background neutrals, for operation at the UCLA Electric Propulsion Test Facility.*

η_v	η_b	η_m	η_d	η_q	$\eta_{a,calc}$	T_{calc} (mN)	$I_{sp,calc}$ (s)	Uncertainty
92%	64%	71%	55%	96%	**22%**	**13**	**1,100**	+50% / -20%

6.2. Concluding Remarks, UCLA EP Test Facility

In this part of Chapter 6, the experimental performance results for testing of the MaSMi-40 at the UCLA Electric Propulsion Test Facility was presented. Observations of the plasma and carbon deposition patterns on the discharge channel suggested significantly longer useful life of at least the outer channel wall, which was well shielded; however, the inner wall showed signs of poor magnetic shielding and higher erosion rates. Based on an assumed beam composition, the thrust and anode specific impulse was calculated to be 13 mN and 1,100 s, respectively, at an anode efficiency of 22%. Large uncertainties were associated with these calculated performance values due to corresponding large uncertainties in the diagnostics measurements. The second part of this chapter discusses a more rigorous test campaign of MaSMi-40 at the JPL High Bay Facility.

CHAPTER 6, PART II: HIGH BAY FACILITY, JPL

6.3. Experimental Results and Discussion, JPL High Bay Facility

6.3.1. Operating Conditions

Experiments were conducted at various operating conditions with discharge voltages ranging from 150 V to 300 V at discharge currents of 1 A to 2.3 A, focusing primarily on the nominal condition of 275 V and 1.2 A. The inner and outer magnet coils were operated at approximately 5.2 A and 1.5 A, respectively. At this nominal condition, the total xenon flow rate was 13 sccm with a cathode flow fraction of approximately 8%. Slightly higher anode flow rates were required due to the significantly improved vacuum environment of the High Bay Facility ($<1x10^{-5}$ Torr vs. $\sim7x10^{-5}$ Torr at the UCLA facility during nominal operation), which suggests a significant drop in background neutral ingestion by the thruster. A keeper current of 2 A was applied during most of this investigation's experiments to maintain the high cathode temperature; removal of the keeper current yielded slightly higher discharge currents but no notable change to the thruster's performance parameters. The thruster was allowed to float from ground during operation; a cathode coupling voltage of approximately -9 V was observed for all tests. During testing, two distinct operating modes were observed that were directly related to the thruster's operating temperature. The shift from a low-temperature "jet" mode to a high-temperature "diffuse" mode occurred consistently at a thruster temperature of approximately 380°C, measured using K-type thermocouples. Once the thruster entered the diffuse mode, it was impossible to revert to the jet mode without a full shut-down and cool-down of the device. The "X-Wing" radiator was used for a portion of the testing to maintain lower operating temperatures. With the radiator, MaSMi-40's stable operating temperature was approximately 300°C; without the radiator, temperatures increased to over 400°C with the temperature rising at

a constant rate until thruster shut-down. The water-cooled thrust stand temperature remained stable at approximately 22°C throughout all testing. A total operation time of approximately 26 h was logged during this series of experiments.

It should be noted that the MaSMi-40 was operated with both an elongated (~2 discharge channel widths) and shortened (~1 discharge channel width) discharge channel during this investigation. This modification was made in an effort to reduce the unfavorable oscillations observed during operation in the low-temperature jet mode by reducing the transit distance of neutral particles from the anode to the ionization region. However, the performance of the thruster (thrust, efficiency, oscillations, etc.) in these two discharge channel configurations was within the error of the measurements.

6.3.2. Magnetic Shielding Assessment

The effectiveness of the magnetically shielded field topology was assessed based on visual observations of the near-exit plasma discharge during thruster operation and an inspection of the discharge channel after operation. During operation in both the jet and diffuse modes, a high-density plasma region in the shape of a torus formed just downstream of the discharge channel exit. This plasma was clearly offset from the outer discharge channel wall, which suggests strong magnetic shielding in this region. It is worth noting that the gap between the plasma torus and outer channel wall appeared to be greater in the diffuse mode than in the jet mode. However, the plasma appeared to be ostensibly close to, if not contacting, the inner wall in both operating modes; this can be seen from Figure 6.3-2. Inspection of the MaSMi-40's discharge channel after operation in either mode showed a layer of carbon deposited along the full length of the outer wall. After operation in the jet mode, a coating of carbon was found on the majority of the inner channel wall with the exception of the downstream chamfered edges,

which were noticeably whiter. By contrast, the inner wall had virtually no signs of carbon deposition after operation in the diffuse mode, suggesting a significant increase in plasma-wall interactions. These findings matched the evidence for the MaSMi-40's partial magnetic shielding observed at the UCLA EP Test Facility. A photograph comparing the discharge channel after operation in the two modes is shown in Figure 6.3-1.

Figure 6.3-1. *Comparison of the MaSMi-40's discharge channel after operation in the jet mode (left) and the diffuse mode (right), showing a significant reduction in carbon deposition along the inner wall.*

6.3.3. Performance Measurements: Thrust Stand

Operation in the jet mode at the nominal operating condition yielded a thrust of approximately 13 mN, corresponding to a specific impulse of approximately 1,100 s. These values matched well with those recorded at the UCLA Electric Propulsion Test Facility. A maximum thrust of over 20 mN was observed at a discharge current of 2.3 A. The low-temperature jet mode was visually characterized by the presence of a plasma spike extending

approximately 10 – 15 cm along the thruster centerline and a region of high luminosity just downstream of the thruster exit.

A thrust stand measurement of approximately 12 mN was recorded at the nominal operating condition in the diffuse mode, corresponding to a specific impulse of approximately 1,000 s. The high-temperature diffuse operating mode showed no plasma spike extending along the thruster centerline and significantly less luminosity of the plasma downstream of the thruster exit, instead having a more diffuse appearance. Additionally, the anode was considerably brighter (increased visual radiation intensity) after thruster shutdown when compared to the jet mode, suggesting elevated anode temperatures.

A comparison of the near-exit thruster plumes for operation of the MaSMi-40 in the jet and diffuse modes is shown in Figure 6.3-2.

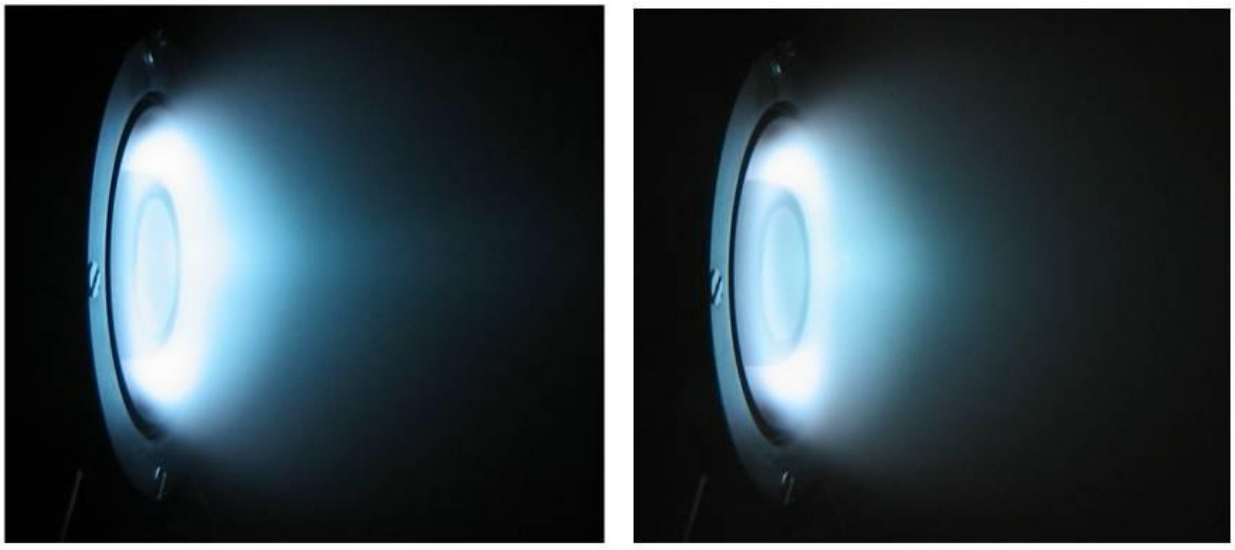

Figure 6.3-2. *The MaSMi-40's near-exit plasma discharge while operating at 275 V and 1.2 A in the low-temperature jet mode (left) and the high-temperature diffuse mode (right).*

6.3.4. Performance Measurements: Plasma Diagnostics

6.3.4.1. Faraday Probe Results

The scanning Faraday probe measured an ion current of approximately 0.82 A, corrected for background charge-exchange collisions, for MaSMi-40 operation in jet mode. The corrected ion current for operation in the diffuse mode was nearly the same at approximately 0.80 A. A beam divergence half-angle of approximately 43° was observed in jet mode while operation in the diffuse mode yielded a divergence half-angle of approximately 48°. Operation in the diffuse mode yielded a 10% increase in divergence half-angle and a 10% reduction in centerline peak ion current. The notable increase in beam divergence is not apparent in the ion current density profiles; however, this result suggests that significantly more ions are being accelerated at high angles relative to the thruster axis, ultimately yielding lower thruster performance (this is further emphasized by the fact that the calculated half-angle is based on the momentum-weighted ion current). Figure 6.3-3 shows a comparison of the ion current density profiles measured for the two operation modes.

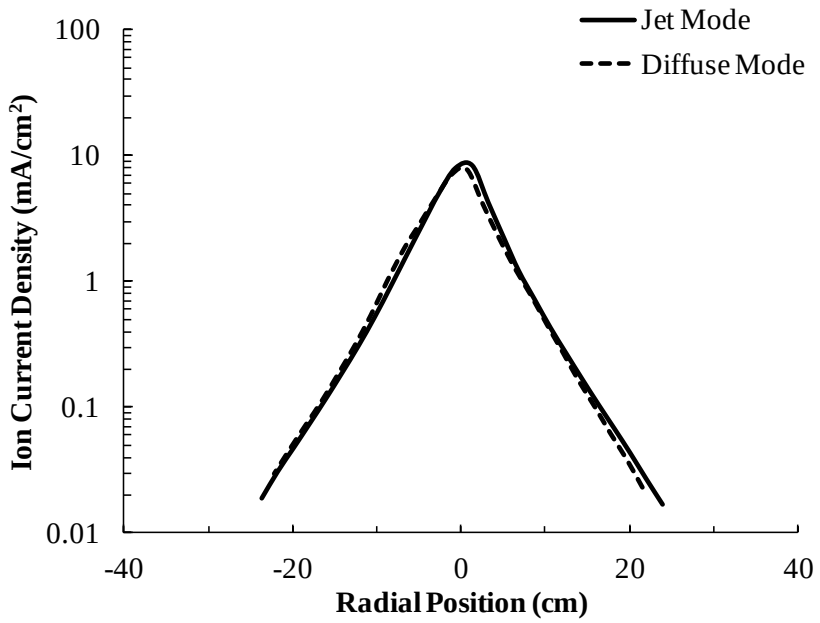

Figure 6.3-3. *Corrected ion current density as a function of lateral position from thruster centerline for the MaSMi-40 operating at nominal conditions in the jet and diffuse operating modes.*

6.3.4.2. Retarding Potential Analyzer Results

For this series of experiments, the JPL-designed 5-grid RPA was used to determine the most probable ion potential. A value of approximately 250 V was reported by the RPA for jet mode operation while approximately 261 V was reported in the diffuse mode; both of these measurements were corrected for the plasma potential local to the RPA during post-processing, which was approximated at 8 V based on the analysis performed in Section 6.1.3. The increase in most probable ion potential during operation in the diffuse mode is likely a result of the increase in divergence half-angle; lower energy ions would be more susceptible to off-axis accelerating potentials (creating the increased beam spread) while higher energy ions would be less affected by these radial fields. Therefore, the ions collected by the RPA positioned along the thruster centerline would tend to be of higher energy in the diffuse mode compared to the jet mode. Plots of the normalized collected current and its derivative with respect to the ion

discriminator bias is presented in Figure 6.3-4 for the two operating modes. The ion saturation portion of the trace is approximated due to poor resolution in the collected current signal (represented by the horizontal dashed line).

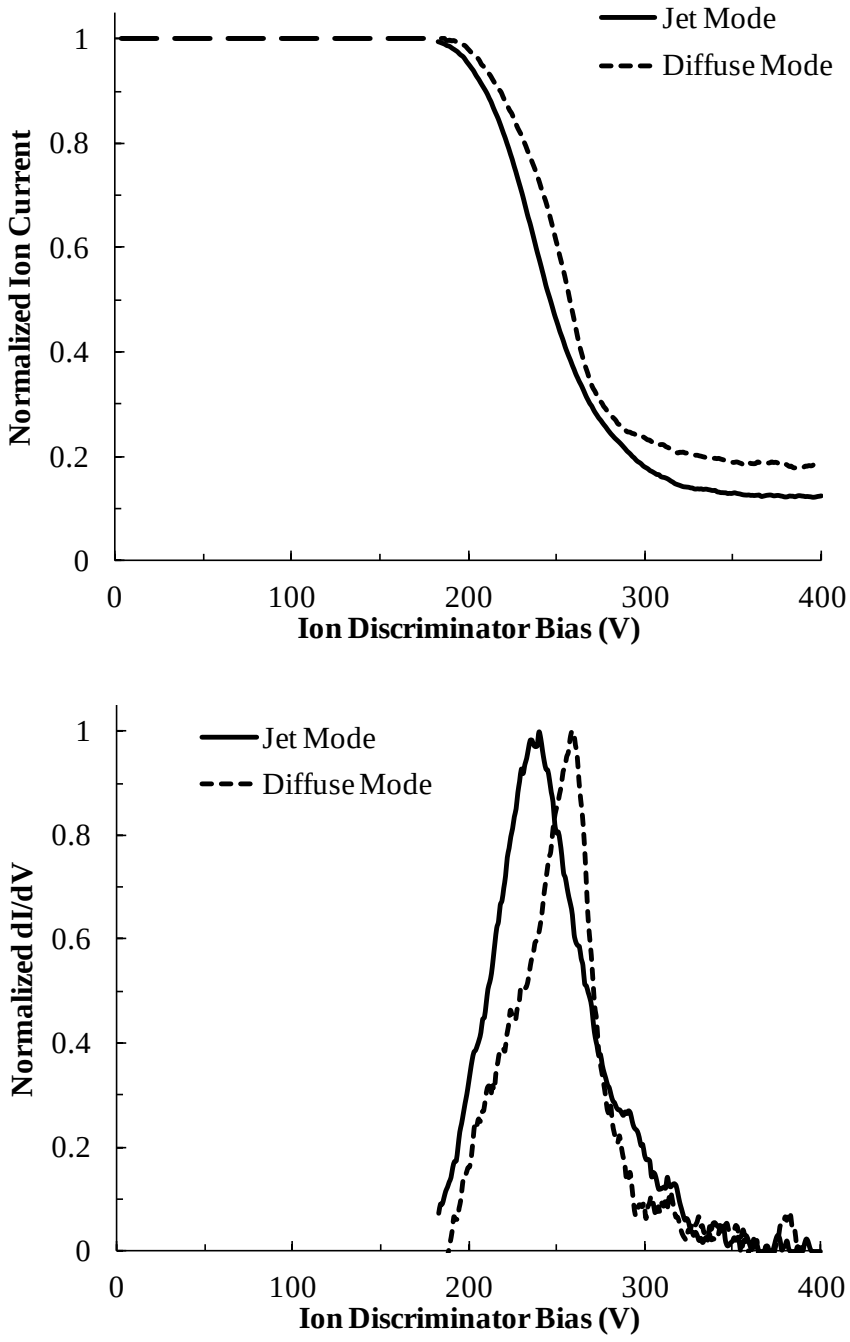

Figure 6.3-4. *Normalized ion current (top) and its derivative (bottom) as functions of ion discriminator bias potential for nominal operation of the MaSMi-40 in the jet and diffuse modes.*

6.3.4.3. ExB Probe Results

During operation in jet mode, the MaSMi-40's plasma discharge was composed of approximately 64.8% singly, 24.4% doubly, and 10.8% triply charged ions. Operation in this mode yielded an ion species mix with relatively high concentrations of doubly and triply charged ions relative to the singly charged ion population. These findings are consistent with published data on the H6MS, suggesting that the MaSMi-40 had achieved a partially-shielded field configuration [37]. In the diffuse mode, the discharge was comprised of approximately 73.6% singly, 19.0% doubly, and 7.4% triply charged ions, showing a 9% increase in singly charged ion current. Unlike jet mode operation, these data are more consistent with unshielded miniature Hall thruster beam compositions, where the singly charged ion current is a significantly larger portion of the total beam current compared to magnetically shielded thrusters [37,88]. Figures 6.3-5 and 6.3-6 presents the normalized ion velocity spectra for the MaSMi-40 at nominal conditions in both operating modes.

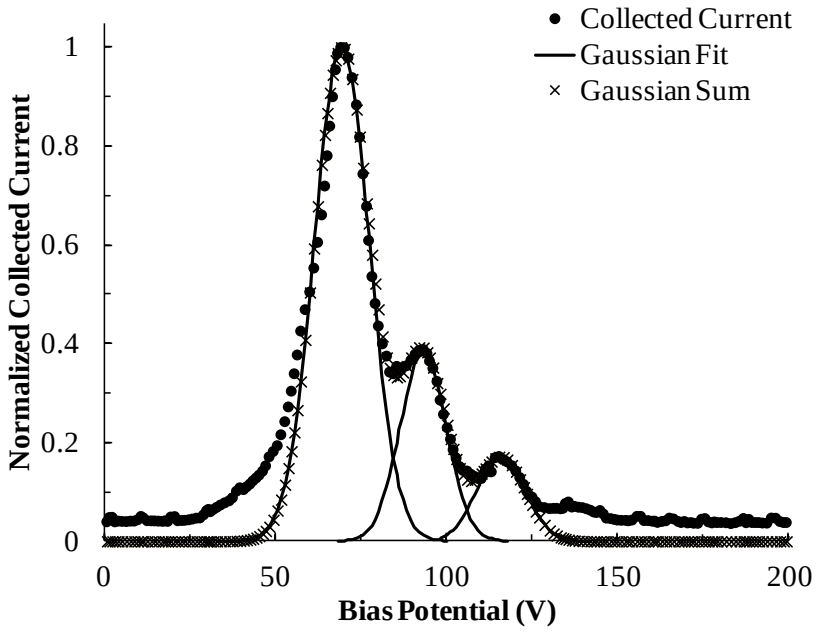

Figure 6.3-5. *Normalized ion velocity spectra showing the MaSMi-40's beam composition during operation at nominal conditions in the jet mode.*

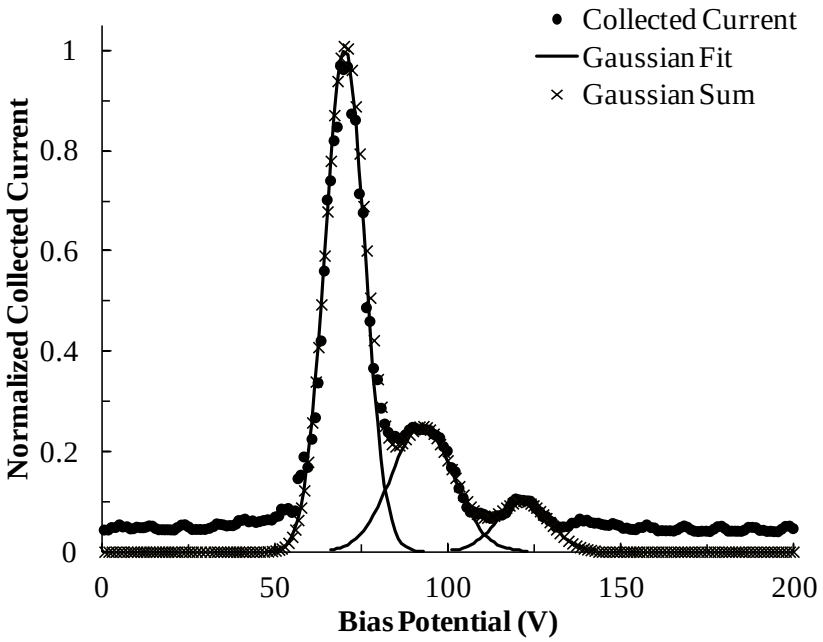

Figure 6.3-6. *Normalized ion velocity spectra showing the MaSMi-40's beam composition during operation at nominal conditions in the diffuse mode.*

6.3.4.4. Calculated Performance Summary

A summary of the voltage utilization, current utilization, mass utilization, divergence, charge utilization, and anode efficiencies measured by the beam diagnostics compared to the anode efficiency measured by the thrust stand is presented in Table 6.3-1. The approximate uncertainties associated with these efficiency calculations are also included. All performance values fell within the uncertainty of the plasma beam measurements, resulting in good matching between the calculated and measured anode efficiency. Additionally, the measured and calculated values matched well with the performance data calculated during testing of the MaSMi-40 at the UCLA Electric Propulsion Test Facility.

Table 6.3-1. *Summary of the MaSMi-40's efficiencies measured and calculated at the JPL High Bay Facility.*

Mode	$\eta_{a,meas}$	η_v	η_b	η_m	η_d	η_q	$\eta_{a,calc}$	Uncertainty ($\eta_{a,calc}$)
Jet	**22%**	88%	68%	76%	54%	97%	**24%**	+15% / -10%
Diffuse	**19%**	92%	67%	79%	45%	97%	**21%**	+14% / -9%

6.3.5. Discharge Current Oscillations

A comparison of the MaSMi-40's performance metrics while operating in the two observed modes revealed that the thruster's overall thrust and efficiency is largely unchanged, slightly favoring the jet mode. In an effort to better characterize the different plasma behaviors in each operating mode, discharge current oscillations were recorded using a commercial current probe (measurement uncertainty <4%) read into a Tektronix oscilloscope. Figure 6.3-7 presents a comparison of the oscillations recorded for the jet and diffuse operating modes. The jet mode exhibited highly oscillatory behavior consistent with a deep breathing mode. For the nominal 1.2 A discharge with a 2 A applied keeper current, fluctuations in the current had a peak-to-peak value of approximately 3-4 A (2.5-3.5 times the mean current) with a frequency of 19-22 kHz. The trough of each cycle reached less than 10% of the mean current, suggesting that the thruster effectively enters a temporary "off" state; operation at under 33% of the mean discharge current persisted for more than 30% of the total oscillation cycle. When the keeper current was removed, the current oscillations increased (approximately 3-4 times the mean current), demonstrating that an applied keeper current had a minor stabilizing effect on the discharge. By contrast, the diffuse mode exhibited minor, randomized discharge current oscillations which remained within approximately 20% of the mean. As with the jet mode, the oscillations in the

diffuse mode increased slightly (to approximately 25-30 % of the mean current) when the keeper current was removed.

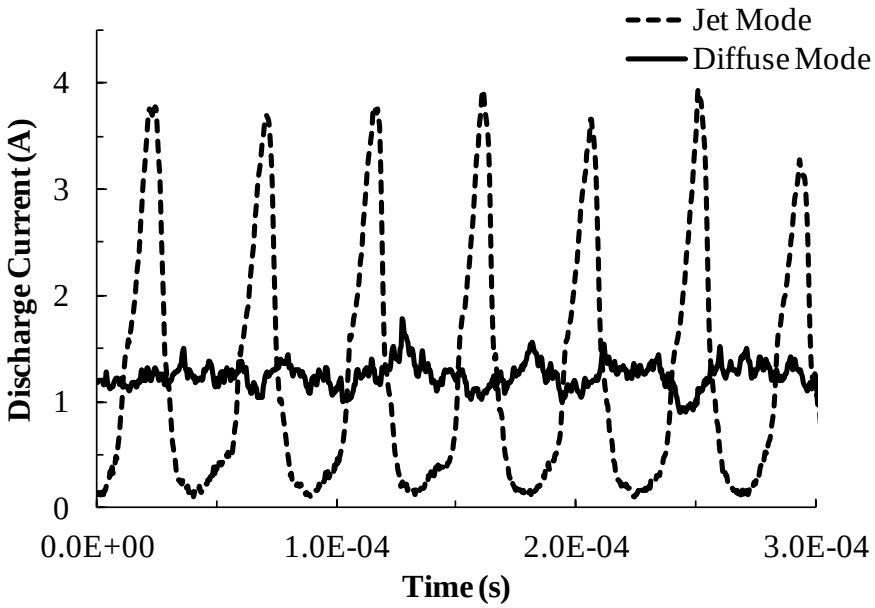

Figure 6.3-7. *Comparison of the discharge current oscillations measured during operation of the MaSMi-40 in the low-temperature jet mode and the high-temperature diffuse mode.*

6.4. MaSMi-40 Performance Overview

The onset of the diffuse mode in the MaSMi-40 was observed to be directly related to the thruster's operating temperature. A similar trend was observed by Azziz when testing a BHT-1500 Hall thruster [100]. Before the BHT-1500 reached thermal equilibrium, only a "jet" mode was observed where the thruster's behavior was insensitive to changes in the applied magnetic field strength. This mode was visually characterized by a large plasma spike along the thruster axis; deep breathing mode oscillations of approximately 100% of the mean discharge current at a frequency of 20 - 30 kHz were also observed. After thermal equilibrium was reached, however, the thruster could be operated in a "collimated" mode by reducing the magnetic field strength across the channel, yielding a cylindrical discharge that converged to a jet approximately 20 cm downstream of the thruster exit [100]. A reduction in thrust performance by approximately 5%

and minimal discharge current oscillations of approximately 35% of the mean were reported. Analysis of the thruster's performance in these two modes suggested that reductions in the permeability of the thruster's magnetic circuit at the (high) equilibrium operating temperatures yielded changes in the magnetic field strength and topology, possibly forcing the ionization region upstream of its nominal position. This, in turn, appeared to cause increased interactions between the plasma and the discharge channel walls, leading to a collimating of the beam; ions born and accelerated at angles sufficiency far from the thruster axis would impact the channel surfaces rather than travel downstream of the thruster to produce thrust. This conclusion was further supported by discharge channel temperature measurements, where higher temperatures were reported in the collimated mode, suggesting increased plasma-wall interactions and plasma heating.

Experiments with the BHT-1500 suggest that the strength and shape of a Hall thruster's applied magnetic field, which is affected (and sometimes limited) by the temperature of the thruster's magnetic circuit, has a the ability to change the operating mode of a Hall thruster. Similar to the BHT-1500, the MaSMi-40 entered a new operating mode once a sufficient operating temperature was reached. The MaSMi-40 could not be reverted to the jet mode by changing the applied magnetic coil currents during operation; a complete shut-down of the thruster followed by a 2- 3 h cool-down period was necessary to reestablish jet mode operation. Assuming the cause of MaSMi-40's diffuse operating mode is similar to the BHT-1500's collimated mode (i.e. an upstream shift of the ionization region due to changes in magnetic field structure and strength), the most likely region for significant changes to MaSMi-40's magnetic field structure would be along the inner wall where poor shielding of the channel was observed. By contrast, the outer channel wall appeared to be well shielded during all testing with a possible

improvement in shielding in the diffuse operating mode. Therefore, an upstream shift in the ionization region would likely be asymmetric across the MaSMi-40's channel, penetrating more deeply along the inner channel wall. This would lead to a skewing of the field's lensing effect, offering an explanation for the observed increase in angular divergence of the beam, the greater plasma-wall interactions along the inner channel surfaces (specifically ion bombardment erosion), and the shift of the ion species mix towards singly charged particles (a significant population of the high-energy electrons responsible for multiply charged ions would be lost to the wall).

An important aspect of the BHT-1500's behavior was the significant reduction in discharge current oscillations observed between the nominal jet mode and the collimated mode, which was characterized by increased plasma-wall interactions. Experiments with the BHT-1500, along with studies using other thrusters, have shown that plasma-wall interactions and sheath effects impart a damping effect on discharge current oscillations [100,101]. This behavior was also observed with the MaSMi-40 where discharge current oscillations dropped from up to 400% of the mean current in jet mode to less than 30% of the mean current in the diffuse mode. The significant increase in plasma-wall and plasma-sheath interactions suggested by these results further supports the theory that MaSMi-40's magnetic field was becoming more asymmetric and biased towards the inner wall after the thruster's temperature reached a critical value.

6.4.1. MaSMi-40 Magnetic Field Topology: Investigation and Correction

Based on the evidence of temperature-dependent changes in the MaSMi-40's magnetic field topology, a thorough investigation of the thruster's magnetic circuit was conducted. Due to the sensitive nature of the investigation's findings, complete details can be found in literature (export-controlled) [79].

6.5. Concluding Remarks, JPL High Bay Facility

The experimental testing of the MaSMi-40 at the JPL High Bay Facility was presented in this part of Chapter 6. The thruster was found to operate in two distinct modes depending on the thruster's temperature. Performance was similar between the two operating modes; a thrust of between 12 – 13 mN, corresponding to a specific impulse of approximately 1,000 - 1,100 s and an anode efficiency of between 19 – 22% was measured. Results from the beam diagnostics showed good matching with these measurements while offering evidence as to the cause of the MaSMi-40's temperature-dependant mode shift and poor performance. While not disclosed here, the findings from an investigation of the MaSMi-40's magnetic circuit were published in an export-controlled paper [79]. The second iteration of the MaSMi Hall thruster, the MaSMi-60, was developed to overcome the design shortfalls of the MaSMi-40. A basic overview of the geometry and features of the MaSMi-60, along with the details of a thorough experimental test campaign, is presented in Chapter 7.

Chapter 7

MASMI-60 DEVELOPMENT AND PERFRMANCE TESTING

This chapter covers the development efforts and experimentally measured performance of the MaSMi-60. Section 7.1 presents an overview of the thruster's geometry and key features. The thorough experimental testing of the MaSMi-60 is discussed in Section 7.2. Concluding remarks follow in Section 7.3.

7.1. MaSMi-60 Thruster Design

The following offers a brief overview of the design and geometry of the MaSMi-60. During the course of this investigation, changes to ITAR (International Trade and Arms Regulations) led to the classification of the MaSMi-60 as ITAR restricted. Further details on the MaSMi-60 can therefore be found in the literature [79].

7.1.1. Geometry

The design for the MaSMi-60's magnetic circuit was completed using the process and key geometry considerations discussed in [74,79]. The MaSMi-60's low-power capabilities were maintained by keeping the discharge channel exit area as small as possible while allowing a sufficient channel width to achieve the desirable magnetic field topology across the channel. The MaSMi-60's discharge channel has a b/d_m ratio of 0.157, which is notably lower than the established b/d_m trends for low-power Hall thrusters [74]. However, this value is very similar to the b/d_m ratios used in moderate- to high-power Hall thrusters, especially those aiming to achieve high specific impulse [27]. A variable-placement anode, using a similar design to the MaSMi-40, allows for a range of discharge channel lengths up to twice the channel width.

7.1.2. Magnetic Field

Near perfect agreement (published in ITAR controlled reference [79]) was observed between the field topologies predicted by the validated magnetic fields software and the measured field; the predicted and measured peak radial field strength along the channel centerline ($B_{r.max}$) matched to within 1%. A symmetric topology was measured to remain constant over a large range of $B_{r.max}$. Further details on the MaSMi-60's magnetic field strength and topology can be found in [79].

7.1.3. Thermal Modeling

The overheating observed during operation of the MaSMi-40 suggested that a significantly improved thermal design was necessary for the MaSMi-60, leading to the development of a more sophisticated thermal model. Details on this model can be found in [79]. In sum, the thruster's internal components were discretized into separate zones between which heat was allowed to freely transfer either radiatively or conductively, depending on the location and geometry of the component inside the thruster. The equation used to model all radiative heat transfer (radiation between components and radiative heat loss) is given by

$$\dot{Q}_{rad} = \sigma \varepsilon A_s (T_1^4 - T_2^4) \tag{7.1-1}$$

where $\dot{Q}_{rad}$ is the radiative heat transfer, σ is the Stefan-Boltzmann constant, ε is the zone's emissivity, A_s is the zone's surface area, and T_1 is the temperature of the zone rejecting heat, and T_2 is the temperature of the zone receiving heat; the view factor between the two zones is assumed to be 1. The conduction of heat between components of the thruster was modeled as

$$\dot{Q}_{cond} = \frac{\kappa A_x (T_1 - T_2)}{d} \tag{7.1-2}$$

where κ is the thermal conductivity of the material through which heat is flowing, A_x is the zone's cross-sectional area perpendicular to the direction of heat flow, and d is the distance,

parallel to the direction of heat flow, over which the temperature gradient is occurring. Power generated by the thruster (discharge plasma and magnet coils) was assumed to be an internal heat source emanating from the nearest affected zone. The result of these simplifications yielded a system of equations, one for each discrete thruster zone, with one unknown temperature for each.

The improved thermal model was validated against temperature measurements taken for the MaSMi-40 and then applied to the MaSMi-60. At an assumed discharge power of 450 W, approximately 170 W of plasma heating of the discharge channel was predicted by the power deposition model presented in [74]. Using this value, along with conservative estimates of 55 W and 22 W for the inner and outer magnet coils (based on the MaSMi-40 coil conditions), respectively, a body temperature of approximately 450°C was predicted for the MaSMi-60. This result, which represents a worst case scenario as it assumes no radiator, high magnet powers, and poor surface emissivity, suggests a significant improvement in thermal design over the MaSMi-40.

In an effort to further ensure that no thermal problems would inhibit the performance of the MaSMi-60, the thruster was mounted to a radiator consisting of a square copper plate with notch removed to allow clearance for the cathode. The overall profile of the radiator was selected to simulate the thruster mounting region of a spacecraft, with the maximum dimensions only as big as necessary to accommodate the hollow cathode used in these experiments. The copper radiator was heat treated with an asetylene torch to achieve a dark surface color, yielding an increased emissivity. While the radiator was used to mount the thruster to the thrust stand, multiple layers of Mica were used between each metal-metal interface to effectively thermally isolate the thruster from the water-cooled thrust stand. An image of the thruster mounted to the radiator and interfaced to the thrust stand is presented in Figure 7.1-1.

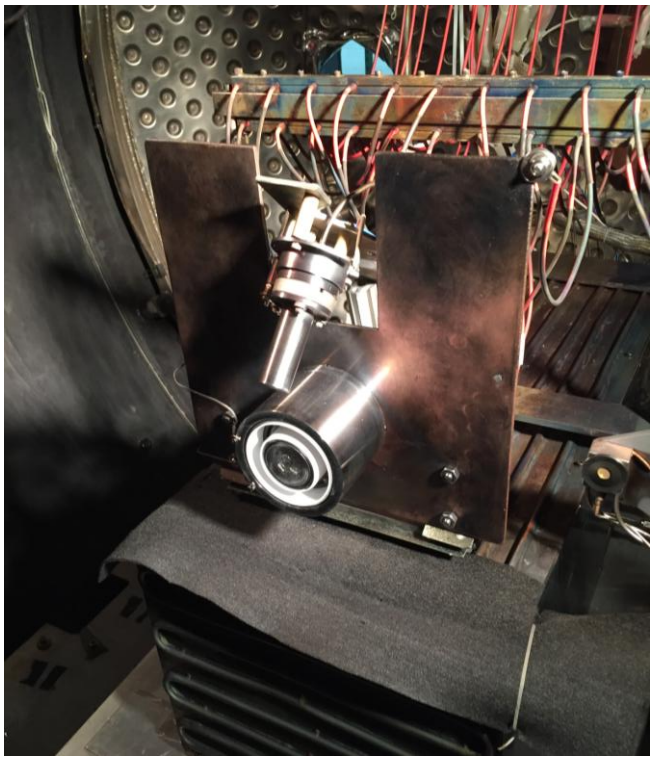

Figure 7.1-1. *The MaSMi-60 mounted to the thermal radiator on the JPL High Bay Facility thrust stand.*

7.2. Experimental Results and Discussion

7.2.1. Operating Conditions

A summary of the operating conditions used for thrust stand measurements is presented in Table 7.2-1. The test matrix shows the nominal power achieved as a function of discharge voltage and anode propellant flow rate. Testing of the MaSMi-60 was conducted at a range of discharge voltages from 200 V to 400 V in increments of 50 V. At each of the five discharge voltages, the propellant flow rate was varied from 12 sccm to 28 sccm in increments of 2 sccm; the flow rate was increased until 28 sccm was achieved with stable thruster operation or until the thruster demonstrated unfavorable behaviors, such as localized wall heating (these conditions are marked with an "X" in Table 7.2-1). This matrix of voltages and flow rates at the nominal

operating point for each condition yielded a range of discharge powers from 160 W to nearly 750 W. A total operation time in excess of 83 hours was logged during this testing campaign.

Table 7.2-1. *Operating conditions for the MaSMi-60 during thrust stand measurements, summarizing nominal power achieved as a function of discharge voltage and anode flow rate.*

		Discharge Voltage (V)				
		200	**250**	**300**	**350**	**400**
Anode Flow Rate (sccm)	**12**	160 W	205 W	243 W	291 W	344 W
	14	200 W	255 W	309 W	368 W	420 W
	16	242 W	308 W	378 W	487 W	596 W
	18	290 W	363 W	453 W	560 W	X
	20	346 W	448 W	549 W	X	X
	22	436 W	548 W	720 W	X	X
	24	502 W	643 W	X	X	X
	26	564 W	745 W	X	X	X
	28	628 W	X	X	X	X

The cathode flow rate was held to approximately 7-9% of the anode flow rate, but was never supplied with less than 1 sccm to maintain stable cathode operation. The thruster was operated both with and without an applied keeper current of 2 A, resulting in no observed sensitivities of the thruster operation to the application of keeper current. The cathode-ground potential remained between -8 V and -20 V, depending on the specific operating condition. During all tests, the thruster was allowed to float from chamber ground and the discharge channel length (based on anode placement) was set to twice the discharge channel width. Temperatures recorded by K-type thermocouples at the front outer pole and near the center core at the back pole remained below 250°C and 220°C, respectively, for all tests; the temperature gradient along the radius of the back pole remained below 30°C.

The inner and outer magnet coils were operated at up to 4.2 A and 2.2 A, respectively, with a varying coil current ratio to achieve a symmetric and shielded field topology across a wide range of magnetic field strengths. This corresponded to a total magnet power between 60 W and 75 W; these high values were due to temperature-related increases in the magnet coil's resistance. Localized wall heating, azimuthally asymmetric discharge plasma shapes near the channel exit, and other unfavorable thruster behaviors were observed at high discharge powers despite the relatively high applied field strength; these data are not presented in Table 7.2-1. Additionally, the MaSMi-60 exhibited inconsistent discharge current oscillations, measured with a commercial current probe (uncertainty <4%) read into a Tektronix oscilloscope, depending on how a specific operating condition was approached (i.e. ramping the coil currents up vs. down, beginning from a lower vs. higher discharge voltage or current, etc.). The oscillations ranged from very quiet modes (peak-to-peak currents less than 30% of the mean discharge current) to highly oscillatory modes (peak-to-peak currents greater than 200% of the mean discharge current). While the measured performance of the thruster was observed to be unaffected by the character of these oscillations, they may affect other aspects of the device such as the observed pole erosion. These unfavorable behaviors, the thruster's inability to achieve true nominal operation at the majority of its available operating conditions, and the thruster's inconsistent discharge current oscillation behavior appeared to be directly related to the strength and topology magnetic field. While further investigation into these issues is beyond the scope of this work, it represents an important future effort for the improved understanding of their effects on thruster performance and life-limitations.

7.2.1.1. Defining Nominal Operation

Based on the behaviors observed during operation of the MaSMi-60, specifying the applied definition of "nominal operation point" is necessary. The nominal operating point is generally defined as the minimum discharge current as a function of inner coil current (i.e. $B_{r,max}$) for a given discharge voltage and propellant flow rate. A true discharge current minimum was realized for only two operating conditions over the MaSMi-60's range of coil currents (200 V and 12 or 14 sccm); these cases are shown in Figure 7.2-1. Therefore, the nominal operation point for the MaSMi-60 was not necessarily the absolute minimum discharge current as a function of inner coil current but rather the minimum current with the attainable magnetic field settings. All results, with the exception of the select conditions that achieved a true discharge current minimum, are presented for operation at the maximum $B_{r,max}$ possible before significant saturation of the magnetic circuit (a maximum inner coil current of 4.2 A). Plots of discharge current against inner coil current for the nine operating conditions presented in Table 7.2-1 are shown in Figure 7.2-2

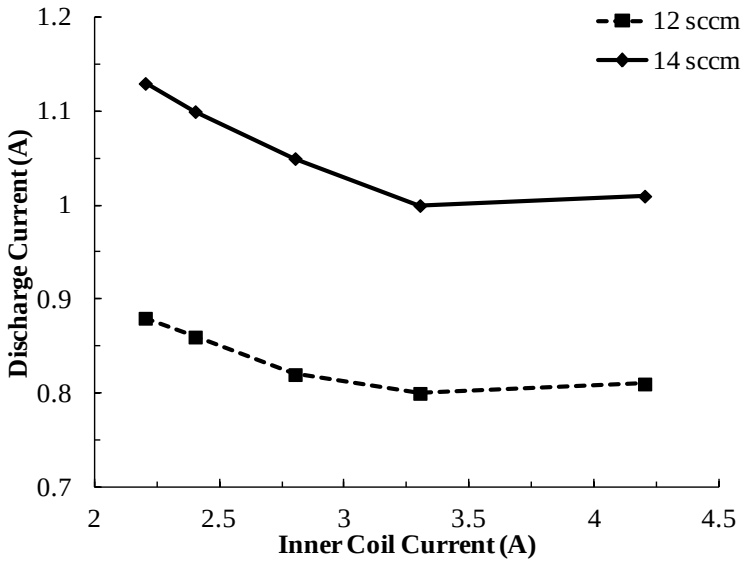

Figure 7.2-1. *Discharge current as a function of inner coil current for operation of the MaSMi-60 at a discharge voltage of 200 V and anode flow rates of 12 and 14 sccm.*

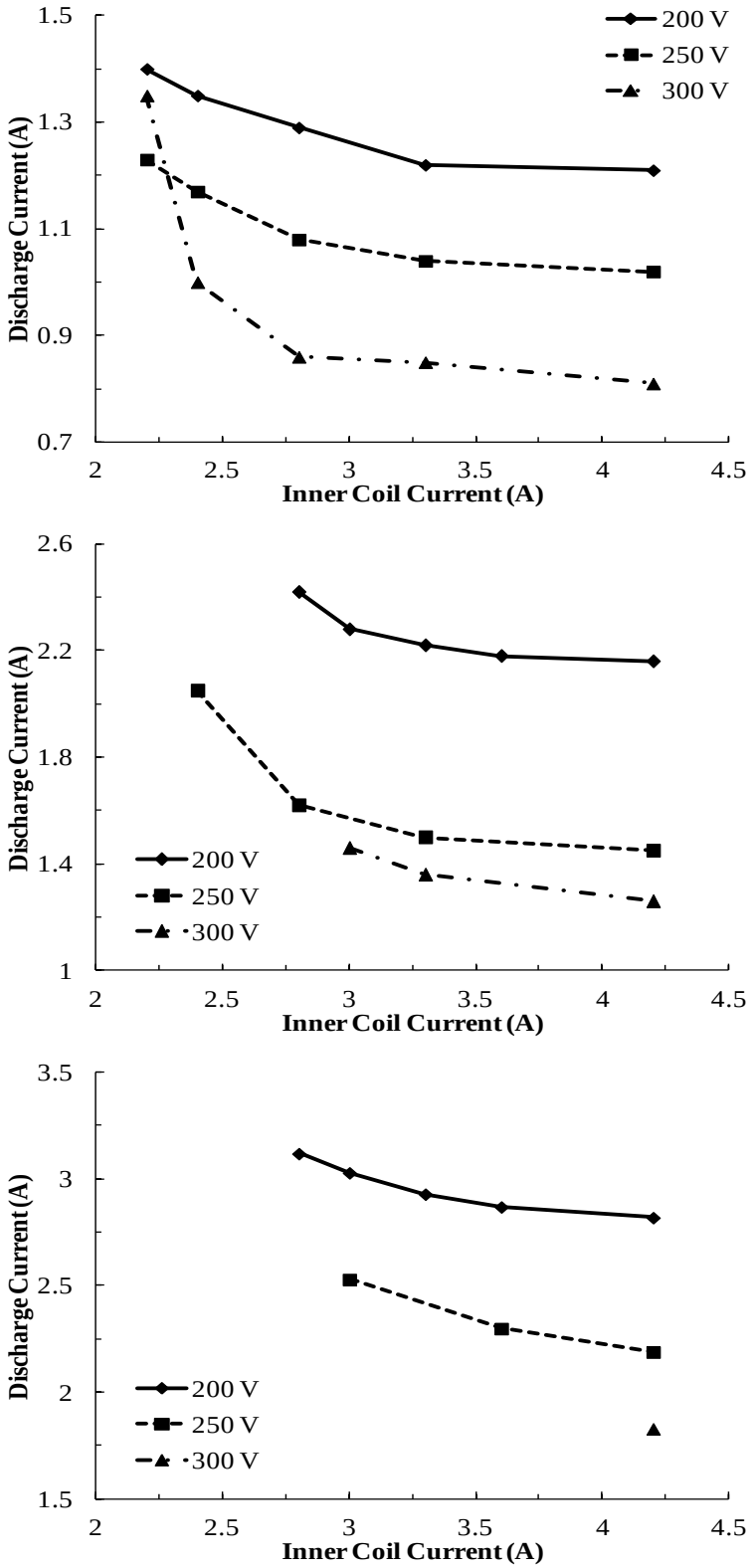

Figure 7.2-2. *Discharge current as a function of inner coil current for operation of the MaSMi-60 at discharge powers of 250 W (top), 400 W (middle), and 550 W (bottom).*

7.2.2. Magnetic Shielding Assessment

Three methods were used to assess the effectiveness of magnetic shielding in the MaSMi-60: (1) visual observations of the plasma discharge contact with the walls, (2) examination of the discharge channel discoloration before and after operation, and (3) erosion calculations based on carbon backsputter measurements.

For the visual observations of the plasma, camera settings were optimized to clearly show the highest plasma densities in the discharge channel. Images of the plasma discharge of the MaSMi-60, such as the one presented in Figure 7.2-3, show that large gaps between the plasma and the discharge channel walls were present, suggesting that both the inner and outer channel walls were successfully shielded [1].

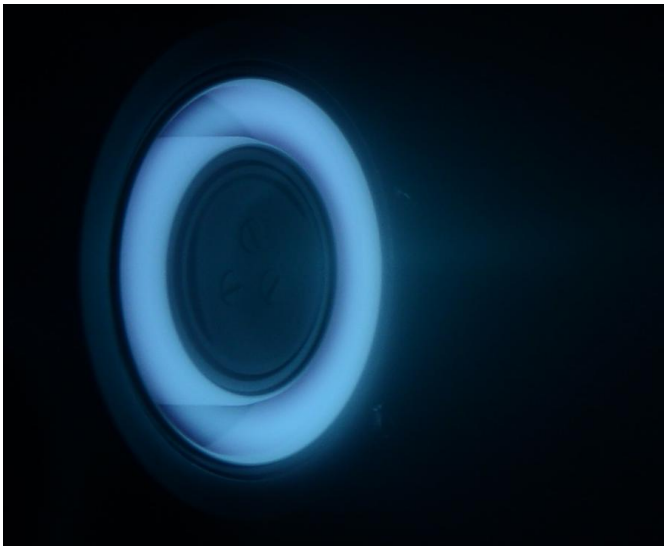

Figure 7.2-3. *Operation of the MaSMi-60 at 250 V and 335 W showing evidence of successful magnetic shielding through a clear offset of the plasma from the inner and outer discharge channel walls.*

Figure 7.2-4 shows an image of the discharge channel before and after thruster operation. The clean white BN channel documented before operation was uniformly coated after operation by a layer of black carbon deposit, back-sputtered from the graphite panels along the walls of the

vacuum chamber. Like the H6MS, these observations are visual evidence of a fully shielded magnetic field topology [1,37].

Figure 7.2-4. *Comparison of the MaSMi-60's discharge channel and pole faces before and after ~20 hours of operation. Note the level of front inner and outer pole face erosion.*

According to the literature, the erosion rate of BN under xenon ion incidence ($\varepsilon_{Xe\text{-}BN}$) can be bounded by

$$\varepsilon_{Xe-BN} \leq \alpha R_C \left(\frac{\rho_C m_{BN}}{\rho_{BN} m_C}\right)\left(\frac{Y_{Xe-BN}}{Y_{Xe-C/BN}}\right) \approx 2Rc\left(\frac{Y_{Xe-BN}}{Y_{Xe-C/BN}}\right) \qquad 7.2\text{-}1$$

where α is the sticking coefficient (assumed to be unity), R_C is the carbon backsputter rate, ρ_C is the mass density of carbon, m_{BN} is the particle mass of BN, ρ_{BN} is the mass density of BN, m_C is the particle mass of carbon, $Y_{Xe\text{-}BN}$ is the sputter yield of BN under xenon ion incidence, and $Y_{Xe\text{-}C/BN}$ is the sputter yield of carbon-coated BN under xenon ion incidence [1]. The yield ratio is conservatively estimated to be 10 based on the literature [1]. By dividing a Hall thruster's discharge channel thickness (t_{BN}) by the erosion rate calculated from Equation 7.2-1, a conservative lower bound on the useful life of the discharge channel (and to some extent, the thruster) can be estimated.

As a means to approximate discharge channel erosion (and therefore channel life), carbon backsputter measurements were taken at discharge voltages of 200 V and 300 V. Near constant deposition rates of approximately 0.03 μm/h and 0.06 μm/h were observed for the 200 V and 300 V conditions, respectively. Applying these values to Equation 7.2-1 suggests a maximum discharge channel erosion rate of approximately 0.63 μm/h at 200 V and 1.13 μm/h at 300 V. Because the discharge channel walls were coated in a layer of backsputtered carbon after operation of the MaSMi-60, the discharge channel erosion rate was bounded by approximately 0.03 - 0.63 μm/h for operation at 200 V and 0.06 - 1.13 μm/h for operation at 300 V. These approximate erosion rates represent a 10x - 100x reduction in discharge channel erosion rates compared to unshielded Hall thrusters, suggesting that increased discharge channel lifetimes of the same magnitude may be realized [1,37].

Interestingly, the carbon deposition rates measured for the MaSMi-60 were approximately an order of magnitude greater than those observed during testing of the H6MS conducted at JPL's Owens (Patio) chamber [1,37]. While testing of the MaSMi-60 in the Owens chamber would give conclusive evidence as to the true extent for this discrepancy (though not an option during this thesis investigation), these observations appear to be related to the relative sizes of the two vacuum chambers. While the two chambers share a similar diameter, the distance from the thruster exit plane to the beam dump in the Owens chamber is approximately twice that of the High Bay chamber. Extending the length of the vacuum chamber increases the fraction of ions impacting the chamber sidewalls (rather than the downstream beam dump) due to the inherent angular divergence of the thruster beam. Due to the ions' low angle of incidence to the sidewalls, sputtered carbon atoms are more likely to be ejected downstream and away from the thruster rather than upstream towards the thruster. This would yield decreasing backsputter

rates as beam dump proximity to the thruster is increased. Conversely, as the length of a vacuum chamber is decreased, a greater fraction of the thruster beam is incident on the beam dump (generally oriented perpendicular to the beam). This encourages sputtered carbon atoms to travel upstream, increased backsputter rates to the thruster. This effect offers a possible explanation for the higher carbon deposition rates observed during testing of the MaSMi-60 in the High Bay chamber. Incorporating this explanation with experimental observations suggests that the factor of ~2 decrease in beam dump proximity to the thruster yielded a factor of ~10 increase in carbon backsputter observed local to the thruster, despite the >10x increase in ion flux generated by the H6MS compared to the MaSMi-60.

Significant erosion of both the inner and outer poles was observed throughout testing of the MaSMi-60. The images of the MaSMi-60 in Figure 7.2-4 show the level of the pole face erosion after approximately 20 hours of operation. This feature is known to affect both high- and low-power magnetically shielded Hall thrusters and may be caused by the MaSMi-60's non-optimized magnetic shielding field topology, cathode plume oscillations producing energetic ions (observed in ion thruster and cathode life tests), or other mechanisms [102,103]. For example, though the MaSMi-60 achieves symmetric shielding of the inner and outer walls, it also imposes a topology around the chamfered regions of the discharge channel with exceedingly high field curvature (termed "over-shielded" as it is much higher than in the designs of other higher power MS thrusters). This, in turn, may lead to higher angular divergence of beam ions and higher pole erosion. Alternatively, combination of the magnetic field structure and cathode plume oscillations may impact the stability of the thruster, leading to higher than desired discharge plasma oscillations which could enhance erosion. While beyond the scope of this

thesis investigation, these and other possible physical mechanism(s) of ion bombardment of the pole faces are under investigation [103].

7.2.3. Performance Measurements: Thrust Stand

7.2.3.1. Thrust

Thrust stand measurements were taken at the 30 operating conditions presented in Table 7.2-1. The thrust produced by the MaSMi-60 as a function of discharge power for each operating discharge voltage is shown in Figure 7.2-5. Increases in discharge power yielded proportional increases in thrust, generating highly linear trends for each discharge voltage. Thrust values ranging from 8 mN to over 33 mN were observed across all operating points, demonstrating a favorable throttling range for the MaSMi-60.

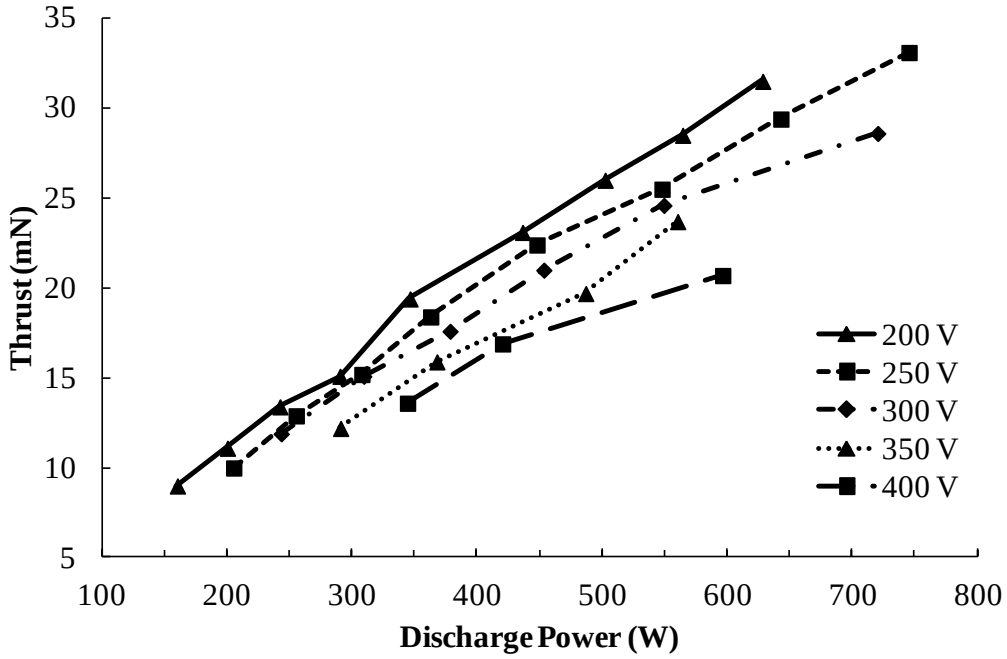

Figure 7.2-5. *Thrust as a function of discharge power for the MaSMi-60.*

7.2.3.2. Anode Specific Impulse

The anode specific impulse (I_{sp}) as a function of discharge power for the MaSMi-60 is shown in Figure 7.2-6. All curves followed the expected trends of increasing I_{sp} with both

discharge voltage and discharge power. Specific impulse values of between 730 s and 1370 s were observed across the full range of operating conditions. These results suggest that the MaSMi-60 achieves slightly lower I_{sp} values at a given power level than conventional low-power Hall thrusters of a similar-scale. This is likely due to the plasma being forced far downstream of the discharge channel exit by the over-shielded magnetic field topology, causing a poor propellant utilization fraction and an associated reduction in specific impulse.

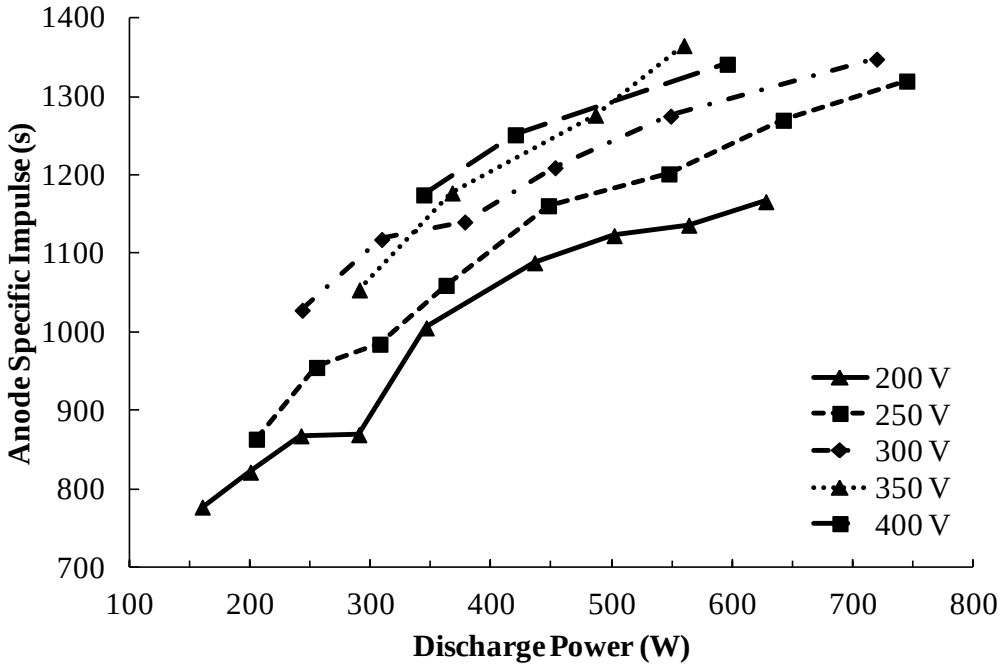

Figure 7.2-6. *Anode specific impulse as a function of discharge power for the MaSMi-60.*

7.2.3.3. Anode Efficiency

The MaSMi-60's anode efficiency as a function of discharge power is presented in Figure 7.2-7. In general, all operating conditions yielded increased efficiency as the discharge power was increased. In every case except the 400 V conditions, however, there appeared to be an efficiency ceiling between 28% and 29% where the thruster's efficiency would remain unchanged with further increases in discharge power. This efficiency ceiling is likely caused, at

least in part, by the over-shielded topology; this forces the plasma far downstream of the discharge channel exit, reducing plasma confinement and focusing while enabling increased neutral leakage.

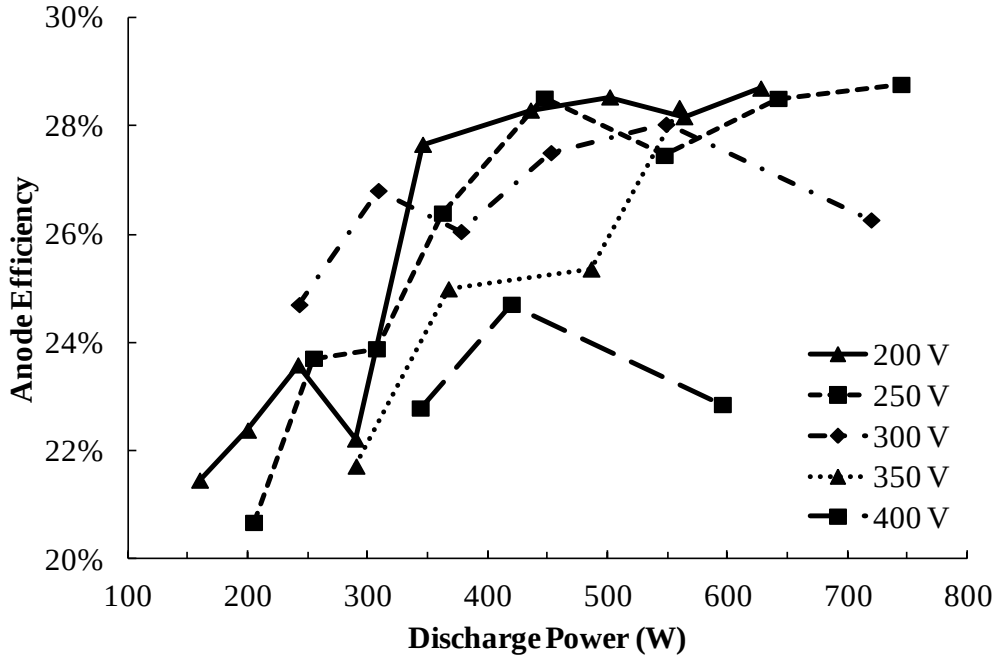

Figure 7.2-7. *Anode efficiency as a function of discharge power for the MaSMi-60.*

7.2.4. Performance Measurements: Plasma Diagnostics

To characterize the MaSMi-60's plasma discharge over the majority of its throttling envelope, plume diagnostics measured the beam characteristics at nine operating conditions. Data was collected at discharge voltages of 200 V, 250 V, and 300 V and discharge powers of 250 W, 400 W, and 550 W. These points were selected as they are sufficient to capture the trends in thruster performance over the throttling range, as seen in Figures 7.2-8 through 7.2-13.

7.2.4.1. Faraday Probe Results

Figure 7.2-8 presents the ion current density profiles, corrected for background charge-exchange collisions, for each of the nine operating conditions used to characterize the MaSMi-60. The figure is broken into three plots, each showing profiles for the three discharge voltage

conditions at a given power level. A slight broadening of the peak in the ion current density profiles is observed with increasing discharge voltage, suggesting a slight widening of the beam. While this effect is apparent in the ion current density profiles, the divergence half-angle of the beam (containing 95% of the momentum-weighted ion current) only showed a very slight increase (if any) with increasing discharge voltage and was nearly constant across all operating conditions. A summary of the corrected beam ion current, beam divergence half-angle containing 95% of the momentum-weighted ion current, and their associated uncertainties is presented in Table 7.2-2.

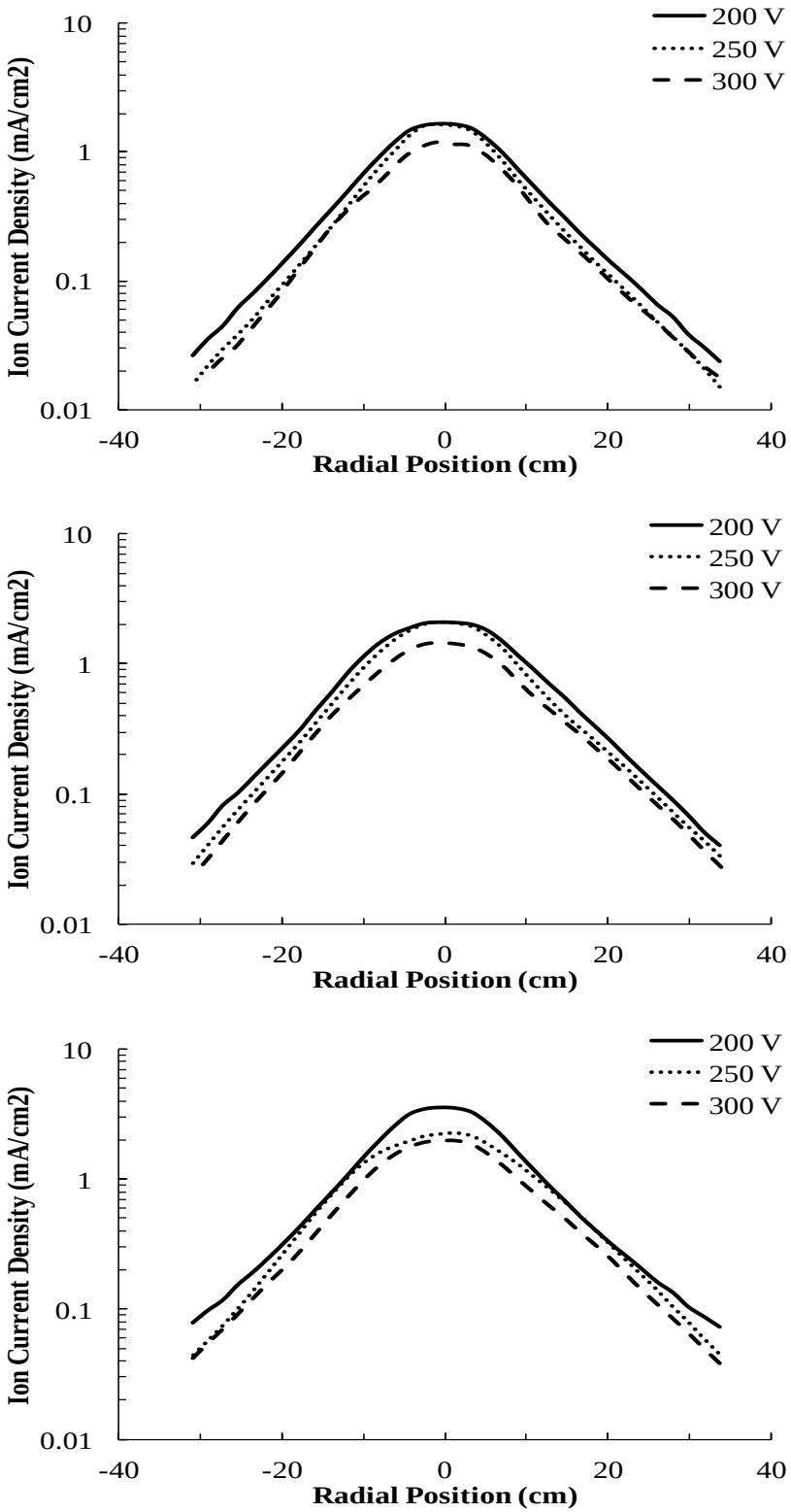

Figure 7.2-8. *Ion current density profiles for the MaSMi-60 at discharge powers of 250 W (top), 400 W (middle), and 550 W (bottom).*

Table 7.2-2. *Summary of ion current density, divergence half-angle, and the associated uncertainties for operation of the MaSMi-60.*

V_d (V)	P_d (W)	I_b (A)	Div. (°)	Uncertainty (I_b)	Uncertainty (Div.)
200	250	0.765	33	+8% / -4%	+/-8%
200	400	1.237	33	+5% / -3%	+/-8%
200	550	1.737	33	+4% / -2%	+/-8%
250	250	0.615	31	+10% / -5%	+/-8%
250	400	1.024	31	+6% / -3%	+/-8%
250	550	1.405	34	+5% / -2%	+/-7%
300	250	0.524	31	+12% / -6%	+/-8%
300	400	0.791	33	+7% / -4%	+/-8%
300	550	1.089	33	+5% / -3%	+/-8%

7.2.4.2. Retarding Potential Analyzer and Emissive Probe Results

Results for the normalized ion current from the UCLA 4-grid RPA measurements at 200 V, 250 V, and 300 V operation of the MaSMi-60 are shown in Figure 7.2-9 while a plot of *dI/dV* for each of these discharge potentials is presented in Figure 7.2-10. One representative curve is shown for each discharge voltage as the variation of the RPA traces was minimal between the three power levels at each applied discharge potential. The full set of nine RPA traces can be found in Appendix A. All RPA traces of ion current against ion discriminator bias were smooth, facilitating the identification of the most probable ion potential. A FWHM value of between approximately 65 V and 70 V was observed for all but one of the RPA scans (the one exception had an FWHM value in excess of 100 V), suggesting a wide thermal distribution of ion energies in the plasma beam. Figure 7.2-11 shows characteristic plots of the emissive probe's measured floating potential against the applied heater current for discharge voltages of 200 V, 300 V, and 400 V (the full range of examined discharge potentials).

The plasma potential, measured directly from the emissive probe local to the RPA, remained between 9 V and 10 V for all operating conditions. Assuming a local electron temperature of approximately 3 eV, the plasma potential was approximately 11 V at the RPA; this is the correction applied to the most probable ion potential measurements. Table 7.2-3 summarizes the peak value of *dI/dV*, the local plasma potential, the most probable ion potential, and the approximate RPA measurement uncertainty for the three discharge voltage operating conditions.

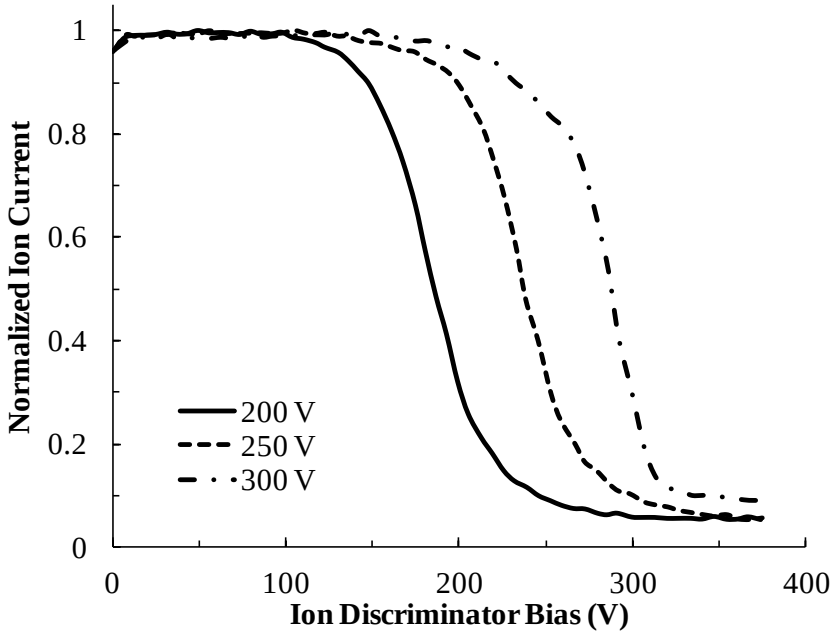

Figure 7.2-9. *Normalized ion current as a function of RPA ion discriminator potential for 200 V, 250 V, and 300 V operation of the MaSMi-60.*

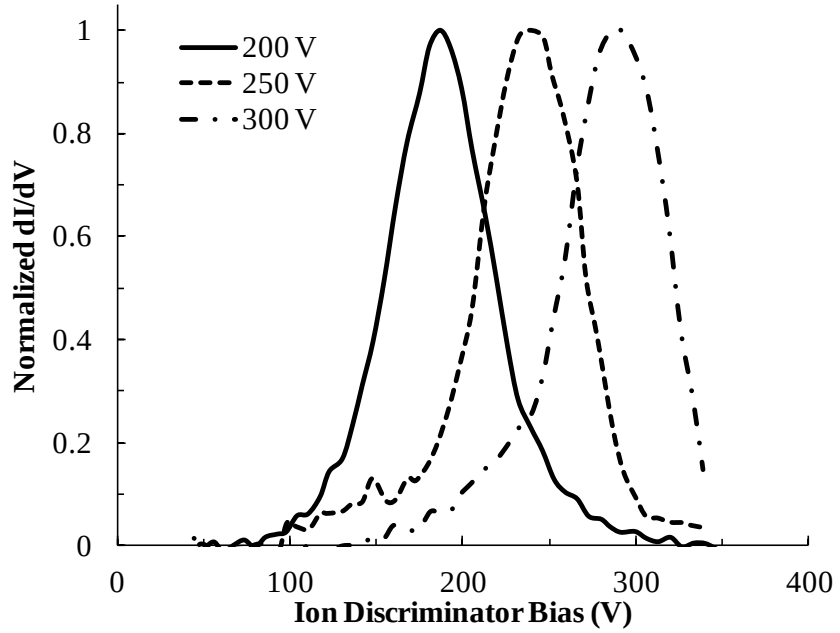

Figure 7.2-10. *Normalized dI/dV as a function of RPA ion discriminator potential for 200 V, 250 V, and 300 V operation of the MaSMi-60.*

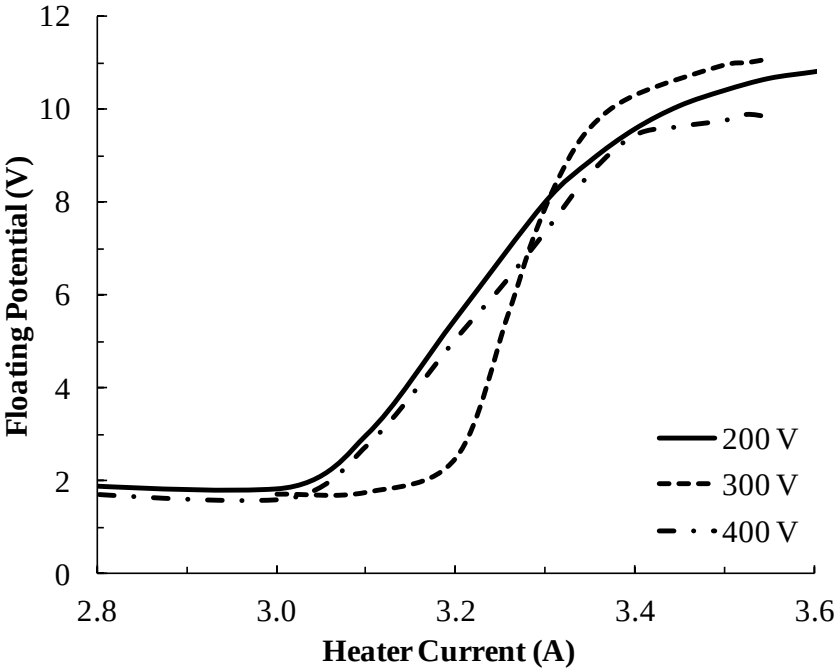

Figure 7.2-11. *Emissive probe floating potential as a function of applied heater current across the full range of examined operating discharge voltages of the MaSMi-60.*

Table 7.2-3. *Summary of the most probable ion potential, downstream plasma potential, and the associated uncertainty for operation of the MaSMi-60.*

V_d (V)	$V_{peak,RPA}$ (V)	V_{plasma} (V)	V_{mp} (V)	Uncertainty	η_v
200	186	11	175	+/- 6%	88%
250	237	11	226	+/- 4%	90%
300	290	11	279	+/- 4%	93%

7.2.4.3. ExB Probe Results

Normalized ion current profiles measured by the **E**x**B** probe for the nine operating conditions considered during the plasma characterization are presented in Figures 7.2-12 through 7.2-14. While its beam is clearly dominated by singly charged ions, there is significant multiply charged ion content in the MaSMi-60's plasma discharge. In general, the MaSMi-60's beam composition matches well with the measurements made on the H6MS Hall thruster across all nine operating conditions, offering evidence that the discharge channel walls of the MaSMi-60 are well shielded [37]. The wide thermal distribution of ions noted during the RPA measurements were also observed in the **E**x**B** probe spectra, where relatively wide Gaussian curves (corresponding to a large spread in ion energies) were required to fit the data. It is important to note that the spectra peaks for each beam voltage occurred exactly at the expected **E**x**B** voltage bias (i.e. electric field); this is best observed in Figure 7.2-14 (300 V operating conditions). The fits to the 200 V and 250 V data sets were made using the same method (i.e. using knowledge of where each specie's peak should occur), enabling the ion species content to be identified with high confidence. A summary of the beam composition at each of the nine operating conditions and their associated uncertainties is shown in Table 7.2-4.

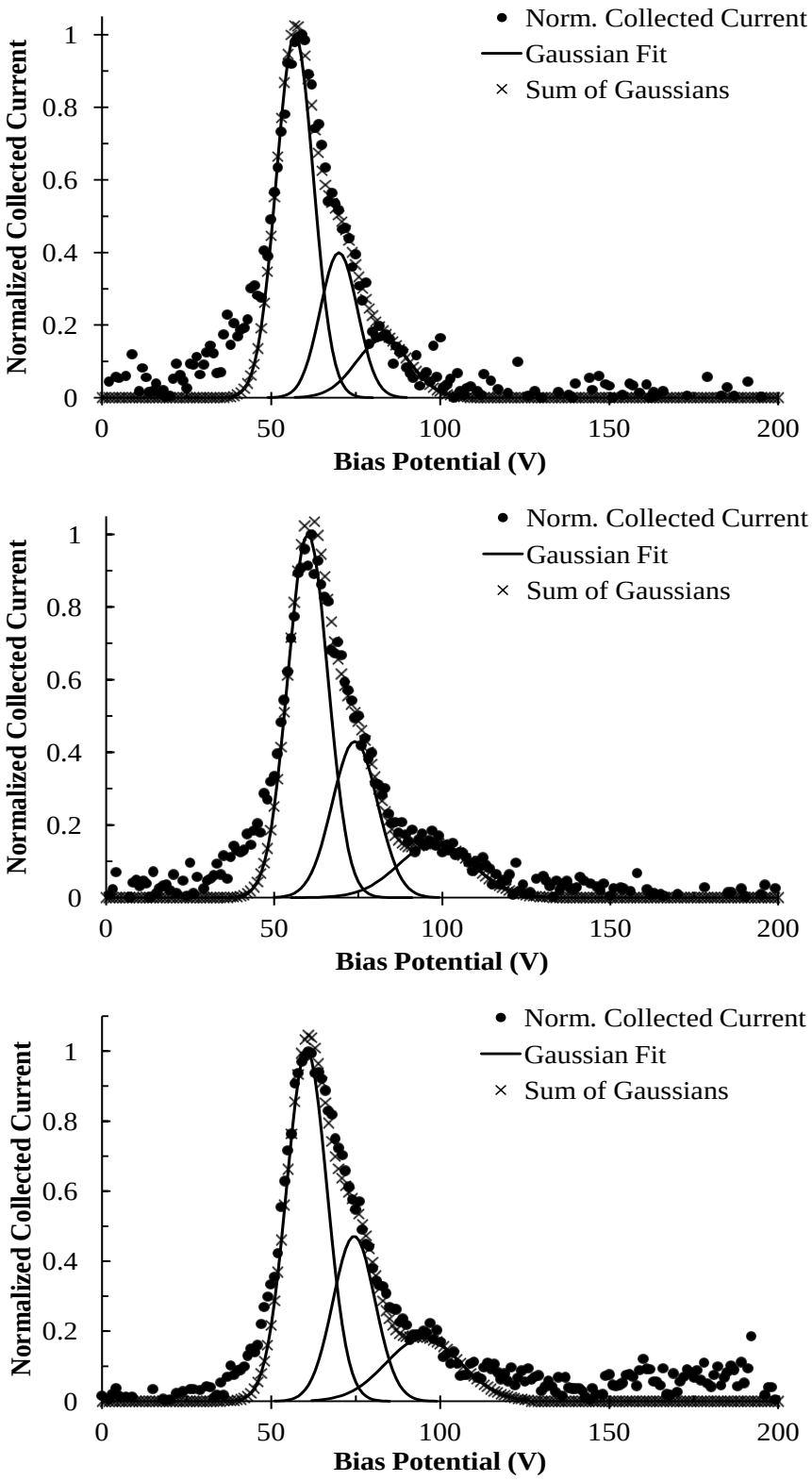

Figure 7.2-12. *Normalized velocity spectra showing the MaSMi-60's beam composition during operation at 200 V and 250 W (top), 400 W (middle), and 550 W (bottom).*

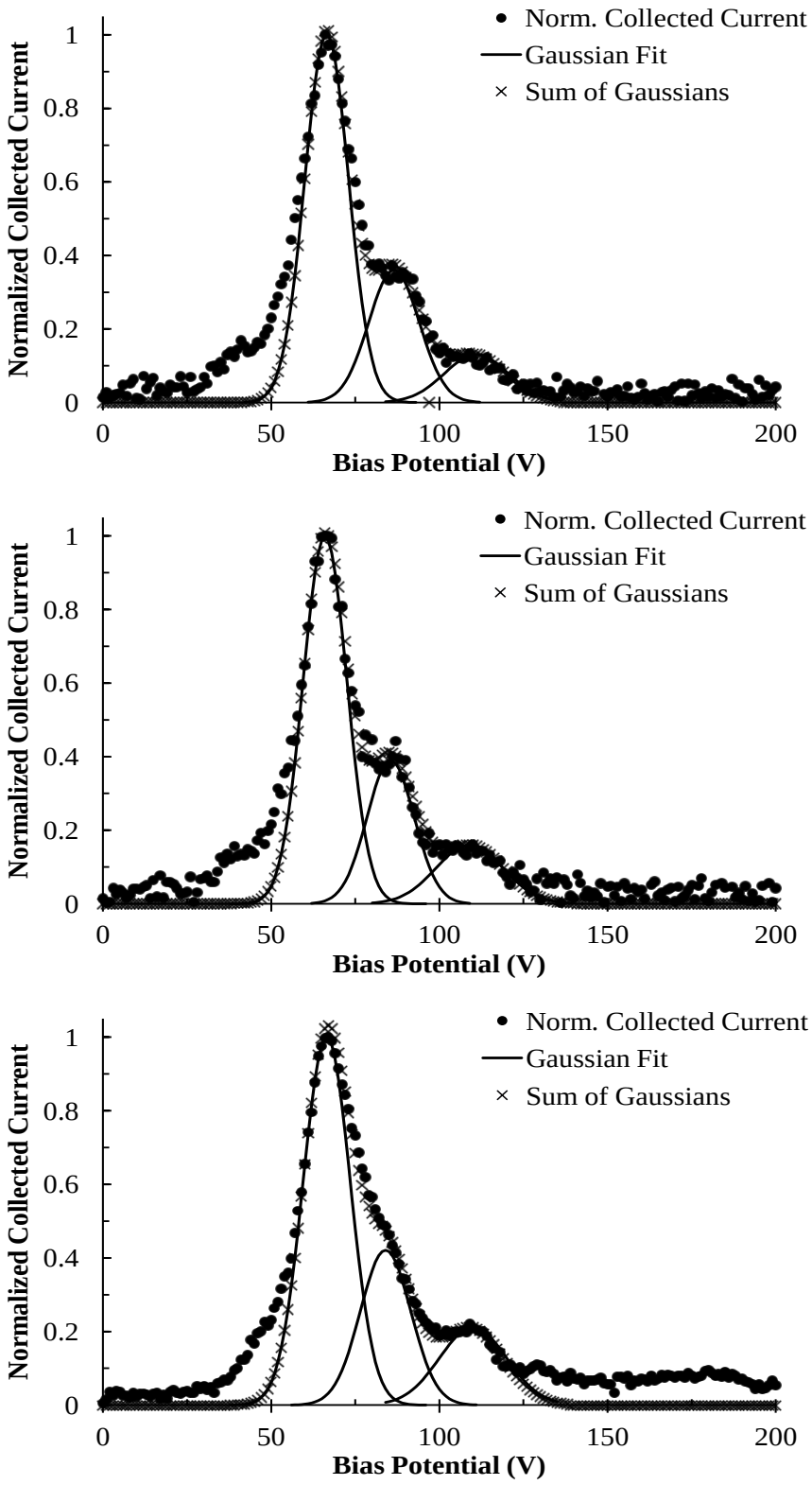

Figure 7.2-13. *Normalized velocity spectra showing the MaSMi-60's beam composition during operation at 250 V and 250 W (top), 400 W (middle), and 550 W (bottom).*

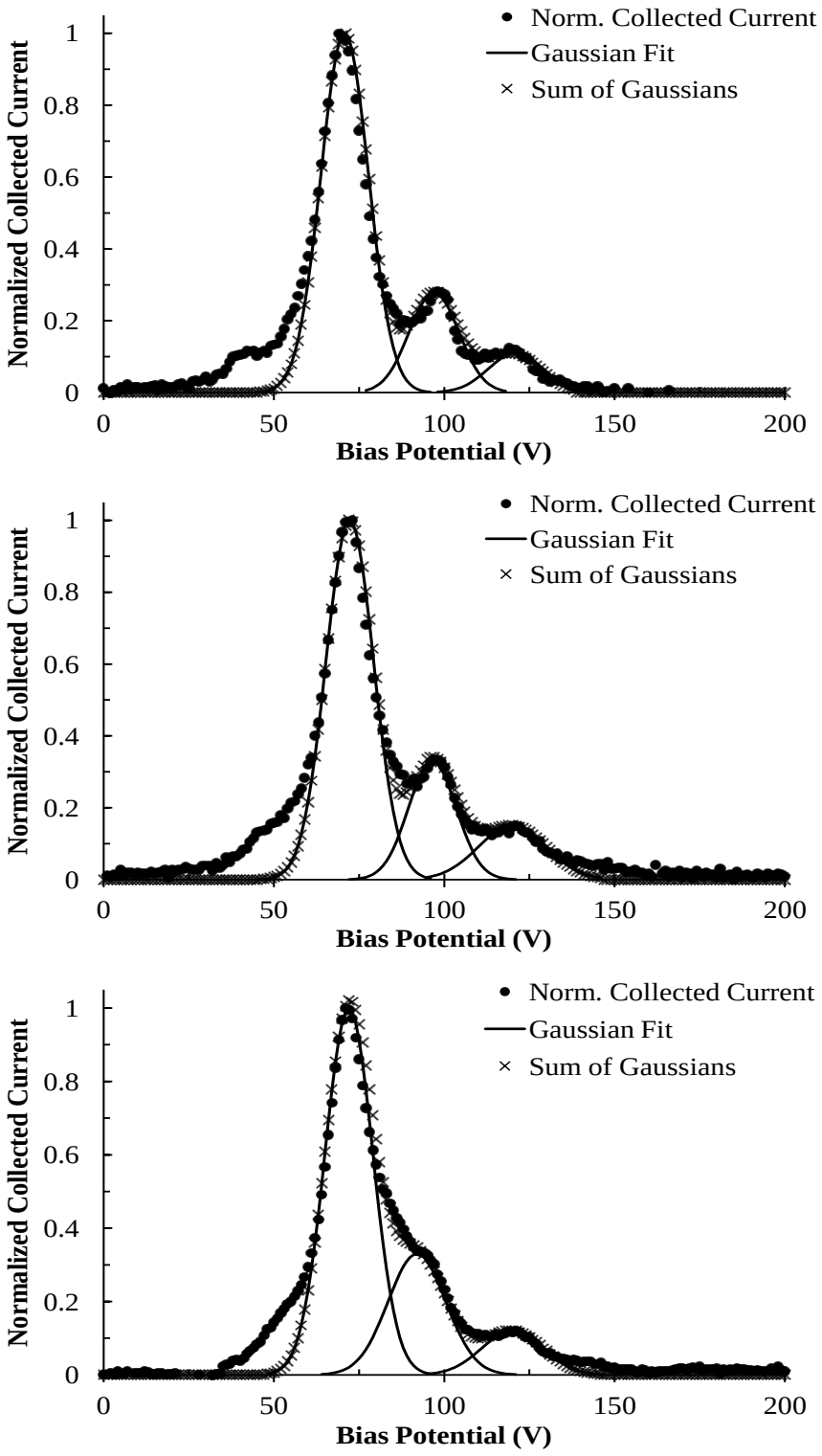

Figure 7.2-14. *Normalized velocity spectra showing the MaSMi-60's beam composition during operation at 300 V and 250 W (top), 400 W (middle), and 550 W (bottom).*

Table 7.2-4. *Summary of ion species' contributions to the beam current for operation of the MaSMi-60.*

V_d (V)	P_d (W)	I^+	I^{++}	I^{+++}	Uncertainty (I^+, I^{++}, I^{+++})		
200	250	0.613	0.245	0.142	+/-8%	+/-20%	+/-35%
200	400	0.569	0.275	0.156	+/-9%	+/-18%	+/-32%
200	550	0.550	0.269	0.181	+/-9%	+/-19%	+/-28%
250	250	0.623	0.259	0.118	+/-8%	+/-19%	+/-42%
250	400	0.601	0.252	0.147	+/-8%	+/-20%	+/-34%
250	550	0.572	0.257	0.171	+/-9%	+/-19%	+/-29%
300	250	0.708	0.204	0.088	+/-7%	+/-24%	+/-57%
300	400	0.648	0.214	0.137	+/-8%	+/-23%	+/-36%
300	550	0.643	0.258	0.099	+/-8%	+/-19%	+/-50%

7.2.4.4. Calculated Performance Summary

A summary of the voltage utilization, current utilization, mass utilization, divergence, charge utilization, and anode efficiencies measured by the beam diagnostics compared to the anode efficiency measured by the thrust stand is presented in Table 7.2-5; the approximate uncertainty in the efficiency calculations is also included. Good matching is observed between the calculated and measured anode efficiency, with all performance values falling well within the uncertainty of the plasma beam measurements.

Insight into the behavior of the MaSMi-60 can be drawn by comparing its performance to that of the high-performing H6MS Hall thruster. The measured anode efficiency of the MaSMi-60 ranged from 24% to 28% whereas the H6MS demonstrated an anode efficiency of 67% [37]. While low-power Hall thrusters are never capable of high (60+%) efficiencies observed in high-power devices, the efficiency demonstrated by the MaSMi-60 is less than that of many comparably sized devices and warrants investigation. An examination of the individual efficiency contributions to the MaSMi-60's anode efficiency clearly shows the primary causes of

the thruster's lower-than-expected performance. The voltage utilization and charge utilization efficiencies were, in general, in the mid-90% range. These values matched well with the H6MS, which demonstrated a voltage utilization efficiency of 93% and a charge utilization efficiency of 96% [37]. The current and mass utilization efficiencies were the two lowest components of the anode efficiency, with an average value of 62% over all thruster operating conditions and no value over 67%; the divergence efficiency was only slightly better, with values peaking at 73%. By contract, the H6MS demonstrated 87% current utilization efficiency, 98% mass utilization efficiency, and 89% divergence efficiency [37]. The strong relationship between the magnetic field parameters (topology, strength, etc.) and its effect on the current utilization, mass utilization, and divergence efficiencies, is well understood. The physical mechanisms specific to the MaSMi-60 which are responsible for these low efficiency values will be explored using computational modeling, presented in the next chapter. While the MaSMi-60's over-shielded topology appears to grant a 10x - 100x increase in the useful life of the discharge channel compared to unshielded devices, the high pole erosion rates and low performance as a result of the topology suggest a clear path forward to improve the MaSMi-60 in future design iterations.

Table 7.2-5. *Summary of the MaSMi-60's measured and calculated efficiencies.*

V_d (V)	P_d (W)	$\eta_{a,meas}$	η_v	η_b	η_m	η_d	η_q	$\eta_{a,calc}$	Uncertainty ($\eta_{a,calc}$)
200	250	**24%**	86%	61%	57%	70%	96%	**20%**	+14% / -8%
200	400	**24%**	88%	62%	64%	70%	96%	**24%**	+14% / -9%
200	550	**25%**	90%	63%	66%	70%	96%	**25%**	+15% / -10%
250	250	**27%**	89%	60%	60%	73%	97%	**23%**	+15% / -9%
250	400	**27%**	92%	64%	63%	73%	96%	**26%**	+14% / -9%
250	550	**28%**	91%	64%	67%	69%	96%	**26%**	+14% / -9%
300	250	**28%**	94%	65%	57%	73%	97%	**25%**	+16% / -9%
300	400	**28%**	94%	59%	58%	70%	96%	**22%**	+13% / -8%
300	550	**28%**	92%	60%	62%	70%	97%	**23%**	+13% / -8%

7.3. Concluding Remarks

This chapter introduced the MaSMi-60 and presented the thruster's performance over a wide range of operating conditions. Strong evidence that the MaSMi-60 achieved a fully shielded magnetic field topology was observed. First, the discharge plasma was clearly offset from the channel walls during thruster operation. Second, the discharge channel surfaces were coated in backsputtered carbon with no signs of asymmetrical deposition patterns or significant ion bombardment erosion. Third, the beam species mix showed a high content of multiply charged ions, matching similar trends observed during testing of the H6MS. Discharge channel erosion estimated based on QCM-measured carbon backsputter rates suggested a 10x - 100x decrease in erosion compared to unshielded Hall thrusters, thereby suggesting a significant increase in discharge channel life. The thruster was tested over a wide discharge power range spanning from 160 W to nearly 750 W. Significant discharge oscillations were observed during operation, and nominal operation (by conventional definition) of the thruster was only achievable at two of the more than 30 points considered. The MaSMi-60 demonstrated thrust values between approximately 8 mN to over 33 mN with a peak specific impulse of 1370 s and a peak anode efficiency of approximately 29%. The calculated anode efficiency based on plasma plume diagnostics showed good agreement with thrust stand measurements while revealing the primary factors contributing to the low anode efficiency: mass utilization, current utilization, and beam divergence. Overall, the MaSMi-60 not only demonstrated a fully shielded magnetic field topology, but also significantly improved performance over the MaSMi-40. To confirm that the MaSMi-60 attained the required plasma properties enabling magnetic shielding and to identify the physics causing the low anode efficiency of the device, computational simulations of the thruster were performed. Results from these computational efforts are presented in Chapter 8.

Chapter 8

COMPUTATIONAL ANALYSIS OF THE MASMI-60 PLASMA DISCHARGE

In this chapter, results from the computational portion of this investigation are presented. Section 8.1 revisits the motivation for numerical simulations and explains their importance to this investigation. Section 8.2 reviews a brief history of the computational modeling of Hall thrusters, covering key developments from the 1970's to the present. An overview of Hall2De, the 2-D axisymmetric code developed at JPL for the simulation of the partially ionized gas in Hall thrusters, is presented in Section 8.3. Section 8.4 continues with results from the Hall2De simulations of the MaSMi-60 that support the conclusion that the designed topology establishes effective magnetic shielding of the channel walls. Experimental validation of the simulations along with a sensitivity study of the Hall2De results is presented in Section 8.5. Section 8.6 reviews the MaSMi-60's plasma behaviors predicted by Hall2De and compares them to results from higher power devices. Concluding remarks follow in Section 8.7.

8.1. Motivation for Plasma Modeling in Low-Power Hall Thrusters

One of the most critical design features of a magnetically shielded Hall thruster is the grazing magnetic field line, which must not intersect any portion of the discharge channel wall while penetrating into the anode region of the thruster. The depth of this penetration determines the temperature of the electrons along this particular field line, and therefore along the discharge channel walls in an MS Hall thruster. In the last five years, wall probe measurements taken along the discharge channel of high-power magnetically shielded Hall thrusters have validated the theoretical predictions of low near-wall electron temperatures and plasma potentials near that

of the discharge voltage along the channel surfaces [1,39,78,104,105]. However, the small channel dimensions of low-power Hall thrusters make the use of wall probes challenging, if not impossible, without affecting the plasma discharge. A computational model must therefore be employed to determine the plasma properties and behaviors inside the discharge channel in order to establish the magnetic shielding effectiveness in reducing channel wall erosion.

8.2. Brief History of Hall Thruster Numerical Models

The first records of theoretical models describing the partially ionized discharge of a Hall thruster dates to the 1970's when Morozov *et al* developed a relatively simple model for the stationary plasma thruster (SPT) [106–108]. One of the first 3D models for the SPT, which used a particle-in-cell (PIC) scheme combined with a Monte Carlo collision model, was developed by Hirakawa and Arakawa [109]. Since the late 1990s, a common computational approach has involved solving the fluid (inertialess) momentum and energy conservation laws for electrons while using discrete-particle methods to track the heavy-species. This hybrid method captures the bulk plasma behaviors and ion kinetics with reasonable computational times. HPHall (hybrid-PIC Hall), one of the first codes to use this approach, relied on a PIC-direct simulation Monte Carlo (DSMC) method for ions in 2D axisymmetric thruster geometry [110]. This code is attributed to being the first to capture the breathing mode oscillations of Hall thrusters in a 2D simulation [111]. HPHall has been extensively used since the late 1990's and has undergone several improvements, such as the upgrade to HPHall(2) by Parra and Ahedo in 2006 [112].

A fundamental component of Hall thruster discharge plasma modeling is the electron Hall parameter (Ω_e), defined as

$$\Omega_e = \frac{\omega_c}{\nu_e} \tag{8.2-1}$$

where ν_e is the electron collision frequency. Ion acceleration in a Hall thruster is based on operation of the device at high electron Hall parameter (Ω_e >100), where the resistance to the transport of mass and heat in the electron flow perpendicular to the magnetic field is much greater (by ~ Ω_e^2) than in the direction parallel to the magnetic field in the majority of the discharge channel [111]. This allows the separation of the electron equations based on their direction relative to the magnetic field: the full partial differential transport equations are solved only perpendicular to the field while the electron equations in the parallel direction are simplified by assuming constant electron temperature and thermalized potential the latter of which yields an algebraic equation for the plasma potential [106]. This simplification is often called the "quasi-1D assumption." In terms of modeling, this assumption allows the electron equations to be discretized in a quadrilateral computational cell that is bounded by two adjacent magnetic field lines rather than one with arbitrary geometry [111]. This is the methodology used in HPHall and is widely applicable to a variety of Hall thruster geometries. However, magnetic field topologies with complex field line arrangements (such as those near magnets, magnetic poles, eroded or chamfered channel surfaces, etc.) and/or reduced Hall parameter values (such as those near the cathode and anode plume) bring into question the applicability of the quasi-1D assumption. Because both of these situations exist for a magnetically shielded Hall thruster, a more general approach is required to discretize the electron equations.

8.3. Hall2De

8.3.1. Code Overview

Hall2De is a 2D axisymmetric code that allows for the simulation of the partially ionized gas in the r-z plane of Hall thrusters. Ions are modeled as a cold (compared to the electrons), isothermal fluid with charge-exchange and multiple-ionization collisions accounted for in the

momentum equations as a friction ("drag") force. For the neutral species, Hall2De assumes that the particles incident on a surface are fully accommodated and that any re-emitted particles follow a cosine distribution. Therefore, the flux of neutrals on a given surface is a function of the view factor of that surface to all other surfaces, making the calculation of neutral particle distributions one primarily based on geometry. A mass-conserving first-order upwind algorithm is used to step the neutral gas particles between grid cells, allowing the neutral density to change as a function of time despite the particles having a fixed velocity (based on the velocity distribution computed from the view factor particle flux model). A 2D form of Ohm's law in directions parallel and perpendicular to the magnetic field and the electron energy equations are discretized on a field-aligned computational mesh. The plasma potential is determined from Ohm's law combined with the current conservation equation [111]. As with all other global Hall thruster codes in existence today, a self-consistent model of the anomalously high transport of electrons known to occur in these devices remains elusive in Hall2De. Nevertheless, with experimentally-guided models of the anomalous collision frequency, results from Hall2De simulations have been validated against measured plasma parameters for numerous high-power Hall thrusters [78,113,114].

Three unique features distinguish Hall2De from HPHall and similar quasi-1D r-z codes:

1) *Magnetic Field Aligned Mesh (MFAM):* The discretization of the governing equations on an MFAM allows for the solution of the highly anisotropic electron equations in both parallel and perpendicular directions without suffering from excessive numerical diffusion. This allows for solutions in thrusters with highly mirrored and/or magnetically shielded field topologies. Unlike quasi-1D r-z Hall thruster codes like HPHall where computational elements defined by two adjacent

magnetic field lines and two boundary segments are interpolated onto an arbitrary mesh, Hall2De further divides the computational elements using an orthogonal set of lines (called the magnetic vector potential, or simply vector potential $\boldsymbol{A}$, and defined by $\boldsymbol{B} = \nabla \times \boldsymbol{A}$). This is especially advantageous when the thruster surfaces disrupt the continuity of a given magnetic field line. Additionally a MFAM allows for a self-consistent plasma simulation in the anode region; by contrast, HPHall is incapable of a self-consistent solution in this region and uses extrapolation to determine a solution between the anode boundary and the nearest magnetic field line.

2) *No Discrete-Particle Methods:* Hall2De solves the conservation equations for the ions by considering them as isothermal, cold (relative to the electrons) fluids; multiple ion fluids (corresponding to multiple ion charge states and sources) can be included in a single simulation. For the collisionless neutrals, line-of-sight formulations accounting for ionization and wall collisions are used to evolve the neutral species in time [115]. All view factors are calculated in a pre-processing phase to reduce total computational time. A main objective of the methods followed for the numerical solution of the heavy species (ions and neutrals) is to eliminate numerical fluctuation errors associated with discrete-particle statistics which, in some cases, may resemble real fluctuations that can occur in these discharges.

3) *Large Computational Domain:* The domain considered by Hall2De encompasses the entire discharge channel and extends several channel lengths downstream of the thruster exit plane, encompassing the cathode boundary and thruster axis of

symmetry. This allows for detailed and self-consistent descriptions of the downstream plasma behaviors based on changes in the ionization and acceleration region plasma while accounting for the cathode boundary conditions self-consistently.

8.3.2. Physics Model

8.3.2.1. Ion Governing Equations

As mentioned above, Hall2De models the ions as a cold, isothermal fluid. The derivation of the momentum conservation equation begins with the Boltzmann equation for the ion distribution function (f_i):

$$\frac{\partial f_i}{\partial t} + \mathbf{v} \cdot \nabla_{\mathrm{r}} f_i + \mathbf{F}_i \cdot \nabla_{\mathrm{v}} f_i = \left(\dot{f}_i\right)_c \qquad 8.3\text{-}1$$

where $\mathbf{F}_i$ is the specific force on the ions, containing contributions from the electric and Lorentz forces. Taking the moment of Equation 8.3-1 yields the momentum conservation law used for ions, expressed in conservative form as follows:

$$\frac{\partial}{\partial t}(n_i M \mathbf{u}_i) + \nabla \cdot (n_i M \mathbf{u}_i \mathbf{u}_i) = q_i n_i \mathbf{E} - \nabla p_i + R_i \qquad 8.3\text{-}2$$

where n_i is ion density, $\mathbf{u}_i$ is the mean ion velocity, q_i is the ion charge, p_i is the ion pressure, and R_i is the ion drag force incorporating contributions to momentum exchange from both elastic and inelastic collisions. Viscous terms in the pressure tensor are neglected and $\mathbf{p}_i = p_i \mathbf{I}$ is assumed where $\mathbf{I}$ is the delta tensor. Derivation of Equation 8.3-2 from the Boltzmann's equation and explicit definitions of the drag force term are presented in [111].

Specification of the computational domain's boundary conditions closes the conservation law for ions. The hydrodynamic Bohm criterion for the normal component of ion velocity (u_i), given by

$$u_i \geq \sqrt{\frac{kT_e}{M}}, \qquad 8.3\text{-}3$$

is imposed at the eclectically insulating boundaries (i.e. discharge channel walls) for ions entering the plasma sheath. This condition holds assuming fully absorbing walls, cold monoenergetic ions, and sheath electrons following a Boltzmann distribution. The Bohm criterion is used for ions with a normal velocity component less than the ion acoustic speed; otherwise, the true ion velocity is used at the boundary. At electrical conductors, no secondary electron emission is allowed and thin-sheath conducting-wall boundary conditions are specified where the boundary is set at ground potential. At the anode, the ion boundary condition encompasses the sheath's evolution from ion attracting to ion repelling through a continuous transition from the Bohm condition for ion velocity to zero velocity (details about this model and its numerical implementation are described in the literature) [116,117]. A reflection boundary condition is applied along the thruster centerline while ions are allowed to flow out of the system freely at the outflow boundaries assuming a zero-current condition. The cathode ion flux is specified at the cathode boundary based on cathode simulations with the OrCa2D code or experimental measurements [78,118,119].

8.3.2.2. Electron Governing Equations

The momentum equation for the electrons, with the viscous terms neglected, takes the form

$$n_e m \frac{D\mathbf{u}_e}{Dt} = -q_e n_e (\mathbf{E} + \mathbf{u}_e \times \mathbf{B}) - \nabla p_e + R_e \qquad 8.3\text{-}4$$

$\mathbf{u}_e$ is the mean electron velocity, q_e is the charge of an electron, p_e is the electron pressure ($\mathbf{p}_e = p_e\mathbf{I}$ is assumed), and R_e is the electron drag force [111]. The curl-free condition for the electric field yields

$$\mathbf{E} = -\nabla\phi \tag{8.3-5}$$

where ϕ is the potential.

Due to the low mass of electrons, their inertia can be neglected. This yields the vector form of Ohm's law:

$$\mathbf{E} = \eta\mathbf{j}_e + \eta\Omega_e\mathbf{j}_e \times \widehat{\mathbf{B}} - \frac{\nabla p_e}{q_e n_e} + \eta_{ei}\bar{\mathbf{j}}_i \tag{8.3-6}$$

where

$$\eta = \frac{m\nu_e}{q_e^2 n_e}\,, \quad \mathbf{j}_e = -q_e n_e \mathbf{u}_e\,, \quad \eta_{ei} = \frac{m\bar{\nu}_{ei}}{q_e^2 n_e}\,, \quad \bar{\mathbf{j}}_\mathbf{i} = \frac{1}{Z^*}\sum_i Z\mathbf{j}_i\,. \tag{8.3-7}$$

and

$$\bar{\nu}_{ei} = \frac{n_e Z^* q_e^4 \ln\Lambda}{3(2\pi k T_e)^{3/2}\varepsilon_0^2\sqrt{m}} \tag{8.3-8}$$

where $\ln\Lambda$ is the Coulomb logarithm, ε_0 is the permittivity of a vacuum, and

$$Z^* = n_e^{-1}\sum_i n_i Z^2\,. \tag{8.3-9}$$

The total electron collision frequency (ν_e) has been defined above as the sum of the individual frequencies, given by

$$\nu_e = \bar{\nu}_{ei} + \nu_{en} + \nu_\alpha \tag{8.3-10}$$

where ν_{en} is the electron-neutral collision frequency and ν_α is the anomalous collision frequency that accounts for non-classical transport mechanisms in the plasma (discussed further at the end of this section). Equation 8.3-6 can be broken up into perpendicular ($\perp$) and parallel ($\parallel$) components with respect to the magnetic field, given as

$$E_\parallel = \eta j_{e\parallel} - \frac{\nabla_\parallel p_e}{q_e n_e} + \eta_{ei}\bar{J}_{i\parallel} \tag{8.3-11a}$$

$$E_{\perp} = \eta(1+\Omega_e^2) j_{e\perp} - \frac{\nabla_{\perp} p_e}{q_e n_e} + \eta_{ei} \bar{j}_{i\perp} \,. \qquad \text{8.3-11b}$$

In most of the regions of the Hall thruster the resistive terms in the parallel direction are negligible, reducing Equation 8.3-10a to

$$E_{\parallel} \approx \frac{\nabla_{\parallel} p_e}{q_e n_e} \qquad \text{8.3-12}$$

which leads to the Boltzmann relation for the electron number density. The relation can then be used to obtain the algebraic equation for the plasma potential alluded to previously.

The electron energy conservation law is used to solve for electron temperature:

$$\frac{3}{2} q_e n_e \frac{\partial T_e}{\partial t} = \mathbf{E} \cdot \mathbf{j}_e + \nabla \cdot \left(\frac{5}{2} T_e \mathbf{j}_e + \mathbf{Q}_e \right) - \frac{3}{2} T_e \nabla \cdot \mathbf{j}_e - \sum_s \Phi_s + Q_e^T \qquad \text{8.3-13}$$

where the thermal conduction heat flux tensor ($\mathbf{Q}_e$) is discretized on the MFAM along and across the magnetic field as

$$Q_{e\parallel} = -\kappa_{e\parallel} \nabla_{\parallel} T_e \qquad \text{8.3-14a}$$

$$Q_{e\perp} = -\kappa_{e\perp} \nabla_{\perp} T_e \,. \qquad \text{8.3-14b}$$

Isothermality of the field lines is preserved when the resistive terms in the parallel direction are negligible, as was the case in Equation 8.3-11a. The summation term in Equation 8.3-13 accounts for inelastic energy losses associated with electron-neutral and electron-ion collisions and is defined in [111]. The last term in Equation 8.3-13, which is generally small in Hall thrusters, accounts for the time-rate of energy exchange between the electrons and heavy species due to deviations from thermal equilibrium.

Equations 8.3-11a and 8.3-11b are substituted into the current conservation equation (shown in Equation 8.3-15) and solved parallel and perpendicular to the magnetic field to determine the plasma potential:

$$\nabla \cdot \mathbf{j} = 0 \tag{8.3-15}$$

where **j** represents the total current density summed over both ions and electrons.

Boundary conditions along all surfaces of the computational domain must be defined to close the electron equations. At the anode, conducting sheath boundary conditions are employed. The electron current density normal to the surface is therefore given by

$$\mathbf{j}_e \cdot \hat{\mathbf{n}} = \begin{cases} -j_{T_e} e^{-\frac{q_e \Delta\phi}{kT_e}}, & \Delta\phi > 0 \\ -j_{T_e}, & \Delta\phi \leq 0 \end{cases} \tag{8.3-16}$$

and the convective heat flux is defined as

$$(\mathbf{j}_e T_e) \cdot \hat{\mathbf{n}} = \mathbf{j}_e \cdot \hat{\mathbf{n}}(2T_e + \Delta\phi)\,. \tag{8.3-17}$$

Note that the conductive heat flux ($\mathbf{q}_e$) at the sheath is set to zero

$$\mathbf{q}_e \cdot \hat{\mathbf{n}} = 0 \tag{8.3-18}$$

In these equations, the potential drop across the sheath is

$$\Delta\phi = \phi - V_A \tag{8.3-19}$$

where V_A is the applied anode potential and the electron thermal flux (j_{Te}) is defined as

$$j_{T_e} = \frac{n_e}{4}\sqrt{\frac{8kT_e}{\pi m}}\,. \tag{8.3-20}$$

Due to the attraction of electrons to the positive anode potential, the sheath structure adjacent to the anode is generally electron repelling (i.e. $\Delta\phi > 0$). The electron boundary conditions at the cathode are guided by independent numerical simulations with the OrCa2D code and/or measurements of the plasma generated by the hollow cathode, leading to values for the neutral particle flux, plasma potential, and electron temperature [78,118,119].

Along electrical insulators (such as the discharge channel walls) the conductive heat flux is set to zero and a zero-current condition is imposed:

$$\mathbf{j} \cdot \hat{\mathbf{n}} = 0 \,. \qquad 8.3\text{-}21$$

Secondary electron emission is calculated based on the electron temperature, plasma potential along the sheath edge, and the material-dependent secondary electron yield. The sheath drop is determined based on the formulations of Hobbs and Wesson [120]. Dirichlet conditions are imposed for electron temperature along the far-plume outflow boundaries; this is a good assumption because the electron temperature far (several channel lengths) from the discharge channel exit of a Hall thruster usually falls between 1 eV and 4 eV, based on direct measurements [78,111,113,114]. A zero-current condition is imposed for the current density at the plume boundaries.

8.3.2.2.1. Model of the Anomalous Collision Frequency

The anomalous collision frequency model in Hall2De is an important aspect of all Hall thruster simulations and therefore warrants further discussion. In the present simulations of the miniature thruster the variation for the anomalous collision frequency profile along the thruster's discharge channel centerline is initially assumed based on the findings of several previous numerical and experimental investigations aimed at identifying general trends of the frequency in both the interior and near-plume regions of Hall thrusters. These investigations revealed that the anomalous collision frequency follows a common form: a shallow positive slope from the global minimum to a local maximum, then a steep negative slope to a local minimum, followed by a steep positive slope to the global maximum, and lastly a shallow negative slope (see Figures 8.5-1 and 8.5-4 for examples). The minimum value occurs approximately at the transition from the ionization to the acceleration region. The shallow negative slope downstream of the channel exit closely follows the electron gyrofrequency profile. In simulations of the Hall thruster plasma, this profile is iteratively altered in magnitude until the operating discharge

current is achieved. In principle, iterations of both the axial and radial positions of the various components of the profile should be performed to quantify the impact of our uncertainty in the model of the anomalous collision frequency on the location of and gradients in the discharge plasma. Such sensitivity studies are warranted since the exact location of the discharge channel plasma is generally known experimentally to only ~10% of the discharge channel length. The results of sensitivity simulations performed for the MaSMi-60 Hall thruster are presented in a later section.

8.3.2.3. Neutral Particle Governing Equations

Ionization collisions experienced by neutral particles occur frequently compared to the particle's transit time inside of the discharge channel. By contrast, collisions between neutral particles are very infrequent. The kinetic conservation equation for the neutral particle distribution function (f_n) is therefore the same as for ions, but with the force term equal to zero:

$$\frac{\partial f_n}{\partial t} + \mathbf{v} \cdot \nabla_{\mathrm{r}} f_n = \left(\dot{f}_i\right)_c \qquad 8.3\text{-}22$$

Only ionization collisions are considered, approximated based on the electron-neutral ionization collision frequency (ν_{en}^I), giving the rate of change of the distribution function the form of

$$\left(\dot{f}_i\right)_c = -\nu_{en}^I f_n \ . \qquad 8.3\text{-}23$$

The neutral density can then be determined by taking the integral of the neutral distribution function over velocity space:

$$n_n(t, \mathbf{r}) = \int_{\mathbf{v}} f_n(t, r, \mathbf{v}') d\mathbf{v}' \qquad 8.3\text{-}24$$

where **r** is the position vector. A more detailed explanation of the neutral gas algorithm used in Hall2De is presented in [115]. In summary, neutral particles are assumed to travel in straight

lines at a constant velocity until they are ionized, strike a wall, or leave the computational domain. The distribution function for neutrals emitted from boundaries takes a cosine distribution which is scaled to reflect ionization losses from the neutral population. The flux of neutrals injected from the anode is specified based on the thruster's operating flow rate. Neutral flux at the cathode boundary is specified based on independent cathode flow simulations.

8.4. Hall2De Simulation Results for the MaSMi-60

8.4.1. Magnetic Shielding

A simulation of the MaSMi-60's plasma discharge was performed with Hall2De using an operating condition near the middle of the thruster's operational envelope: a discharge voltage of 300 V and a discharge current of 1.4 A. Results for the electron temperature and plasma potential contours are presented in Figure 8.4-1; these values plotted along the outer and inner discharge channel surfaces are shown in Figure 8.4-2. According to Figure 8.4-1, the plasma potential remains constant while the electron temperature remains well below 10 eV along the discharge channel surfaces. This is confirmed by the results of Figure 8.4-2, where the plasma potential was predicted to be nearly constant at approximately 312 V +/-5 V and electron temperature was predicted to remain below approximately 4 eV +/-2 eV. The Hall2De simulation results for the MaSMi-60 match well with published data on the H6MS, presented in Figure 8.4-3, supporting the conclusion that the MaSMi-60 was magnetically shielded. In sum, the MaSMi-60's constant plasma potential and low electron temperature along the discharge channel walls predicted by Hall2De meet the two key requirements to achieve magnetic shielding, supporting the conclusion that MS was successfully achieved at the miniature scale.

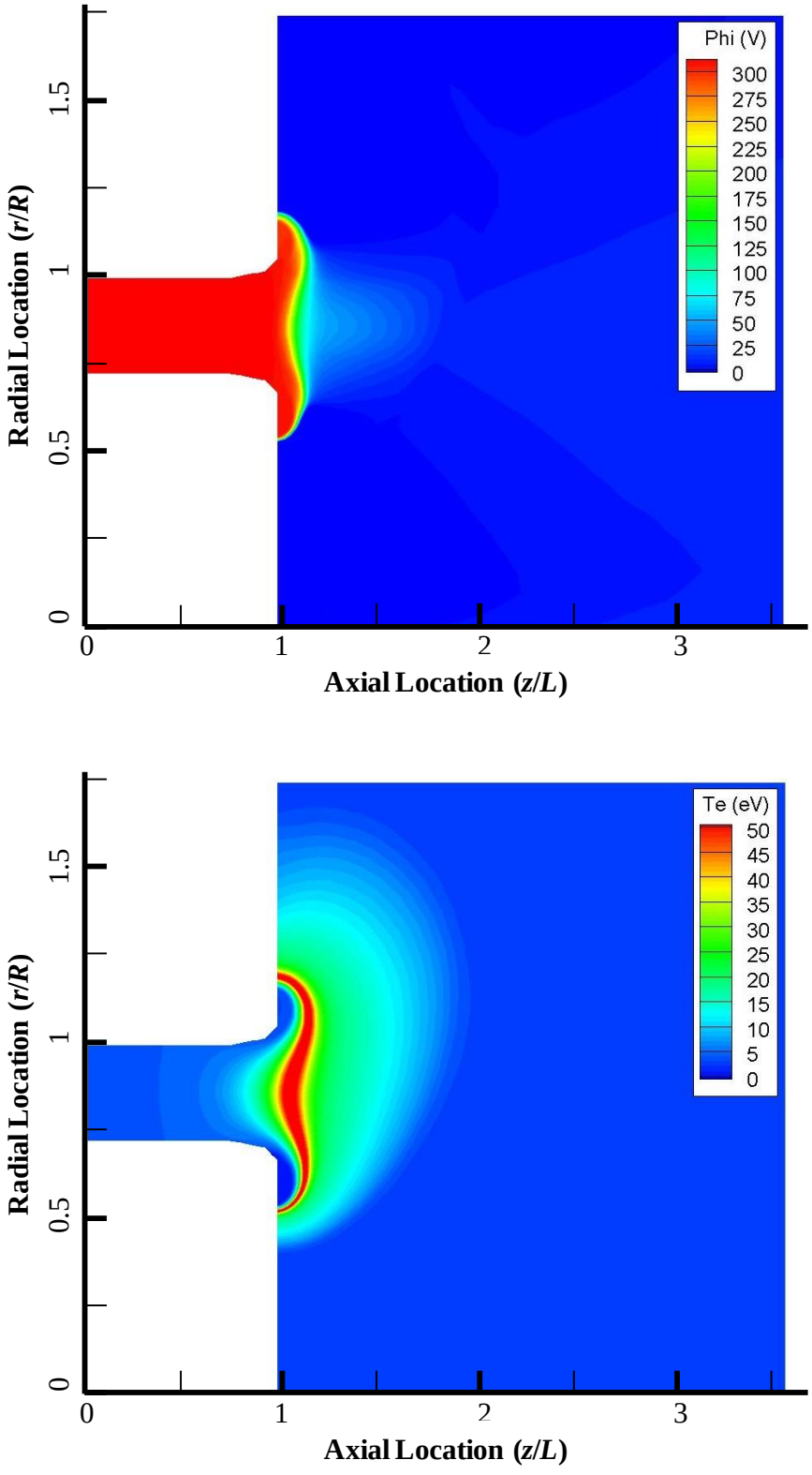

Figure 8.4-1. *Plasma potential (top) and electron temperature (bottom) contours from Hall2De simulations of the MaSMi-60 operating at 300 V and 1.4 A.*

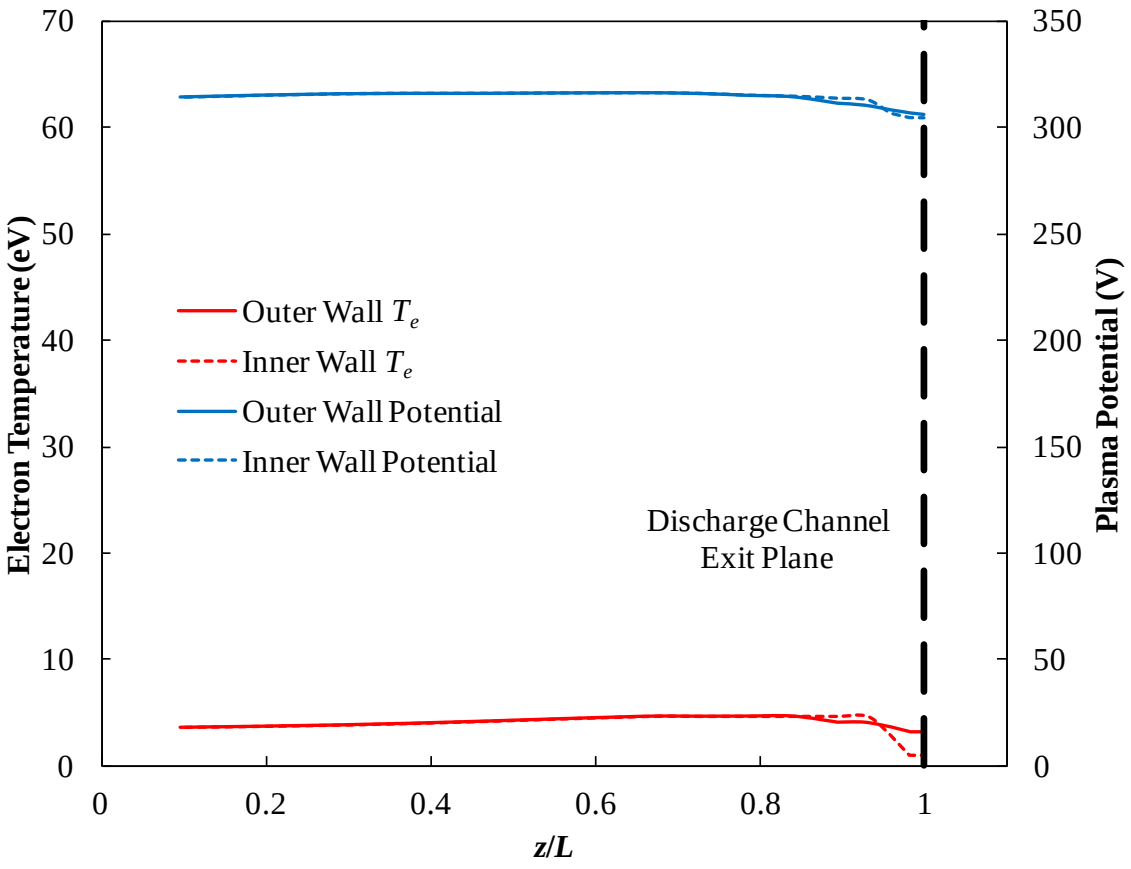

Figure 8.4-2. *Plasma potential (blue) and electron temperature (red) plotted along the outer and inner discharge channel walls from Hall2De simulations of the MaSMi-60 operating at 300 V and 1.4 A.*

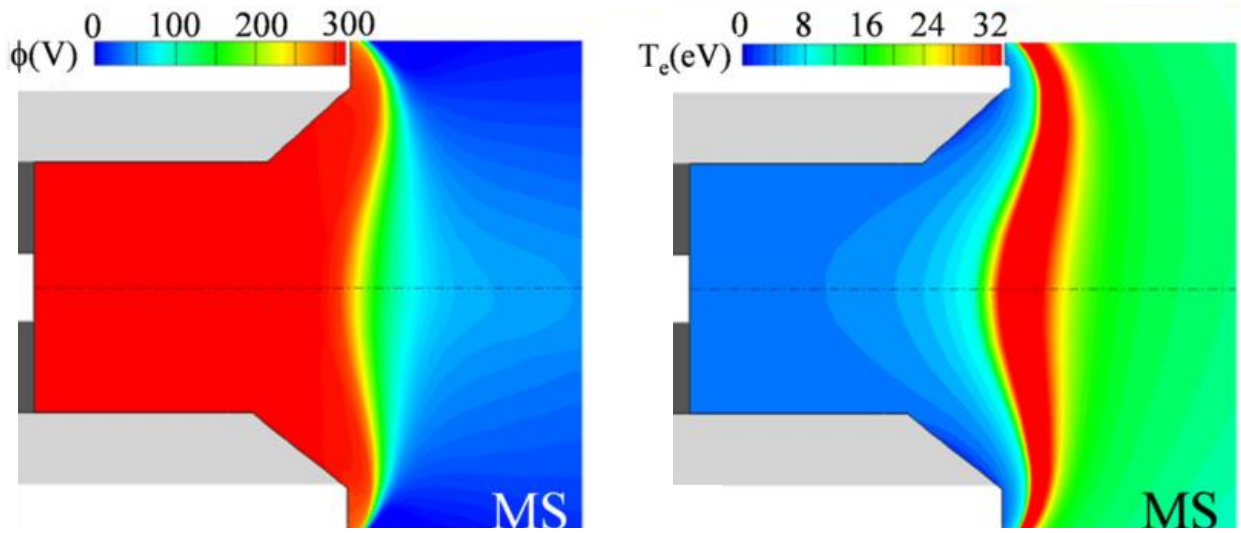

Figure 8.4-3. *Published plasma potential (left) and electron temperature (right) contour plots for the H6MS (predicted using Hall2De) [78].*

With the MaSMi-60 achieving the discharge channel plasma conditions required for magnetic shielding, the Hall2De-predicted channel wall erosion rate was examined. A detailed description of the erosion rate model in Hall2De is described in [121–123]. Briefly, Hall2De computes the total kinetic energy and flux of ions that bombard the channel surfaces and determines the erosion rate based on a model of the material sputtering yield [121–123]. It is typical in magnetically shielded thrusters that the ion energy is below the threshold energy for sputtering in which case the erosion rate is set to zero. The total kinetic energy is calculated as the sum of the energy gained by ions accelerated by radial components of the electric field and the energy gained by ions passing through the wall sheath. The Hall2De simulations predicted zero erosion along the entire length of the inner and outer discharge channel walls. This offers further evidence that the low-power MaSMi-60 successfully achieved an MS configuration.

8.4.2. Thruster Performance and Associated Physics

The primary contributors to the MaSMi-60's experimentally measured sub-29% anode efficiency were the mass utilization, current utilization, and beam divergence efficiencies, as

presented in Section 7.2. To better understand the physics causing these low efficiency values, the relevant parameters were extracted from the Hall2De simulation of the MaSMi-60 operating at 300 V and 1.4 A. The physics governing these parameters were then closely examined.

8.4.2.1. Physics Governing the MaSMi-60's Low Mass Utilization

The MaSMi-60's mass utilization predicted by Hall2De was approximately 56%, which nearly perfectly captures the demonstrated value of 58% at the selected operating condition. An examination of the MaSMi-60's neutral density profile predicted by Hall2De, shown in the upper cell of Figure 8.4-4, reveals that no significant drop in neutral density was predicted in the expected ionization zone; peak ionization is generally believed to be located in the mid-channel region. Additionally, no significant change in neutral density is seen along the expected path of the ion beam [27]. Instead, a high density of neutrals were predicted to flow beyond the exit plane and then diffuse gradually into the surrounding vacuum. This feature is in contrast to the nominal neutral density profile predicted for the H6MS, shown in the lower cell of Figure 8.4-4. A significant drop in neutral density is observed in the ionization zone, leading to high mass utilization and low neutral density along the expected path of the ion beam. These results suggest that a significant fraction of the neutrals injected into the MaSMi-60's discharge channel freely flow out of the thruster without being ionized, causing poor mass utilization.

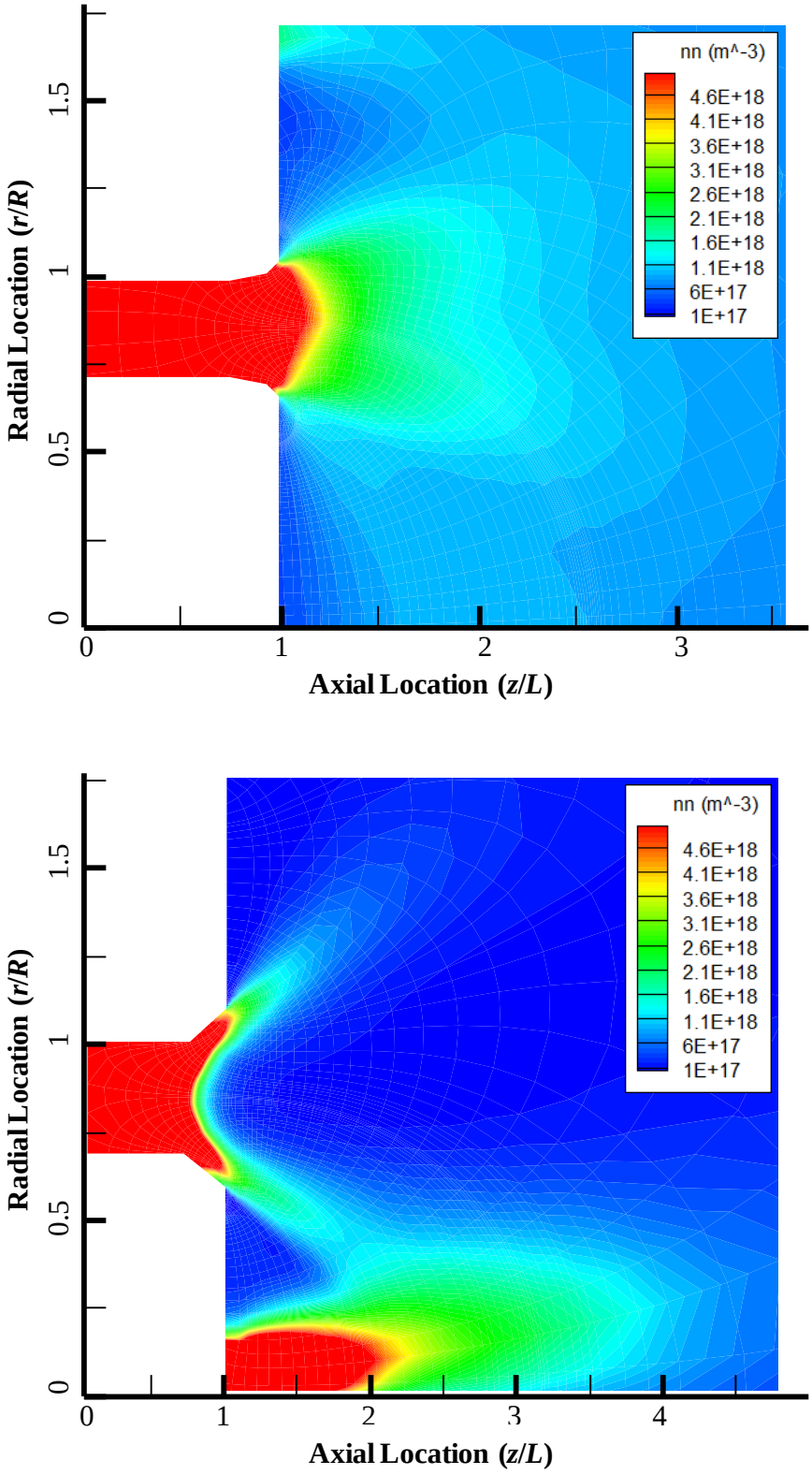

Figure 8.4-4. *Neutral density profiles for the MaSMi-60 (top) and H6MS (bottom).*

To further explore this phenomenon, a simplified phenomenological computational model was developed to examine the ionization fraction of neutrals leaving the MaSMi-60's anode, passing through the ionization and acceleration regions, and traveling downstream of the thruster exit. For this model, it was assumed that the neutral gas density will decrease with time due to ionization according to

$$\frac{dn_n}{dt} = -n_n n_e \langle \sigma_i v_e \rangle \qquad 8.4\text{-}1$$

where σ_i is the ionization cross section and $\langle \sigma_i v_e \rangle$ is the ionization reaction rate coefficient for Maxwellian electrons [3]. By definition, the flux of neutrals incident on the plasma (Γ_n) is

$$\Gamma_n = n_n v_n \, . \qquad 8.4\text{-}2$$

where v_n is the neutral particle velocity. Assuming $\Gamma_n \approx n_n v_{th}$, where v_{th} is the most probable value for the reduced axial component of the neutral velocity such that $v_n \approx v_{th} \approx dz/dt$ (an approximation that is discussed below) and applying Equation 8.4-2 to Equation 8.4-1 yields

$$\frac{d\Gamma_n}{\Gamma_n} \approx -\left(\frac{n_e \langle \sigma_i v_e \rangle}{v_{th}}\right) dz \qquad 8.4\text{-}3$$

dz is the axial distance along the channel. With the exception of v_{th}, all variables in Equation 8.4-3 depend on the electron temperature and/or electron density; because T_e and n_e are functions of axial location in the channel, these variables are also dependent on axial position. Equation 8.4-3 represents the fraction of unionized neutral particles as a function of axial position. The ionization mean free path (λ_i) appears in Equation 8.4-3 as the inverse of the term in parenthesis:

$$\lambda_i = \frac{v_{th}}{n_e \langle \sigma_i v_e \rangle} \, . \qquad 8.4\text{-}4$$

The ionized propellant fraction was calculated from the anode face to approximately 1.5 channel lengths downstream of the exit plane in 1 mm axial steps. The neutral particles entering the discharge channel were modeled to leave the anode surface in a cosine distribution. The

neutral population traveling along each angular trajectory from 0 to $\pi/2$ in increments of 1° were considered separately, yielding two important effects. First, fewer neutrals are on high-angle trajectories due to the initial cosine distribution of the gas injected into the channel from the anode. Second, and more importantly, the axial velocity of neutral particles on non-zero angle trajectories is reduced by the cosine of the angle. Because we are interested in the ionization of neutrals during their transit through the discharge channel, only the axial component of v_{th} is needed to determine the effective mean free path, λ_i. As can be seen from Equation 8.4-4, the reduced axial velocity of high-angle particles leads to a shorter ionization mean free path lengths and therefore an increased probability for ionization.

Neutrals that collide with a channel wall were assumed to be specularly reflected such that the particles' axial velocity would remain unchanged. No chemistry occurs between the neutral particles and the walls; therefore, this is a good assumption as it upholds the conservation of momentum in the discharge channel, which is a region of free molecular flow based on its high Knudsen number ($Kn = \lambda/b > 0.5$, where λ is the collision mean free path and the channel width is the characteristic length of the vessel containing the neutral gas). Note that this is in contrast to ions impacting the channel surfaces: this case generally leads to neutralization of the ions through an energy exchange between the particles and the walls, making a cosine distribution of the neutralized particles leaving the walls is a more appropriate assumption. Ion-wall collisions, which result in cosine distribution trajectories of newly neutralized particles from the channel surfaces, local changes in neutral population that affect the ionization fraction, etc., were not considered in this simplified ionization model; however, it is accounted for in Hall2De as specified above. It should be noted that Hall2De uses cosine distributions for neutral particles impacting the channel walls; due to the complexity of this aspect of the code and the desire for

maintaining a simplified, physics-informed model of propellant ionization, this feature was not incorporated into the ionization model. All unionized neutrals that leave the discharge channel exit plane on angular trajectories greater than 15° (the angle from the center of the anode surface to the discharge channel downstream tips) were assumed to remain unionized and be radially lost into the surrounding vacuum.

The fraction of unionized neutrals was calculated at each axial location from a modified version of Equation 8.4-3:

$$[\Gamma_n]_{ii+1} = \left[\Gamma_n\left(1 - \frac{n_e\langle\sigma_i v_e\rangle}{v_{th}}dz\right)\right]_{ii} = [\Gamma_n(1 - \lambda_i^{-1}dz)]_{ii} \qquad 8.4\text{-}5$$

where the subscript ii outside the square brackets represents the index of the axial step. As mentioned above, all parameters inside the brackets of the right-hand term depend on the electron temperature and/or electron density profiles and therefore vary with changes to axial position, except for v_{th}. The fraction of ionized propellant (f_i) was then calculated at each axial step by comparing the unionized neutral flux with the initial number of particles released from the anode ($\Gamma_{n,o}$):

$$[f_i]_{ii} = 1 - \frac{[\Gamma_n]_{ii}}{\Gamma_{n,0}} \; . \qquad 8.4\text{-}6$$

After neutral particles on all angular trajectories from 0 to π/2 were considered, the total ionization fraction was calculated by taking the ratio of the sum of all ionized particles on all angular trajectories divided by the total number of particles released from the anode:

$$f_i = 1 - \frac{1}{\Gamma_{n,0}}\left(\sum_{ii}[\Gamma_n]_{ii}\right) \; . \qquad 8.4\text{-}7$$

A total initial flux of 10^6 neutral particles was injected into the discharge channel from the anode. A neutral temperature of 500°C was assumed for the propellant entering the

discharge channel, leading to an initial neutral density of approximately 1.25×10^{18} m^{-3} at the anode flow rates and a most probable neutral thermal velocity of approximately 312 m/s based on the following equations:

$$n_n = 9.66 \times 10^{24} \left(\frac{P_T}{T_n}\right) \quad 8.4\text{-}8$$

$$v_{th} = \sqrt{\frac{2kT_n}{M}} \quad 8.4\text{-}9$$

where Equation 8.4-8 is a simplified version of the ideal gas law, $PV=NkT$, converted to pressure in units of Torr (P_T) [3]. The electron temperature and electron density profiles from the MaSMi-60's Hall2De simulation results were approximated using three fitted polynomials capturing the near-anode, thruster exit, and near-plume features of each profile. These approximate curve fits were then fed into the ionization model.

It is recognized that the maximum electron temperature of over 50 eV predicted by Hall2De for the MaSMi-60 operating at 300 V appears to be a significant over-prediction compared to published results in MS Hall thrusters, which show a peak T_e of between 30 eV to 35 eV at 300 V discharge voltages [1,39,78,114]. While this may be partially caused by a simplifying assumption in Hall2De that incorporates the electrons' azimuthal Hall current energy with the total electron temperature, efforts are currently underway to determine the magnitude of the contribution of this assumption to the peak T_e and to achieve more realistic T_e predictions. The MaSMi-60 produced an ion species mix very close to that of the H6MS (i.e. high multiply charged species beam content), suggesting that the peak electron temperature should be similar between the two thrusters [37]. Therefore, for the purposes of this ionization model, the MaSMi-60's electron temperature profile was linearly scaled to achieve a maximum temperature of approximately 32 eV (~10% of V_d), which falls in line with published experimental

measurements. This scaling of the electron temperature down and closer to the commonly found value of 10% of the discharge voltage matches well with the experimentally measured electron temperature in the near-plume region shown later in Figure 8.5-8. The experimentally measured species mix and electron temperature profile at a discharge voltage of 300 V validates the T_e scaling applied to the Hall2De results.

The results from the above ionization analysis are presented for the MaSMi-60 and H6MS (for comparative purposes) in the following paragraphs. The small size of the MaSMi-60's discharge channel and its effects on electron temperature and density is illustrated in Figure 8.4-5 where the electron temperature and electron density for the MaSMi-60 and H6MS used in the ionization model are plotted against axial position normalized to the MaSMi-60 discharge channel length. Comparing the predicted electron temperature curves for the two thrusters reveals that the MaSMi-60's profile is very narrow with a FWHM that spans approximately 0.2 $L_{MaSMi\text{-}60}$, suggesting there are very high axial gradients in the magnetic field that confine the hot electrons to an axially short region. By contrast, the H6MS's profile is much broader with a FWHM spanning approximately 1 $L_{MaSMi\text{-}60}$, showing the thruster's lower axial magnetic field gradients and wider band of hot electrons. As suggested by the Hall2De contour plots in Figure 8.4-1, the MaSMi-60's peak electron temperature (and maximum plasma potential gradient, which is not shown in Figure 8.4-5) are located downstream of the thruster's exit plane ($z/L_{MaSMi\text{-}60}$ of approximately 1.1); the position of these features in the H6MS are in the plane of its discharge channel exit. Both devices show a peak electron density at the approximate axial midpoint of their respective discharge channels and the density profiles have a similar overall shape. However, the MaSMi-60's density profile is approximately 2.5x narrower than that of the H6MS. Additionally, despite the MaSMi-60's higher initial density gradient, the H6MS is

predicted to achieve approximately 18% greater peak electron density and (expectedly, based on its larger discharge channel dimensions) maintain a high density over a longer axial length than the MaSMi-60. These results show that the plasma parameters primarily responsible for ionization of the injected propellant are more axially compressed and located further downstream (relative to the thruster's exit plane) in the MaSMi-60 compared to the H6MS.

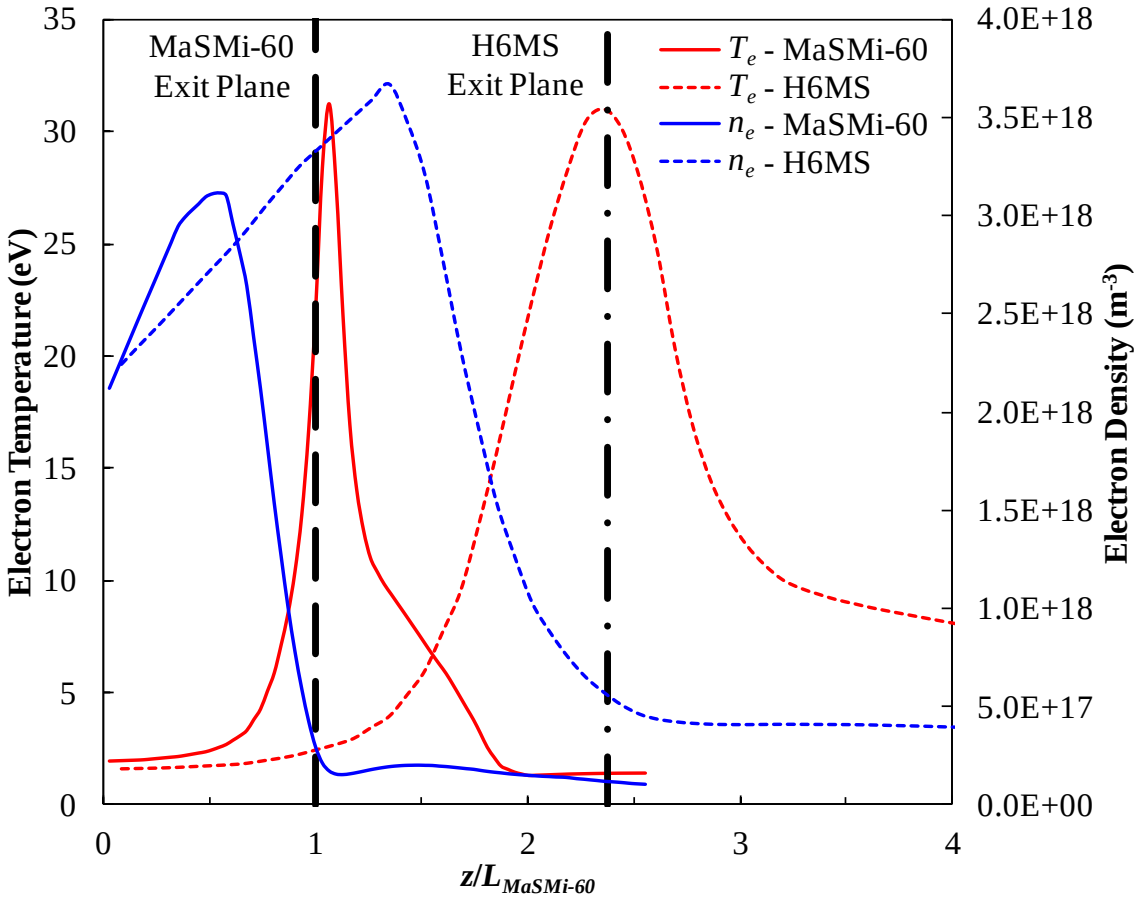

Figure 8.4-5. *Electron temperature (T_e) and electron density (n_e) predicted for the MaSMi-60 and H6MS as functions of axial position normalized to the MaSMi-60's discharge channel length.*

The effects of the MaSMi-60's narrow ionization region can be seen in Figure 8.4-6, which compares the ionization mean free path predicted for the MaSMi-60 and the H6MS as a function of axial distance, both normalized to each thrusters' respective discharge channel length.

The minimum predicted ionization mean free path for the MaSMi-60 is approximately 1.3 $L_{MaSMi\text{-}60}$ while the average value is approximately 1.5 $L_{MaSMi\text{-}60}$ before increasing sharply at a z/$L_{MaSMi\text{-}60}$ of around 1.4. In the case of the H6MS, the minimum predicted λ_i is considerably lower, approximately 0.3 L_{H6MS} with an average value of less than 0.5 L_{H6MS} until a z/L_{H6MS} of greater than approximately 1.5. Note that, despite the significantly different physical dimensions of the two thrusters' discharge channels, the H6MS's minimum λ_i is predicted to be approximately 50% smaller (in an absolute sense) than that of the MaSMi-60. These results suggest that the ionization mean free path of neutrals injected into the MaSMi-60's discharge channel is too long compared to the length of the ionization region generated by the thruster; a significant population of neutrals do not have enough time (i.e. axial distance coupled with particle velocity) to become ionized before they flow out of the discharge channel.

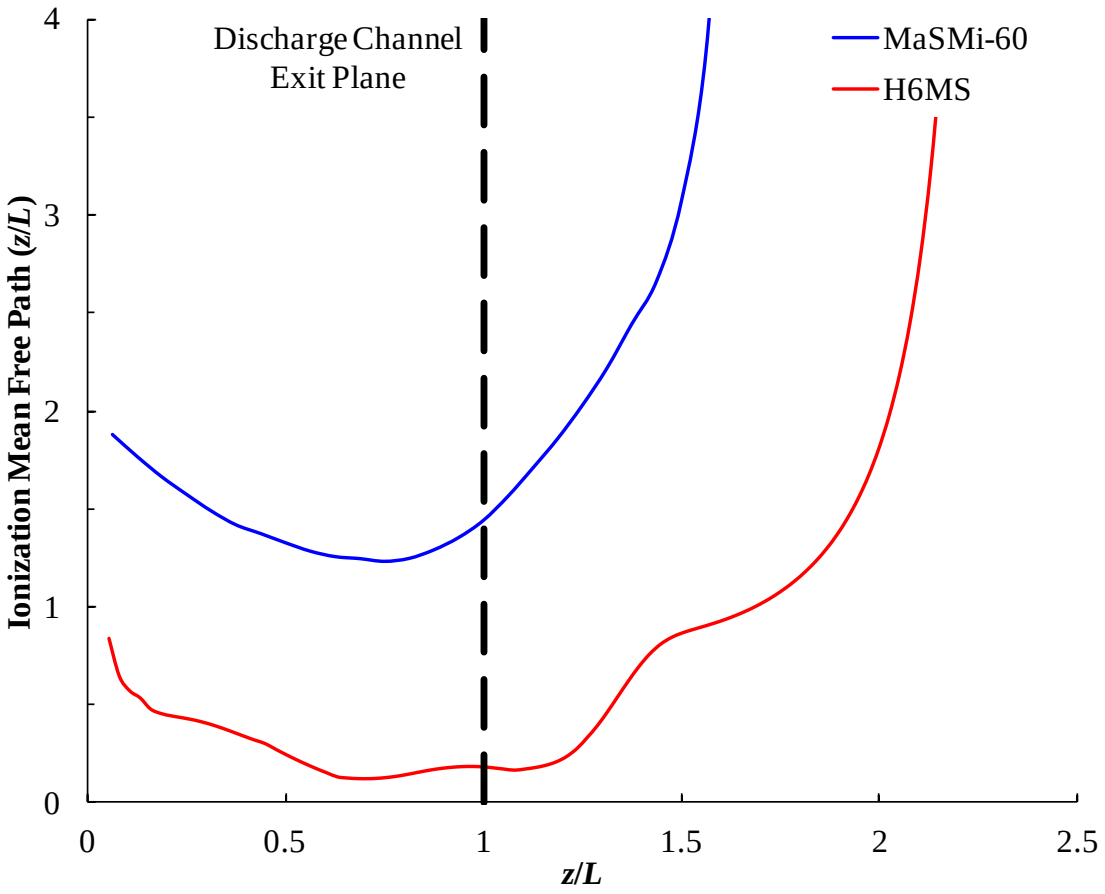

Figure 8.4-6. *Ionization mean free path predicted for the MaSMi-60 and H6MS as a function of axial position, both normalized to the respective thruster's discharge channel length.*

Figure 8.4-7 presents the spatial evolution of the ionization fraction for the MaSMi-60 and the H6MS as a function of axial distance normalized to the discharge channel length of the MaSMi-60. The maximum predicted value of the ionization fraction for the MaSMi-60 was approximately 61%, which matches well with the measured mass utilization efficiency of 58%. Approximately 25% of the MaSMi-60's ionization events were predicted to occur beyond the discharge channel exit; this result matches the Hall2De predictions shown in the upper cell of Figure 8.4-4, where a stream of unionized particles are predicted to exit the thruster. By contrast, a maximum ionization fraction of more than 99% was predicted by this simple model for the H6MS, matching well to its high mass utilization efficiency of approximately 98%. The

maximum ionization fraction for the H6MS was predicted to be achieved significantly upstream of the discharge channel exit and well upstream of the acceleration zone. The slope of the H6MS's ionization fraction profile is also notably steeper than that of the MaSM-60. This is likely a combination of thee effects: (1) the H6MS's longer channel length, which creates a wide band of high electron density and therefore increased probability of ionization in the near-anode and mid-channel ($z/L \sim 0.5$) regions; (2) the larger channel width (in conjunction with increased channel length), which allows neutrals on high-angle trajectories to travel further before encountering a wall and thereby increasing dwell time in the ionization zone (i.e. increasing the probability for ionization); (3) the H6MS's anode design, which may yield a more diffuse flow of neutrals into the channel compared to the MaSMi-60, thereby encouraging large angle trajectories for the injected propellant.

It is interesting to note that, despite the low electron temperatures (T_e <5 eV) predicted in the near-anode and mid-channel regions, a significant fraction of the propellant is predicted to be ionized in these regions: over 25% for the MaSMi-60 and nearly 75% for the H6MS. Conventionally, the ionization zone is believed to perform the majority of the ionization events over an axial length of approximately 1/2 the discharge channel length with the downstream limit located near the upstream edge of the acceleration region (the center of which is located at or near the peak electron temperature) [27]. The results from this ionization model presented in Figure 8.4-7, which shows strong agreement with measured values, suggests that the useful ionization zone extends much further upstream of the channel exit (nearly to the anode face) than conventionally thought with a near constant increase in ionization fraction until the maximum value is reached. This trend was predicted for both the MaSMi-60 and H6MS.

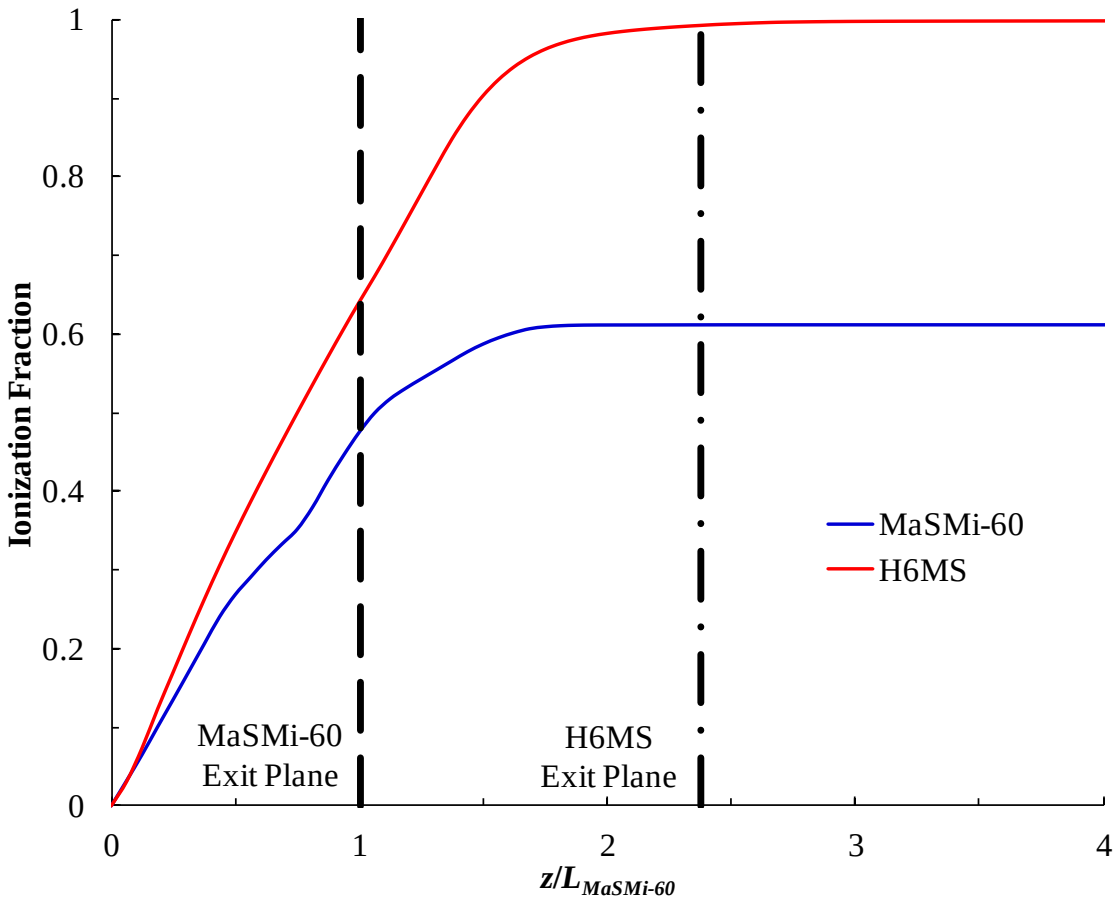

Figure 8.4-7. *Ionization fraction as functions of axial position normalized to the MaSMi-60's discharge channel length for the MaSMi-60 and H6MS.*

The results presented in Figures 8.4-5 through 8.4-7 suggest that ionization mean free path of the neutrals injected into the MaSMi-60's discharge channel is too long to enable more complete ionization of the propellant. This is likely caused by a combination of two features of the MaSMi-60: an insufficient discharge channel length and an anode design that results in relatively high axial velocities of the injected propellant. The H6MS was predicted to have a lower initial electron density gradient than the MaSMi-60; however, the high density region spanned a long axial distance (greater than the MaSMi-60's discharge channel length), driving the ionization mean free path to a low value. While higher initial electron densities were predicted for the MaSMi-60 compared to the H6MS, the narrow range of this high density region

caused by the short length of the discharge channel appears to facilitate long ionization mean free path lengths. Combined with a high axial velocity component of the neutral propellant, this results in injected neutral particles spending an insufficient amount of time in the ionization region to achieve high ionization fractions. Studies at Princeton Plasma Physics Laboratory (PPPL) examining the relationship between discharge channel length and propellant utilization, which show that propellant utilization increases with increasing discharge channel length (up to some limit), are in the published literature [124]. For a low-power Hall thruster on the same scale as the MaSMi-60 and operated at similar discharge voltage and propellant flow conditions, increases in propellant utilization of up to approximately 7% were observed for a 1.5x increase in discharge channel length and up to approximately 15% for a 2x increase in channel length [124]. In summary, the high ionization mean free path length in the MaSMi-60's ionization zone, likely caused by an insufficient discharge channel length and a sub-optimal anode design, appears to be the key physical mechanism that causes poor propellant utilization in the MaSMi-60. Incorporating a longer discharge channel and an anode that promotes high radial velocities for injected neutrals in future design iterations may therefore significantly increase the mass utilization efficiency of the MaSMi-60.

8.4.2.2. Physics Governing the MaSMi-60's Low Current Utilization

It is well understood that insufficient magnetic field strength can cause unfavorable oscillatory Hall thruster behavior and lead to increased electron streaming to the anode [125]. This is primarily caused by inadequate confinement of electrons in the high-field region due to enhanced charge carrier, and therefore electron, mobility across magnetic field lines [125]. The observations made in the MaSMi-60, including high discharge current oscillations combined with an inability to achieve a minimum discharge current versus magnetic field strength,

followed the abovementioned trends. This suggests that a higher-than-nominal electron current was flowing to the anode due to an insufficient magnetic field strength. Because excess electron current is included in the power supply's applied discharge current and has no contribution to increasing the ion beam current, it effectively decreases the current utilization efficiency by increasing the denominator of η_b, presented in Equation 3.1-8.

Further evidence supporting this theory was provided by Hall2De simulations of the MaSMi-60. The thruster's magnetic field strength was artificially increased by 20% while all other parameters, including the topology of the field and the operating condition of the thruster, were left unchanged. The result was an increase in the predicted current utilization efficiency by nearly 10%, supporting the claim that increasing the MaSMi-60's magnetic field strength would lead to improved thruster performance. Future iterations of the MaSMi Hall thruster will include a magnetic circuit that provides a higher magnetic field strength across the discharge channel than the current MaSMi-60, thereby improving electron confinement, reduce electron streaming, and providing higher current utilization efficiency.

8.4.2.3. Physics Governing the MaSMi-60's High Beam Divergence

Published results for the H6US (unshielded) and H6MS, as well as the MaSMi-40 and MaSMi-60, have shown that the application of magnetic shielding requires increased curvature of the magnetic field near the discharge channel downstream edges [1,37,74,79,102]. A result of this modification to the magnetic field is a downstream shift of the discharge plasma (i.e. the acceleration region); however, this appears to have a negligible effect on beam divergence [1,37,74,79,102]. In the case of the H6, a 5° increase in divergence half angle (from 15° to 20°) was observed when converting the thruster from the US configuration to the MS configuration [37]. By contrast, a beam divergence half angle of more than 30° was observed during testing of

the MaSMi-60. The MaSMi-60's higher beam divergence can be attributed to the thruster's over-shielded magnetic field topology, featuring tightly curved magnetic field lines near the exit plane, which leads to a larger downstream shift of the acceleration zone (relative to the channel exit plane) compared to the H6MS.

The MaSMi-60's over-shielded field topology (discussed in Chapter 7) exhibits considerably more curvature downstream of the discharge channel edges than the H6MS's field topology. This can be seen by comparing the electron temperature contours, which closely follow the magnetic field lines, in Figures 8.4-1 (upper cell) and 8.4-3 (right cell). As discussed in Chapter 3, the applied electric field points perpendicular to the magnetic field and is directed away from the anode. Therefore, an increase in magnetic field curvature causes an increase in the off-axis angle of the electric field vector. The concave field structure along the channel centerline has a focusing (i.e. lensing) effect on the beam ions; the electric field vectors are forced to point towards the channel centerline, causing a convergence of accelerated ions into a coherent beam. The convex field structures downstream of the discharge channel edges in the magnetically shielded thrusters, however, cause increased angular divergence of the beam because the electric field vectors point away from the channel centerline, leading to ion acceleration away from the channel centerline. Because the MaSMi-60 generates greater field curvature in the regions downstream of the discharge channel edges compared to the H6MS, higher angular beam divergence is expected. Through careful redesign of the magnetic circuit to maintain a magnetically shielded field topology while reducing the over-shielded features of the field structure, the low beam divergence efficiency demonstrated by the MaSMi-60 can likely be improved.

A result of the MaSMi-60's over-shielded MS field topology is the relatively large downstream shift in the acceleration region. Because of the extreme curvature of the magnetic field around the discharge channel downstream edges, the penetration depth of the magnetic field lines into the channel is limited [79]. This forces the acceleration zone, which is defined by the steep near-exit region drop in plasma potential and closely tied to the field structure, further downstream of the exit plane than is observed in more optimally shielded Hall thrusters such as the H6MS. The downstream shift in the discharge plasma is therefore a byproduct of the magnetic field topology and not a contributor to the increased beam divergence. Figure 8.4-8 presents the plasma potential for the MaSMi-60 and H6MS as a function of axial distance normalized to each thrusters' respective channel length. This plot shows that the MaSMi-60's acceleration region begins approximately 20% further downstream than that of the H6MS.

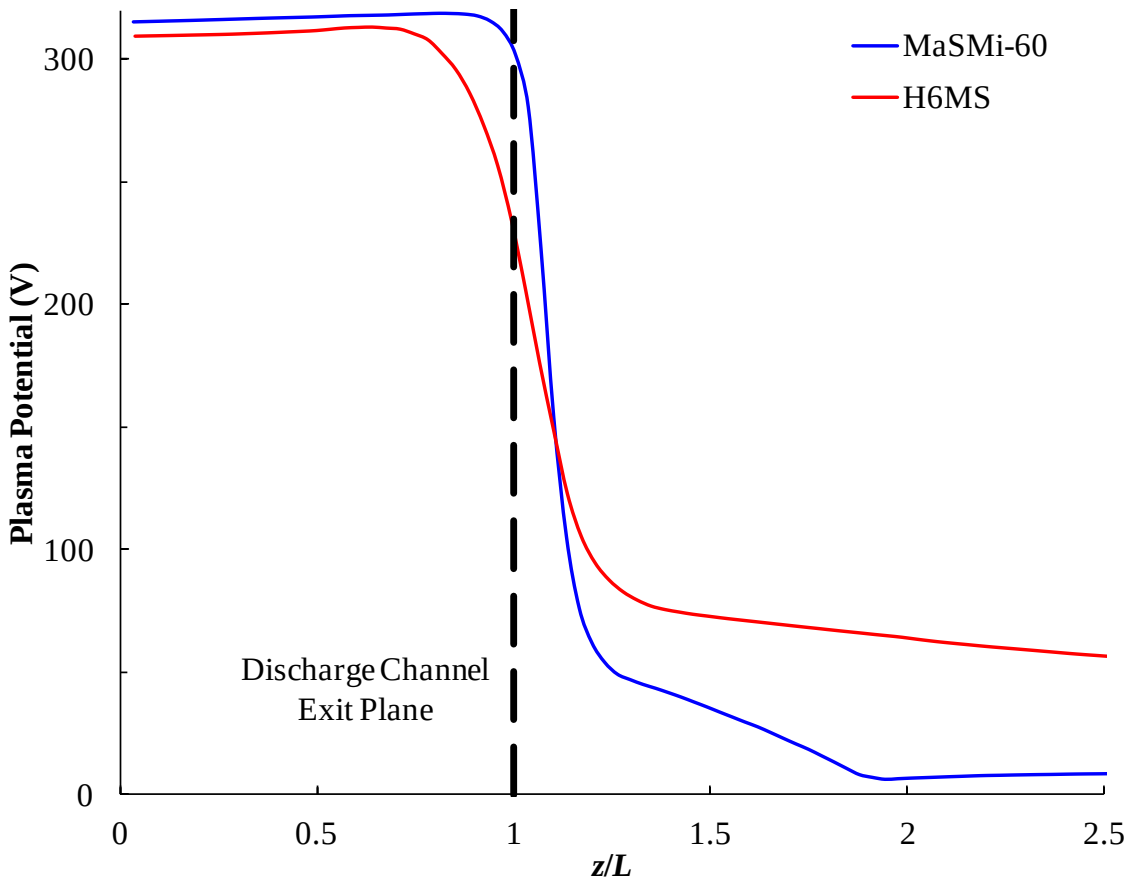

Figure 8.4-8. *Plasma potential for the MaSMi-60 and H6MS from Hall2De simulations as a function of axial position normalized to the each thruster's respective discharge channel length.*

This feature of the MaSMi-60 and other MS devices in no way related to the collimating effect of the discharge channel walls observed in unshielded Hall thrusters. Because the discharge plasma in unshielded devices is generally located at or just upstream of the thruster exit plane and is in contact with the channel walls, the channel surfaces can reduce angular beam divergence by intercepting ions accelerated at high off-axis angles. This effect was observed in the BHT-1500 when it was operated in what Azziz defined as a "collimated" mode, characterized by a narrowing of the plasma beam compared to nominal "jet" mode operation [100]. It was hypothesized that the ionization zone (and therefore, effectively, the acceleration zone) moved further upstream than nominal due to temperature-related changes in the BHT-1500's magnetic

field topology, thereby causing a portion of the beam to be lost to the walls and a resulting collimation of the beam [100]. By the same token, operation of the BHT-1500 in the nominal "jet" mode operation yielded greater beam divergence than the "collimated" mode due to a lack of channel wall collimation. While this may lead to the conclusion that a downstream shift in the ionization and acceleration regions directly correlates to increased beam divergence in Hall thrusters, the ion focusing effects generated by the curvature of a magnetically shielded field topology, in addition to the plethora of published data on MS devices, refutes this argument. The downstream shift in the discharge plasma is an inherent feature of state-of-the-art MS Hall thruster designs; however, improvements to the MaSMi-60's magnetic circuit to eliminate the over-shielded topology should reduce the magnitude of the downstream plasma shift relative to the thruster exit.

8.5. Results Verification

In the past, probes inserted into the discharge have been used to verify the results from Hall2De [78,114,119]. The probes, which were either injected into the discharge channel plasma using fast-drive probe stages or embedded in the discharge channel walls, provided measurements of electron temperature and discharge plasma potential. This has been common practice in high-power Hall thrusters where the discharge channel width is significantly larger than in low-power devices. It was generally assumed that if the probe did not significantly disturbed the plasma, accurate measurements of the plasma properties could be obtained. However, a recent study by Jorns *et al* using the unshielded H6 clearly demonstrated that invasive probe measurements significantly perturb the discharge plasma despite the short transit time of the probe inside the discharge channel [126]. When the invasive probe crossed the approximate peak magnetic field location, the global structure of the near-exit plume changed

significantly and was characterized by a ~0.125 z/L downstream shift in the plasma [126]. The magnitude of the perturbations to the plasma was observed to be less pronounced at lower operating voltages and currents, with the perturbations being more dependent on discharge voltage [126]. Note that wall probe measurements or fast-scan probe measurements taken downstream of the exit plane have not been shown to significantly affect the plasma properties.

In the case of low-power Hall thrusters, invasive probe measurements are even more challenging due to small channel dimensions. Furthermore, greater degrees of perturbation of the plasma would occur based on the relative sizes of the injected probe, the discharge channel, and the discharge plasma. In light of the limited discharge plasma measurements inside and near to the channel exit of the MaSMi-60, the fidelity of the Hall2De simulations was addressed as follows. First, a sensitivity study was performed to demonstrate that the Hall2De results on the effectiveness of magnetic shielding were insensitive to variations in the location and shape of the anomalous collision frequency profile inside the discharge channel. Second, electron temperature measurement were taken in the near-plume region downstream of the discharge channel exit and compared with the values computed by Hall2De. These results are described in the following sections.

8.5.1. Sensitivity Study Results

A "nominal" profile of the anomalous collision frequency in the MaSMi-60 was first employed and was based on previous investigations of Hall thrusters for which the minimum value was located just downstream of the discharge channel exit (~1.05 L). To confirm that the Hall2De solutions were insensitive to (i.e. not heavily dependent on) the shape and location of the anomalous resistivity profile inside of the discharge channel, several additional Hall2De simulations were completed using the MaSMi-60 geometry. The first set of simulations checked

the solution's sensitivity to changes in the shape of the anomalous collision frequency profile upstream of the discharge channel exit while maintaining the global profile's axial location. Figure 8.5-1 shows a comparison of the nominal and altered collision frequency profiles along with the electron gyrofrequency and the electron-neutral and electron-ion frequencies; the resulting changes to the plasma potential and electron temperature along the channel centerline are shown in Figure 8.5-2. Figure 8.5-3 presents the predicted electron temperature and plasma potential along the inner and outer channel walls. A slight upstream shift in the electron temperature profile was observed for the altered collision profile, along with an associated increase in the peak temperature by approximately 10%. The plasma potential's profile for the modified anomalous collision frequency profile was also largely unchanged relative to the nominal case; only a slight upstream shift and a slight decrease in magnitude downstream of the channel exit was observed. The electron temperature was predicted to remain below 5 eV while a near constant plasma potential near that of the discharge voltage was predicted along the full channel length. A comparison of these results to those presented in Figure 8.4-2 further demonstrates the lack of the solution's sensitivity to the applied changes to the collision frequency profile.

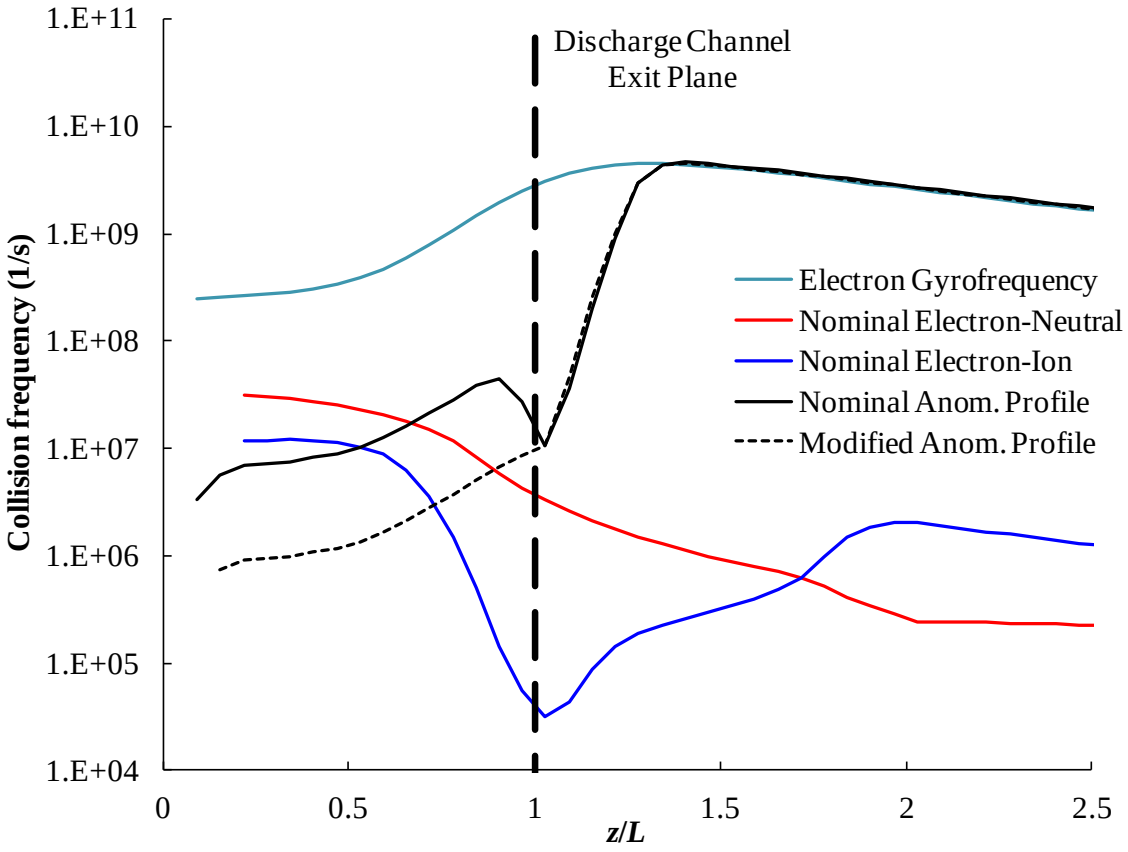

Figure 8.5-1. *Comparison of the nominal and modified anomalous resistivity profiles with the relevant collision frequencies for the MaSMi-60.*

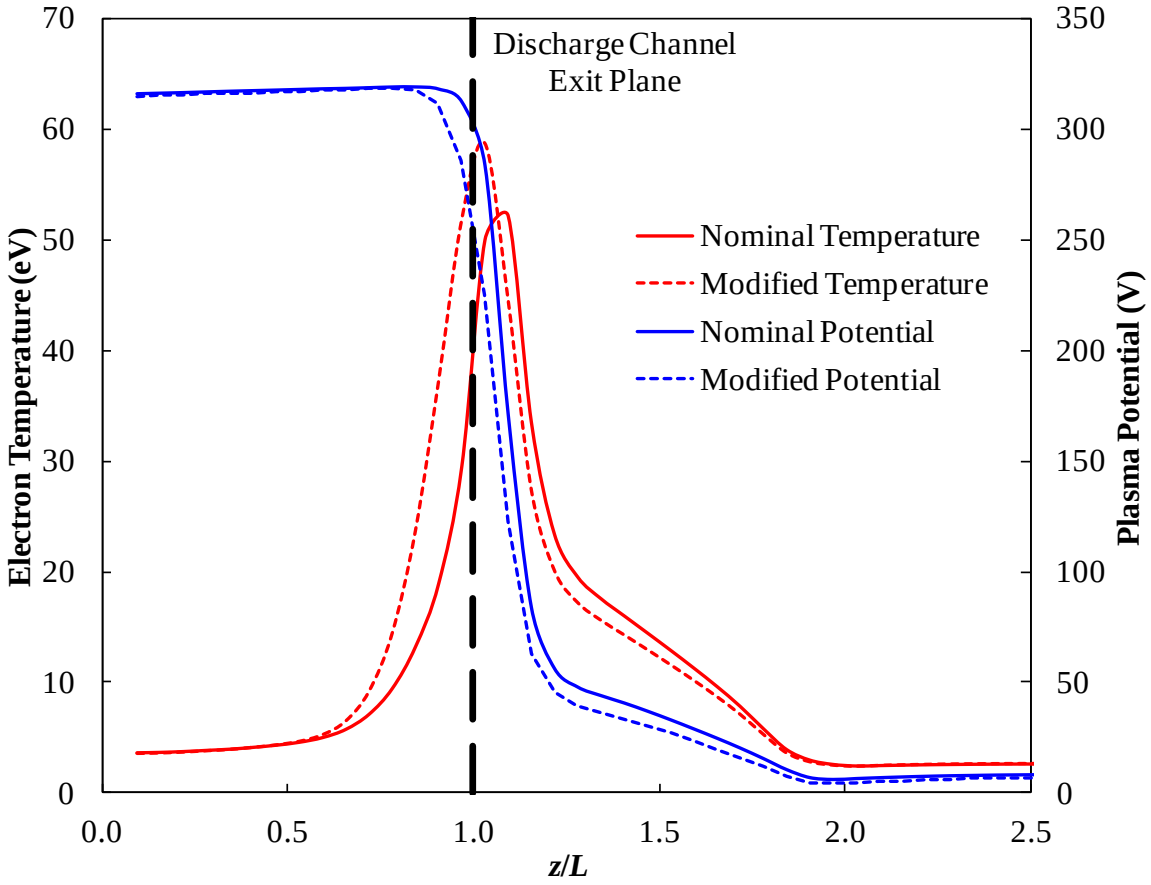

Figure 8.5-2. *Comparison of the electron temperature and plasma potential profiles along the channel centerline based on the nominal and modified anomalous collision frequency profile for the MaSMi-60.*

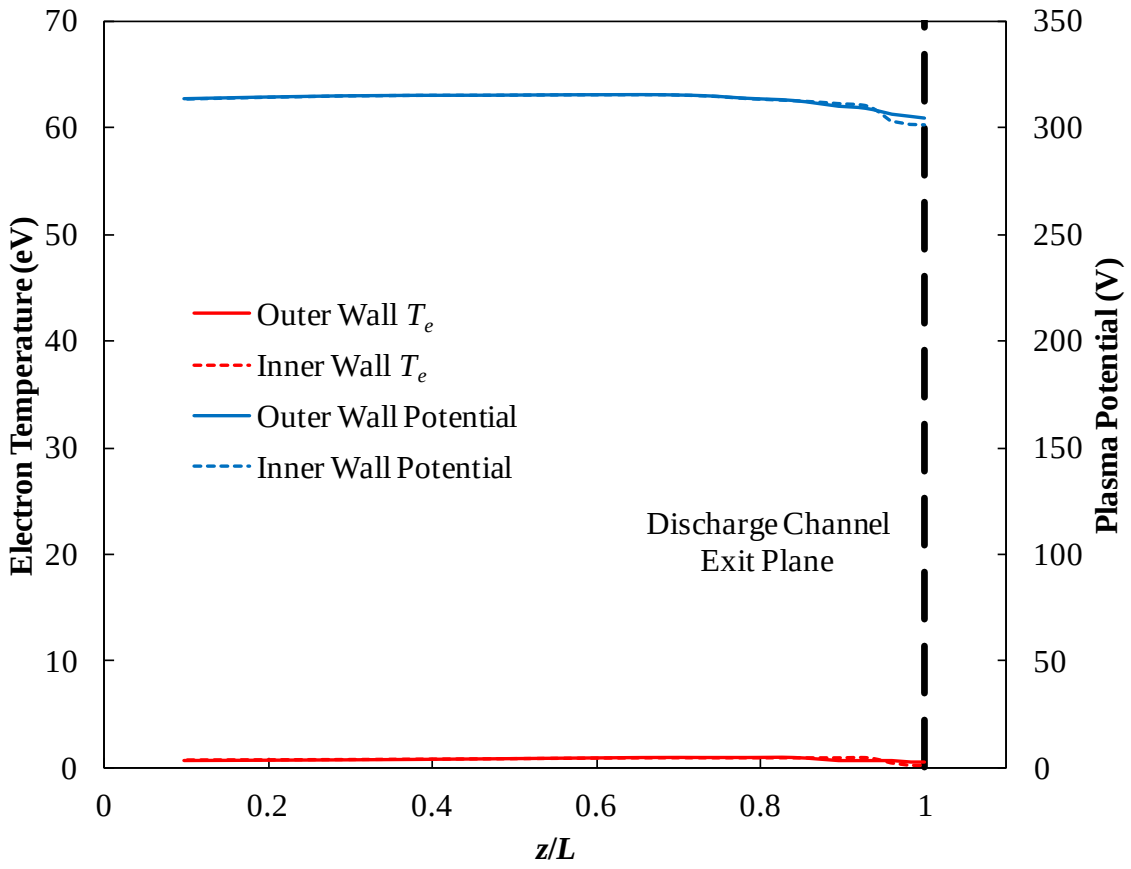

Figure 8.5-3. *Plasma potential (blue) and electron temperature (red) plotted along the outer and inner discharge channel walls from Hall2De simulations of the MaSMi-60 operating at 300 V and 1.4 A with the modified anomalous collision frequency profile.*

The second set of simulations were completed to demonstrate that reasonable axial shifts in the location of the anomalous collision frequency profile relative to the discharge channel exit (<20% of the discharge channel length) would have a minimal impact on the converged solution. The nominal collision frequency profile's central minimum was shifted upstream to approximately 0.8 L and downstream to approximately 1.2 L. During the execution of the simulations, the magnitudes of the profiles' various components were modified to keep the final portion of the profile approximately equal to the electron gyrofrequency while attaining the measured performance values for the MaSMi-60. This resulted in a decrease of the contributions

of the anomalous collision frequency to electron transport inside the discharge channel for the upstream-shifted profile compared to the nominal case, suggesting that classical transport mechanisms were sufficient to maintain the discharge plasma. By contrast, a slight increase in the contributions of the anomalous resistivity profile for the downstream-shifted case relative to the nominal profile was observed, suggesting the need for a greater contribution of non-classical transport mechanisms to maintain the discharge. Figure 8.5-4 shows the nominal, upstream-shifted, and downstream-shifted anomalous collision frequency profiles along with the other relevant collision frequencies. The electron temperature and plasma potential profiles along the channel centerline associated with the nominal and shifted collision profiles are presented in Figure 8.5-5. The electron temperature and plasma potential profiles along the discharge channel walls for the upstream- and downstream-shifted collision frequency profiles are plotted in Figures 8.5-6 and 8.5-7, respectively. Axially shifting the collision frequency profiles had a minimal impact on the magnitude of the electron temperature and plasma potential; the global trends of each set of profiles were nearly identical with less than 4% difference between the three cases. However, a notable axial shift was observed in the profiles; this shift was in direct proportion to the associated anomalous collision frequency profiles' shift. Despite these changes to the anomalous collision frequency profile's axial location, the electron temperature and plasma potential along the channel walls were predicted to remain below 5 eV and at approximately 300 V, respectively. These results agree well with those presented in Figure 8.4-2, showing that the simulation results were insensitive to the applied shifts in the anomalous collision frequency profile.

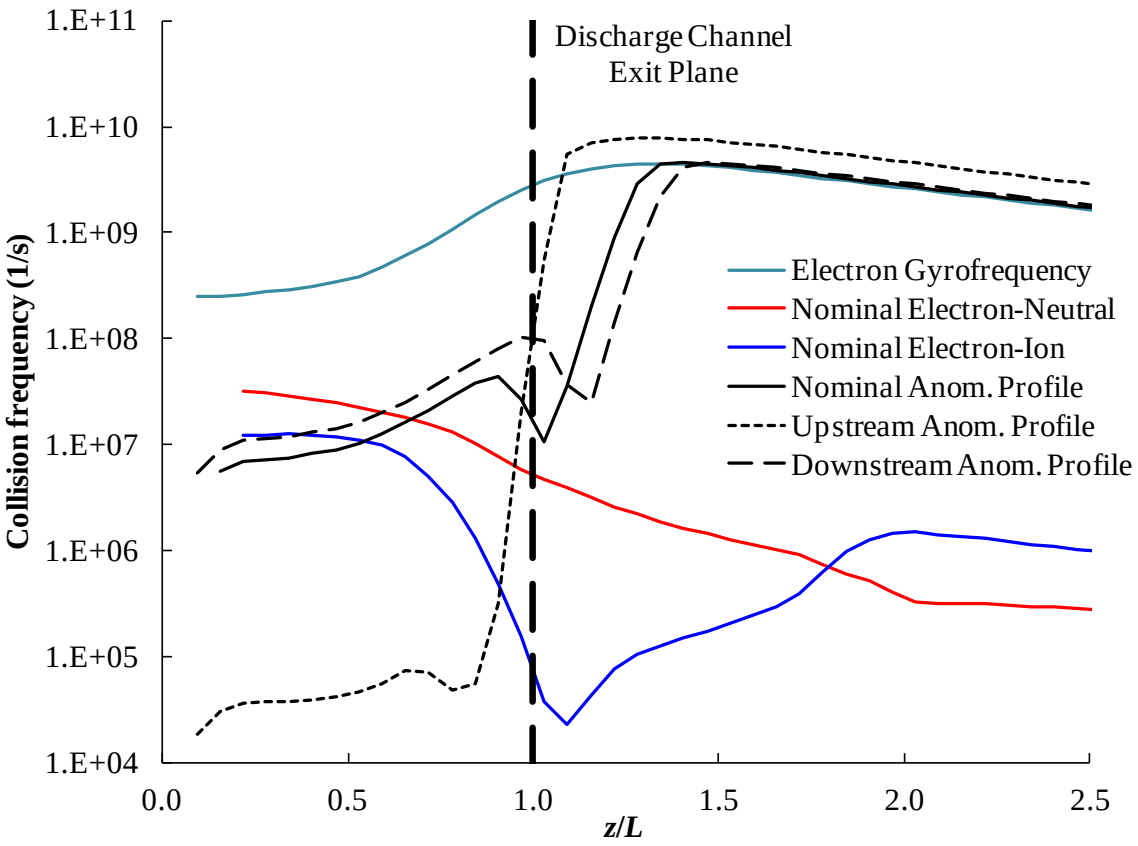

Figure 8.5-4. *Comparison of the nominal, upstream-shifted, and downstream-shifted anomalous collision frequency profiles with the relevant collision frequencies for the MaSMi-60.*

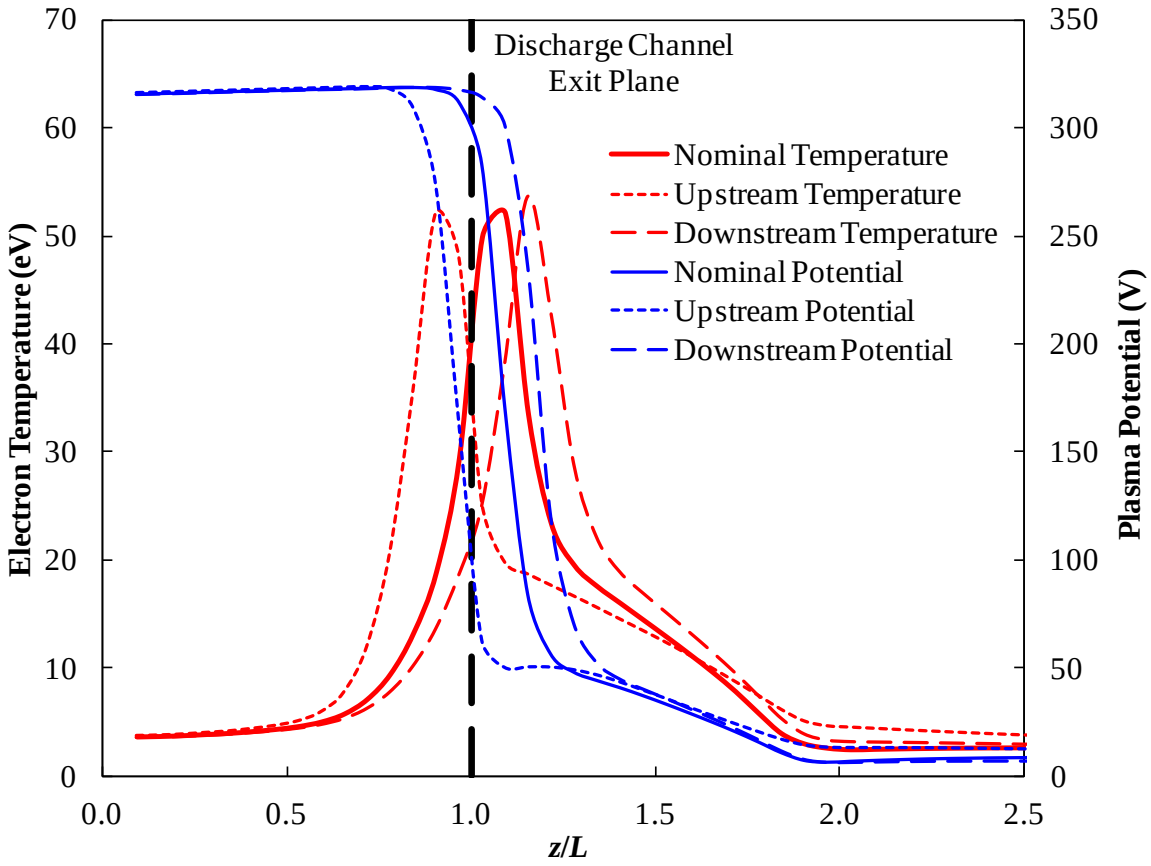

Figure 8.5-5. *Comparison of the electron temperature and plasma potential profiles along the channel centerline based on the nominal, upstream-shifted, and downstream-shifted anomalous collision frequency profile for the MaSMi-60.*

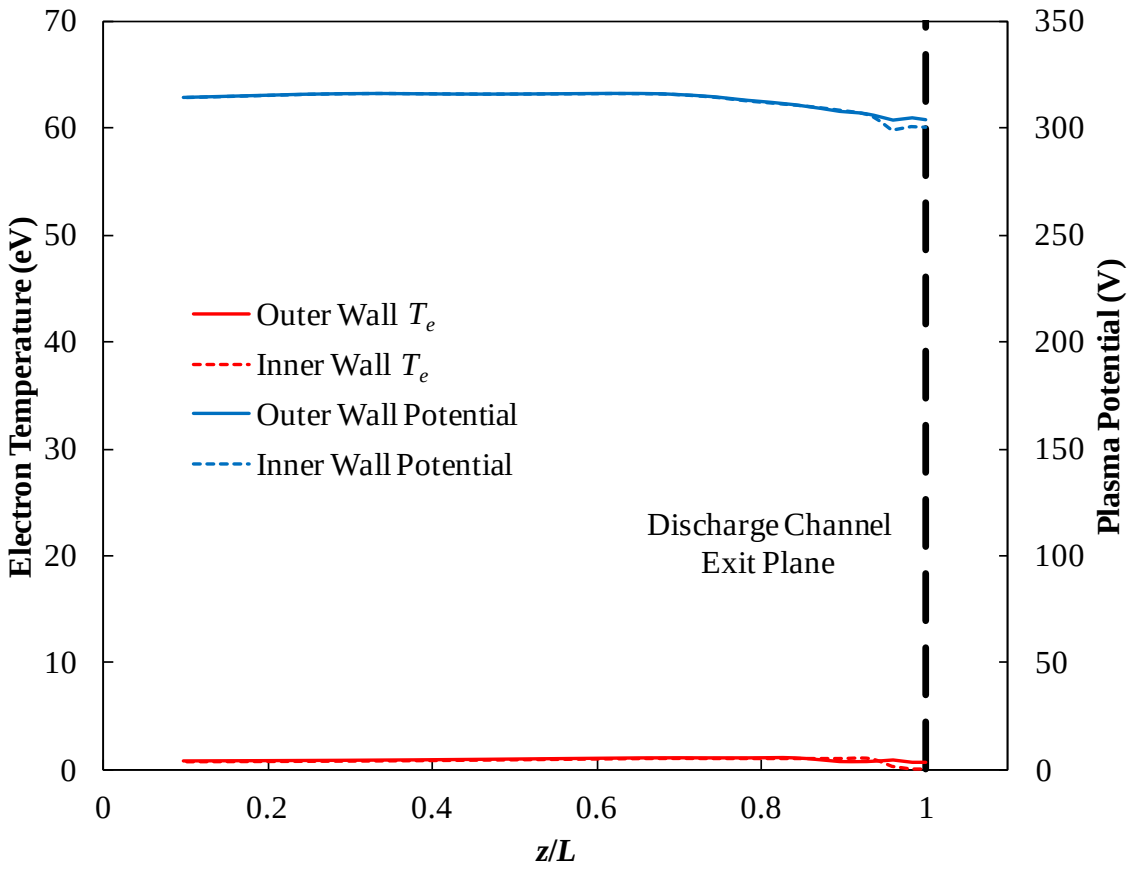

Figure 8.5-6. *Plasma potential (blue) and electron temperature (red) plotted along the outer and inner discharge channel walls from Hall2De simulations of the MaSMi-60 operating at 300 V and 1.4 A with the upstream-shifted anomalous collision frequency profile.*

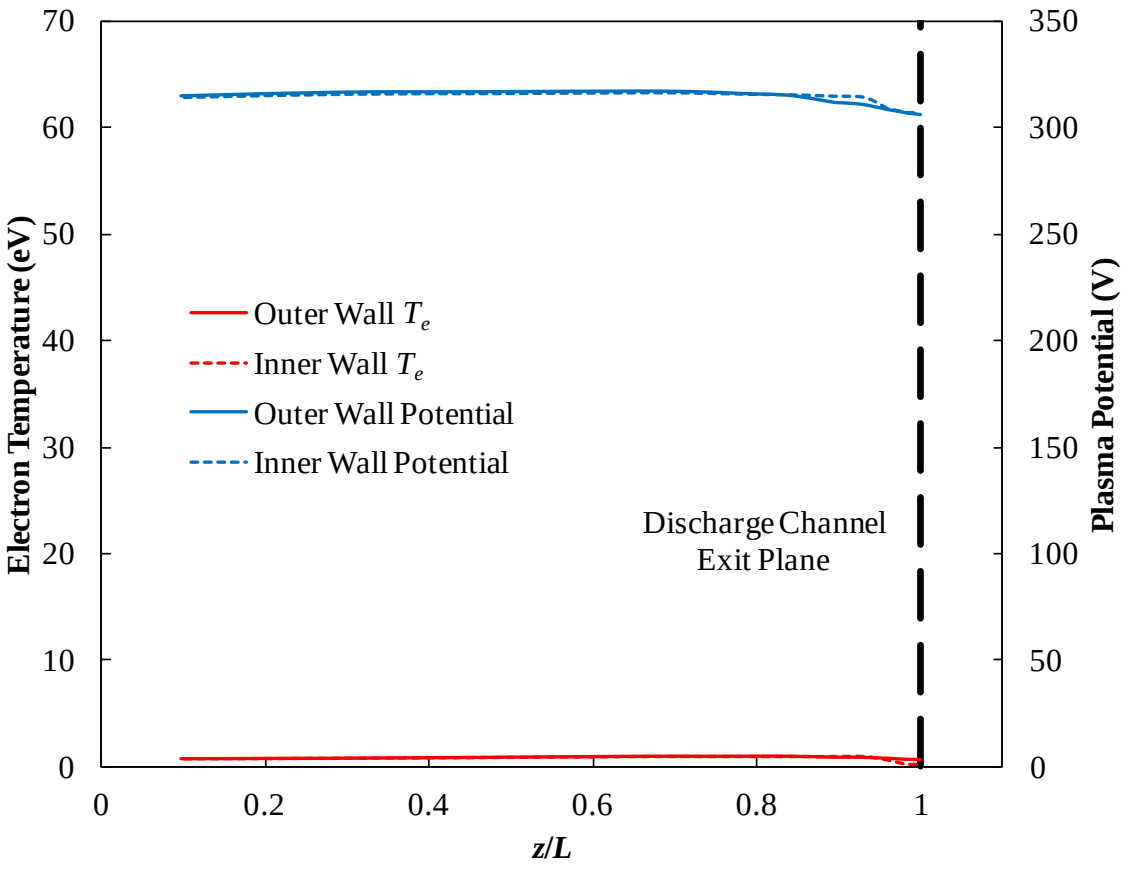

Figure 8.5-7. *Plasma potential (blue) and electron temperature (red) plotted along the outer and inner discharge channel walls from Hall2De simulations of the MaSMi-60 operating at 300 V and 1.4 A with the downstream-shifted anomalous collision frequency profile.*

No significant changes were observed in the Hall2De-predicted plasma properties required for magnetic shielding of the MaSMi-60, despite changes to the simulation's anomalous collision frequency profile shape and location. This confirms a lack of sensitivity to both the shape of the profile inside the discharge channel, corresponding to the extent of classical and non-classical electron transport mechanisms to maintain the plasma discharge, and the axial location of the profile's central minimum, corresponding to the location of the discharge plasma's ionization and acceleration zones. Therefore, the applied changes to the location of the discharge plasma had a negligible impact on the magnetic shielding of the MaSMi-60. This suggests that the uncertainty in the exact location of the plasma's ionization and acceleration regions does not

impact the thruster's ability to achieve and maintain a magnetically shielded configuration. These results show that changes to the primary variable in Hall2De (i.e. the anomalous collision frequency profile) had a negligible effect on the prediction of the magnetic shielding parameters (T_e and Φ at the channel surfaces) near and the erosion rates of the channel walls. For more conclusive validation of Hall2De, however, experimental probe measurements of the electron temperature and plasma were compared to the simulation results.

8.5.2. Near Exit Plane Plasma Measurement Results

In an effort to experimentally validate the Hall2De results for the MaSMi-60, plasma measurements were taken in the near exit region of the thruster to compare to the simulations. A Langmuir probe scanned through the near-field plume plasma yielded values for the electron temperature and plasma potential just downstream of the thruster exit. Electron temperature measurement results are plotted in Figure 8.5-8 against both the unmodified nominal Hall2De simulation results and the nominal Hall2De simulation results scaled to a peak electron temperature of approximately 32 eV (discussed in Section 8.4.2.1). Based on the measurements, the scaled simulation T_e profile appears to be a much more accurate representation of the actual electron temperature profile. Figure 8.5-9 presents the measured plasma potential data compared to the Hall2de-predicted potential profile. Overall, good agreement was observed between the measurements and simulation, suggesting that Hall2De was able to capture the key physics and plasma parameters of the MaSMi-60. The Hall2De plasma model was therefore considered sufficiently validated, allowing for the physics-based conclusions regarding the discharge plasma's behavior and the quality of the MaSMi-60's magnetic shielding to be drawn above.

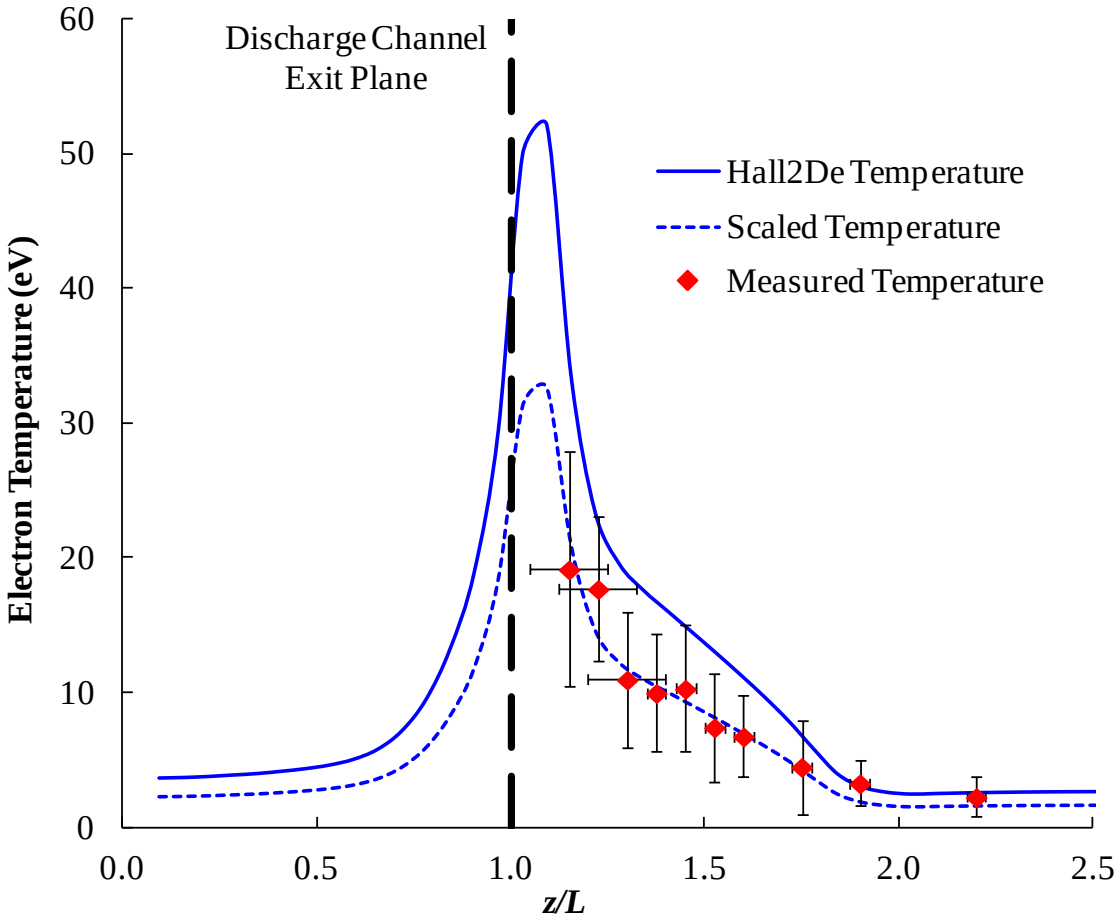

Figure 8.5-8. *Comparison of experimental measurement, the nominal Hall2De simulation, and the scaled Hall2De simulation of electron temperature along the channel centerline for the MaSMi-60 operating at 300 V and 1.4 A.*

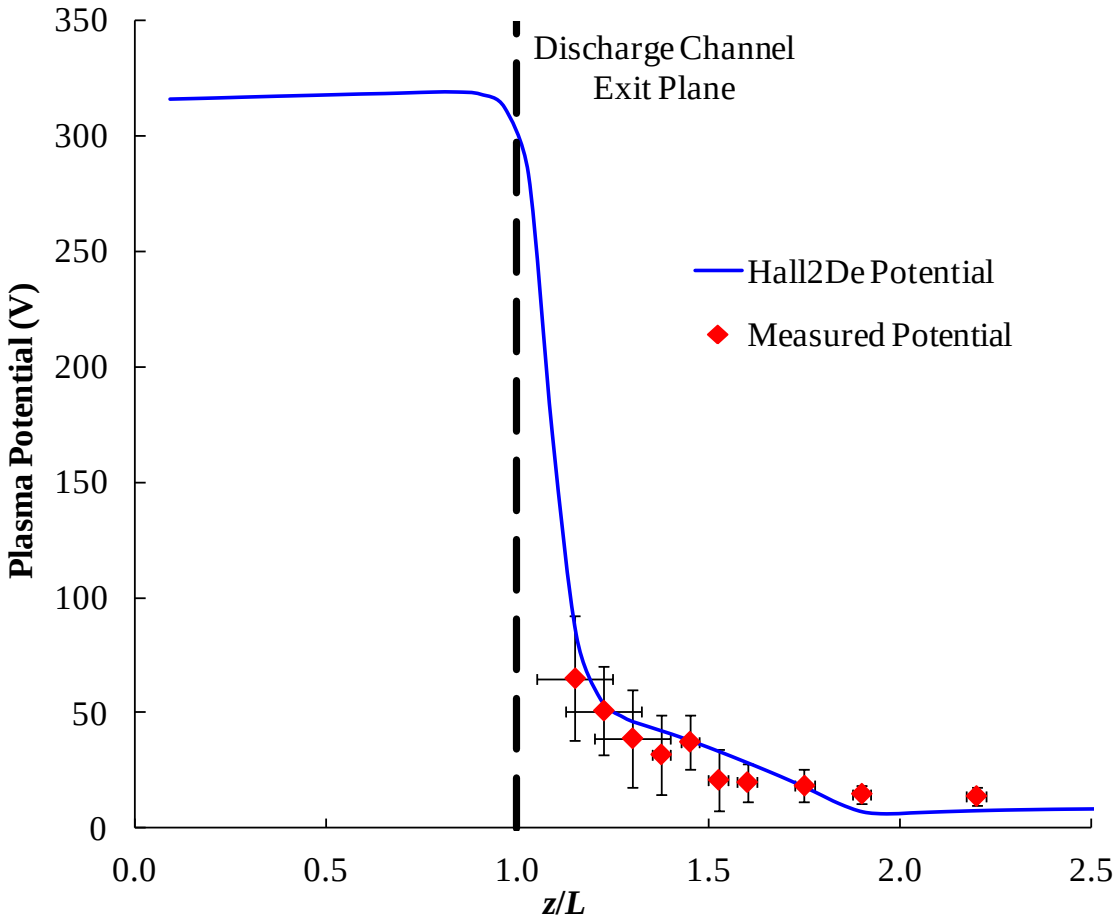

Figure 8.5-9. *Comparison of experimental measurements and the nominal Hall2De simulation of the plasma potential along the channel centerline for the MaSMi-60 operating at 300 V and 1.4 A.*

8.6. Plasma Physics and Behaviors of Low-Power MS Hall Thrusters

While more work is required to make conclusive arguments about the unique plasma physics of low-power magnetically shielded Hall thrusters, the observations made during the testing of the MaSMi-60 suggest possible trends that may be seen in future miniature MS devices. The global behavior of the discharge plasma produced by the MaSMi-60 followed well understood trends established by high-power MS Hall thrusters. The two fundamental plasma parameters governing magnetic shielding (low T_e and near constant $\Phi \sim V_d$ along the channel surfaces) in high-power devices were demonstrated to be obtainable at the low-power thruster

scale. Hall2De predicted sub-5 eV electron temperatures and nearly constant plasma potentials equal to that of the discharge voltage across the channel and along the channel surfaces of the MaSMi-60, suggesting that it reproduced the necessary conditions for magnetic shielding [78]. According to measurements taken in the near-plume region of the H6MS and the MaSMi-60, the application of an MS field topology appears to generate similar electron temperatures profiles at the same discharge voltage regardless of thruster discharge power. This is supported by the similar ion species mix measured in the plasma beam observed in both high- and low-power MS Hall thrusters, which was biased towards higher multiply charged ions than in unshielded devices. Additionally, the application of a shielded field topology has been shown to cause an increase in angular divergence of the plasma beam due to the increased magnetic field curvature near the discharge channel edges. The associated downstream shift in the discharge plasma (specifically, the acceleration zone) was shown to have a negligible effect on angular divergence. These trends were present regardless of thruster power level.

Despite these similarities, certain key aspects of the performance and plasma behaviors were unique to the MaSMi-60. It should be noted that many of the unique behaviors of the MaSMi-60 may be a result of the thruster's particular design and, as it is the only sub-400 W MS thruster currently available for testing, it is difficult to discern general physics trends against individual thruster behaviors. In the following paragraphs, an effort was made to focus solely on general physics portrayed by the MaSMi-60 rather than observations that can be attributed to the thruster's specific design.

One key difference between high- and low-power MS Hall thrusters can be seen in the ionization fraction and the related propellant utilization. The small channel dimensions of low-power thrusters yield a narrow axial region of high electron density in the near-anode and mid-

channel regions, effectively shortening the ionization zone. This effect may exist in many, if not all, low-power Hall thrusters and mitigation techniques in the form of creative anode designs or longer channel lengths have been demonstrated; however, a small discharge channel combined with a miniature scale MS field topology yields unique physics [124,127]. The magnetic field gradients in a shielded Hall thruster are inherently steeper than in a similarly sized unshielded device [79]. Additionally, these gradients are notably steeper in low-power Hall thrusters than in high-power devices solely based on scale length arguments [79]. This feature of low-power MS Hall thrusters causes a further reduction in the probability for ionization, yielding decreased mass utilization. By contrast, high-power MS devices benefit from physically larger dimensions (specifically, longer and wider discharge channels), enabling sufficiently long ionization zones to be established.

Another effect of low-power magnetic shielding was a significant increase in discharge current oscillations relative to unshielded low-power Hall thrusters [47,58]. While the character of these oscillations appear to be related to the thruster's breathing mode, the specific reason for the increase in oscillation magnitude relative to unshielded devices has not been conclusively identified. The evidence presented in Chapter 7 suggests that the cause may be an insufficient magnetic field strength across the discharge channel. Large discharge current oscillations are observed in Hall thrusters with the application of both too much field strength (high oscillations enable enhanced electron conductivity across strong fields) and insufficient field strength (free electron streaming across weak fields promote increased predator-prey oscillations); the latter case is more likely given the MaSMi-60's inability to achieve a minimum discharge current as a function of magnetic field setting across the majority of the examined operating range [125]. This poses a significant obstacle for low-power MS Hall thruster development as a variety of

unique challenges are associated with achieving high field strengths in miniature MS Hall thrusters, as described in [79].

In summary, the experimental and computational investigation of the MaSMi-60 suggests that the global plasma physical phenomena governing magnetic shielding are achievable at the miniature scale. However, unique physical mechanisms appear to be encountered when MS is applied to low-power Hall thrusters, making the design and development of such devices challenging.

8.7. Concluding Remarks

The computational modeling of the MaSMi-60's discharge plasma using Hall2De was the focus of this chapter. The conditions for magnetic shielding, namely low electron temperature and constant plasma potential along the discharge channel walls, were predicted by the codes for the MaSMi-60, offering further evidence that a fully shielded field topology was achieved. Hall2De also predicted zero net erosion of the discharge channel walls based on the total kinetic energy of ions incident on the channel surfaces. The physics governing the low mass utilization, current utilization, and beam divergence efficiency experimentally demonstrated by the MaSMI-60 were identified via Hall2De simulations and explained via simplified physics-based models of the thruster's discharge plasma. Results from these models were compared to measurements and simulations of the H6MS, leading to a better understanding of the unique physical mechanisms encountered at the miniature scale. Code validation efforts showed that the Hall2De simulations had minimal sensitivity to the anomalous collision profile (a key source of uncertainty in the simulations). Electron temperature and plasma potential measurements taken in the MaSMi-60's near-plume region matched well the scaled simulation's results, offering some confidence in Hall2De's results. An overview of the similar and unique plasma physics resulting

from applying magnetic shielding to low-power Hall thrusters was also presented. The concluding statements for this dissertation and suggestions for future low-power magnetically shielded Hall thruster efforts follow in Chapter 9.

Chapter 9

CONCLUSION

The primary goal of this dissertation, to investigate the miniature-scale application of magnetic shielding to extend the operational lifetime of low-power Hall thrusters, has been accomplished. The scalability of magnetic shielding to low-power Hall thrusters was first examined through the development of the MaSMi-40. A second design iteration, the MaSMi-60, successfully demonstrated magnetic shielding over a discharge power range of 160 W to nearly 750 W. These findings were confirmed both experimentally, through measurements of the near-plume plasma parameters, and computationally, through the simulation of the MaSMi-60 using a validated plasma modeling code. The experimental and computational results suggest that the MaSMi-60 generates an over-shielded magnetic field topology, causing a reduction in overall thruster performance (thrust, efficiency, etc.) compared to similarly-sized low-power Hall thrusters. The over-shielded topology did reveal, however, that an optimal magnetic field topology may exist for MS thrusters at nearly all power levels and sizes, suggesting the need to trade the level of channel wall shielding (i.e. operational lifetime) against thruster performance. Discharge channel erosion rates on the MaSMi-60 were shown to be at least one to two orders of magnitude less than unshielded Hall thrusters, signifying dramatically increased operational lifetime of the discharge channel walls. Additionally, several of the key challenges and limitations of magnetic shielding for low-power (<500 W) Hall thrusters were identified.

In the remaining sections of this chapter, the major conclusions from the various sections of this dissertation are summarized. Suggestions for future investigation into low-power applications of magnetic shielding are also proposed.

9.1. The Applicability of Magnetic Shielding to Low-Power Hall Thrusters

The MaSMi-40 and MaSMi-60 Hall thrusters were designed and developed to demonstrate that magnetic shielding could be applied to low-power Hall thrusters. The MaSMi-40 generated a partially-shielded field topology; the outer discharge channel wall showed evidence of strong shielding while the inner wall appeared to be weakly shielded, suggesting an asymmetric field topology across the discharge channel gap. The thruster's performance was measured at two experimental facilities, resulting in a peak thrust of approximately 13 mN at a specific impulse of approximately 1,100 s and an anode efficiency of approximately 22%. The causes of the asymmetric magnetic field topology in the MaSMi-40 were identified, leading to the development of a second-generation low-power magnetically shielded Hall thruster.

The MaSMi-60 successfully demonstrated a fully shielded magnetic field topology at low operational powers ranging from 160 W to nearly 750 W. These operating conditions corresponded to thrusts ranging from approximately 8 mN to 33 mN, anode specific impulses of up to approximately 1370 s, and anode efficiencies of over 28% . The magnetic shielding of the MaSMi-60 was experimentally confirmed by visual observations of the discharge plasma, carbon deposition patterns on the discharge channel walls after operation, and calculated discharge channel erosion rates based on carbon backsputter measurements. The thruster showed a reduction in channel wall erosion by a factor of approximately 10x-100x compared to unshielded devices, suggesting an increase in useful life of the discharge channel of the same order**.** These

results were confirmed with an experimentally validated computational model of the discharge plasma inside and downstream of the MaSMi-60's exit plane; low electron temperatures and constant plasma potential along the discharge channel walls were predicted, satisfying the requirements for magnetic shielding, along with zero net erosion of the channel surfaces.

9.2. Physics and Limitations of Magnetic Shielding at Low Powers

The demonstration of magnetic shielding on the MaSMi-60 led to an investigation into the plasma's physical behaviors inside the discharge channel. A comparison of plasma simulations of the low-power MaSMi-60 and the low-power H6MS showed that the physics governing magnetic shielding were maintained at the low-power regime. Several unique physical mechanisms leading to low mass and current utilization as well as high beam divergence in the MaSMi-60 were identified at the miniature scale. However, because the MaSMi-60 attained the necessary conditions for MS (low electron temperature and a plasma potential near that of the discharge voltage along the channel walls), low erosion rates of the discharge channel and an associated extension of the thruster channel's predicted useful life resulted.

It should be noted that significant pole erosion was observed after operation of the MaSMi-60, which is believed to be associated with the excessive curvature (over-shielding) of the magnetic field topology around the downstream edges of the discharge channel. While further investigation into this phenomenon beyond the scope of this thesis, similar erosion has been observed in low-power MS Hall thrusters and is currently a major topic of study.

As a consequence of this research, several limitations to the scalability of magnetic shielding were discovered. Because these findings contain design-related information about the

MaSMi-60, which is an ITAR-controlled technology, details on these limitations can be found in existing and future ITAR publications [79].

9.3. Proposed Future Work

A solid foundation for the development of low-power magnetically shielded Hall thrusters has been established by the research described in this dissertation. However, numerous related studies are worthy of consideration. These topics include, but are not limited to:

1) **Investigation of Low-power MS Discharge Oscillations and Mode Transitions.** This thesis investigation revealed that both the MaSMi-40 and the MaSMi-60 exhibited unique and interesting plasma behaviors not generally observed in low-power Hall thrusters. These included very high discharge current oscillations, up to 400% of the mean discharge current, and global plasma mode shifts, which corresponded to changes in the thruster's performance. While the potentially detrimental effects of mode transitions have been documented for various Hall thrusters, the possible link between discharge oscillations and pole face erosion (especially in magnetically shielded devices) make this area of research important for the future development of low-power MS devices [103].
2) **Conducting Wall Low-Power MS Hall Thrusters.** Due to the novelty of low-power applications of magnetic shielding, traditional BN discharge channels were used in the testing of the MaSMi Hall thrusters. Studies conducted by Goebel *et al.*, however, have demonstrated that, due to the significantly reduced plasma-wall interactions in MS Hall thrusters, such devices may be operated with discharge channels fabricated from conducting materials such as graphite [73]. The improved thermal emissivity of graphite compared to BN ceramics resulted in significant

reductions in discharge channel temperatures, allowing for higher power operation, with minimal changes to thruster performance. Additionally, conducting materials such as graphite are less expensive and more tolerant to launch loads than ceramics, making them attractive for use on Hall thrusters. This thesis identified that significant challenges exist to maintain low temperatures during operation of a low-power MS Hall thruster. Therefore a high emissivity conducting discharge channel capable of radiating a significant portion of the discharge plasma's thermal loads rather than conducting them to the thruster magnetic circuit would be an important design feature and should be pursued in the near future.

3) **Pole Erosion Physics and Mitigation in Low-Power Magnetically Shielded Hall Thrusters.** While pole face erosion has been identified in both high- and low-power Hall thrusters, qualitative observations suggest that the erosion rates are considerably higher at small thruster scales [102,103]. While engineering solutions to mitigate this erosion have been identified, the physical mechanism responsible for this erosion is still unknown. As this phenomenon appears to be the life-limiting factor for MS Hall thrusters, especially at the low-power scale, investigation into the source of pole erosion in low-power MS Hall thrusters is a crucial area of research.

4) **Low-Power Lensed / Partially Shielded Hall Thrusters.** This thesis investigation was focused on the demonstration of magnetic shielding at miniature thruster scales in an effort to identify and characterize the performance, challenges, and limitations of low-power MS Hall thrusters. While further miniaturization of MS Hall thrusters beyond the scale of the MaSMi-60 (especially for flight applications) appears to be extremely challenging, the development of smaller scale (sub-4 cm discharge channel

outer diameter) devices using a strongly lensed magnetic field topology (i.e. symmetric and partially-shielded) are certainly possible. Such devices may demonstrate lower electron temperatures and a plasma potential nearer to that of the discharge voltage along the channel walls compared to unshielded miniature Hall thrusters. Similar to the benefits of magnetic shielding on the MaSMi-60 and low-power Hall thrusters, the application of a strongly lensed magnetic field topology to a device with a ~50 W to 150 W nominal power could certainly result in favorable performance and lifetimes.

Appendix A

MASMI-60 RETARDING POTENTIAL ANALYZER PROFILES

In Chapter 7, the performance of the MaSMi-60 was presented. A representative plot was shown for the most probable ion potential as the data for each discharge voltage condition was very consistent between power levels. The nine sets of data taken by an RPA for the operating conditions considered are presented here.

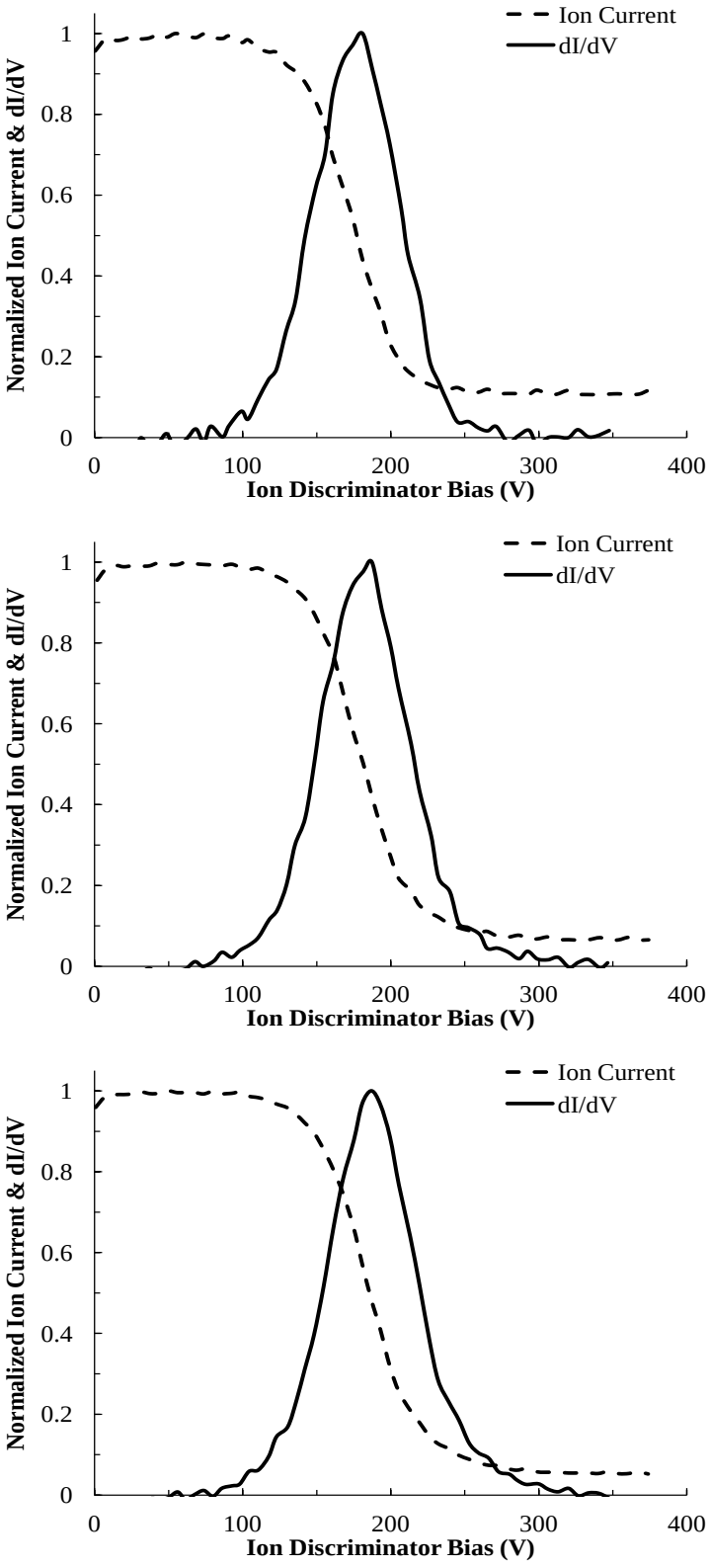

Figure A-1. *Normalized ion current and dI/dV as a function of RPA ion discriminator potential for operation of the MaSMi-60 at 200 V and 250 W (top), 400 W (middle), and 550 W (bottom).*

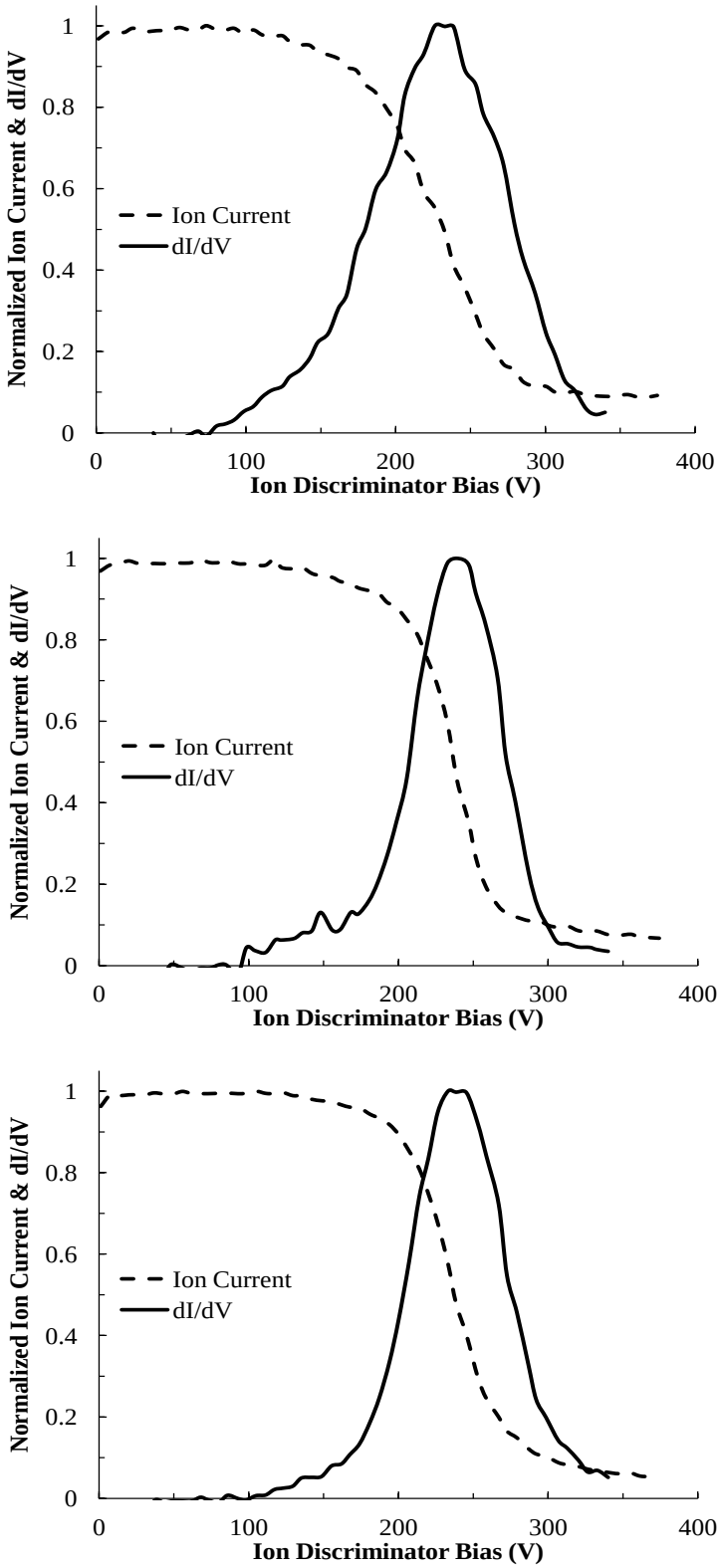

Figure A-2. *Normalized ion current and dI/dV as a function of RPA ion discriminator potential for operation of the MaSMi-60 at 250 V and 250 W (top), 400 W (middle), and 550 W (bottom).*

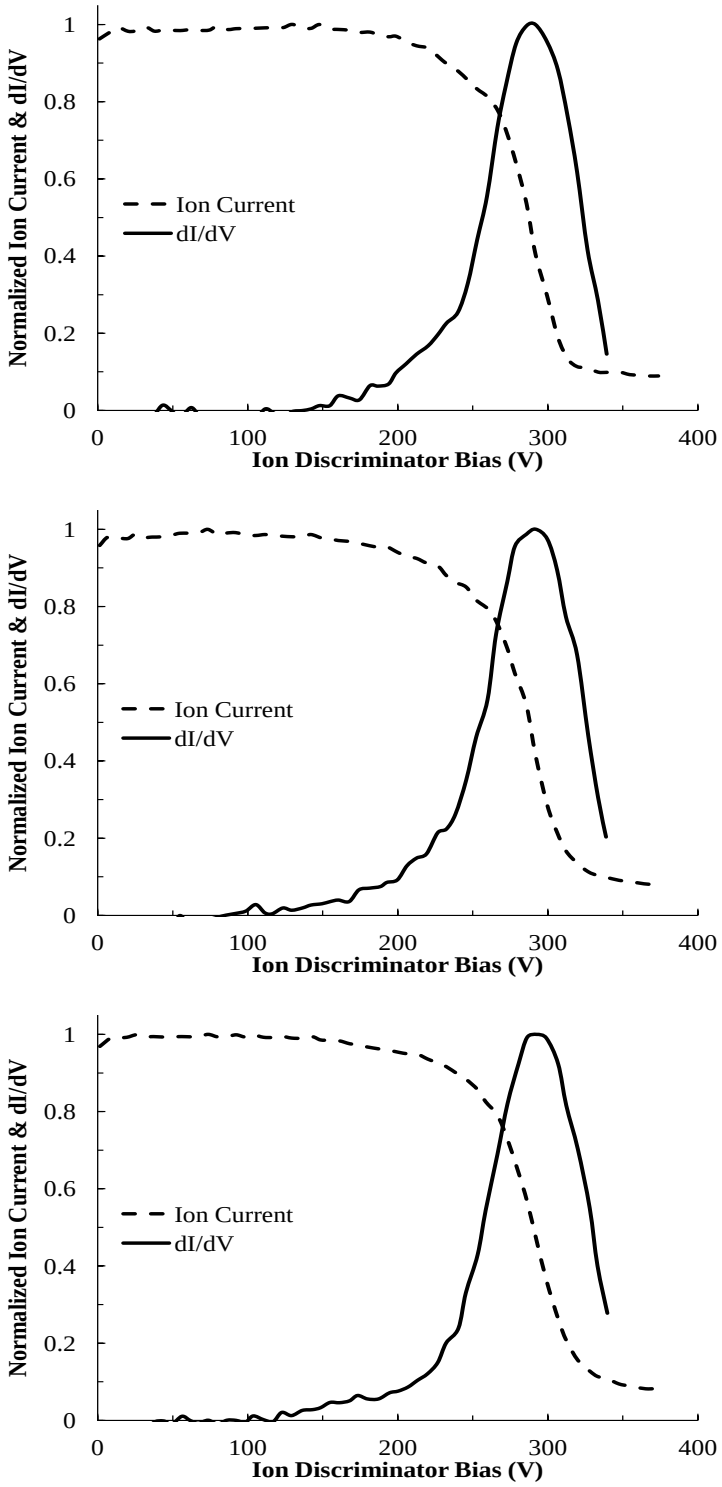

Figure A-3. *Normalized ion current and dI/dV as a function of RPA ion discriminator potential for operation of the MaSMi-60 at 300 V and 250 W (top), 400 W (middle), and 550 W (bottom).*

REFERENCES

[1] Hofer, R. R., Goebel, D. M., Mikellides, I. G., and Katz, I., "Magnetic shielding of a laboratory Hall thruster. II. Experiments," *J. Appl. Phys.*, vol. 115, no. 043303 (2014).

[2] Grys, K. De, Mathers, A., and Welander, B., "Demonstration of 10,400 Hours of Operation on a 4.5 kW Qualification Model Hall Thruster," AIAA-2010-6698, *46th AIAA/ASME/SAE/ASEE Joint Propulsion Conference*, Nashville, TN, Jul. 2010.

[3] Goebel, D. and Katz, I., *Fundamentals of Electric Propulsion: Ion and Hall Thrusters*. Hoboken, NJ: John Wiley & Sons, Inc., 2008.

[4] Goddard, R. H., *The Green Notebooks*. Worchester, MA: The Dr. Robert H. Goddard Collection at the Clark University Archives, 1906.

[5] Mel'kumov, T. M., *Pioneers of Rocket Technology*. Moscow: Academy of Sciences of the USSR, Institute for the History of National Science and Technology, 1964.

[6] Stuhlinger, E., *Ion Propulsion for Space Flight*. New York: McGraw-Hill, 1964.

[7] Jahn, R. G., *Physics of Electric Propulsion*. New York: McGraw-Hill, 1968.

[8] Brewer, G. R., *Ion Propulsion Technology and Applications*. New York: Gordon and Breach, 1970.

[9] Kaufman, H. R., "Technology of Electron-Bombardment Ion Thrusters," *Adv. Electron. Electron Phys.*, vol. 36, (1974).

[10] Turchi, P. J., "Electric Rocket Propulsion Systems," in *Space Propulsion Analysis and Design*, R. W. Humble, G. N. Henry, and W. J. Larson, Eds. New York: McGraw-Hill, 1995.

[11] Wertz, J. R. and Larson, W. J., *Spacecraft Mission Analysis and Design*. New York: Springer Publishing Co., 1999.

[12] Sutton, G. P. and Biblarz, O., *Rocket Propulsion Elements*. New York: John Wiley & Sons, Inc., 2001.

[13] Boever, A. S., Kim, V., Koroteev, A. S., Latyshev, L. A., Morozov, A. I., Popov, G. A., Rylov, Y. P., and Zhurin, V. V, "State of the Works of Electric Thrusters in the USSR," IEPC-91-003, *22nd International Electric Propulsion Conference*, Viareggio, Italy, 1991.

[14] Pidgeon, D. J., Corey, R. L., Sauer, B., and Day, M. L., "Two Years On-Orbit Performance of SPT-100 Electric Propulsion," AIAA-2006-5353, *24th AIAA International Communications Satellite Systems Conference,* San Diego, CA, 2006.

[15] Shimada, S., Dato, K., Takegahara, H., and Kajiwara, K., "20-mN Class Xenon Ion Thruster for ETS-VI," AIAA-1987-1029, *19th International Electric Propulsion Conference*, Colorodo Springs, CO, 1987.

[16] Beattie, J. R., "XIPS Keeps Satellites on Track," *The Industrial Physicist*, Jun-1998.

[17] Brophy, J. R., "NASA's Deep Space 1 Ion Engine," *Rev. Sci. Instrum.*, vol. 73, no. 2 (2002).

[18] Kuninaka, H., Nishiyama, K., Funakai, I., Tetsuya, Shimizu, Y., and Kawaguchi, J., "Asteroid Rendezvous of HAYABUSA Explorer Using Microwave Discharge Ion Engines," IEPC-2005-10, *29th International Electric Propulsion Conference*, Princeton University, NJ, Oct. 2005.

[19] Koppel, C. and Estublier, D., "The SMART-1 Hall Effect Thruster Around the Moon: In Flight Experience," IEPC-2005-119, *29th International Electric Propulsion Conference*, Princeton University, NJ, Oct. 2005.

[20] Brophy, J. R., Rayman, M. D., and Pavri, B., "Dawn: An ion-propelled journey to the beginning of the solar system," IEEEAC-2008-1504, *IEEE Aerospace Conference Proceedings*, 2008.

[21] Brophy, J. R., Garner, C. E., and Mikes, S. C., "Dawn Ion Propulsion System: Initial Checkout After Launch," *J. Propuls. Power*, vol. 25, no. 6 (2009).

[22] Garner, C. E., Rayman, M. D., Brophy, J. R., and Mikes, S. C., "In-Flight Operation of the Dawn Ion Propulsion System Through Orbit Capture at Vesta," AIAA 2011-5661, *47th AIAA/ASME/SAE/ASEE Joint Propulsion Conference & Exhibit*, San Diego, CA, Jul. 2011.

[23] Brophy, J., "The Dawn ion propulsion system," *Space Sci. Rev.*, vol. 163, no. 1–4 (2011).

[24] Garner, C. E., Rayman, M. D., Brophy, J. R., and Mikes, S. C., "In-Flight Operation of the Dawn Ion Propulsion System Through the Preparations for Escape From Vesta," AIAA-2012-4182, *48th AIAA Joint Propulsion Conference*, Atlanta, GA, Jul. 2012.

[25] Garner, C. E., Rayman, M. D., and Brophy, J. R., "In - Flight Operation of the Dawn Ion Propulsion System Through Year One of Cruise to Ceres," AIAA-2007-4112, *49th AIAA/ASME/SAE/ASEE Joint Propulsion Conference*, San Jose, CA, Jul. 2013.

[26] Kim, V., Popov, G., Arkhipov, B., Murashko, V., Gorshkov, O., Koroteyev, A., Garkusha, V., Semenkin, A., and Tverdokhlebov, S., "Electric Propulsion Activity in Russia," IEPC-01-05, *27th International Electric Propulsion Conference*, Pasadena, CA, Oct. 2001.

[27] Hofer, R. R., "Development and Characterization of High-Efficiency, High-Specific Impulse Xenon Hall Thrusters," University of Michigan, 2004.

[28] Reid, B. M., "The Influence of Neutral Flow Rate in the Operation of Hall Thrusters," 2009.

[29] Grishin, S. and Leskov, L., *Electrical Rocket Engines of Space Vehicles*. Moscow: Mashingstroyeniye Publishign House, 1989.

[30] Zhurin, V., Kaufman, H. R., and Robinson, R., "Physics of Closed-Drift Thrusters," *Plasma Sources Sci. Technol.*, vol. 8, no. 1 (1999).

[31] King, L. B., "A (Re-) examination of electron motion in Hall thruster," IEPC-2005-258, *29th International Electric Propulsion Conference*, Princeton University, NJ, Oct. 2005.

[32] Kaufman, H. R., "Technology of Closed-Drift Thrusters," *AIAA J.*, vol. 23, no. 1 (1985).

[33] Kim, V., "Main Physical Features and Processes Determining the Performance of Stationary Plasma Thrusters," *J. Propuls. Power*, vol. 14, no. 5 (1998).

[34] Morozov, A. I. and Savelyev, V., "Fundamentals of Stationary Plasma Thruster Theory," *Rev. Plasma Phys.*, vol. 21, (2000).

[35] Brophy, J., Barnett, J., Sankovic, and Barnhart, D., "Performacne of the Stationary Plasma Thruster: SPT-100," AIAA-92-3155, *28th AIAA/ASME/SAE/ASEE Joint Propulsion Conference*, Nashville, TN, Jul. 1992.

[36] Arhipov, B., Krockak, L., Kudriavcev, S., Murashko, V., and Randolph, T., "Investigation of the Stationary Plasma Thruster (SPT-100) Characteristics and Thermal Maps at the Raised Discharge Power," AIAA-98-3791, *34th AIAA Joint Propulsion Confernece Confernece*, Cleveland, OH, Jul. 1998.

[37] Hofer, R. R., Goebel, D. M., Mikellides, I. G., and Katz, I., "Design of a Laboratory Hall Thruster with Magnetically Shielded Channel Walls , Phase II : Experiments," AIAA-2012-3788, *48th AIAA/ASME/SAE/ASEE Joint Propulsion Conference*, Atlanta, GA, Jul. 2012.

[38] Mikellides, I. G., Katz, I., Hofer, R. R., Goebel, D. M., de Grys, K., and Mathers, A., "Magnetic shielding of the channel walls in a Hall plasma accelerator," *Phys. Plasmas*, vol. 18, no. 033501 (2011).

[39] Mikellides, I. G., Katz, I., Hofer, R. R., and Goebel, D. M., "Magnetic shielding of walls from the unmagnetized ion beam in a Hall thruster," *Appl. Phys. Lett.*, vol. 102, no. 023509 (2013).

[40] Hofer, R. R., Mikellides, I. G., Katz, I., and Goebel, D. M., "BPT-4000 Hall thruster discharge chamber erosion model comparison with qualification life test data," *30th International Electric Propulsion Conference*, Florence, Italy, Sep. 2007.

[41] Ahedo, E. and Gallardo, J. M., "Scaling Down Hall Thrusters," IEPC-2003-104, *28th International Electric Propulsion Conference*, Toulouse, France, Mar. 2003.

[42] Ito, T., Gascon, N., Crawford, W. S., and Cappelli, M. a., "Experimental Characterization of a Micro-Hall Thruster," *J. Propuls. Power*, vol. 23, no. 5 (2007).

[43] Ito, T., Gascon, N., Crawford, W. S., and Cappelli, M. A., "Further Development of a Micro Hall Thruster," AIAA-2006-4495, *42nd AIAA/ASME/SAE/ASEE Joint Propulsion Conference*, Sacramento, CA, Jul. 2006.

[44] Hruby, V., Monheiser, J., Pote, B., Kolencik, J., Freeman, C., and Rostler, P., "Development of Low Power Hall Thrusters," AIAA-99-3534, *30th Plasmadynamics and Lasers Conference*, Norfolk, VA, Jul. 1999.

[45] Smirnov, A., Raitses, Y., and Fisch, N. J., "Parametric investigation of miniaturized cylindrical and annular Hall thrusters," *J. Appl. Phys.*, vol. 92, no. 10 (2002).

[46] Hargus, W. A. and Charles, C. S., "Near Exit Plane Velocity Field of a 200 W Hall Thruster," AIAA-2003-5154, *39th AIAA/ASME/SAE/ASEE Joint Propulsion Conference*, Huntsville, AL, Jul. 2003.

[47] Beal, B., Gallimore, A., and Hargus, W. A., "Preliminary Plume Characterization of a Low-Power Hall Thruster Cluster," AIAA-2002-4251, *38th AIAA/ASEE/SAE/ASME Joint Propulsion Confernece*, Indianapolis, ID, Jul. 2002.

[48] Cheng, S. and Martinez-Sanchez, M., "Hybrid Particle-in-Cell Erosion Modeling of Two Hall Thrusters," *J. Propuls. Power*, vol. 24, no. 5 (2008).

[49] Kim, V., "Stationary Plasma Thrusters in Russia : Problems and Perspectives," *J. Tr. MAI (Moscow Aviat. Institute)*, vol. 60, (2014).

[50] Conversano, R. W. and Wirz, R. E., "CubeSat Lunar Mission Using a Miniature Ion Thruster," AIAA-2007-6083, *47th AIAA/ASME/SAE/ASEE Joint Propulsion Conference*, San Diego, CA, Jul. 2011.

[51] Conversano, R. W. and Wirz, R. E., "Mission Capability Assessment of CubeSats Using a Miniature Ion Thruster," *J. Spacecr. Rockets*, vol. 50, no. 5 (2013).

[52] Wirz, R., Polk, J., Marrese, C., Mueller, J., Escobedo, J., and Sheehan, P., "Development and Testing of a 3cm Electron Bombardment Micro-Ion Thruster," IEPC-01-343, *27th International Electric Propulsion Conference*, Pasadena, CA, Oct. 2001.

[53] Wirz, R., Gale, M., Mueller, J., and Marrese, C., "Miniature Ion Thrusters for Precision Formation Flying," AIAA-2004-4115, *40th AIAA/ASMA/SAE/ASEE Joint Propulsion Conference*, Fort Lauderdale, FL, Jul. 2004.

[54] Wirz, R., "Computational Modeling of a Miniature Ion Thruster Discharge," AIAA-2005-3887, *41st AIAA/ASME/SAE/ASEE Joint Propulsion Conference*, Tucson, AZ, Jul. 2005.

[55] Wirz, R., "Discharge Plasma Processes of Ring-Cusp Ion Thrusters," California Institute of Technology, 2005.

[56] Wirz, R., Sullivan, R., Przybylowski, J., and Silva, M., "Hollow Cathode and Low-Thrust Extraction Grid Analysis for a Miniature Ion Thruster," *Int. J. Plasma Sci. Eng.*, vol. 2008, no. 693825 (2008).

[57] Wirz, R., Polk, J., Marrese, C., and Mueller, J., "Experimental and Computational Investigation of the Performance of a Micro-Ion Thruster," AIAA-2002-3835, *38th AIAA/ASME/SAE/ASEE Joint Propulsion Conference*, Indianapolis, ID, Jul. 2002.

[58] Jacobson, T. and Jankovsky, R., "Test Results of a 200W Class Hall Thruster," AIAA-98-3792, *34th AIAA Joint Propulsion Confernece*, Cleveland, OH, Jul. 1998.

[59] Misuri, T. and Battista, F., "HET Scaling Methodology : Improvement and Assessment," AIAA-2008-4806, *44th AIAA/ASME/SAE/ASEE Joint Propulsion Conference*, Hartford, CT, Jul. 2008.

[60] Battista, F., Marco, E. A. De, Misuri, T., and Andrenucci, M., "A Review of the Hall Thruster Scaling Methodology," *30th International Electric Propulsion Conference*, Firenze, Italy, Sep. 2007.

[61] Guerrini, G., Michaut, C., and Bacal, M., "Parameter Analysis of Three Small Ion Thrusters (SPT-20, SPT-50, A-3)," *2nd European Spacecraft Propulsion Conference*, 1997.

[62] Eytan, R., Lev, D., Alon, G., Warshavsky, A., Kapulkin, A., and Rubanovitz, M., "Wall Material Selection Process for CAM200 Low Power Hall Thruster," IEPC-2015-103 / ISTS-2015-b-103, *34th International Electric Propulsion Conference*, Kobe, Japan, Jul. 2015.

[63] Potapenko, M. Y., Gopanchuk, V. V., and Olotin, S. V., "PlaS-40 Development Status : New Results," IEPC-2015-99 / ISTS-2015-b-99, *34th International Electric Propulsion Conference*, Kobe, Japan, Jul. 2015.

[64] Misuri, T., Ducci, C., Albertoni, R., Andrenucci, M., and Pedrini, D., "Sitael Low Power Hall Effect Thrusters for Small Satellites," IEPC-2015-102 / ISTS-2015-b-102, *34th International Electric Propulsion Conference*, Kobe, Japan, Jul. 2015.

[65] Matlock, T. S., Hargus, W. A., and Larson, C. W., "Thermographic Characterization and Comparison of 200W and 600W Hall Thrusters," AIAA-2007-5241, *43rd AIAA/ASME/SAE/ASEE Joint Propulsion Conference*, Cincinnati, OH, Jul. 2007.

[66] Nakles, M. R., Brieda, L., Reed, G. D., Hargus Jr., W. A., and Spicer, R. L., "Experimental and Numerical Examination of the BHT-200 Hall Thruster Plume," AIAA-2007-5305, *43rd AIAA/ASME/SAE/ASEE Joint Propulsion Conference*, Cincinnati, OH, Jul. 2007.

[67] Azziz, Y., "Instrument Development and Plasma Measurements on a 200-Watt Hall Thruster Plume," Massachusetts Institute of Technology, 2003.

[68] Lowry, A., "BHT-200 Hall Effect Thruster." High-Power Electric Propulsion Laboratory, Georgia Insitute of Technology.

[69] Kamhawi, H., Haag, T. W., Jacobson, D. T., and Manzella, D. H., "Performance Evaluation of the NASA-300M 20 kW Hall Effect Thruster," AIAA-2011-5521, *47th AIAA/ASME/SAE/ASEE Joint Propulsion Conference*, San Diego, CA, 2011.

[70] Hofer, R. R., Jorns, B. A., Polk, J. E., Mikellides, I. G., and Snyder, J. S., "Wear test of a magnetically shielded Hall thruster at 3000 seconds specific impulse," IEPC-2013-033, *33rd International Electric Propulsion Conference*, Washington D.C., Oct. 2013.

[71] Goebel, D. M., Hofer, R. R., Mikellides, I. G., Katz, I., Polk, J. E., and Dotson, B. N., "Conducting Wall Hall Thrusters," IEPC-2013-276, *33rd International Electric Propulsion Conference*, Washington D.C., 2013.

[72] Mikellides, I. G., Hofer, R. R., Katz, I., and Goebel, D. M., "The Effectiveness of Magnetic Shielding in High-Isp Hall Thrusters," AIAA-2013-3885, *49th AIAA/ASME/SAE/ASEE Joint Propulsion Conference*, San Jose, CA, 2013.

[73] Goebel, D. M., Hofer, R. R., Mikellides, I. G., Katz, I., Polk, J. E., and Dotson, B. N., "Conducting Wall Hall Thrusters," *IEEE Trans. Plasma Sci.*, vol. 43, no. 1 (2015).

[74] Conversano, R. W., Goebel, D. M., Hofer, R. R., Matlock, T. S., and Wirz, R. E., "Development and Initial Testing of a Magnetically Shielded Miniature Hall Thruster," *IEEE Trans. Plasma Sci.*, vol. 43, no. 1 (2015).

[75] Conversano, R. W., Goebel, D. M., Mikellides, I. G., Hofer, R. R., Matlock, T. S., and Wirz, R. E., "Magnetically Shielded Miniature Hall Thruster: Performance Assessment and Status Update," AIAA-2014-3896, *50th AIAA/ASME/SAE/ASEE Joint Propulsion Conference*, Cleveland, OH, Jul. 2014.

[76] Morozov, A. I., "Focusing of Cold Quasineutral Beams in Electromagnetic Fields," *Sov. Phys. - Dokl.*, vol. 10, no. 8 (1966).

[77] Morozov, A. I., Esipchuk, Y. V, Tilinin, G. N., Trofimov, A. V, Sharov, Y. A., and Shchepkin, G. Y., "Plasma Accelerator with Closed Electron Drift and Extended Acceleration Zone," *Sov. Phys. - Tech. Phys.*, vol. 17, no. 1 (1972).

[78] Mikellides, I. G., Katz, I., Hofer, R. R., and Goebel, D. M., "Magnetic shielding of a laboratory Hall thruster. I. Theory and validation," *J. Appl. Phys.*, vol. 115, no. 043303 (2014).

[79] Conversano, R. W., Goebel, D. M., Hofer, R. R., Mikellides, I. G., Katz, I., and Wirz, R. E., "Development and Validation Overview for the Design of Low Power Magnetically Shielded Hall Thrusters," *62nd JANNAF Propulsion Meeting*, Nashville, TN, Jun. 2015.

[80] Garnier, Y., Veil, V., Roussel, J. F., and Bernard, J., "Low Energy Xenon Ion Sputtering of Ceramics Investigated for Stationary Plasma Thrusters," *J. Vac. Sci. Technol. A*, vol. 17, no. 6 (1999).

[81] Mikellides, I. G., Katz, I., and Hofer, R. R., "Design of a Laboratory Hall Thruster with Magnetically Shielded Channel Walls , Phase I : Numerical Simulations," AIAA-2011-5809, *47th AIAA/ASME/SAE/ASEE Joint Propulsion Conference*, San Diego, CA, Jul. 2011.

[82] Sommerville, J. D. and King, L. B., "Hall-Effect Thruster--Cathode Coupling, Part I: Efficiency Improvements from an Extended Outer Pole," *J. Propuls. Power*, vol. 27, no. 4 (2011).

[83] Sommerville, J. D. and King, L. B., "Hall-Effect Thruster--Cathode Coupling, Part II: Ion Beam and Near-Field Plume," *J. Propuls. Power*, vol. 27, no. 4 (2011).

[84] Tartz, M. and Neumann, H., "Sputter Yields of Carbon Materials under Xenon Ion Incidence," *Plasma Process. Polym.*, vol. 4, no. S1 (2007).

[85] Day, M., Maslennikov, N., Randolph, T., and Rogers, W., "SPT-100 Subsystem Qualification Status," AIAA-96-2713, *32nd AIAA/ASME/SAE/ASEE Joint Propulsion Conference*, Buena Vista, FL, Jul. 1996.

[86] Nakles, M. R., Hargus, W. A., Delgado, J. J., and Corey, R. L., "A Performance and Plume Comparison of Xenon and Krypton Propellant on the SPT-100," AIAA 2012-4116, *48th AIAA/ASME/SAE/ASEE Joint Propulsion Conference*, Atlanta, GA, Jul. 2012.

[87] Corey, R. L. and Pidgeon, D. J., "Electric Propulsion at Space Systems/Loral," IEPC-2009-270, *The 31st International Electric Propulsion Conference*, Ann Arbor, MI, Sep. 2009.

[88] Ekholm, J. M. and Hargus, W. A., "E × B Measurements of a 200 W Xenon Hall Thruster," AIAA-2005-4405, *41st AIAA/ASME/SAE/ASEE Joint Propulsion Conference*, Tucson, AZ, Jul. 2005.

[89] Brown, D. L., Larson, C. W., Beal, B. E., and Gallimore, A. D., "Methodology and Historical Perspective of a Hall Thruster Efficiency Analysis," *J. Propuls. Power*, vol. 25, no. 6 (2009).

[90] Shastry, R., Hofer, R. R., Reid, B. M., and Gallimore, A. D., "Method for analyzing E x B probe spectra from Hall thruster plumes.," *Rev. Sci. Instrum.*, vol. 80, no. 063502 (2009).

[91] Sheridan, T. E., "How big is a small Langmuir probe?," *Phys. Plasmas*, vol. 7, no. 7 (2000).

[92] Hofer, R. R., Haas, J. M., and Gallimore, A., "Ion voltage diagnostics in the far-field plume of a high-specific impulse Hall thruster," AIAA-2003-4556, *39th AIAA/ASME/SAE/ASEE Joint Propulsion Conference*, Huntsville, AL, 2003.

[93] Chu, E., Goebel, D. M., and Wirz, R. E., "Reduction of Energetic Ion Production in Hollow Cathodes by External Gas Injection," *J. Propuls. Power*, vol. 29, no. 5 (2013).

[94] Hutchinson, I. H., *Principles of Plasma Dynamics, Second Edition*. Cambridge: Cambridge University Press, 2002.

[95] Lemmer, K. M., Gallimore, A. D., Smith, T. B., and Austin, D. R., "Review of Two Retarding Potential Analyzers for Use in High Density Helicon Plasma," IEPC-2007-161, *30th International Electric Propulsion Conference*, Florence, Italy, 2007.

[96] Enloe, C. L. and Shell, J. R., "Optimizing the Energy Resolution of Planar Retarding Potential Analyzers," *Rev. Sci. Instrum.*, vol. 63, no. 2 (1992).

[97] Chen, F., "Electric Probes," in *Plasma Diagnostics Techniques*, R. Huddelstone and S. Leonard, Eds. New York, NY: Academic Press, 1966.

[98] Bohm, D., *The Characteristics of Electrical Discharges in Magnetic Fields*. New York, NY: McGraw-Hill, 1949.

[99] Jameson, K. K., "Investigation of Hollow Cathode Effects on Total Thruster Efficiency in a 6 kW Hall Thruster," University of California, Los Angeles, 2008.

[100] Azziz, Y. and Martinez-sanchez, M., "Experimental and Theoretical Characterization of a Hall Thruster Plume," Massachusetts Institute of Technology, 2007.

[101] Matlock, T. S., "An Exploration of Prominent Cusped-Field Thruster Phenomena : The Hollow Conical Plume and Anode Current Bifurcation," 2012.

[102] Conversano, R. W., Goebel, D. M., Hofer, R. R., Mikellides, I. G., Katz, I., and Wirz, R. E., "Magnetically Shielded Miniature Hall Thruster: Design Improvement and Performance Analysis," IEPC-2015-100 / ISTS-2015-b-100, *34th International Electric Propulsion Conference*, Kobe, Japan, Jul. 2015.

[103] Goebel, D. M., Jorns, B. a., Hofer, R. R., Mikellides, I. G., and Katz, I., "Pole-piece Interactions with the Plasma in a Magnetically Shielded Hall Thruster," AIAA 2014-3899, *50th AIAA/ASME/SAE/ASEE Joint Propulsion Conference*, Cleveland, OH.

[104] Shastry, R., Huang, W., Haag, T. W., and Kamhawi, H., "Langmuir Probe Measurements Within the Discharge Channel of the 20-kW NASA-300M and NASA-300MS Hall Thrusters," IEPC-2013-122, *33rd International Electric Propulsion Conference*, Washington D.C., Oct. 2013.

[105] Katz, I., Mikellides, I. G., Jorns, B. A., and Ortega, A. L., "Hall2De Simulations with an Anomalous Transport Model Based on the Electron Cyclotron Drift Instability," IEPC-2015-402 / ISTS-2015-b-402, *34th International Electric Propulsion Conference*, Kobe, Japan, Jul. 2015.

[106] Morozov, A. I. and Melikov, I. V, "Similitude in Hall-Current Plamsa Accelerators," *Zhurnal Tekhnicheskoi Fiz.*, vol. 44, (1974).

[107] Iakunin, S. A., Sveshnikov, A. G., Morozov, A. I., and Volkov, B. I., "Numerical modeling of ion dynamics in a plasma accelerator with azimuthal electron drift," *Vychislitel'nye Metod. i Program.*, vol. 32, (1980).

[108] Volkov, B. I., Morozov, A. I., Sveshnikov, A. G., and Iakunin, S. A., "Numerical simulation of ion dynamics in closed-drift systems," *Fiz. Plazmy*, vol. 7, (1981).

[109] Hirakawa, M. and Arakawa, Y., "Numerical simulation of plasma particle behavior in a Hall thruster," AIAA-96-3195, *32nd AIAA/ASME/SAE/ASEE Joint Propulsion Conference*, Buena Vista, FL, Jul. 1996.

[110] Fife, J. M., "Hybrid-PIC Modeling and Electrostatic Probe Survey of Hall Thrusters," Massachusetts Institute of Technology, 1998.

[111] Mikellides, I. G. and Katz, I., "Numerical simulations of Hall-effect plasma accelerators on a magnetic-field-aligned mesh," *Phys. Rev. E - Stat. Nonlinear, Soft Matter Phys.*, vol. 86, no. 4 (2012).

[112] Parra, F. I., Ahedo, E., Fife, J. M., and Martinez-sanchez, M., "A Two-Dimensional Hybrid Model of the Hall Thruster Discharge," *J. Appl. Phys.*, vol. 100, no. 023304 (2006).

[113] Mikellides, I. G., Katz, I., Hofer, R. R., and Goebel, D. M., "Hall-Effect Thruster Simulations with 2-D Electron Transport and Hydrodynamic Ions," IEPC-2009-114, *31st International Electric Propulsion Conference*, Ann Arbor, MI, Sep. 2009.

[114] Mikellides, I. G., Katz, I., Hofer, R. R., Goebel, D. M., de Grys, K., and Mathers, A., "Magnetic shielding of the channel walls in a Hall plasma accelerator," *Phys. Plasmas*, vol. 18, no. 033501 (2011).

[115] Katz, I. and Mikellides, I. G., "Neutral gas free molecular flow algorithm including ionization and walls for use in plasma simulations," *J. Comput. Phys.*, vol. 230, no. 4 (2011).

[116] Andrews, J. G. and Varey, R. H., "The sheath at an electrode close to plasma potential," *J. Phys. A Gen. Phys.*, vol. 3, no. 4 (2001).

[117] Mikellides, I. G., Goebel, D. M., Snyder, J. S., Katz, I., and Herman, D. a., "The discharge plasma in ion engine neutralizers: Numerical simulations and comparisons with laboratory data," *J. Appl. Phys.*, vol. 108, no. 11 (2010).

[118] Mikellides, I. G., Katz, I., Goebel, D. M., Jameson, K. K., and Polk, J. E., "Wear Mechanisms in Electron Sources for Ion Propulsion, II: Discharge Hollow Cathode," *J. Propuls. Power*, vol. 24, no. 4 (2008).

[119] Mikellides, I. G., "Effects of viscosity in a partially ionized channel flow with thermionic emission," *Phys. Plasmas*, vol. 16, no. 1 (2009).

[120] Hobbs, G. D. and Wesson, J. a, "Heat flow through a Langmuir sheath in the presence of electron emission," *Plasma Phys.*, vol. 9, no. 85 (1967).

[121] Mikellides, I. G., Hofer, R. R., Katz, I., and Goebel, D. M., "Magnetic shielding of Hall thrusters at high discharge voltages," *J. Appl. Phys.*, vol. 116, no. 053302 (2014).

[122] Mikellides, I. G. and Ortega, A. L., "Assessment of Pole Erosion in a Magnetically Shielded Hall Thruster," AIAA 2014-3897, *50th AIAA/ASME/SAE/ASEE Joint Propulsion Conference*, Cleveland, OH, Jul. 2014.

[123] Ortega, A. L., Mikellides, I. G., and Katz, I., "Hall2De Numerical Simulations for the Assessment of Pole Erosion in a Magnetically Shielded Hall Thruster," IEPC-2015-249 / ISTS-2015-b-249, *34th International Electric Propulsion Conference*, Kobe, Japan, Jul. 2015.

[124] Raitses, Y., Ashkenazy, J., and Guelman, M., "Propellant Utilization in Hall Thrusters," *J. Propuls. Power*, vol. 14, no. 2 (1998).

[125] Hargus, W. A. and Strafaccia, J., "Optical Boron Nitride Insulator Erosion Characterization of a 200 W Xenon Hall Thruster," AIAA-2005-3529, *41st AIAA/ASME/SAE/ASEE Joint Propulsion Conference*, Tucson, AZ, Jul. 2005.

[126] Jorns, B. A., Goebel, D. M., and Hofer, R. R., "Plasma Perturbations in High-Speed Probing of Hall Thruster Discharge Chambers : Quantification and Mitigation," AIAA 2015-4006, *51st AIAA/ASME/SAE/ASEE Joint Propulsion Conference*, Orlando, FL, Jul. 2015.

[127] Monheiser, J., Hruby, V., Freeman, C., Connolly, W., and Pote, B., "Development and Testing of a Low-Power Hall Thruster System," in *Micropropulsion for Small Spacecraft*, M. M. Micci and A. D. Ketsdever, Eds. Washington D.C.: AIAA, 2000.